UNIVERSITY OF LJUBLJANA
FACULTY OF MATHEMATICS AND PHYSICS

Damijan Škrk

Calibration of the Ring Imaging Čerenkov Counter of the HERA-B Spectrometer

DOCTORAL THESIS

SUPERVISOR: PROF. DR. PETER KRIŽAN

Ljubljana, 1999

UNIVERZA V LJUBLJANI
FAKULTETA ZA MATEMATIKO IN FIZIKO

Damijan Škrk

Umeritev detektorja Čerenkovih obročev pri spektrometru HERA-B

DISERTACIJA

MENTOR: PROF. DR. PETER KRIŽAN

Ljubljana, 1999

Doktorsko delo, ki je potekalo v okviru raziskovalnega programa Odseka za eksperimentalno fiziko osnovnih delcev Instituta Jožef Stefan, sem opravil pod mentorstvom prof. dr. Petra Križana. Financiralo ga je Ministrstvo za znanost in tehnologijo Republike Slovenije.

Iskreno se zahvaljujem mentorju prof. dr. Petru Križanu za vso pomoč in prijateljske nasvete.

Neštete zagate in vprašanja sta mi s svojimi bogatimi izkušnjami in znanjem z eksperimentalnega področja pomagala rešiti doc.dr. Samo Korpar in doc.dr. Marko Starič.

Za večkratno skrbno prebiranje rokopisa in številne koristne nasvete se zahvaljujem prof. dr. Alešu Stanovniku.

Juretu Erženu se zahvaljujem za vso tehnično pomoč.

Robertu Jeraju se bi rad zahvalil za ves trud in čas, ki si ga je vzel za pomoč pri oblikovanju tega dela.

Vsem sodelavcem odseka se želim zahvaliti za prijazno ter prijetno delovno vzdušje, ki so ga ustvarili. Še posebej Andreju Gorišku in Roku Pestotniku s katerima sem poleg ostalih članov kolaboracije HERA-B delil dobre in slabe strani dela v tujini.

Na koncu se želim zahvaliti staršema za njuno razumevanje in podporo v času študija.

Abstract

The present doctoral thesis is dedicated to construction of some aspects of the HERA-B spectrometer. An apparatus at DESY in Hamburg, which intends to measure CP symmetry violation in the system of neutral B mesons. The topic of the work is devoted to the calibration of the Ring Imaging Čerenkov counter as part of the HERA-B spectrometer. The work includes the construction of the photon detector module and evaluation of its performance in the electron beam. In addition, measurements of detector response to weak illumination with a controlled light source and to the Čerenkov light, emitted by particles at different interaction rates have been carried out as part of the calibration procedure. The expected detector performance was confirmed by successful detection of Čerenkov rings.

Keywords: ring imaging Čerenkov detector, photomultiplier tubes, HERA-B

Izvleček

Doktorsko delo je povezano z izgradnjo spektrometra HERA-B. Aparatura v DESY v Hamburgu je namenjena meritvi kršitve simetrije CP v sistemu nevtralnih mezonov B. Težišče doktorskega dela je umeritev detektorja Čerenkovih obročev pri spektrometru HERA-B. Delo obsega izdelavo prototipa osnovnega modula fotonskega detektorja ter preizkus delovanja osnovnih komponent v testnem žarku elektronov. V sklopu postopkov za umeritev celotnega detektorja v eksperimentalni dvorani, so bile izvedene meritve odziva detektorja v primeru šibke osvetljenosti s kontrolnim izvorom in meritve odvisnosti odziva od interakcijske pogostosti. Pričakovano delovanje detektorja je bilo potrjeno z uspešnim zaznavanjemČerenkovih obročev.

Ključne besede: števec Čerenkovih obročev, fotopomnoževalka, HERA-B

PACS:

- 20. NUCLEAR PHYSICS
- 29. Experimental methods and instrumentation for elementary particle and nuclear physics
- 29.40.-n Radiation detectors
- 29.40.Ka Cherenkov detectors

Contents

Introduction

One of the most interesting observations in particle physics is the violation of charge conjugation - parity (CP) symmetry. Although CP violation was observed in the neutral K meson decays it is still one of the least understood phenomena within the Standard Model. Neutral B mesons provide one of the other systems in nature, where CP violation might be further investigated and where stringent tests of the Standard Model description of the CP violation mechanism can be made. Unlike in the kaon system, some B decay modes are predicted to show large CP asymmetries whose strength is directly related to the parameters of the Cabibo Kobayashi Maskawa (CKM) matrix without involving poorly known hadronic matrix elements [9].

Most of today's knowledge about B mesons comes from experiments at e^+e^- colliders such as ARGUS,CLEO and LEP experiments. However, CP violation in the B meson system cannot be explored at existing machines but requires high luminosity e^+e^- colliders with different energies of the two colliding beams. Asymmetric B factories of this type have been built at SLAC in California and at KEK in Tsukuba.

Hadron accelerators provide an alternative source of B mesons. About seven years ago a group centered around DESY's Argus Collaboration realized that the HERA storage ring at DESY could be used very effectively as a B hadron factory if operated with an internal fixed target in the beam halo. A proposal for ”An Experiment to Study CP Violation in the B System Using an Internal Target at the HERA Proton Ring” was thus submitted and approved [1].

Although the experiment is primarily optimised for measuring CP violation, it addresses a wide range of topics in heavy quark physics. Other topics which are accessible with HERA-B detector include a measurement of the $\mathrm{B_s^0}$ oscillation frequency, measurement of the CKM matrix parameters $\mathrm{V_{cb}}$ and $\mathrm{V_{ub}}$, the precise measurements of lifetimes of individual beauty mesons and baryons and the whole field of charm physics.

The experience gained at HERA-B will be extremely valuable for the next generation of experiments, which will provide the ultimate precision measurements of CP parameters in B decays, and will allow the most stringent tests of the Standard Model predictions of CP violation and of rare decays. At the same time HERA-B implements most of the technologies required for future dedicated B experiments planned at CERN's Large Hadron Collider (LHC) ring in particular for the LHC-B experiment.

The decay channel, theoretically and experimentally accepted as the best candidate, for the study of CP asymmetries, to which the HERA-B experiment is optimised, is $\mathrm{B}\ \mathrm{or}\ (\overline{\mathrm{B}}^0) \rightarrow \mathrm{J}/\psi + \mathrm{K_s} \rightarrow \ell^+\ell^-\pi^+\pi^-$. CP violation in these decays would thus manifest itself in a difference between the $\mathrm{B}^0\ \mathrm{and}\ \overline{\mathrm{B}}^0$ transition rates. Since the state $\mathrm{J}/\psi\ \mathrm{K_s}$ is a CP eigenstate, the flavour of the B meson has to be tagged. This is performed by identifying the charged kaon into which the associated B meson decayed.

HERA-B is a large acceptance forward spectrometer reflecting the fixed target nature of the experiment. It consists of several detector subsystems which enable identifying, selecting and cleanly reconstructing the B decay modes of interest. The proton beam energy of 920 GeV implies a center of mass energy of approximately 40 GeV. Measurements of the cross section per nucleon for the $\mathrm{b\overline{b}}$ quark production are available from Fermilab fixed target experiments. They are ranging from 6 nb to 42 nb and are in rough agreement with the similar uncertain theoretical expectations [4]. This cross section is about six orders of magnitude smaller than the cross section for normal inelastic proton nucleon scattering at the same center of mass energy. Taking into account the branching ratios into the interesting decay channels $\mathrm{J}/\psi + \mathrm{K_s} \rightarrow \ell^+\ell^-\pi^+\pi^-$, triggering and reconstruction efficiencies, only about one in 10^{12} interactions is useful for the CP measurement. Thus extremely high total interaction rates of 40 MHz are needed to achieve the required event statistics of about 1000 signal decays per year. Each single proton bunch crossing generates tracks in the detector with high particle densities. Such a high radiation environment is thus forcing the HERA-B detector system to cope with very high rates [5].

The main emphasis of the doctoral thesis is given to the Ring Imaging Čerenkov (RICH) detector as a part of the HERA-B spectrometer. The specific task of the RICH detector is to tag the $\mathrm{B}^0\ \mathrm{or}\ \overline{\mathrm{B}^0}$ meson by identifying the charged kaon into which the associated B meson decayed.

In order to identify particles, the RICH technique exploits a feature of high speed particles passing through a medium in which they generate an optical shock wave called Čerenkov radiation. The opening angle of the Čerenkov cone depends on the particle velocity. If the momentum of the particles is accurately measured in other components of the HERA-B detector, separation in velocity is equivalent to separation in mass and hence particle's identity is revealed.

The environment of the experiment, the physics goals and the particle separation needed, together with the available technology, determined the choice of a particular RICH detector construction technique. The main building block of the RICH counter is a vessel filled with $\mathrm{C_4F_{10}}$ radiator gas, where charged particles radiate Čerenkov light which is reflected by spherical and planar mirrors to the photon detector planes. Light photons are detected by a total of 2240 multianode photomultiplier tubes. The inner region of the photon detector uses 16 channel photomultiplier tubes, and outer region uses 4 channel photomultiplier tubes.

It is therefore expected of the RICH counter to be capable of separating kaons from pions over the kaon momentum range from 10 GeV/c to 50 GeV/c and of resolving between particles belonging to successive bunch crossings. This task must be performed reliably over long periods of time in the high radiation environment, which could cause aging or rate problems on the photon detector.

This doctoral thesis is organised as follows. In Chapter 1 the theoretical background of CP symmetry violation is reviewed, including a description of the physics reach of the experiment. The rest of this chapter serves to provide an overview of the HERA-B spectrometer with subsystem design descriptions and their expected performance. Theory explaining Čerenkov radiation phenomena and basic principles behind some of the commonly used types of Čerenkov counters are described in Chapter 2. The design criteria for the HERA-B RICH detector are summarized in Chapter 3. A detailed description of the HERA-B RICH detector follows in Chapter 4 where also technical criteria which governed the component design with a set of installation and commissioning procedures are presented. Tests of the detector prototype with an electron beam is presented in Chapter 5, followed by the first experience with the photon detector imaging properties. Chapter 6 is devoted to measurement and procedures of detector calibration in the experimental area and observation of the Čerenkov ring images. In the conclusion the obtained results are summarised and evaluated. The summary in the Slovene language is given after the conclusions. Additional technical information is given in the appendices at the end.

1

The HERA-B experiment

1.1 The violation of combined charge conjugation and parity symmetry in B meson decays

The large predominance of matter over antimatter in the visible universe and the observed charge conjugation - parity (CP) asymmetry in the neutral K meson decays are two manifestations of CP symmetry violation. In the neutral kaon system CP violation has been clearly observed in the measurement of the parameter ϵ. While the experimental value of quantity ϵ can be accommodated in the Standard Model, it does not by itself test this model [7].

In the Standard model, weak transitions between quarks are parametrised by a unitary 3×3 Cabbibo Kobayashi Maskawa (CKM) matrix of coefficients, which can be symbolically written as

$$V = \begin{pmatrix} V_{ud} & V_{us} & V_{ub} \\ V_{cd} & V_{cs} & V_{cb} \\ V_{td} & V_{ts} & V_{tb} \end{pmatrix} . \tag{1.1}$$

The parametrisation is constructed from the rotation matrices in the flavour space involving three angles and one phase. Matrix elements describing weak decays include CKM factors and terms related to quark wave functions. Descriptions of antiparticle decays differ because there we have to deal with the complex conjugates of the CKM matrix factors if compared to particle decays. So CP symmetry can be violated in decays where amplitudes with different CKM matrix element phases interfere [8].

Studies of CP asymmetries in neutral B decays are expected to provide an observation of CP violation in a new system and are subject to a clean theoretical interpretation. They test whether the single phase of the CKM matrix is the only source of CP violation [9].

The CKM matrix elements obey unitary constraints which lead to six orthogonality conditions

$$\sum_k V_{ki}^* V_{kj} = \delta_{ij}. \tag{1.2}$$

One of the most interesting unitary conditions for CKM matrix is

$$V_{ud}V_{ub}^* + V_{cd}V_{cb}^* + V_{td}V_{tb}^* = 0, \tag{1.3}$$

where the absolute values of all three factors are of the same order of size. This condition can be visualised as a triangle in the complex plane (see Fig. 1.1). The length of triangle sides can be measured in B meson decays, while all angles are related to the CKM matrix phase. They can be determined by measuring CP violation in the B meson system.

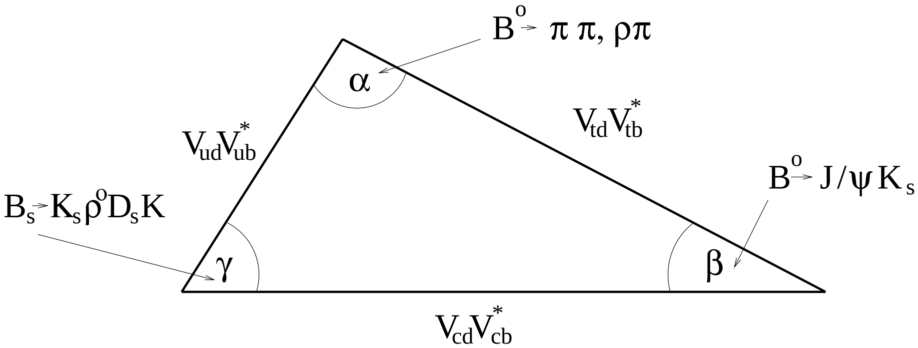

Figure 1.1: Visualisation of the unitarity condition as a triangle in the complex plane. The length of triangle sides can be measured in B meson transitions, while angles can be independently measured via CP violation measurements in the B meson system.

The measurement of a special neutral B meson decay where a B^0 decays to the CP eigenstate $\mathrm{J}/\psi\ \mathrm{K_s}$ is expected to show strong CP asymmetries directly related to the angle β of the unitarity triangle and so present an important contribution to the understanding of the physics of the CKM matrix and of CP violation.

The two amplitudes interfering to generate a particle antiparticle asymmetry are the direct decay $\mathrm{B}^0 \to \mathrm{J}/\psi\ \mathrm{K_s}$ and the decay through mixing $\mathrm{B}^0 \to \overline{\mathrm{B}}^0 \to \mathrm{J}/\psi\ \mathrm{K_s}$

For beams of B^0 and $\overline{\mathrm{B}}^0$ mesons the decay rates into $\mathrm{J}/\psi\ \mathrm{K_s}$ are given by [9]

$$\begin{aligned} n(t) &\propto e^{-\frac{t}{\tau}}(1+\sin(2\beta)\sin(x\frac{t}{\tau})) \\ \overline{n}(t) &\propto e^{-\frac{t}{\tau}}(1-\sin(2\beta)\sin(x\frac{t}{\tau})). \end{aligned} \tag{1.4}$$

The mixing parameter x is given by the mass difference of the mass eigenstates $\Delta\mathrm{M}$ and by the neutral B mesons lifetime τ as shown in the following equation

$$x = \frac{\Delta M c^2 \tau}{\hbar}. \tag{1.5}$$

The observable asymmetry of the time integrated rates which measures the size of the CP asymmetry is

$$A_{int} = \frac{\int n(t)dt - \int \overline{n}(t)dt}{\int n(t)dt + \int \overline{n}(t)dt} = \frac{x}{1+x^2}\sin(2\beta). \tag{1.6}$$

Thus in order to detect CP violation one needs to measure B^0 and $\overline{\mathrm{B}}^0$ decay rates into $\mathrm{J}/\psi\ \mathrm{K_s}$. The initial flavour of a neutral B meson needs to be determined from the associated B^0 or $\overline{\mathrm{B}}^0$ meson in the event.

1.2 The HERA-B Spectrometer

The Hadron Elektron Ring Anlage (HERA) is a double storage ring at DESY in Hamburg. It is designed for colliding a 920 GeV proton beam with a 30 GeV electron beam. The rings with a length of 6335.8 m, their multi step injector chain and their four interaction regions are shown in Fig. 1.2. The North and the South hall house the collider experiments H1 and ZEUS, while in the other two experimental areas the beams are not brought to collision. The HERMES detector, which is using only the electron beam, is installed in the East hall. Thus the West hall offers space for a fourth experiment, called HERA-B, which is using only the proton beam.

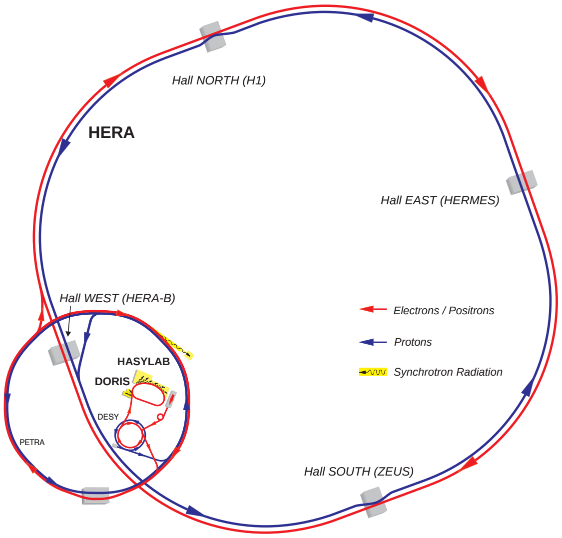

Figure 1.2: Layout of the HERA rings with the location of the four experimental areas.

The HERA-B experiment is designed to search for CP violation in decays of neutral B mesons. The decay $\mathrm{B}^0 \to \mathrm{J}/\psi\ \mathrm{K_s} \to \ell^+\ \ell^-\ \pi^+\ \pi^-$, with multiple leptons in the final state, is accepted as the best candidate, both theoretically and experimentally, for the study of CP asymmetries [3]. The HERA-B spectrometer is thus optimised to detect such, so called ”gold plated ” decays.

The B mesons are produced in interactions of protons in the HERA proton beam with an internal wire target in the beam halo in order not to disturb other experiments. The neutral B meson decaying into the signal channel $J/\psi\ K_s$ has an average momentum of 120 GeV and thus decays after an average flight distance of about 9 mm into J/ψ and a K_s. J/ψ further decays into two leptons, either e^+e^- or $\mu^+\mu^-$, while K_s decays after a typical flight distance of about 1.1 m into charged pions of large momentum. The most powerful tagging methods for the beauty content of the decaying neutral B meson make use of the second beauty particle, i.e. charged or neutral meson or baryon. The cleanest tag, although occurring with rather small probability, is provided by the charge of a lepton with high transverse momentum from the semileptonic decays of the associated B meson. Less clean but more frequent is the tag provided by the charge of a kaon, produced in the subsequent charm decay (see Fig. 1.3).

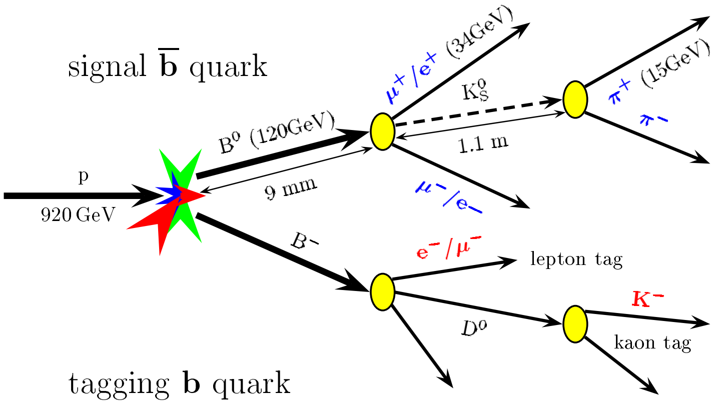

Figure 1.3: The ” gold platted ” $B^0 \to J/\psi\ K_s$ decay with some kinematical quantities at the HERA-B experiment.

At the energy provided by the HERA proton beam, the cross section for $b\overline{b}$ quark production is about six orders of magnitude smaller than the cross section for inelastic proton nucleus scattering at the same centre of mass energy. The branching ratios for the production of a neutral B meson and its subsequent decay $B^0 \to J/\psi\ K_s \to \ell^+\ \ell^-\ \pi^+\ \pi^-$ reduce the fraction of interesting signal events further by almost five orders of magnitude. Another order of magnitude is lost due to the triggering and reconstruction efficiencies. Thus in total, the reconstructed signal rate is suppressed by a factor $\approx 10^{-12}$ with respect to the total inelastic proton nucleus interaction rate. In order to accumulate about 1000 signal decays per year, the HERA-B detector should be operated at an interaction rate of about 40 MHz, which corresponds to an average of four superimposed interactions in a single crossing of proton bunches [1]. The HERA-B detector system should thus cope with very high interaction rates, where each bunch crossing generates tracks in the detector with extremely high particle densities (see Fig. 1.4). This requires fast track detectors which provide high precision in the decay reconstruction. To achieve the necessary precision, the detector elements with sufficiently high granularity and high rate capabilities are required to be as close as 1 cm from the beam, where they are hit by some $10^7\ \mathrm{particles/cm^2s}$. Leptons from B decays have to be identified with high purity in order to suppress backgrounds from the ordinary proton nucleus interactions and charm decays. Also the identification of the tagging kaon with its momentum between a few GeV/c and 50 GeV/c should be performed. Due to restricted access to the detector, given by the fact that HERA-B is not the main user, it has to be designed such that even the components very close to the beam have a minimum lifetime of about 10^7 seconds operating at full target rate.

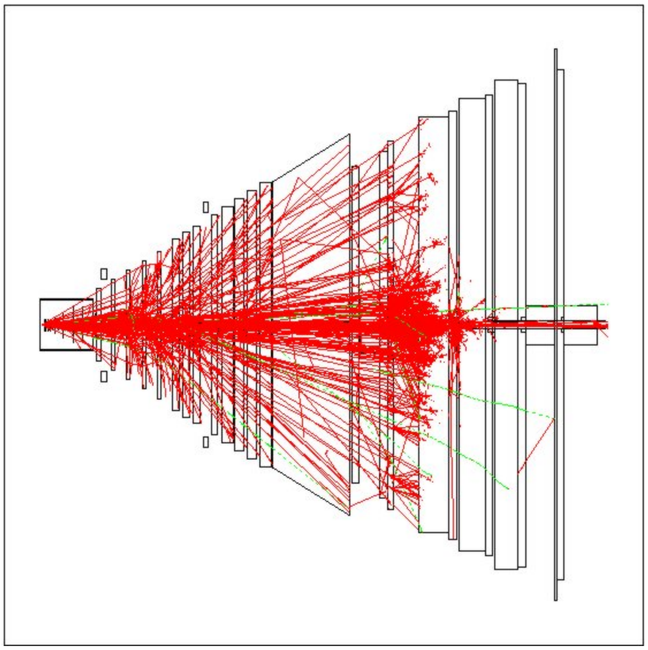

Figure 1.4: Simulated tracks due to one bunch crossing in the HERA-B detector.

All in all the detector has to provide a good B meson decay vertex resolution, lepton and kaon identification, and multiple event reconstruction per bunch crossing. To meet these requirements, the spectrometer consists of several detector subsystems which can be grouped into tracking and particle identification systems according to their tasks. The tracking system consists of the magnet, the vertex detector, and the inner and outer tracker detectors, while the transition radiation detector, the ring imaging Čerenkov detector, the electromagnetic calorimeter and the muon identification system compose the particle identification system. The HERA-B spectrometer (Fig. 1.5) reflects the fixed target nature of the experiment, with finer detector granularity for small production angles, where higher particle densities are expected. Its outer dimensions are $20 \times 9 \times 7\mathrm{m}^3$. The acceptance of the detector is from 10 mrad to 160 mrad vertically and from 10 mrad to 220 mrad horizontally. This is equivalent to 90% of the solid angle in the proton nucleus centre of mass frame.

In what follows, each HERA-B detector subsystem design shall be briefly described and its main tasks presented.

- An intrinsic part of the experiment, which is integrated into the detector and positioned in the halo of the HERA proton beam is **an internal target**. The basic idea of the target is to bring protons, which leave the beam core, drift outwards and would be lost anyhow, to interact in the target before they hit any aperture limitation in the beam tube. An efficient competition of the target with collimators, which define the aperture of the beam is thus needed.

  As already mentioned four proton interactions with the target are required per bunch crossing which should be compared with the natural loss rate of the proton beam. With a typical proton bunch current of 0.5 mA (i.e. 7×10^{10} protons) and a lifetime of 100 hours the HERA proton beam looses 2×10^5 protons per second. This demonstrates that the target has to collect very efficiently the protons before they get lost, due to the fact that interactions take place on average after 250 target hits which occur on average once in 100 bunch turns [10]. It is accepted that the target operation shouldn't reduce the proton beam lifetime below 50 hours [1]. At this level the target doesn't severely interfere with the efficiency of the other experiments, because the HERA luminosity lifetime is usually less than 10 hours, mainly determined by the electron lifetime.

  The target mechanics is mounted inside a conical extension of the beam pipe, which houses the movable parts of the vertex detector. The target consists of a set of eight movable ribbons with $50\,\mu\mathrm{m}$ width perpendicular to the beam, $500\mu\mathrm{m}$ thickness along the beam and 30 mm length. The ribbons are positioned around the beam at a distance of $4\,\sigma$ to $6\,\sigma$. The ribbons are grouped in two stations separated by 4 cm along the beam. Within one station the four ribbons are located and they approach the beam from four different sides (see Fig. 1.6). Each ribbon is mounted on a ceramic fork, which can be independently moved with a nominal step size of 50 nm. A constant target interaction rate with equal sharing among ribbons can be achieved by an automatic feedback system which continuously adjusts the wire positions via stepping motors.

  The described target system provides a well localised source of B hadrons. It also allows multiple interactions in a single bunch crossing over up to eight ribbons, which result in an unambiguous assignment of particles to vertices and last but not least it is robust and simple to operate.

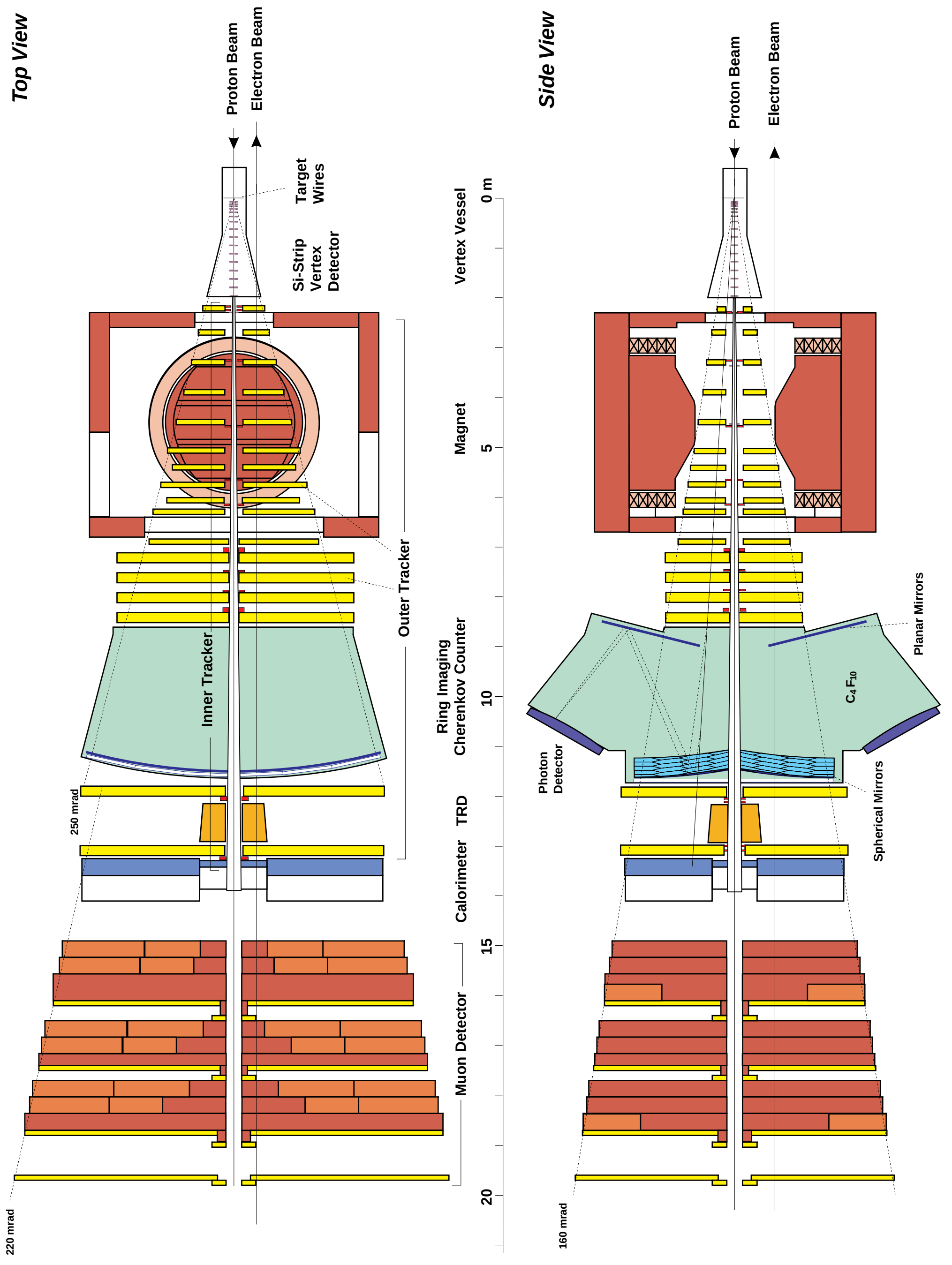

Figure 1.5: Configuration of the HERA-B spectrometer with the silicon vertex detector, the main tracking system with a dipole magnet, transition radiation detector and ring imagingČerenkov counter for particle identification, followed by the electromagnetic calorimeter and the muon system.

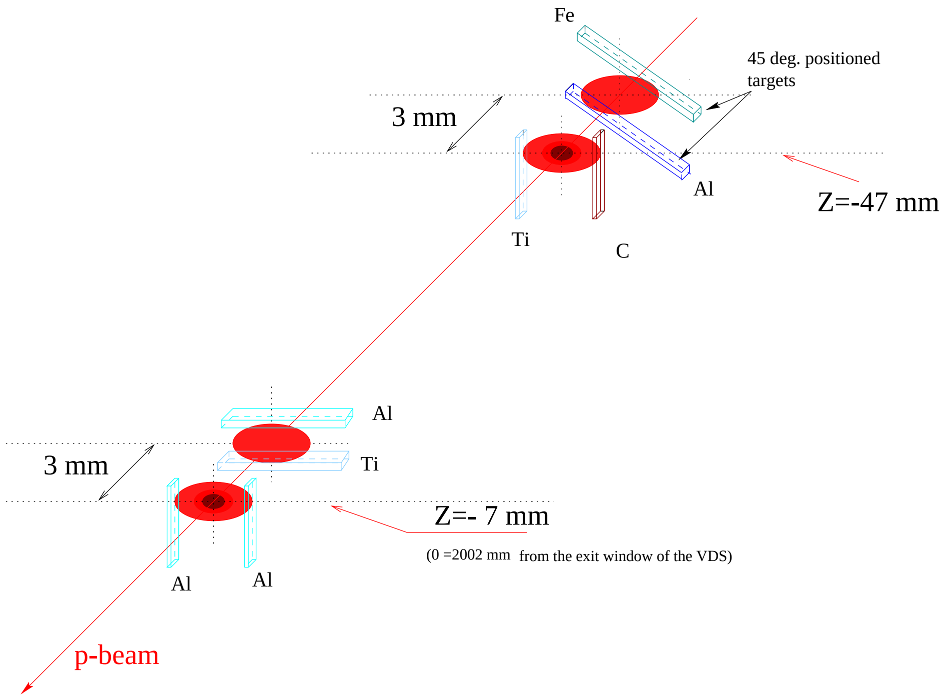

Figure 1.6: Schematic view of the halo target, consisting of eight ribbons positioned in two stations around the beam.

- The spectrometer uses **a dipole magnet** of 2 Tm field integral for momentum analysis. It consists of two iron poles, an iron flux return yoke and two cylindrical copper coils. The magnet position presents a compromise between the acceptance for late decaying $\mathrm{K_s}$ and magnet aperture for fixed solid angle coverage. The location of the magnet centre is fixed at 4.5 m downstream of the target, which determines the vertical magnet aperture to 160 mrad and the horizontal aperture to about 250 mrad.

- The tracking of charged particles is performed by a vertex detector, followed by an inner tracking system closer to the proton beam and an outer tracking system at distances larger than 20 cm from the beam.

  The vertex detector system provides the track coordinates information for reconstruction of the $\mathrm{J}/\psi \to \mathrm{e}^+\,\mathrm{e}^-,\ \mu^+\,\mu^-$ decay vertices and the impact parameters of all tagging particles. The information of the vertex detector is also used at the trigger level in order to reject events, where the two leptons do not form a common vertex which is displaced from the target wire.

  The vertex detector system acceptance is from 10 mrad up to 250 mrad vertically and horizontally. The minimum distance between the active area of the silicon detectors and beam is 1 cm. The overall detector length is 2.5 m. The resolution of the vertex detector is limited by multiple scattering in the material between track vertex and the point of the first track measurement [13]. Thus the detector layout is based on a roman pot system, which allows the minimisation of the in-between material. The roman pots are mounted inside a cone shaped vacuum vessel (Fig. 1.5). Each roman pot provides a secondary vacuum of 10^{-6} mbar, because it would be impractical to operate in the primary HERA vacuum of 10^{-8} mbar. Individual modules have a $150\ \mu\mathrm{m}$ thin aluminium cap separating the primary from the secondary vacuum. The detectors can be retracted during the beam injection or adjustment.

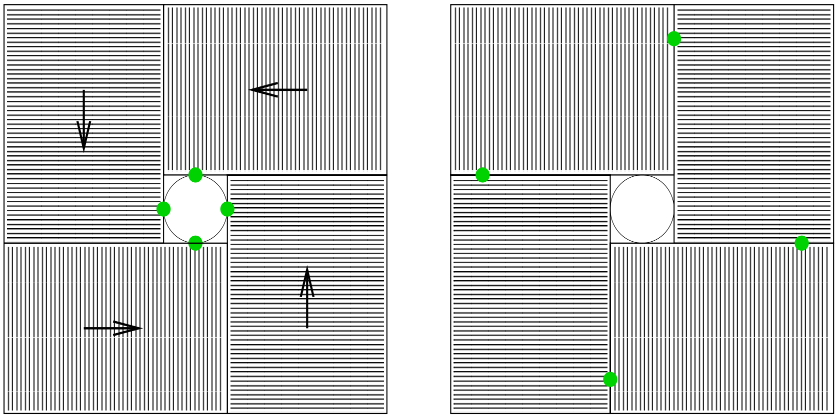

Figure 1.7: Two possible arrangement of the vertex detectors around the beam axis. The detector positions can be shifted laterally in order to move the points (green dots) of highest irradiation on the detector.

The vertex detector system has seven layers with four modules in each layer. Each module carries two double sided silicon detectors and the front end electronics. For layers four and beyond each module is mounted in a separate roman pot. The first three modules in a quadrant are integrated in one pot. All detectors are mounted perpendicular to the beam. As the highest flux is in the corner of each detector, it becomes possible to distribute the radiation damage by shifting the detectors laterally (Fig. 1.7). The vertex detector system uses $300\ \mu\mathrm{m}$ thick double sided n type bulk silicon strip detectors. Their overall size is $53 \times 73\ \mathrm{mm}^2$, while active area is $50 \times 70\ \mathrm{mm}^2$. On the two detector sides the strips are orthogonal and are tilted by 2.5^0 with respect to the detector edge. The two detectors in a module are mounted back to back (Fig. 1.8). That results in four views per module with a stereo angle of 5^0. Electronics and detectors are mounted on separate plates to establish different cooling paths. The vertex detectors have to be replaced once per year due to the radiation damage.

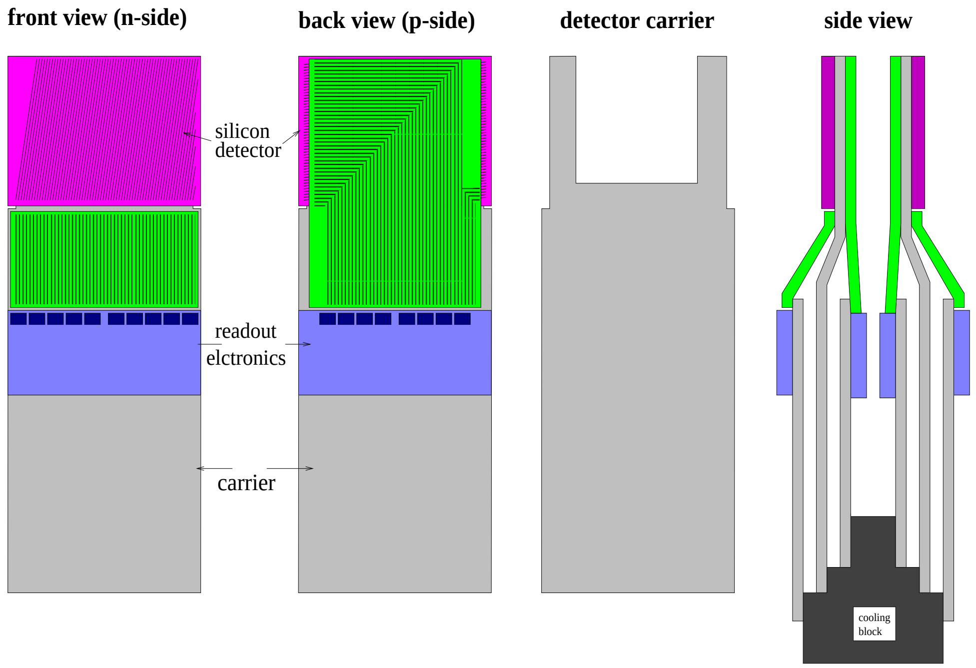

Figure 1.8: Schematic view of the vertex detector module.

- The main tracking system is segmented into parts of different granularity, in order to keep occupancies bellow a level of 20%. In accordance with the increasing particle densities towards small polar angles the system is divided into an inner and an outer section. Besides track information it also provides momentum measurements.

The inner tracker is covering the angular range larger than 10 mrad and extends up to radial distances of 20 cm from the proton beam. This region comprises about half of all the tracks of a typical event, thus the detectors have to cope with particle rates of up to $10^4\mathrm{mm}^{-2}\mathrm{s}^{-1}$. The inner tracker detector consists of low gain micro strip gas chambers (MSGC) operated with Ar/DME gas mixture and combined with a gas electron multiplier (GEM) [11]. It has 48 detector layers, each being composed of four independent L shaped detector planes (see Fig. 1.9). Tracking is performed by using three stereo strip orientations i.e. vertical strips (0^o) and strips with $(\pm 5^o)$ orientation. Several layers with different strip orientation, mounted together in a common support structure form eleven super modules. Two super modules in front of the calorimeter are used for triggering. Four supermodules between magnet and RICH are used to start track finding and pattern recognition. They provide three dimensional hit information. Six layers of those supermodules are also used for triggering. The remaining supermodules near the vertex detector and in the magnet are used to extrapolate the tracks to the vertex detector (see Fig. 1.5).

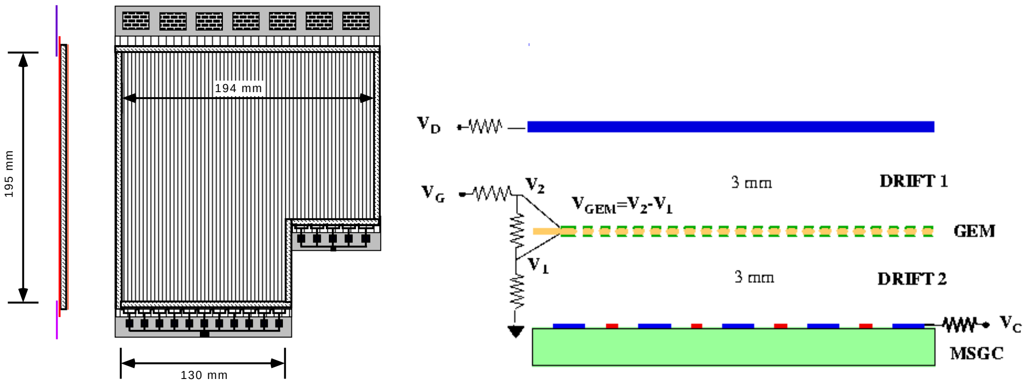

Figure 1.9: Geometry of the inner tracker detector in front of the RICH detector and a schematic view of a low gain micro strip gas chamber combined with a gas electron multiplier foil.

The micro strip gas chamber cover consists of a G10 plate to ensure mechanical stability and a kapton foil covered with copper, which serves as the drift cathode. Below the drift gap the gas electron multiplier foil is mounted. It consists of a $50\ \mu\mathrm{m}$ thick kapton foil, which is covered with $7\ \mu\mathrm{m}$ copper on each side. The kapton holes are staggered with a pitch of $140\ \mu\mathrm{m}$ and have a diameter of about $55\ \mu\mathrm{m}$, The charge produced in the GEM foil is transfered by an electrical field through the transfer gap of 2.8 mm to the standard MSGC substrate. A gold layer is deposited onto glass wafer and the electrode structure which consists of $10\ \mu\mathrm{m}$ wide anodes and $170\ \mu\mathrm{m}$ wide cathodes strips, with a gap of $60\ \mu\mathrm{m}$ in between (see Fig. 1.9). The micro strip gas chambers pitch of $300\mu\mathrm{m}$ provides maximum occupancies of about 5% and the spatial resolution better than $80\mu\mathrm{m}$. The momentum resolution is limited by multiple scattering, while photon conversions represent a significant background source. Single detector layer thickness is thus minimised and presents less than 0.35 % of a radiation length.

- The purpose of **the outer tracking system** is to measure charge particle tracks in almost the whole geometrical acceptance of the experiment, down to a distance of $20\ \mathrm{cm}$ from the proton beam. The outer limit of the spectrometer acceptance is at 250 mrad in the horizontal plane and at 220 mrad in the vertical plane. This translates to lateral dimensions of about $6\ \mathrm{m}$ by $4.5\ \mathrm{m}$ for the sensitive area of the largest subdetectors. The outer tracking system consists of fifteen planar drift tube stations orientationed perpendicular to the beam direction and at distances from about 2 m up to 13 m downstream from the target (see Fig. 1.5). In the region from the end of the target vessel to the end of the magnet nine chambers are positioned.

They are used for finding and fitting the curved continuations of already found straight track sections. Four layers in the region from the end of the magnet up to the front side of the RICH vessel are used for pattern recognition of straight tracks and for trigger decisions. The remaining two stations in the region between the RICH and the electromagnetic calorimeter are used by the trigger and to extrapolate tracks to the calorimeter and the muon system.

A modular design has been adopted in the construction of the stations. Each detector plane consists of an array of independent honeycomb modules which are fixed to a common support. These modules have a standard width of 32 cm, whereas their length differs from station to station, such that one module covers the full height of the sensitive area. The basic driftcell in an honeycomb drift chamber is a tube of hexagonal cross section with a signal wire strung along its centre (Fig. 1.10). The tube is formed from a conductive foil which acts as cathode. In order to minimise the number of readout channels while keeping the cell occupancy at an acceptable level, two different cell sizes are used. Modules with a cell size of 5 mm are placed in the regions nearer to the beam pipe, the outer regions are covered by modules with 10 mm cell size (see Fig. 1.10).

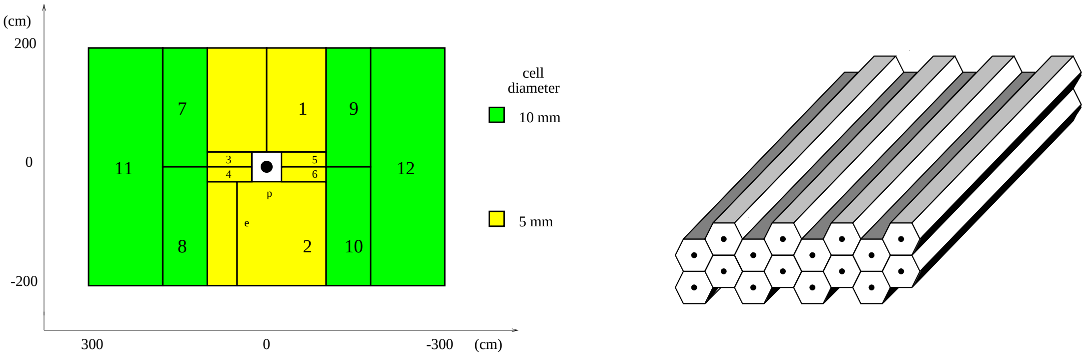

Figure 1.10: A lateral segmentation of a superlayer station into twelve sections on the left side figure The thick line indicates the mechanical separation of a superlayer into two retractable segments. Schematic view of double honeycomb drift chamber layer on the right side.

The basic station design consists of detector planes with wires strung at 0^0 and $\pm 5^0$ with respect to the vertical direction. The coincidence of hits in the three layers thus assures spatial resolution of the order of $150\mu\mathrm{m}$ per station.

- Identification of a tagging kaon is performed by a **ring imaging Čerenkov counter** which uses a perfluorobutane gas $(\mathrm{C_4F_{10}})$ as the radiator, and a photon detector consisting of multianode photomultiplier tubes.

The structure and operation of the ring imaging detector system will be described in detail in the following chapters.

- **The transition radiation detector** is a part of the electron identification system. It efficiently separates electrons from hadrons in the region where the angular density of secondary particles and occupancy are highest. The transition radiation detector is positioned between the last two outer tracker super layers and covers the region around the proton beam pipe in transverse dimensions of $(134 \times 89 \mathrm{cm}^2)$.

  The detector is designed of fine granulated structure of the transition radiator interleaved with planes of straw proportional drift chambers as detecting elements. It has a modular structure and consists of two halves of four different blocks surrounding the beam pipe. In one half straw planes are positioned horizontally, while in the other they are placed vertically. Each block contains sixteen single layer planes as presented in Fig. 1.11.

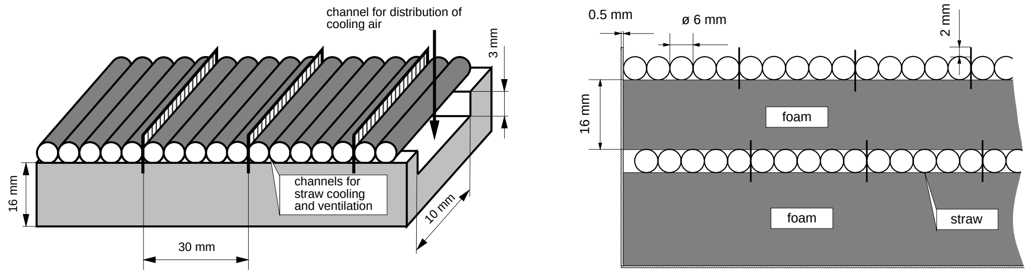

Figure 1.11: The design of a single layer and the cross section of a block of the transition radiation detector.

  The radiator consists of polypropylene fibres of $20\mu\mathrm{m}$ diameter with layer thickness of 1.6 cm. The straws are manufactured by spiralling the kapton films which are transparent for transition radiation photons and have good radiation hard properties. Straws are operating with $\mathrm{Xe} + \mathrm{CF}_4 + \mathrm{CO}_2$ gas mixture at a gas gain of 2.5×10^4 and maximal electron drift time of about 60 ns.

- **The electromagnetic calorimeter** provides pretrigger signals on lepton candidates of $\mathrm{J}/\psi \to \mathrm{e}^+\mathrm{e}^-$ decays, a good hadron electron separation as well as energy and position measurements, mainly used at the trigger level. The calorimeter is positioned at 13.25 m from the target. In order to have high detection efficiency both for the electrons produced in J/ψ decays and for tagging electrons, the calorimeter covers the range of 310 cm horizontally and 235 cm vertically. The geometrical acceptance to detect both electron and positron from J/ψ is 70% [1]. The corresponding acceptance loss is caused mainly by the inner hole of the calorimeter, where the proton beam pipe goes through.

The calorimeter has modular structure with basic unit of $11 \times 11\mathrm{cm}^2$ transverse dimensions. The modules were built using shashlik technology with a sampling plastic scintillator and absorber sandwich. The scintillator and absorber plates are perforated to let the plastic wavelength shifter fibres penetrate perpendicular through the plates. The light is collected by these wavelength shifter fibres which are joined in bundles arriving at a photomultiplier face.

The granularity of the detector is increasing by decreasing the distance from the beam axis (see Fig. 1.12). Thus the inner, middle and outer modules comprise twenty five, four and one calorimeter basic cell respectively.

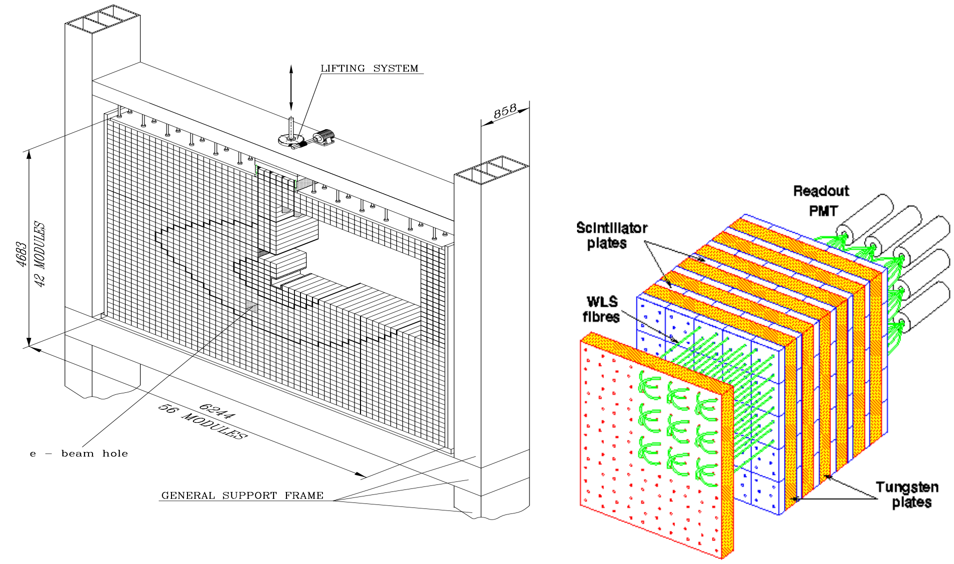

Figure 1.12: The electromagnetic calorimeter geometry (left). The 84 modules of the inner section are composed of 25 channels, the 532 ones of the middle section of 4 channels, while each of 1728 outer modules represent one channel. Schematic view of the inner module (right).

The schematic view of the inner calorimeter module is shown in Fig. 1.12. Each module is made of alternating perforated tungsten and scintillator plates being $2\ \mathrm{mm}$ and $1\ \mathrm{mm}$ thick respectively. Altogether there are 40 tungsten and scintillator layers resulting in a total thickness of 23 radiation lengths. Each module has a transverse segmentation of 5×5 basic cells. Each basic cell employs its own photomultiplier tube. The middle and outer calorimeter modules consist of 37 layers of 3 mm thick lead and 6 mm thick scintillator plates resulting in a 20 radiation length depth. The outer calorimeter module consists of one individual basic cell, while the middle module is subdivided into 2×2 basic cells. The modules are stacked together into 6×6 supermodule structure. In total there are 14 and 62 supermodules for the middle and outer calorimeter sections respectively.

- **The muon system** detects muons in the momentum range between a few GeV up to about 200 GeV. Identified muon pairs with an invariant mass in the region of the J/ψ meson provide the trigger signal for $\mathrm{B}^0 \rightarrow \mathrm{J}/\psi\mathrm{K_s}$ decays. The muon system also serves to select additional single muons from semileptonic decays, which provide a tag of the B meson flavour. Angular detector acceptance is 250 mrad horizontally and 160 mrad vertically. The geometrical acceptance for detection $\mu^+\mu^-$ with momenta above $5\ \mathrm{GeV/c}$ from J/ψ decays is 71%, while the acceptance for the tagging muon is 81% [1]

  The separation of muons from hadrons in the muon system is achieved by exploiting the higher penetration capability of muons. The muon system consists of the muon filter and four superlayers of muon chambers. Three hadron absorber segments, built of iron and armoured concrete blocks, alternate with three detector superlayers. A fourth superlayer is added to provide a clean multiple scattering free measurement of track directions (see Fig. 1.5).

  The muon detection superlayers are composed of three different chamber types. In the outer regions of the first two superlayers muon tube chambers are used, while the last two employ pad chambers. In the region around the beam pipe gas pixel chambers in all four layers are used. The basic sensitive element of the tube chamber is a $15 \times 12\ \mathrm{mm}^2$ large drift cell with anode wire stretched in the centre. To ensure a high efficiency, each chamber consists of two layers of 2×16 cells shifted one against other by half a cell (see Fig. 1.13). The pad chambers are assembled using two sided aluminium profiles with attached pad structure. Two rows of 16 open cells each are shifted by half a cell width with respect to each other. Anode wires are stretched inside the $15 \times 12\ \mathrm{mm}^2$ large open cells (see Fig. 1.13). Gas pixel chambers are composed of square cells formed by one sense wire and four potential wires. Cells of a size of $9 \times 9\ \mathrm{mm}^2$ are used in the first three superlayers,

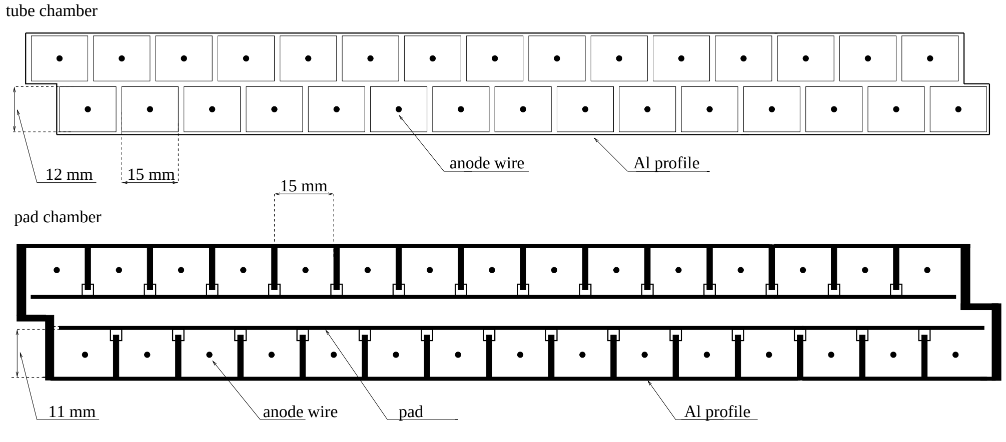

Figure 1.13: Schematic drawing of the tube chamber and pad chamber construction.

while cell size of $9.4 \times 9.4\ \mathrm{mm}^2$ is chosen for the last superlayer in order to follow the projective geometry. The cell sizes of the muon chambers are determined exclusively by the maximum allowed drift time as the accuracy for the measurement of the track position is limited by multiple scattering in the calorimeter and in the absorber.

The first and the second superlayers consist of three layers of muon tube chambers, with anode wires perpendicular to the horizontal plane in one layer and wires oriented by $\pm 20^0$ with respect to the vertical line in the other two. Information is used in the trigger decision and in the off line analysis (see Fig. 1.14). The third and fourth superlayer consist of one layer with pad and wire readout. Information from the superlayers is used to determine particle directions and for the trigger decision.

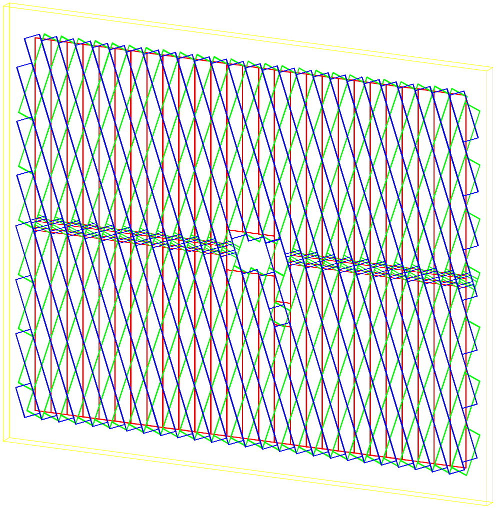

Figure 1.14: View of the superlayer with three layers of muon tube chambers.

The data acquisition (DAQ) and triggering system at the HERA-B experiment must cope with more than half a million of detector channels, a 10 MHz event rate and a signal to background ratio of 10^{-10}. The maximal requirement to the DAQ system is to use the complete event data when performing the selection. A typical HERA-B event has a size of 100 kbyte, which corresponds to a data flow rate of 1 Tbyte/s at an event rate of 10 MHz. The complete event reconstruction takes a few seconds on the state of the art processors. Clearly the required processing power cannot be implemented and events must be selected before they are saved on tape or disk. The maximal requirement to the DAQ is thus modified to accommodate to the HERA-B experiment. Since the signal to background ratio is very small the event selection scheme is divided into four sequential triggering levels. The physics program of the experiment determines the trigger algorithms, which are used to define the requirements to the DAQ system. The DAQ system can be viewed as a servant to the trigger system. Its task is to house the trigger processing elements and distribute data to them as required. Each of the trigger levels has a characteristic data flow and rate requirement. The DAQ and triggering system architecture is presented in Fig. 5.6 and will be briefly described in the following.

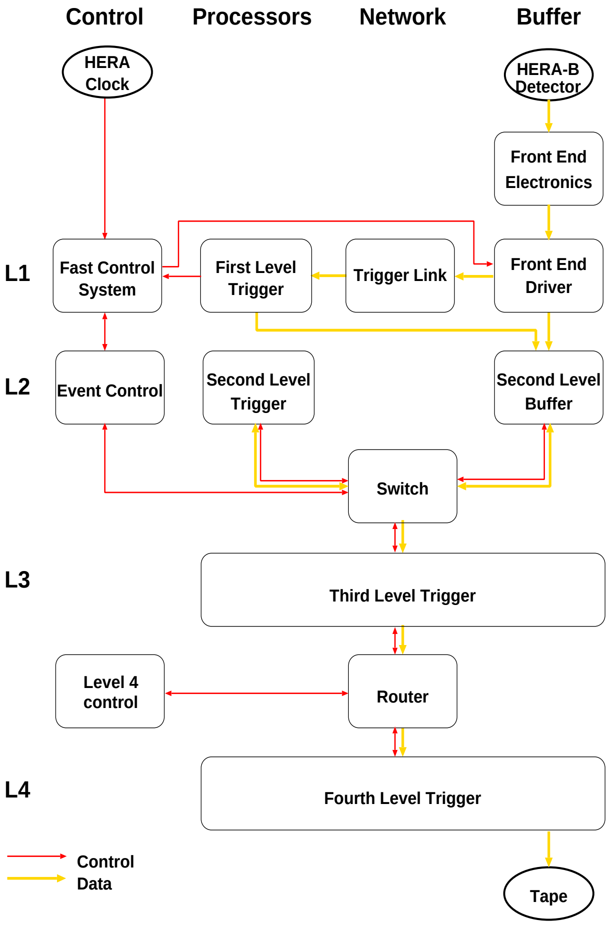

Figure 1.15: Data acquisition and triggering system architecture used in the HERA-B experiment.

During the processing of the triggers the data is stored in the front end electronics pipeline buffers in order to avoid dead time. Pipelining is implemented by storing the labelled hit information of 128 bunch crossings. Front end electronics is connected to the fast control system via the front end driver system. The fast control system prime goal is to synchronise the whole detector and assign the detector signals to events. Therefore it distributes the bunch clock signals, the front end driver specific delay between bunch clock and detector signals information, the event number and event numbers of the first level trigger accepted event to the front end drivers.

The first level trigger accepts only selected event information with data stream of 150 Gbyte/s and delivers its result after a delay not longer than $12\ \mu\mathrm{s}$. It searches for $\mathrm{e}^+\mathrm{e}^-$ and $\mu^+\mu^-$ track pairs with a J/ψ signature. The high rejection rate of the first level trigger reduces the input event rate by a factor of 200. After an event is accepted by the first level all data belonging to this event are read out of the pipelines and pushed into second level buffer, which is implemented with the SHARC cluster VME boards [14]. The same SHARC cluster board is used to implement a switch which carries the event control traffic, the dialog between second level trigger and second level buffer and runs the event controller. The second level trigger operates only on selected data information at 50 kHz to 100 kHz input rate and therefore digests 50 Mbyte/s. Data from the silicon vertex detector and remaining tracking system is added to subsets of the data defined by the first level trigger information and routed to the second level trigger processors. The second level trigger redoes the first level trigger algorithm with higher precision. It adds more hits with the full chamber resolution in the tracking layers behind the magnet and projects tracks through the magnet and vertex detector. The silicon tracker data is used to reject dileptons generated in different interactions during the same bunch crossing and to enhance J/ψ candidates from secondary vertices downstream of the target. A rejection factor of 10 is obtained by eliminating events which do not contain real tracks and additional rejection of factor 10 is achieved after vertex cuts are applied. Events surviving second level trigger cuts are passed to the third level trigger. It is the first trigger level which doesn’t use only selected information, but requires a complete event data assembled and available in processor memory. The third step operates at a rate below 1 kHz which amounts to a data rate of 100 Mbyte/s. The third level trigger does the full track and vertex fitting with high precision. More stringent cuts on particle mass and vertex positions for all the tracks in the event reduces the data stream by a factor of 10. Accepted events are routed to the fourth level trigger. It actually doesn’t act as a real trigger because it performs the full event reconstruction which calls for the entire detector alignment and calibration data. The fourth step works at the event input rates smaller than 50 Hz which presents a data stream of moderate 5 Mbyte/s. A few seconds of computing time per event is needed for pattern recognition and event reconstruction procedure due to the high track densities and occupancies in the detector. A reduction of a factor 2.5 is achieved and the event data is routed to the storage media at a moderate event rate of 20 Hz as a final step of the DAQ and triggering system procedure.

2

Ring imaging Čerenkov counters

2.1 Čerenkov radiation

A charged particle, traversing a dielectric medium with a refractive index n with a velocity $v = \beta c$ exceeding the velocity of light c/n in that medium, emits characteristic electromagnetic radiation, called Čerenkov radiation. Čerenkov radiation is emitted because the charged particle polarises the atoms along its track so that they become electric dipoles. The time variation of the dipole field leads to the emission of the electromagnetic radiation. As long as $v < c/n$, the dipoles are symmetrically arranged around the particle's path, so that the dipole field integrated over all dipoles vanishes and no radiation results. If however the particle moves with $v > c/n$, the symmetry is broken resulting in a non vanishing dipole moment, which leads to the emission of radiation. Figure 2.1 illustrates the difference in polarisation for the cases $v < c/n$ and $v > c/n$.

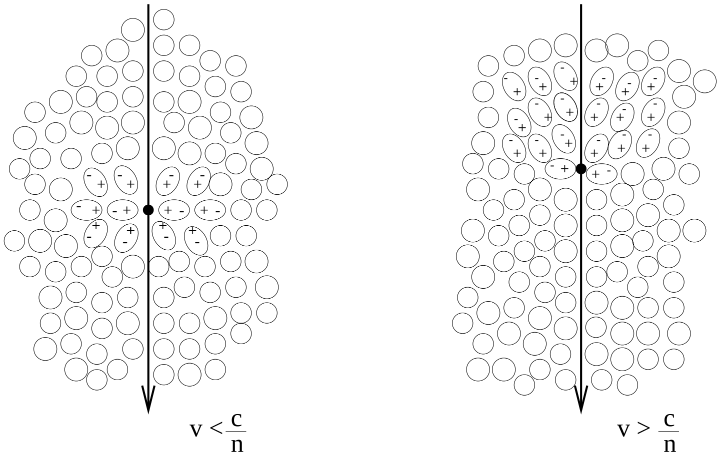

Figure 2.1: The polarisation in a dielectric by the passage of a charged particle at low and at high velocity.

In the same way as an acoustical shock wave generated by a body moving with supersonic velocity, the Čerenkov wave front construction can be illustrated by the superposition of spherical elementary Huygens waves produced by the particle along its trajectory. The construction is shown in Fig. 2.2.

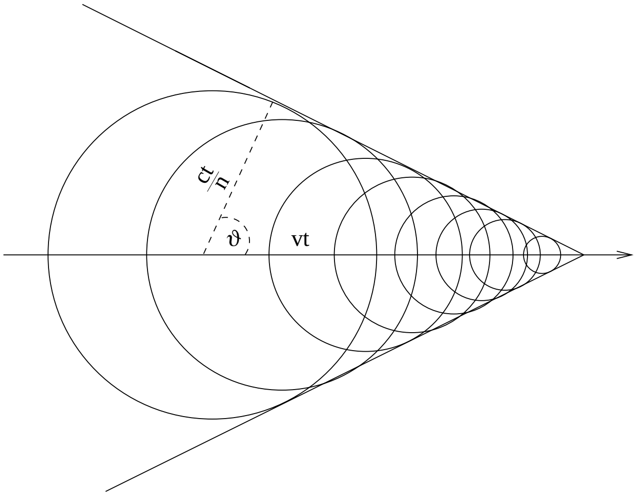

Figure 2.2: The Čerenkov wave front construction by the superposition of spherical elementary Huygens waves produced by the particle along its trajectory.

While the particle has travelled the distance βct, the photon has advanced by ct/n. Therefore the Čerenkov polar emission angle ϑ relative to the particle direction is given by the relation

$$\cos\vartheta = \frac{1}{\mathrm{n(E)}\beta}. \tag{2.1}$$

The azimuthal emission angle φ has a flat distribution between 0 and 2π. The Čerenkov radiation is only emitted if $\beta \geq 1/n(E)$. At threshold particle velocity $v_{th} = c/n(E)$ the Čerenkov radiation is emitted in the forward direction. The Čerenkov angle increases with increasing particle velocity until it reaches a maximum for $\beta = 1$.

The intensity and spectrum of the radiation is given by the Frank-Tamm [15] relation

$$\frac{\mathrm{dN}}{\mathrm{dE}} = \left(\frac{\mathrm{e}_0^2}{4\pi\varepsilon_0\hbar^2\mathrm{c}^2}\right)\mathrm{Z}^2\mathrm{L}\sin^2\vartheta, \tag{2.2}$$

where dN is the number of photons with energy between E and $E + dE$, L is the particle path length in the medium and Ze is the charge of the particle. Combining both equations one obtains the spectral dependence

$$\frac{\mathrm{dN}}{\mathrm{dE}} = \left(\frac{\mathrm{e}_0^2}{4\pi\varepsilon_0\hbar^2\mathrm{c}^2}\right)\mathrm{Z}^2\mathrm{L}\left[1 - \left(\frac{1}{\mathrm{n(E)}\beta}\right)^2\right]. \tag{2.3}$$

The dispersion of an optical medium is expressed by a function $n = n(E)$. This functional dependence must be included when integrating Eq.2.3 to obtain the number of produced Čerenkov photons.

2.2 Čerenkov counters

Čerenkov counters exploit both features of Čerenkov radiation, the presence of Čerenkov light above the certain threshold, and the correlation between the particle velocity and the size of the Čerenkov emission angle, in order to separate and identify particles.

2.2.1 Threshold Čerenkov counters

As already mentioned the Čerenkov radiation is only emitted if β exceeds $1/n$. This phenomena is used to distinguish particles with different masses in the so called threshold Čerenkov counters [16]. Lets consider two particles with different masses with the same momentum. To be able to distinguish these two particles in a threshold Čerenkov counter, it is required that the lighter particle emits Čerenkov radiation, while the heavier particle does not radiate. By use of solid, liquid or gaseous Čerenkov radiators a large range of refraction indices can be covered in order to select the threshold which suits the given separation requirements. The presence of light in the threshold Čerenkov counters is detected with photomultiplier tubes. It is common practice to use a combination of several threshold Čerenkov counters with different refractive indices which allows particle identification in the momentum range up to 30 GeV/c.

2.2.2 Differential Čerenkov counters

Apart from utilisation of the Čerenkov threshold, the angle of Čerenkov emission can also be measured in order to identify particles.

The cone of Čerenkov light emitted in a radiator of finite length forms a ring when intercepted by a plane some distance away from the radiator. It is therefore possible to make differential counters where only photons transmitted through an adjustable diaphragm of certain diameter are collected by the photomultipliers. Differential Čerenkov counters [16] thus directly measure the particle velocity. Changing the radius of the diaphragm allows a scan through velocity regions. An alternative to changing the radius of the diaphragm consists in changing the gas pressure and leaving the optical system in place. The mentioned projection technique is more practical for dense radiators such as liquids and solids, since they produce a sufficient quantity of light in a short radiator.

If the Čerenkov light emitted along the trajectory of a charged particle is reflected by a spherical mirror of radius R, the light is focused onto circular ring image at the mirror focal surface of $R/2$. The radius of the ring image is $r = R/2 \tan\vartheta$. In differential isochronous self collimating Čerenkov counters a ring diaphragm of radius r, located in the focal plane of the mirror is used to select the velocity range of interest. The transmitted photons are detected with photomultipliers located behind the diaphragm. With differential isochronous self collimating Čerenkov counters π and K mesons up to momentum of several 100 GeV/c can be separated.

Differential Čerenkov counters drawback is their limitation to distinguish only among particles with trajectories parallel to the optical axis, which means that in storage ring experiments where particles are produced in the full solid angle, they can not be used.

2.2.3 Ring imaging Čerenkov counters

Velocity measurement for particles diverging from an interaction region calls for a different approach accomplished by ring imaging Čerenkov counters proposed by Seguinot and Ypsilantis two decades ago.

In ring imaging Čerenkov counters a spherical mirror of radius R, centred at the interaction point, projects the cone of Čerenkov light produced in the radiator onto a ring shaped image with radius r. The focus of the image is situated half way between the mirror and its centre of the curvature on the spherical surface photon detector of radius $R/2$. A schematic view of a ring imaging Čerenkov counter is illustrated in Fig. 2.3.

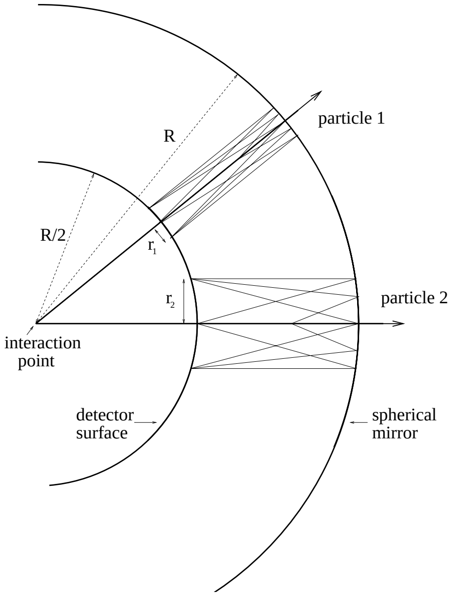

Figure 2.3: Principle of the ring imaging Čerenkov counters. The Čerenkov cone is focused onto a ring with radius r on the detector sphere.

The gas radiator fills the volume between the spherical surfaces. Due to the spherical shape of the mirrors the focusing point on the photon detector for photons in the gas radiator does not depend on the emission point along the particle trajectory.

The measurement of the radius of the Čerenkov ring allows a determination of the angle of emission of the Čerenkov light ϑ via $\tan\vartheta = 2r/R$, and by knowing this one can obtain the particle velocity (see Eq.2.1). If momentum of the particle is known from a measurement of the curvature of its trajectory in magnetic field, this enables a determination of particle mass and thereby its identity by use of the relation

$$\mathrm{p} = \frac{\mathrm{m_0 c}\beta}{\sqrt{1-\beta^2}}. \tag{2.4}$$

The most crucial aspect of ring imaging Čerenkov counters is the efficient detection of Čerenkov photons on the detector surface. Since one is not only interested in detecting photons, but also in measuring their coordinates, a large surface area position sensitive detector with high resolution is necessary. These properties can be obtained with detectors utilising the photoionisation process in gases in combination with charge multiplication due to electron avalanche generation in strong electric fields, or by using photomultiplier tubes.

Using equation 2.3, the average number of the detected photoelectrons N_{det} can be written as

$$\mathrm{N_{det}} = \int \mathrm{T_r(E)} \cdot \mathrm{R_m(E)} \cdot \epsilon_{\mathrm{d}}\mathrm{(E)} \cdot \frac{\mathrm{dN(E)}}{\mathrm{dE}}\,\mathrm{dE}, \tag{2.5}$$

where $\mathrm{T_r(E)}$ is the radiator transmission, $\mathrm{R_m(E)}$ is the mirror reflectivity and $\epsilon_{\mathrm{d}}\mathrm{(E)}$ is the detection efficiency of the photon detector. Neglecting dispersion in the radiator, the integral of Eq.2.5 can be rewritten

$$\mathrm{N_{det}} = \mathrm{N_0 Z^2 L sin^2}\vartheta, \tag{2.6}$$

where N_0 is the detector response parameter or the so called merit factor of the photon detector

$$\mathrm{N_0} = \left(\frac{\mathrm{e_0^2}}{4\pi\varepsilon_0\hbar^2\mathrm{c}^2}\right)\int \mathrm{T_r(E) R_m(E)}\epsilon_{\mathrm{d}}\mathrm{(E)\,dE}. \tag{2.7}$$

The constant factor in front of the integral can be evaluated as

$$\left(\frac{\mathrm{e_0^2}}{4\pi\varepsilon_0\hbar^2\mathrm{c}^2}\right) = 370\mathrm{cm^{-1}eV^{-1}}. \tag{2.8}$$

Ring imaging Čerenkov counters velocity measurement error [17] originates from the experimental uncertainties in the determination of the radius r of the Čerenkov ring and from the variation of the radiator refractive index with the photon energy which is not measured

$$\frac{\sigma_\beta}{\beta} = \sqrt{\sum_{\mathrm{i}} \left(\sigma_\vartheta^{\mathrm{i}}\right)^2}\ \tan\vartheta, \tag{2.9}$$

where $\sigma_\vartheta^{\mathrm{i}}$ are contributions to Čerenkov angle measurement error.

In addition deviations of the particle trajectory in the radiator from a straight line and optical system imperfections the evaluation of the Čerenkov ring radius is limited due to two dominant sources:

- the chromatic aberration, a consequence of the variation of the refractive index over the sensitive energy range of the photon detector, is

  $$\sigma_\vartheta{}^{\mathrm{dis}} = \frac{1}{\mathrm{n}\sqrt{\mathrm{n}^2\beta^2 - 1}}\frac{\mathrm{dn}}{\mathrm{dE}}\sigma_{\mathrm{E}} \approx \frac{1}{\sqrt{2\mathrm{n}-1}}\frac{\mathrm{dn}}{\mathrm{dE}}\sigma_{\mathrm{E}}, \tag{2.10}$$

  where σ_{E} is the standard deviation of the energy distribution of detected photons and approximations $(\mathrm{mc/p}) \ll 1$ and $(\mathrm{n}-1) \ll 1$ are used and

- the finite coordinate resolution of the photon detector, if hits within the pad are uniformly distributed amounts to

  $$\sigma_\vartheta{}^{\mathrm{det}} = \frac{\mathrm{a}}{\mathrm{f}\sqrt{12}}, \tag{2.11}$$

  where f is the focal length of the spherical mirror and a is photon detector pad size.

3

Design criteria for the RICH of the HERA-B experiment

The prime function of the Ring Imaging Čerenkov counter (RICH) in the HERA-B experiment is the tagging of the B meson flavour. Tagging of the of B^0 or $\overline{\mathrm{B}^0}$ meson is accomplished by identifying the charged kaon into which the associated B meson decayed. The momentum distribution of charged kaons, resulting from decays of the B mesons, is shown in Fig. 3.1. Identifying the charged kaon essentially means separating it from

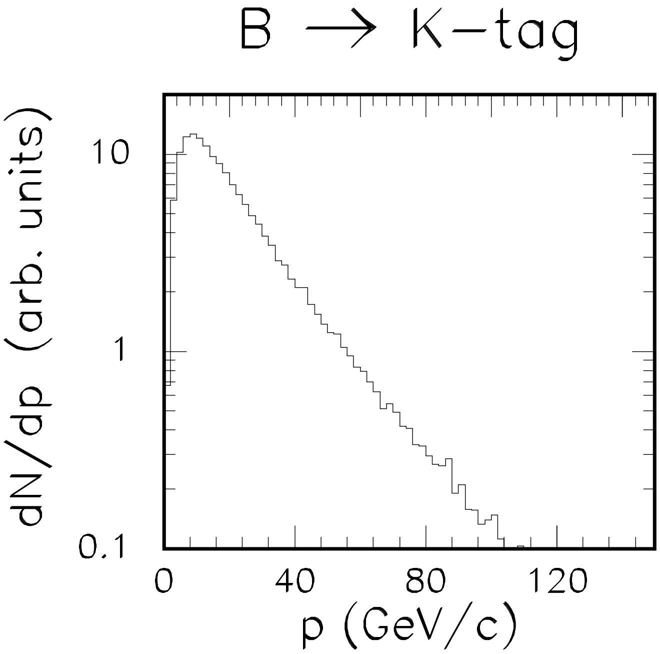

Figure 3.1: The momentum distribution of charged kaons produced in decays of B mesons associated to the production of B^0 or $\overline{\mathrm{B}^0}$ meson by proton nucleus interactions at HERA-B.

the pion of the same momentum. Since the momentum is accurately measured in other components of the HERA-B detector, the separation in mass is equivalent to separation in velocity.

3.1 Radiator choice

At high momenta $(\mathrm{pc} \gg \mathrm{mc}^2)$ the difference in velocity of the two particles is proportional to the inverse square of the momentum, so the separation becomes increasingly more difficult.

$$\Delta\beta \approx \frac{\mathrm{m}_\mathrm{K}^2\mathrm{c}^2 - \mathrm{m}_\pi^2\mathrm{c}^2}{2\mathrm{p}^2}. \tag{3.1}$$

For example, the $\pi - \mathrm{K}$ velocity difference is $\Delta\beta = 1.1 \times 10^{-3}$ at a momentum of 10 GeV/c, and it reduces to $\Delta\beta = 4.5 \times 10^{-5}$ at 50 GeV/c. The ring imaging Čerenkov detector is expected to achieve the required $\pi - \mathrm{K}$ separation by accurately measuring the Čerenkov angle, so that σ_β stays below $\Delta\beta$ up to the highest momenta. To simplify the further discussion I shall also express the difference in the Čerenkov angle between two species by quoting

$$\Delta\vartheta \approx \sqrt{2}\left(\sqrt{\mathrm{n}-1-\frac{\mathrm{m}_\pi^2\mathrm{c}^2}{2\mathrm{p}^2\mathrm{n}}} - \sqrt{\mathrm{n}-1-\frac{\mathrm{m}_\mathrm{K}^2\mathrm{c}^2}{2\mathrm{p}^2\mathrm{n}}}\right). \tag{3.2}$$

In Fig. 3.2 one can see that this difference at 50 GeV/c is larger if a radiator with lower refractive index is used. Since the resolution in Čerenkov angle is expected to be below 0.2 mrad, the difference in Čerenkov angle of π and K should be around 1 mrad. This limits the choice to radiators with refractive index of $\mathrm{n} - 1 \leq 10^{-3}$. Only gases have such a low refractive index. In the same figure the threshold momentum for Čerenkov radiation as a function of the radiator refractive index is presented. In order to use the detector in a momentum range greater than a few GeV/c one should choose a radiator with $\mathrm{n} - 1 \geq 10^{-3}$. Thus both features limit the choice of the radiator to gases with $\mathrm{n} - 1 \approx 10^{-3}$.

Perfluorobutane gas ($\mathrm{C_4F_{10}}$) (See Appendix A) has been chosen for HERA-B RICH radiator, since it combines relatively high refractive index

$$n(3.3eV) - 1 = 1.330 \cdot 10^{-3} \tag{3.3}$$

and low dispersion

$$\frac{\Delta n}{\Delta E}(3.3eV) = 3 \cdot 10^{-5}\frac{1}{eV} \tag{3.4}$$

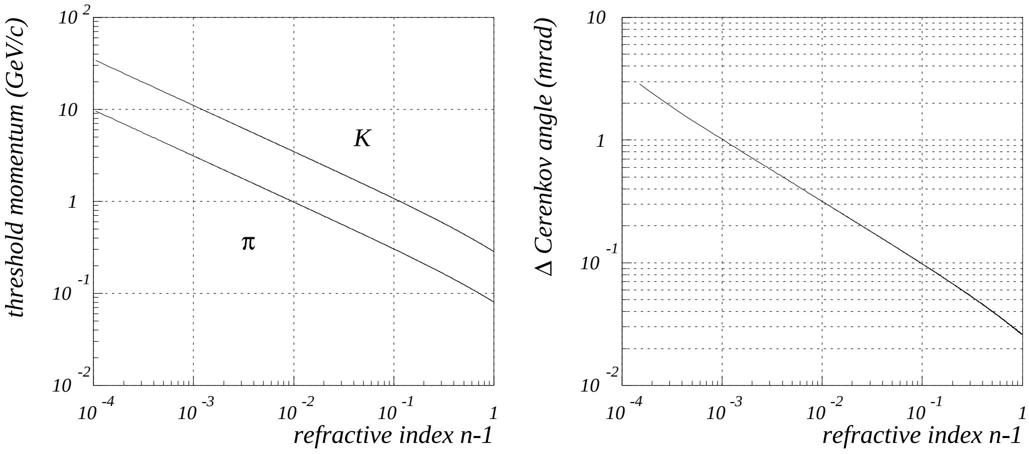

Figure 3.2: Čerenkov radiation threshold momentum for π and K (left) and Čerenkov angle difference for π and K at 50 GeV/c dependence on radiator refractive index.

In this gas the Čerenkov radiation threshold momenta for pions and kaons are at

$$p_{thr,\pi} = \frac{m_\pi c}{\sqrt{n^2-1}} = 2.7 GeV/c \quad \text{and} \quad p_{thr,K} = \frac{m_K c}{\sqrt{n^2-1}} = 9.6 GeV/c. \tag{3.5}$$

For $\beta = 1$ particles, the Čerenkov angle is 51.5 mrad, while the $\pi - \mathrm{K}$ difference in Čerenkov angle is 34 mrad at 10 GeV/c and falls to 0.9 mrad at 50 GeV/c.

3.2 The HERA-B RICH design considerations

The Ring Imaging Čerenkov detector design choices are governed by the following criteria:

- the length of the gas radiator is fixed to a few meters in order to detect enough photons for each ring image and so to achieve the necessary detector performance,
- the photon detector has to be kept out of the solid angle for charge particles and conversion products in order to be able to detect single photoelectrons at low electronics threshold,
- the photon detection surface has to be divided into pads to accomplish position detection and to cope with a high rate environment and
- the spherical mirrors focal length is kept at several meters to achieve the required high resolution in the measurement of the Čerenkov angle, assuming a pad size of the order of $\leq 1\mathrm{cm}$ (see equation 2.11).

According to the listed criteria the RICH detector is composed of two arms, one above and the other below the beam pipe. Each arm consists of

- a spherical mirror which projects Čerenkov photons onto the corresponding planar mirror,
- a planar mirror which reflects photons to the photon detector surface and
- position sensitive photon detectors placed in the focal surface which are capable of detecting photons with high efficiency and with good position resolution in two dimensions.

In addition a gas system providing radiator gas to the vessel and a readout system are parts of the RICH detector assembly. A cross sectional view of the RICH detector is shown in Fig. 3.3.

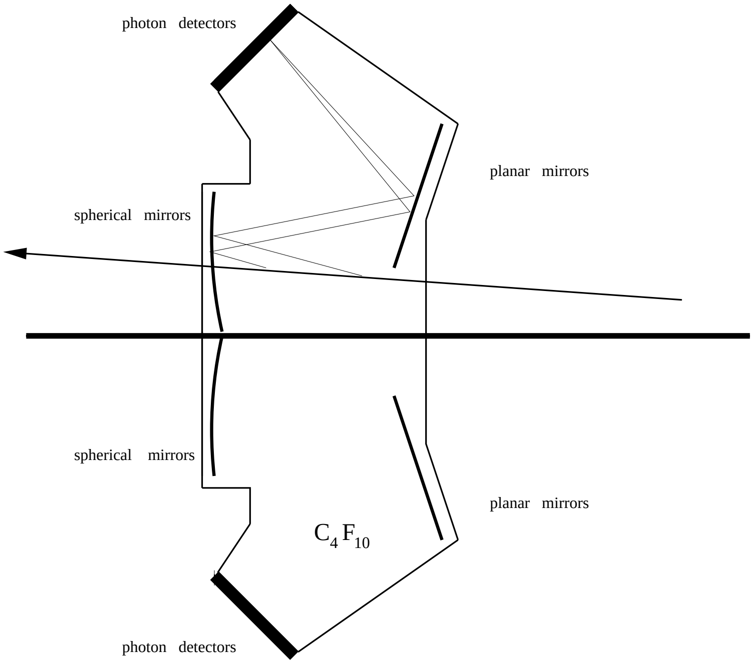

Figure 3.3: Cross sectional view of the RICH detector with spherical and planar mirrors assembled inside of the stainless steel sealed vessel and photon detection modules.

3.3 Expected number of detected Čerenkov photons

The photon detector response parameter, as already noted in equation 2.7 depends on the following quantities

$$N_0 = \left(\frac{e_0^2}{4\pi\varepsilon_0\hbar^2c^2}\right)\int T_r(E)R_m(E)\epsilon_d(E)\,dE.$$

If one takes into account the values for the RICH photon detector

- $\mathrm{T_r}$ radiator gas transparency (≈ 1) [26],
- $\mathrm{R_r}$ mirror reflectivity (see Fig. 3.4) and
- ε_d the detection efficiency of the photon detector (see Fig. 3.4), which depends on
  - photomultiplier tubes quantum efficiency,
  - optical system transparency,
  - photon detector fraction of active area $(\approx 0.9(\mathrm{see\ the\ following\ chapter}))$ and
  - transfer and collection efficiencies of photoelectrons (≈ 0.75) [33].

one calculates the merit factor $\mathrm{N_0} = 43\,\mathrm{cm}^{-1}$ and using the equation 2.6 the expected number of photons for particles approaching the velocity of light

$$N_{det} = N_0 L \sin^2\vartheta = 31,$$

where L is 2.7 m and $\vartheta = 51.5\ \mathrm{mrad}$.

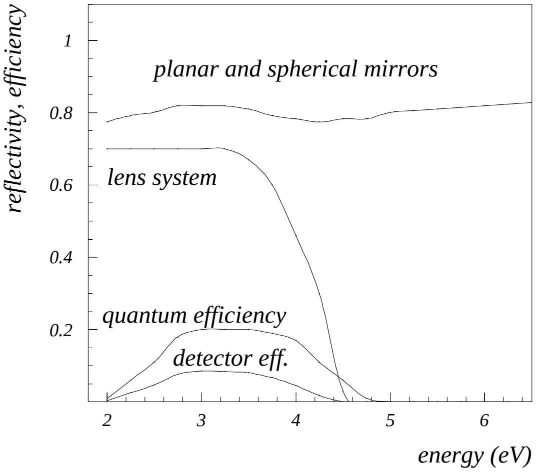

Figure 3.4: Reflectivity of plannar and spherical mirrors and the detection efficiency of the photon detector as a function of photon energy. The photon detector efficiency is a product of photomultiplier tube quantum efficiency, optical system transparency, geometrical acceptance of the photon detector and its photoelectron detection efficiency.

3.4 Expected resolution of the Ring Imaging Čerenkov detector

The Čerenkov angle and thus the velocity of the particles is obtained from the photon hit coordinate as measured by the photon detector and from the particle trajectory as given by tracking devices. The angular spread of Čerenkov photons, emitted by a single particle and particle track uncertainties are sources of error in the velocity determination. In the following, contributions to error of Čerenkov angle measurement are listed [22].

- The chromatic aberration amounts to

$$\sigma_\vartheta{}^{\mathrm{dis}} \approx \frac{1}{\sqrt{2\mathrm{n}-1}}\frac{\mathrm{dn}}{\mathrm{dE}}\sigma_{\mathrm{E}} = 0.36 \ \ \mathrm{mrad} \tag{3.6}$$

  where σ_{E} is the standard deviation of the energy distribution of detected photons (0.57 eV) (see Fig. 3.4), while dispersion dn/dE is presented in Appendix A.

- The finite coordinate resolution of the photon detector is

$$\sigma_\vartheta{}^{\mathrm{det}} = \frac{\mathrm{a}}{\mathrm{f}\sqrt{12}}. \tag{3.7}$$

  The focal length f of the spherical mirror is 5.70 m and a is photon detector pad size. Because two different sizes of pads are used in the photon detector (see the following chapter), $9 \ \mathrm{mm} \times 9 \ \mathrm{mm}$ for inner part and $18 \ \mathrm{mm} \times 18 \ \mathrm{mm}$ for outer part, the obtained standard deviation of the Čerenkov angle distributions are

$$\sigma_\vartheta{}^{det,in} = 0.46 \ \ \mathrm{mrad} \quad \mathrm{and} \quad \sigma_\vartheta{}^{det,out} = 0.92 \ \ \mathrm{mrad} \tag{3.8}$$

  respectively.

- The multiple Coulomb scattering contribution [17] in 2.7 m of $\mathrm{C_4F_{10}}$ gas amounts to

$$\sigma_\vartheta{}^{\mathrm{msc}} = \frac{2}{3}\frac{\mathrm{E_o}}{\beta\mathrm{cp}}\sqrt{\frac{\mathrm{x}}{\mathrm{X_0}}}\left(1+\mathrm{k}\ln\left(\frac{\mathrm{x}}{\mathrm{X_0}}\right)\right) = 0.1 \ \ \mathrm{mrad}, \tag{3.9}$$

  at particle momentum of 50 GeV/c, where $\mathrm{x/X_0}$ is the thickness of the scattering medium in radiation lengths and $\mathrm{E_o}$ = 13.6 MeV, k = 0.038 and radiation length $\mathrm{X_0} = 35\mathrm{m}$ [18].

- The spherical aberration due to the nonzero angle of incidence of photons upon the spherical mirror amounts to [20]

$$\sigma_\vartheta{}^{sa} = 0.16 \ \ \mathrm{mrad} \tag{3.10}$$

  for tracks with the angle of incidence upon the spherical mirror of 9^{o}.

- The optical errors due to the imperfections on the mirror surface and mirror misalignment are estimated to [1]

  $$\sigma_\vartheta{}^{mi} = 0.15 \ \mathrm{mrad}, \tag{3.11}$$

  and

  $$\sigma_\vartheta{}^{al} = 0.18 \ \mathrm{mrad}. \tag{3.12}$$

- The uncertainties of the particle trajectory due to the error in track parameters as determined by the tracking system amounts to [1]

  $$\sigma_\vartheta{}^{tr} = 0.06 \ \mathrm{mrad}. \tag{3.13}$$

Because the listed errors are uncorrelated, the combined error is obtained by summing them in squares. An estimate for the standard deviation of the Čerenkov angle distribution determined from a single photon hit for high momentum tracks thus amounts to

$$\sigma_\vartheta^{1,in} = 0.65 \ \mathrm{mrad} \ \text{ and } \ \sigma_\vartheta^{1,out} = 1.02 \ \mathrm{mrad} \tag{3.14}$$

for inner and outer photon detector respectively. The corresponding resolution in β is $\sigma_\beta{}^{1,\mathrm{in}} = 3 \times 10^{-5}$ and $\sigma_\beta{}^{1,\mathrm{out}} = 5 \times 10^{-5}$.

However more than one Čerenkov photon is detected per charged particle track, with the result that their average angle is determined to a better accuracy. The standard deviation of this average angle is proportional to the inverse square root of the number of the detected photons per ring.

$$\sigma_\vartheta{}^N = \frac{\sigma_\vartheta^1}{\sqrt{N}} \quad \text{or} \quad \sigma_\beta{}^N = \frac{\sigma_\beta^1}{\sqrt{N}}. \tag{3.15}$$

Assuming 31 detected photons the particle velocity measurement precision is

$$\sigma_\beta{}^{N,in} = 6.1 \times 10^{-6} \ \text{ and } \ \sigma_\beta{}^{N,out} = 9.5 \times 10^{-6}. \tag{3.16}$$

With 31 detected photons, this ring imaging Čerenkov counter should achieve a $3\sigma_\beta$ $\pi - \mathrm{K}$ separation up to about 80 GeV/c in the inner part of the photon detector. However, the estimate quoted above would be valid only for the case of isolated single particles with no background. In fact also other charged particles produced within the same event emit Čerenkov photons, which present background and thus cause additional problems in disentangling the pattern of overlapping Čerenkov rings.

A photon detector hit pattern as shown in Fig. 3.5 is generated by Čerenkov radiation of large number of simultaneous particles, produced during one proton bunch crossing. Simulation and reconstruction of such events shows [19] that a 90% efficiency for resolving a kaon up to particle momentum of 50 GeV/c allowing 5% of pion fake probability can be obtained.

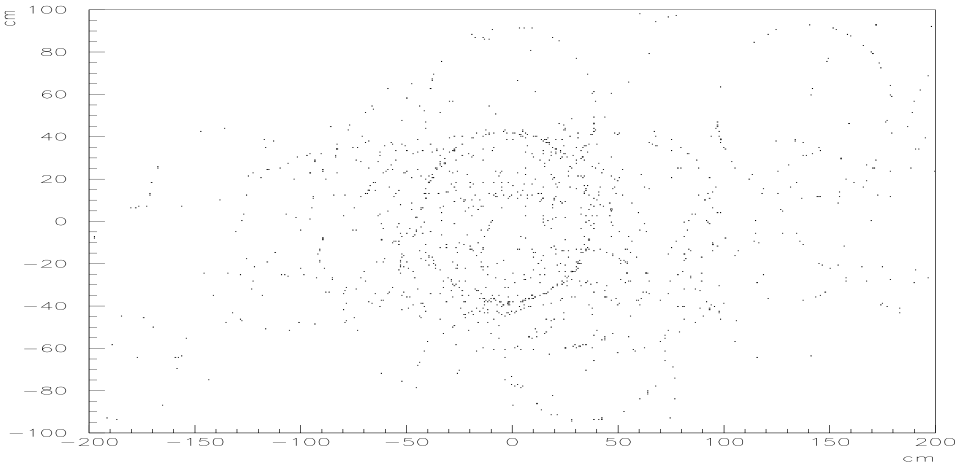

Figure 3.5: A computer simulated pattern of Čerenkov photon hits on the photon detector due to one bunch crossing.

4

The HERA-B RICH components

4.1 Introduction

The overall mechanical frame of the RICH detector is provided by the gas radiator vessel which is located in the region between 8.5 m and 12.0 m downstream of the target (see Fig. 1.5). The top, bottom and sides of the vessel are made from stainless sheets to guarantee mechanical stability. The particle entry and exit windows, i.e. front and rear walls of the vessel, are constructed from 1 mm thick aluminium sheets. The holes for the proton and electron beam pipes are cut in the windows. The gas volume around the two beam pipes is closed by two beam shrouds. The vessel and beam shrouds are painted black with low outgasing colour. Two 3 mm thick plexi glass exit windows for Čerenkov photons, which support more than 20 mbar overpressure close the vessel on top and bottom. In what follows the RICH detector system elements construction and their tasks are described.

4.2 Gas System

The general goals of the RICH gas system are [26]

- providing radiator gas to the vessel,
- regulating the vessel pressure relative to ambient,
- maintaining appropriate radiator gas purity,
  - $\mathrm{O_2}$ and $\mathrm{H_2O}$ concentrations below 100 ppm to reduce forming hydrofluoric acids from broken radiator gas molecules and
  - inert gas component (e.g. nitrogen) below $10\ \%$ to limit the radiator refractive index changes,

- minimising the radiator gas losses and leak rates to below $0.01\ \mathrm{dm}^3/\mathrm{hour}$,
- providing indicators for different stages of operation and
- enabling a flow rate up to $10\ \mathrm{m}^3/\mathrm{hour}$ to maintain the cumulative contamination level at the 1000 ppm level.

The gas system basic design criteria were adopted from the existing system used in the forward part of the RICH counter of the DELPHI experiment [26], which includes four subsystems connecting the storage tank with the vessel:

- a compressor system,
- a purification system,
- a liquid and gas phase separation system and
- a volume flow regulation system.

A schematic diagram of the gas system design is presented in Fig. 4.1, and the gas sub-

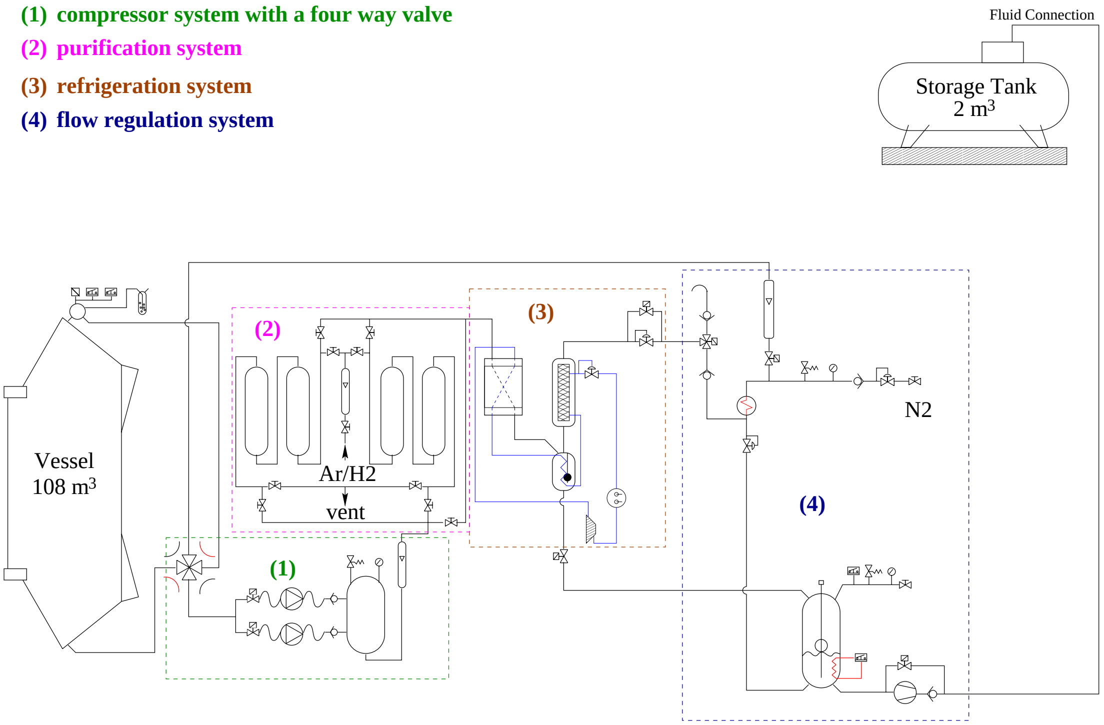

Figure 4.1: A drawing of the system showing the vessel with a safety bubbler, a four way valve, a compressor system, a O_2 and H_2O cleaning cycle, a three step refrigeration system connected to a buffer volume, a volume flow regulation cycle and a storage volume.

system parts are described in the following:

- The volume of the **radiator vessel** was calculated to be $108\,\mathrm{m}^3$ with an uncertainty of $\pm\,2\%$. The filling of the volume thus amount to 1070 kg of $\mathrm{C_4F_{10}}$ which corresponds to $710\ \mathrm{dm}^3$ of liquid phase. The vessel is equipped with pressure sensors which are insensitive to the ambient magnetic field and with pressure limiting switches in order to stabilise the overpressure in the radiator volume to $\pm\ 6\ \mathrm{mbar}$ [26]. Three pressure monitors are positioned on the top and bottom, and in the middle of the vessel. The first two help the steering of the gas flow, and allow an estimate of the concentration of contaminations during filling using the difference of the hydrostatic pressure. The pressure monitor in the middle is provided for the safety of the beam shrouds. The vessel is also protected with a large volume safety over and under pressure bubbler.

- The **compressor system** is set up from a pressure four way valve which allows gas input and output on top or bottom of the vessel and two compressors with ability to change the pressure in steps.

  The oil free single piston compressor model SOGX 50 is employed in the RICH gas system because it sustains a 5 bar exit pressure at a flow rate of $\approx 4\mathrm{m}^3/\mathrm{h}$ and 12 bar exit pressure at flow rate $\leq 2\mathrm{m}^3/\mathrm{h}$. Two compressors in parallel are used to attain flow rates grater than $4\mathrm{m}^3/\mathrm{h}$. The operating frequency of the compressors is remotely controlled on the basis of data from pressure indicators. The $\mathrm{C_4F_{10}}$ gas from the vessel is coming to the compressor input side with pressure of 5 bars and gets condensed inside of a concentric pipe. To provide a better separation of the gas and the liquid phase the mixture is pressed to a porous block into the work storage.

- **The purification circuit** is designed to remove oxygen and water from the circulating $\mathrm{C_4F_{10}}$ gas. The level of contamination with oxygen and water at a few ppm is maintained by flowing the radiator gas through traps of molecular sieve and activated copper. The oxygen and water cleaning lines are doubled so that the system can be cleaned while running the experiment.

- The primary purpose of **the liquid and gas phase separator circuit** is to separate the unwanted inert gas from $\mathrm{C_4F_{10}}$ during filling. This subsystem can also be turned on during recirculation of the $\mathrm{C_4F_{10}}$ when low boiling point impurities reach critical level. The liquid and gas phase separator circuit consists of two heat exchangers and a liquid gas separator. A purified gas liquid mixture passes through the warmest heat exchanger to make the initial liquefication of the $\mathrm{C_4F_{10}}$. Liquid begins to accumulate in the separator, which has a level switch to open the valve for transfer to the buffer volume and or back to the radiator vessel. The vapour over the liquid then passes through the coldest heat exchanger, where the remaining $\mathrm{C_4F_{10}}$ condenses and accumulates in the separator. The remaining inert gas is vented.

- **The flow regulation system** is composed of flow controller circuit, radiator buffer volume and liquid pump. The flow controller circuit is made up of a pressure release valve and a heater to insure that only the gas phase is let through. A setable flow rate system regulation in the range between $1\ \mathrm{dm}^3 \rightarrow 10\ \mathrm{m}^3/\mathrm{hour}$ is used to maintain the cumulative contamination levels at 1000 ppm level due to a $10^{-3}\ \mathrm{dm}^3 \rightarrow 10\ \mathrm{dm}^3/\mathrm{hour}$ range contamination rates.

In order to be able to compensate radiator losses and atmospheric pressure variations of maximal 40 mbar/day observed by H1 experiment with high enough speed an amount of $\mathrm{C_4F_{10}}$ in liquid phase is stored in the buffer volume.

A liquid pump is used to transfer the liquid $\mathrm{C_4F_{10}}$ from the buffer volume 20 m upwards to the storage container.

- **Temperature controlled storage volume** houses the radiator $\mathrm{C_4F_{10}}$ in liquid phase. It is equipped with visual and electronic depth gauge, of 1 mm precision in order to detect possible leaking by observing liquid level shifts. The storage volume is also rigged with internal pressure gauge, pressure release valve and heating and cooling mechanism.

4.2.1 Modes of Operation

Switching among the various modes of gas system operation like flushing with nitrogen, purification of $\mathrm{C_4F_{10}}$ gas, filling the vessel with $\mathrm{C_4F_{10}}$ and collection of $\mathrm{C_4F_{10}}$ in the supply tank is enabled by using several electromagnetic valves of the system. Whole gas system operation can be described by four modes.

- **Gas System Preparation Mode**
  At the beginning of operation the gas system is filled with air. The first step is to clean the entire system, which is achieved by flowing dry inert gas through the entire system except through the cleaning system and radiator storage tank which are initially cleaned by evacuation. When oxygen concentration is at an acceptable level and leak checking is finished, the filling operation can start.

- **Radiator Filling Mode**
  At the beginning of this mode of operation the gas system is filled with a dry inert gas and the storage tank is filled with $\mathrm{C_4F_{10}}$. The buffer volume is filled with $\mathrm{C_4F_{10}}$ which is then passed to the evaporater and flow controller unit. The level indicator in the buffer volume regulates the transfer of $\mathrm{C_4F_{10}}$ from storage. The radiator vessel is filled from the bottom with $\mathrm{C_4F_{10}}$ while the inert gas is removed from the top. The removed gas mixture is passed through the purification and the gas liquid separator circuit. The recovered $\mathrm{C_4F_{10}}$ is sent back to the vessel while the vapour mixture is vented to the atmosphere. The recovered $\mathrm{C_4F_{10}}$ in the liquid state is transfered to the buffer volume. As the vessel is filled with $\mathrm{C_4F_{10}}$ the pressure

difference between the top and bottom of the vessel increases to the hydrostatic pressure difference based on C_4F_{10} density. The hydrostatic pressure difference of 8.3 mbar indicates that the vessel is filled with C_4F_{10} and the subsequent mode may begin.

- **Recirculation Mode**
  During the recirculation mode the radiator vessel is filled with C_4F_{10} gas from the bottom and emptied from the top. The removed gas is passed through the cleaning cycle and sent back to the vessel. The total leak and out gassing rate is monitored by the H_2O and O_2 content of the gas mixture leaving the radiator vessel. The gas liquid separator system running depends on the total leak rate. While the total leak rate doesn't influence the desired performance, the gas liquid separator circuit is not running and its vapour output is not vented to atmosphere, but sent back to the vessel. In the opposite situation the separator is switched on and gas system essentially returns to filling mode.

- **Radiator Removal and Storage Mode**
  The radiator gas is removed from the bottom by switching the four way valve and flowing inert gas into the top of the vessel. The liquid and gas phase separator circuit is switched on and the vapour output is returned to the vessel. The liquid output is used to fill the buffer volume with liquid which is then transferred to the storage tank by the liquid pump. When the hydrostatic pressure difference in the vessel and the accumulation of liquid in the separator are zero it indicates that all of the C_4F_{10} has been recovered.

4.3 Mirrors

The system of mirrors consists of two spherical and two planar mirror planes. The radius of curvature of the ring forming spherical mirror plane is $11.4\ \mathrm{m}$. The spherical mirror plane, 6 m wide and 4 m high, is split horizontally at the medium plane (see Fig. 4.2). The upper section is tilted up, while the lower is tilted down by 9^o. The spherical mirror plane is formed from 80 discrete mirror units, full or partial hexagons. Holes were cut out from four segments to let the electron and the proton beam pipe through. All the different types of spherical mirror segments are shown in Fig. 4.3. Spherical mirror tiles are made of 7 mm thick pyrex base coated with 200 nm Al and 30 nm MgF_2.

The optical quality of spherical mirror segments was checked during all phases of the mirror production [23]. As a final step in the quality inspection, several measurements of optical and physical characteristics were done at the factory by the RICH group representative. For each segment the following characteristics were measured :

- physical dimensions (thickness, diagonals, heights),
- radius of curvature,

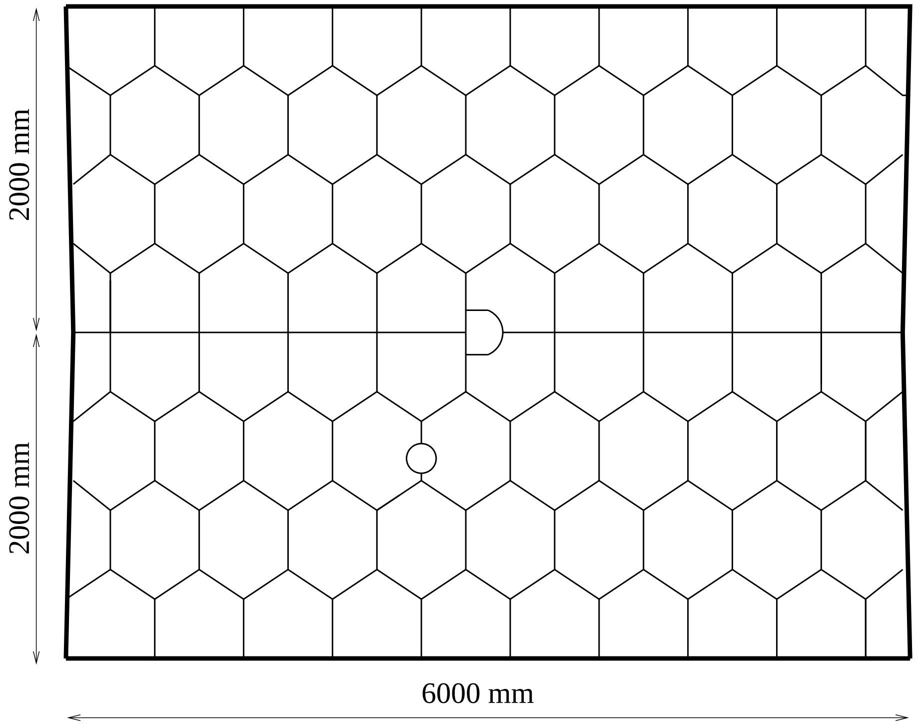

Figure 4.2: The spherical mirror plane with horizontally split at the medium plane.

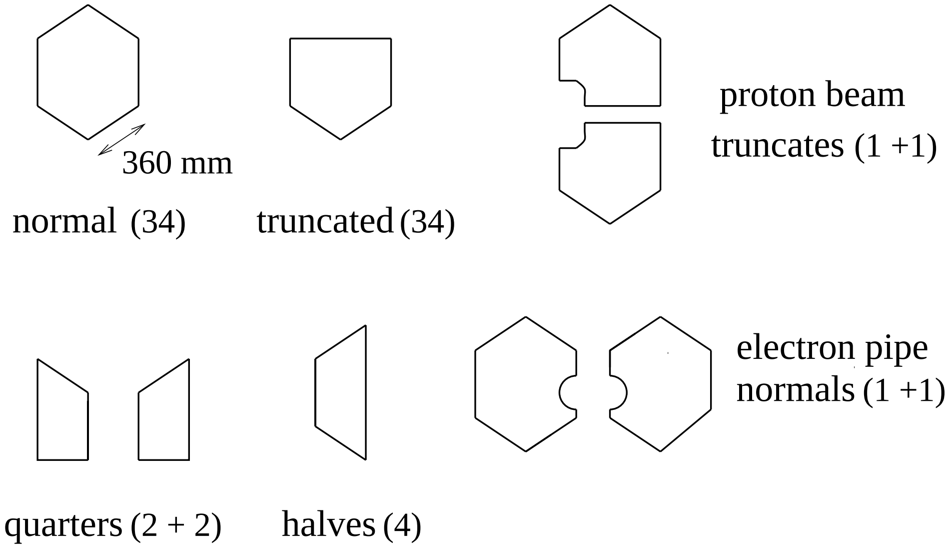

Figure 4.3: Different types of spherical mirror segments. Cipher in brackets denote numbers of necessary pieces of each type.

- surface quality (visual inspection of the surface, adhesion test, fraction of power from a point source that is focused into 7 mm and 3 mm aperture, size of the light spot on the screen plane, surface homogeneity) and
- spectrometer reflectance curve.

More detailed information about mentioned tests can be found in Appendix B. The acceptance test required that

- 95% of the reflected light from a point source is focused into a 7 mm aperture,
- the radius range is 11.40 m ± 0.1 m and
- the reflectivity exceeds 85 $\%$ in the wavelength interval from 250 nm to 600 nm.

Accepted mirror segments were then grouped in the tiling scheme according to their optical quality and resolution requirements. The mirrors that are closer to the proton beam shroud see more Čerenkov photons than mirrors at the edges. Hence the quality of a mirror that fills a specific location is chosen according to the locations distance from the proton beam pipe. In order to optimise the performance of the RICH detector, mirrors with the best optical characteristics are placed nearest the proton shroud and the difference between the radii of neighbouring mirrors are selected to be as small as possible. Only the measurement of the radius of curvature and focusing properties were used to rank the mirrors according to their optical quality, because in the other tests the mirrors showed similar characteristics [23]. Each spherical mirror segment is mounted at three points on a support panel. The segment position can be adjusted by moving two out of three points. The moving points are motor driven via a transmission mechanism with a feed through to the exterior of the vessel.

The planar mirror system is divided into two planes which direct the Čerenkov light to the photon detectors. The plane mirror support structure allows only rather small planar mirror segments. Each plane is thus divided into six equally big vertical sections which are further divided into three equally big segments. One plane of planar mirror system is so composed of 18, 750 mm wide and 635 mm high, rectangular mirror segments of float glass mounted on the suspension wall (see Fig. 4.4). In each vertical section the rectangular segment closest to the beam pipe is fixed to a movable frame. The other two segments are individually adjustable relative to the frame.

Spherical mirror segments were aligned using an autoreflection procedure, while planar mirrors segments were aligned by using the autocollimator. An accuracy of 0.05 mrad for all segments was achieved. Layout of spherical and planar mirror plane after the alignment procedure was finished is presented in Fig. 4.5. Before the vessel was closed, the scaffoldings seen on both photographs were dismounted and dust on mirror planes was removed by flushing them with nitrogen.

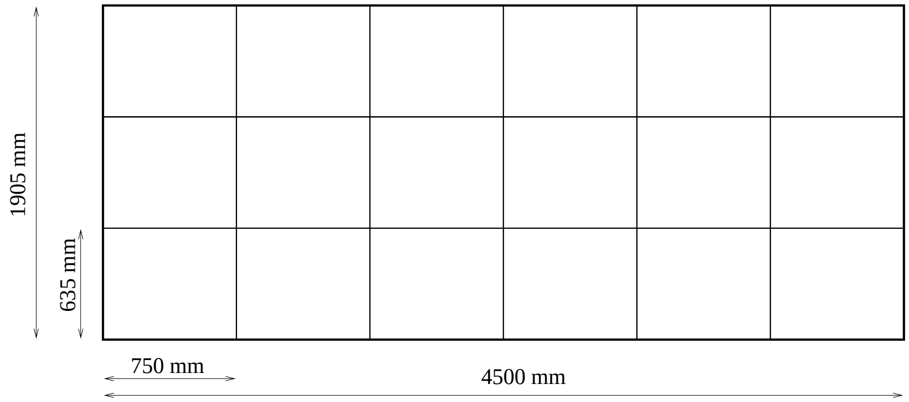

Figure 4.4: Planar mirror plane composed of 18 rectangular segments.

Figure 4.5: Spherical (left side) and planar (right side) mirror plane layout before the scaffolding was removed.

4.4 The photon detector system

After extensive experimental work on wire chambers based photon detectors, it was realised that neither of the investigated candidates for the RICH photon detector met our design criteria. Two types of chambers were tested, a gaseous TMAE (tetrakis dimethyl amino ethylen) based chamber and a multiwire chamber with solid CsI photocathode. The TMAE detector showed a prohibitive decrease of avalanche gain due to aging effects [28, 29], while the detector with CsI photocathode had operational problems at rates in excess of a few kHz per pixel. An additional problem was encountered with routinely produced CsI photocathodes because we could not maintain their quantum efficiency at sufficiently high level [27]. Simultaneously a new generation of commercial multianode photomultipliers become available and it was proven that they can be used for single photon counting with a high efficiency and very low cross-talk [30]. So the decision [31] was made to equip the RICH photon detector exclusively with photomultiplier tubes.

4.4.1 The supermodule

The upper and the lower photon window of the radiator tank are both equipped with a set of seven grid structures, called supermodules. The supermodule construction assures the fundamental mechanical support and alignment as well as magnetic shielding for the photomultiplier tubes. The supermodule elementary cell accepting one photomultiplier tube is a square of 36 × 36 mm^2. Each supermodule has a structure which is 32 elementary cells high and 12 wide (see Fig. 4.6).

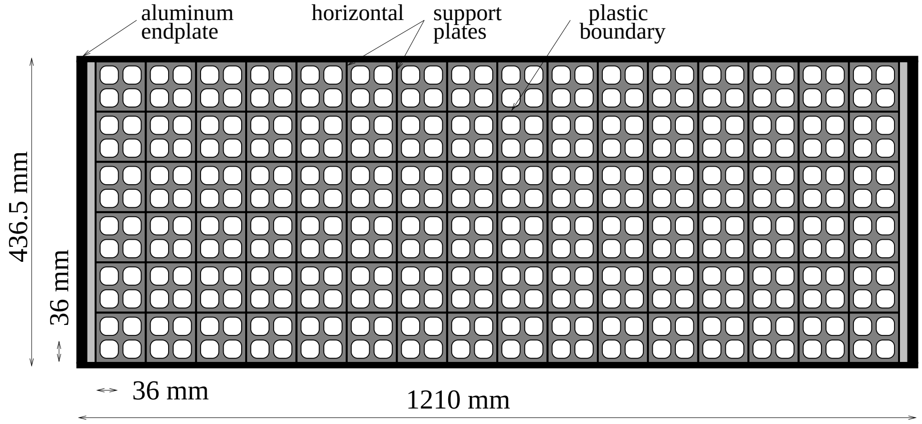

Figure 4.6: Supermodule grid structure made from plastic molded sheet steel.

The stability of the supermodule is guaranteed by vertical and horizontal 1 mm thick steel plates, which separate one elementary cell from the other. The supermodule design is presented in Appendix C.

During the production procedure the steel sheet grid structure was fixed on a milled aluminium plate, and then covered by black liquid plastic, which after hardening provides stability and light seal [32]. The space for photomultiplier tubes was saved by screwing aluminium cubes of $30\ \mathrm{mm} \times 30\ \mathrm{mm}$ cross section onto the milled aluminium plate. The plastic molded iron sheet structure is attached to aluminium top and bottom plates, which mount to the detector flanges of the radiator gas vessel. The molds provide a $70.3\mathrm{mm} \times 70.3\mathrm{mm}$ square free space for the photomultiplier tube base board modules, due to a 1.7 mm wide and 3 mm high plastic boundary between two boards (see Fig. 4.6).

Each second horizontal steel plate is 36 mm higher and is carrying holes to which the photomultiplier tube base modules are aligned. Besides alignment they also provide support for front end electronic boards.

4.4.2 Photomultiplier tube base module

The basic photomultiplier tube module consists of four multianode photomultiplier tubes mounted in 2×2 arrays on a printed circuit baseboard. Two different types of basic photomultiplier tube modules are made due to the use of two photomultiplier tube types. One module type is housing Hamamatsu photomultiplier tubes R5900 of type M16, while the other is housing tubes of M4 type. The employed multianode photomultiplier tube types M16 and M4 have anodes divided into 16 pads of $4 \times 4\ \mathrm{mm}^2$ each and 4 pads of $9 \times 9\ \mathrm{mm}^2$ each, respectively [33]. The outer dimensions of the tubes are $25.7 \times 25.7\ \mathrm{mm}^2$, thus the photocathode occupies only about 40% of the photomultiplier tube surface. The 12 stage and 10 stage metal foil dynode systems used in M16 and M4 tubes, respectively, allow good single photoelectron resolution [30]. The quantum efficiency of the bialkali photocathode with a borosilicate window has a broad plateau in the energy region between 2.5 eV and 4.1 eV, with a maximum value of 20% [33]. If a UV light transparent window is used the photomultiplier sensitivity can be extended to higher photon energies. The photomultiplier tube characteristics are presented in Appendix D.

At the front side, baseboards are equipped with sockets in plastic frames which accept photomultiplier tube pins and thus also align the photomultiplier tube position. A 3 mm wide and 3 mm thick foam gasket is glued at the edge of each baseboard to provide a light tight seal. Layouts of both modules front sides are schematically presented in Fig. 4.7. To get a better impression of the basic module construction, only two photomultiplier tubes are drawn in both figures, so that also sockets in plastic frames can be clearly seen.

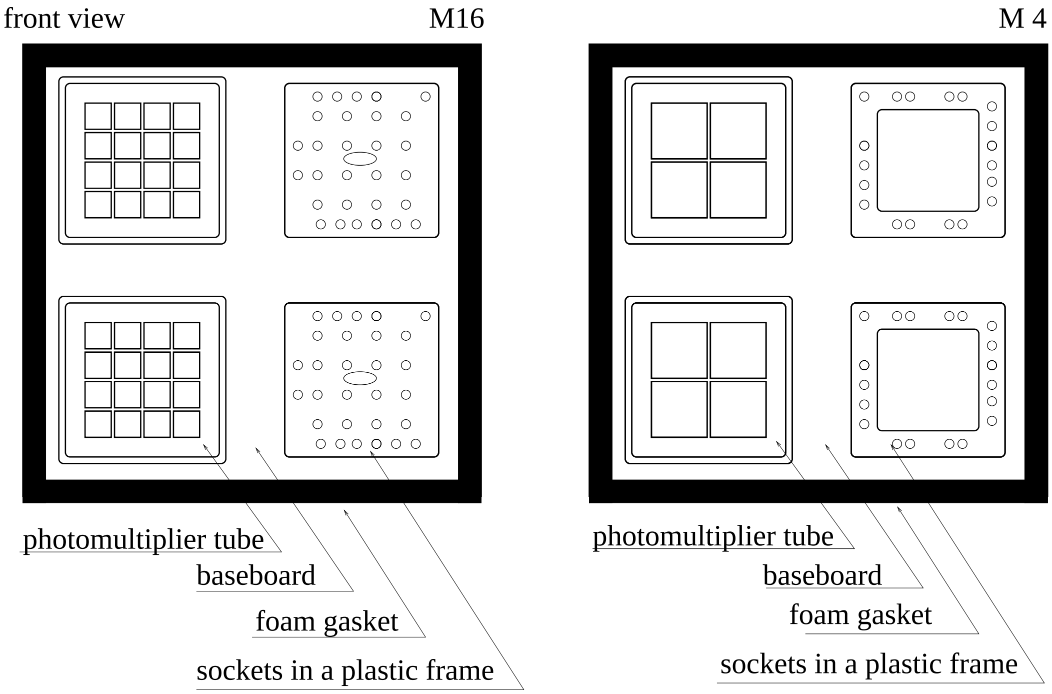

Figure 4.7: Schematical presentation of both types of photomultiplier basic module equipped only with two photomultiplier tubes.

A 70 mm square baseboard houses four high voltage divider chains, one for each photomultiplier tube and signal lines connecting photomultipier tube output channels with readout electronics. The main differences between baseboards employed in the two module types are dictated by the different number of photomultiplier tube readout channels and by the different number of stages in the photomultiplier dynode system. Electronic circuit designs for both types of baseboards are presented in Appendix F. Each baseboard is equipped with two high voltage connectors and with surface mounted single row connectors at the rear side in order to connect signal lines to the readout cards. At the rear side of the baseboard also two L shaped brackets (see Appendix G) with two spring rails to guide read out electronics boards are attached with screws and nuts. Spring rails also provide electrically grounded connections between baseboard and read out board to prevent oscillations. Sixteen channel front end electronic boards (see Appendix E) consist of two amplifier shaper discriminator units ASD8 which transfer photomultiplier tube signals to the digital pipeline units of the data acquisition system. The modules which house photomultiplier tubes of M16 type thus use four readout cards, while the modules housing tubes of M4 type have only one. Rear and side views of both modules are schematically presented in Fig. 4.8 and Fig. 4.9, respectively.

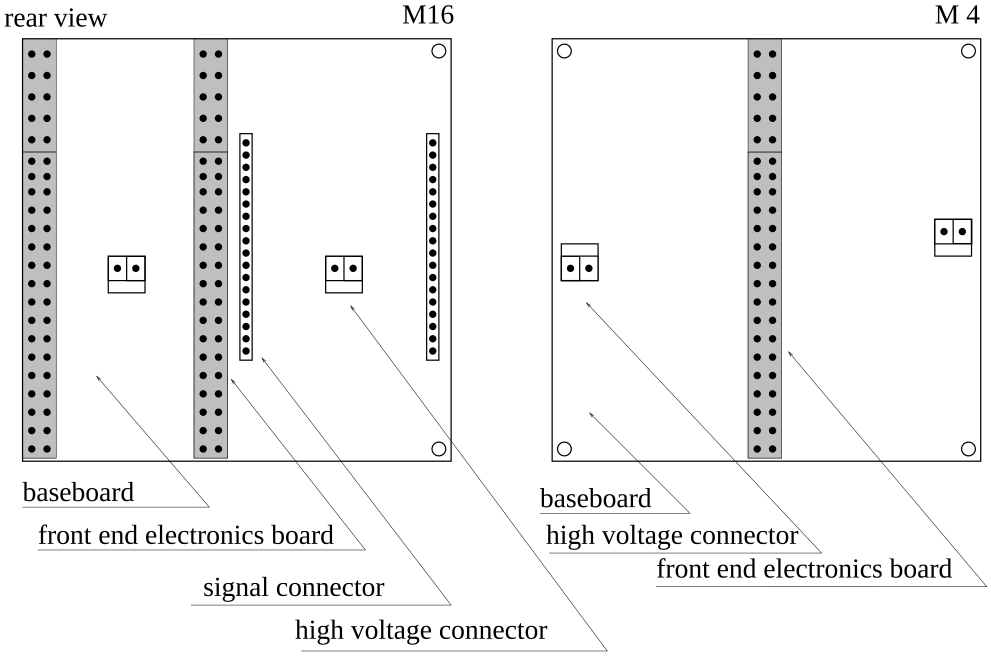

Figure 4.8: Rear view of photomultiplier base modules. Module housing photomultiplier tubes of M16 type is shown with two, out of four readout cards, while module housing photomultiplier tubes of M4 type is equipped with only one required readout card.

In a side view scheme two holes on each L shaped bracket which are used to align and to fix photomultiplier modules to the supermodule horizontal steel plates are clearly seen.

Module alignment and fastening to the supermodule construction is accomplished by using specially designed clamps with short rods (Appendix G). Clamps sandwich hori-

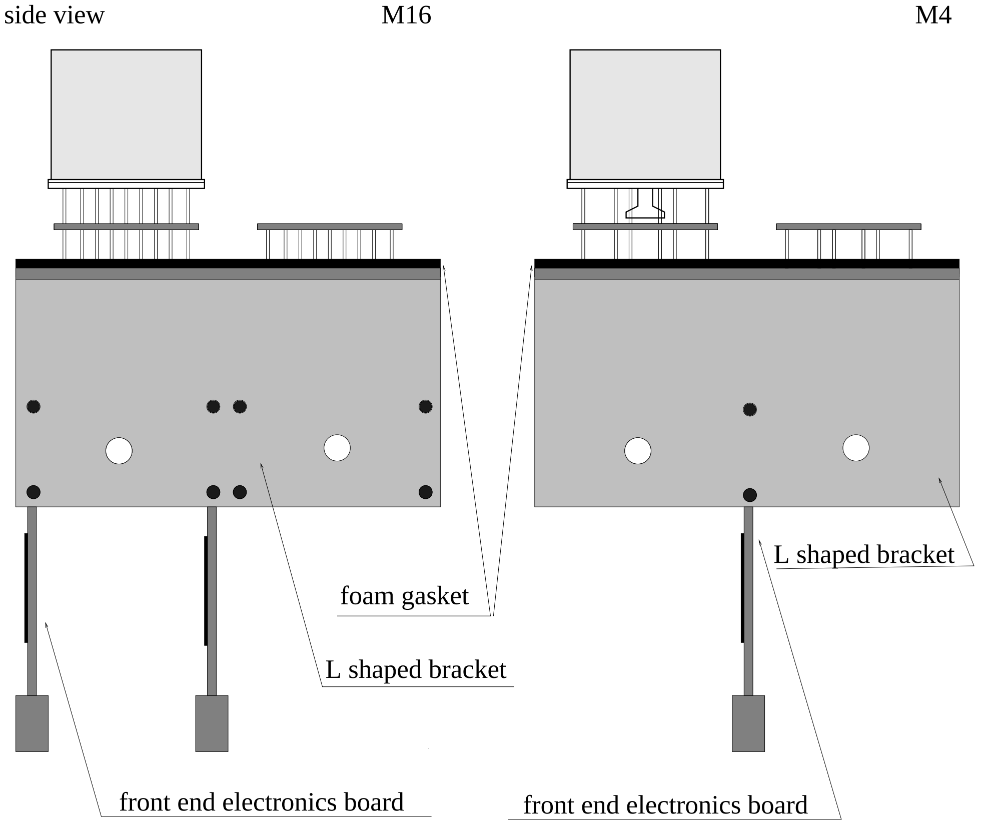

Figure 4.9: Side view of photomultiplier base modules. Besides photomultipier tubes and readout cards positions scheme also reveals L shaped brackets basic construction lines with two alignment holes .

zontal supermodule plates with L shaped brackets. Each clamp rod penetrates through two bracket holes of two photomultipier modules positioned in the neighbouring rows and in the same column of the supermodule grid structure and in between, through a hole in the horizontal steel plate of the supermodule construction.

In Fig. 4.10 photographs of fully equipped basic modules for M16 and M4 photomultiplier tubes are presented.

Besides the active modules, so called blind modules are used to cover the unused marginal parts of the supermodules. They are made of 1 mm thick aluminium plates which are bended in such a way to resemble the shape of a basic module baseboard equipped with two L shaped brackets. They are painted black, equipped with rubber gaskets and carry two alignment holes on each side, so the technique of fastening to the supermodule construction remains the same.

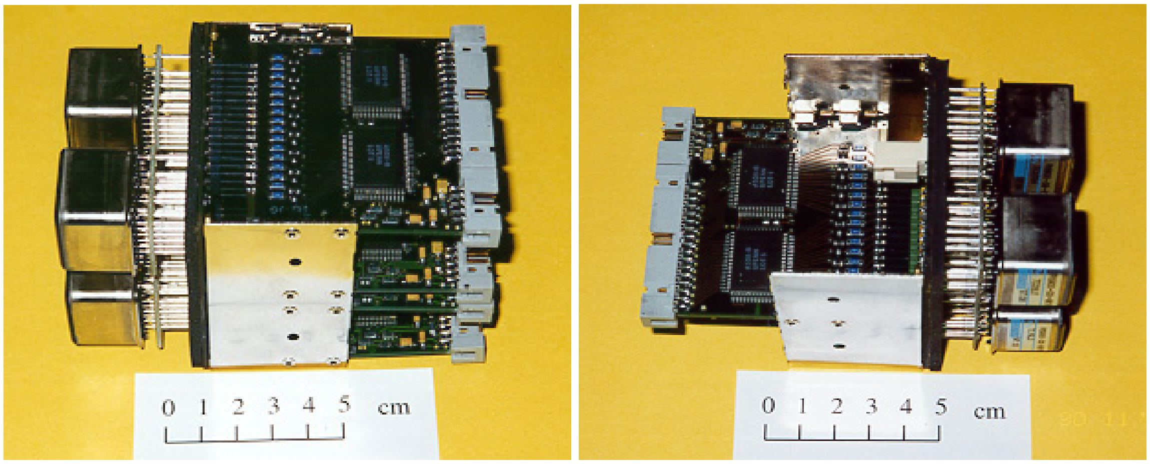

Figure 4.10: Fully equipped photomultiplier basic modules housing Hamamatsu R5900 photomultiplier tubes type M16 (left side) and M4 (right side).

4.5 Lens system

According to the photomultiplier tube base module geometry it can be calculated that the photocathode surface covers about 23% of the occupied focal plane area. In order to overcome the loss of detector efficiency that occurs due to dead gaps within the acceptance area a two lens demagnification system was designed [38, 39, 40]. The two lens system consists of a square field lens and a round collector lens as shown in Fig. 4.11.

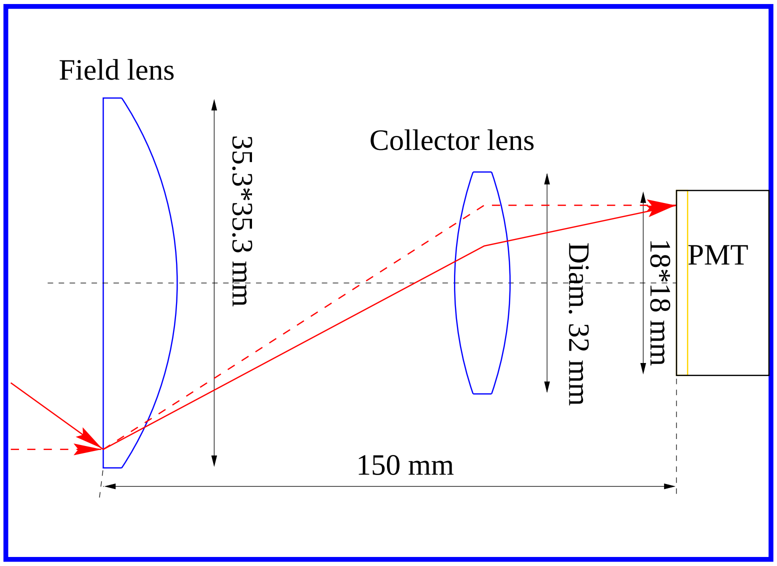

Figure 4.11: The light collection system consists of a square field lens and a round collector lens.

At the spherical mirrors focal surface an array of square planoconvex field lenses are positioned. They are followed by a grid array of symmetric biconvex collector lenses positioned at the field lenses focal plane. Each field lens covers an area of $35.3\ \mathrm{mm} \times 35.3\ \mathrm{mm}$ and has a focal length of 95 mm, while the biconvex collector lens has a focal length of 30 mm and a diameter of 32 mm. Both lens types are fabricated from UV light transmitting plastic, having the transmission characteristics of Cyro Acrylite. The curves for light transmission and index of refraction are presented in Fig. 4.12.

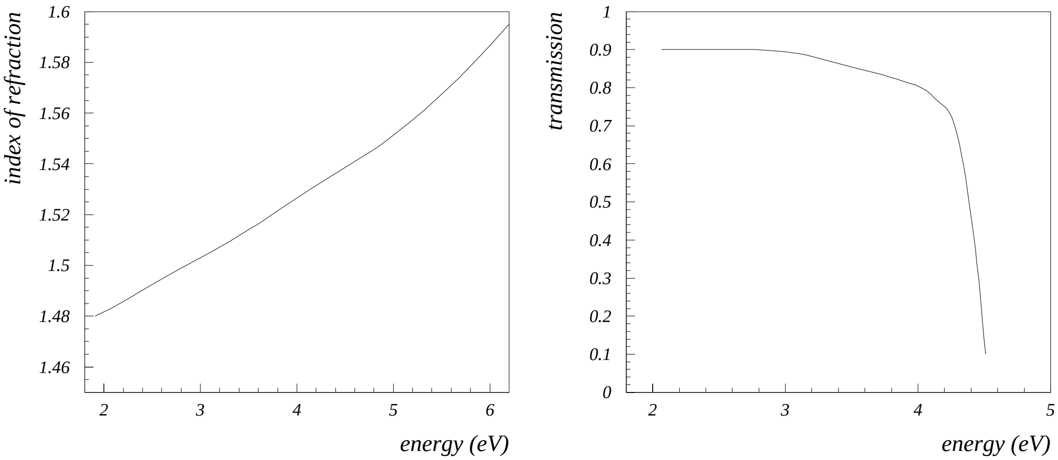

Figure 4.12: Optical qualities for Cyro Acrylite sheet. In the left side figure the refraction index dependence is presented, while in the right side figure the absorption curve for a 6.35 mm thick acrylite sheet is shown.

The lens doublet system demagnifies detector focal plane area by a factor of two in each linear dimension while maintaining an accurate mapping from the focal plane area to the corresponding pad size area of the photomultiplier cathode.

Light guides are organised in modules of 2 rows by 12 columns. The lens holders are produced from molded plastics and have the following dimensions $71.3\ \mathrm{mm} \times 432\ \mathrm{mm} \times 102\ \mathrm{mm}$ (see Fig. 4.13).

The lens holder structures are attached and aligned to the 2 mm thick vertical steel side walls, which are added to the supermodule construction. The mounting plates extend to cover the exposed sides of the lenses out to the field lens position. The mounting panels are spaced out on each side of the super module with shims, giving a nominal 432.5 mm space for the lens holders and thus allowing stress less mounting of the lens holders on the super module. The remaining 0.7 mm space on the boundary between neighbouring holders is reserved for a thin partition.

The overall efficiency of the two lens telescope is approximately 65% at the wavelength of 350 nm (see Fig. 4.14). The loss is due to reflection (15%), to absorption

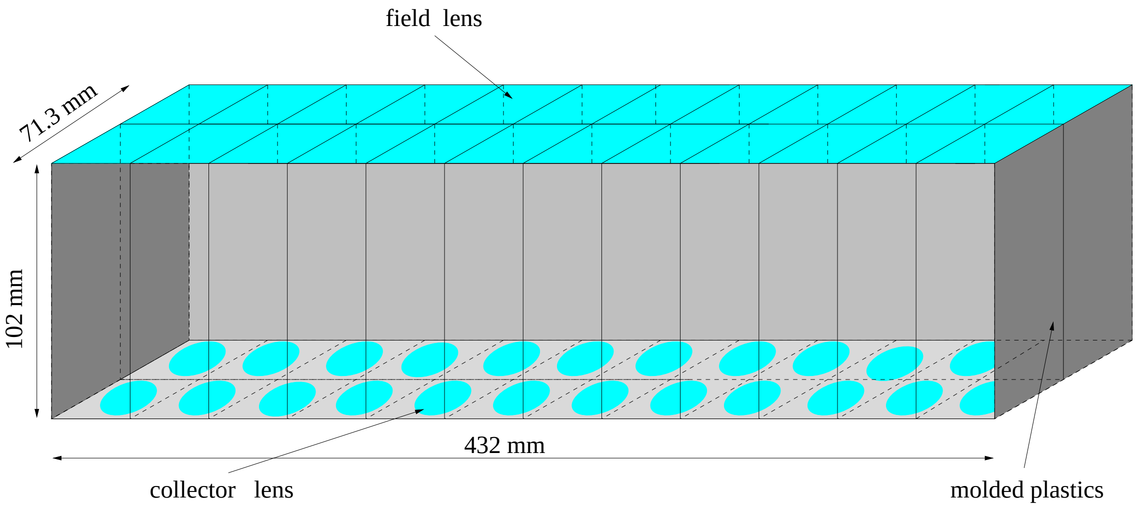

Figure 4.13: The schematic view of the lens holder structure organised in modules of 2 rows and 12 columns.

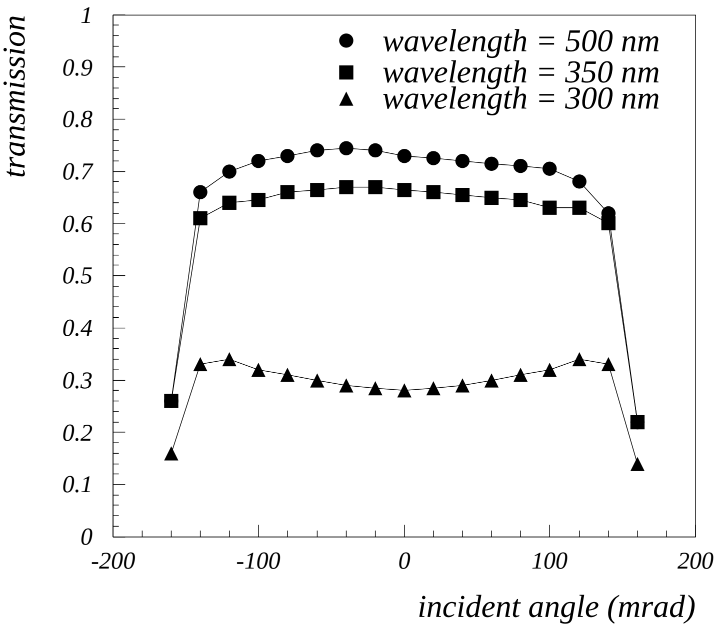

Figure 4.14: Angular dependence of the lens collection efficiency at three different wavelengths [41].

(15%), and to miscellaneous geometrical losses (5%). The figure of merit for the lens system, confirmed by measurements [42] is 2.8, because the light collected without the lens system amounts to 23%. Figure 4.14 also shows that the angular acceptance of the optical system is approximately constant for incident angles below about 120 mrad.

The measured performance of the two lens system is shown in Fig. 4.15. The lens system is effective up to approximately 120 mrad. At larger angles the collector lens aperture is blocked, but this presents no serious limit to our system because almost all photons strike the focal surface at angles substantially below this cutoff [42].

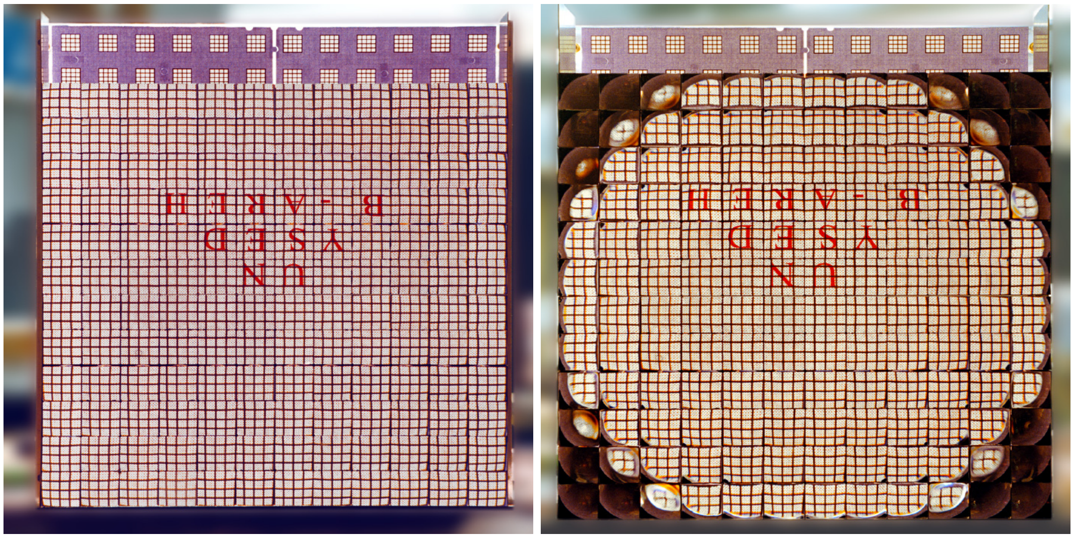

Figure 4.15: A square array of 12×12 lens systems is positioned in front of a simulated array of M16 photomultiplier tubes. In the left figure the camera was located at 3 m from the array. The pattern of letters reading

HERA-B
DESY
NU

has been superimposed on the mock cathodes. Each letter is rotated by 180^0. In the right figure the photo taken at a distance of 1.5 m is presented. It is demonstrated that the the lens system is effective up to incident angles below approximately 120 mrad, because at larger angles the collector lens aperture is blocked and corners fail to be recorded.

4.6 Photomultiplier tubes tiling scheme

Monte Carlo studies of the photon occupancy on the photon detector planes were used to determine the photomultiplier tubes tiling scheme [36]. While the originally planned photon detector active area coverage was nearly $7\ \mathrm{m}^2$, the final scheme coverage is less than $3\ \mathrm{m}^2$. The reduction in the active area was necessary because of the cost consideration, when the photomultiplier tubes were chosen as the photon detectors instead of the TMAE or CsI based system [30]. This reduction was possible since large angle tracks with low momentum and low background overlap can successfully be identified with only half or even less of the ring within the active detector area. Therefore, parts of the low photon occupancy and large angle regions of the focal planes were not covered with photomultiplier tubes, without loosing the efficiency. The active area was filled with the

	super module 1 and 12	super module 2 and 11	super module 3 and 10	super module 4 and 9	super module 5 and 8	$\sum$
No. of M4 modules	26	15	12	15	26	188
No. of M16 modules	7	53	66	53	7	372
No. of blank modules	63	28	18	28	63	400
No. of M4 PMTs	104	60	48	60	104	752
No. of M16 PMTs	28	212	264	212	28	1488
No. of M4 channels	416	240	192	240	416	3008
No. of M16 channels	448	3392	4224	3392	448	23808
M4 active area (mm^2)	134784	77760	62208	77760	134784	974592
M16 active area (mm^2)	36288	274752	342144	274752	36288	1928448
No. of lens holders	8	12	13	12	8	106

Table 4.1: Some parameters of the RICH photon detector plane building elements.

photomultiplier tubes of M16 or M4 type in a way to best accommodate the expected photon density and required position resolution (see Figures 4.16, 4.17, 4.18 and 4.19). Table 4.6 summarizes essential facts about photon detector construction. In order to reduce the contribution of spherical aberration to the overall resolution of the Čerenkov angle and to ensure a better acceptance for Čerenkov photons, an optimal surface of the photon detector has been calculated [20, 21]. Individual supemodules of each half of the photon detector are thus placed approximately on the optimal surface, which is close to the shape of a flattened (ellipsoidal) cylinder.

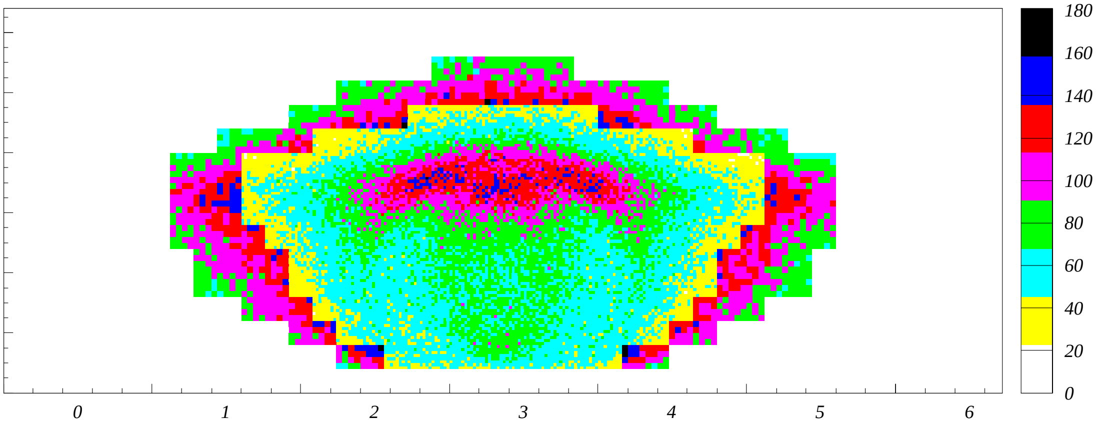

Figure 4.16: Expected photon occupancy on the photon detector plane.

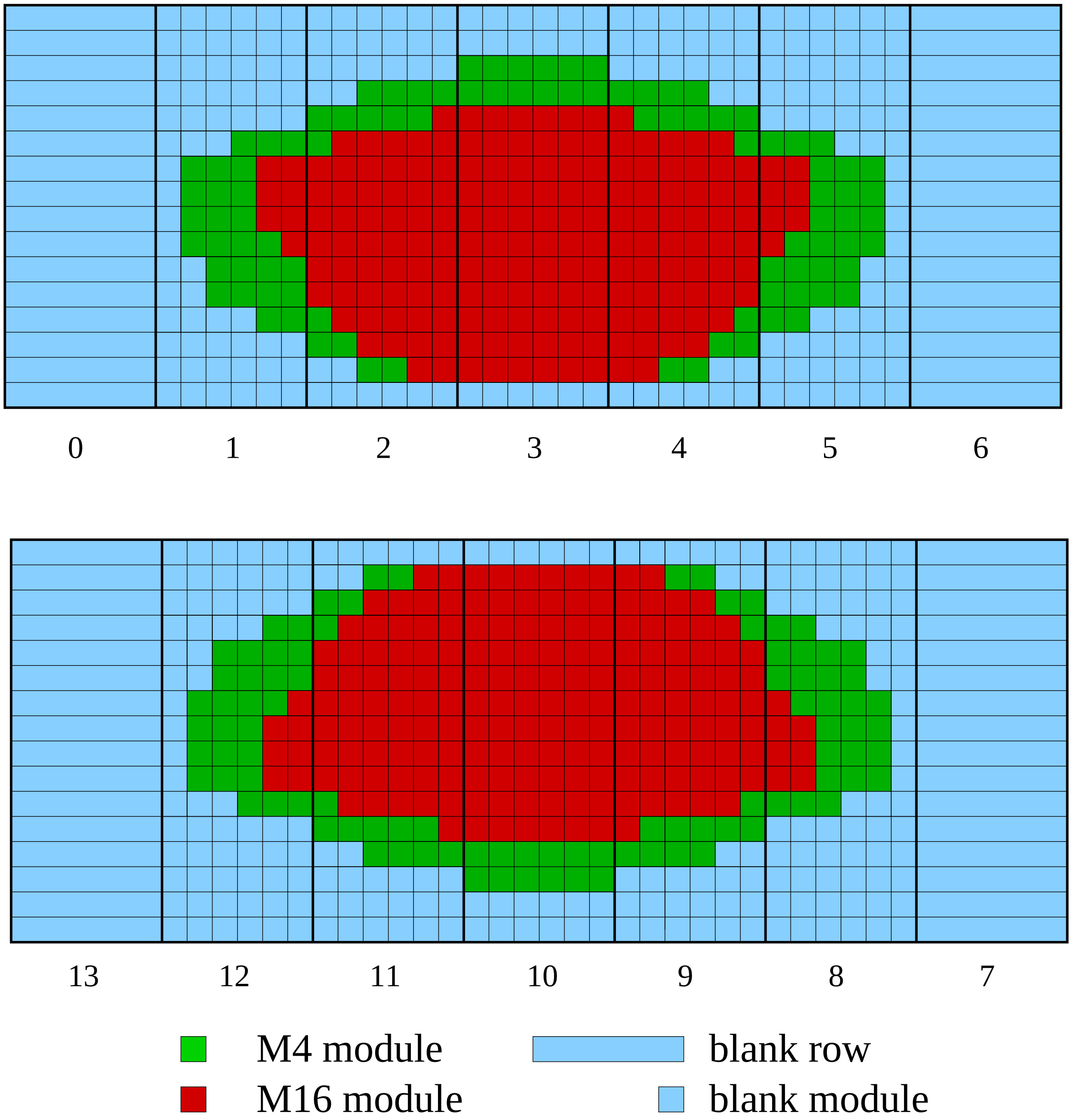

Figure 4.17: Arrangement of the photomultiplier tube modules on the RICH photon detector focal planes. The upper and the lower photon detectors consist of seven supermodules, which notations are also presented in the figure. The whole detector system consists of 1488 sixteen anode (M16) and 752 four anode (M4) photomultiplier tubes.

Before arrangement in the photon detector plane all photomultiplier tubes were tested. The quality assessment was performed to check their quality and to provide the characteristic data. The optimal value of high voltage as well as the plateau count rate of all the photomultiplier tube channels were provided for analysis. This data were used for an appropriate assignment of tubes to groups with equal high voltage [34, 35]. In order to prevent the introduction of an asymmetry bias in the system, special care was taken in the photomultiplier tubes distribution. The groups of tubes with equal optimal high voltage are composed of tubes randomly selected from different delivery boxes, corresponding to different production dates, and the groups of similar optimal high voltage are spread on the whole surface with a left-right symmetry.

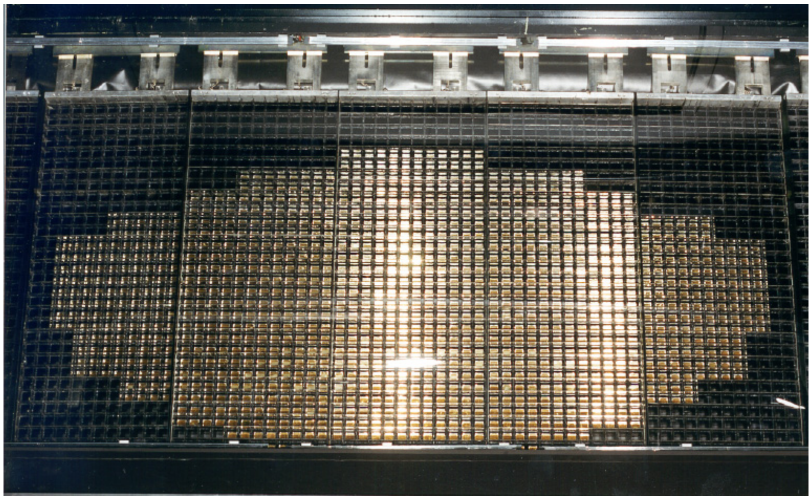

Figure 4.18: View of the upper photon detector plane from the inside of the radiator tank.

Figure 4.19: Arrangement of the photomultiplier tube base modules on the focal plane of the lower photon detector back plane.

The narrow 3 mm gaps between the inner sides of the neighbouring super modules were sealed using black foam, while welcro sheets were used to make a light seal around super modules.

4.7 High voltage distribution

The main requirement for a high voltage system of the RICH detector is a large number of channels with independently controllable voltages up to approximately 1000 V. The smallest photon detector group which can be powered by one high voltage channel is one baseboard equipped with four photomultiplier tubes either of M16 or M4 type. As already mentioned, all baseboards have two parallel high voltage connectors to allow daisy chaining. Thus it is possible to connect several baseboards equipped with photomultiplier tubes of the same optimal high voltage in such a way that they are powered by the common high voltage channel. Each M16 baseboard with a divider chain resistance of $(8.6\mathrm{M}\Omega/\mathrm{base})$ draws a bleeder current of $4 \times 95\mu\mathrm{A} = 380\mu\mathrm{A}$ at 820 V, while each M4 baseboard with a divider chain resistance of $(12.5\mathrm{M}\Omega/\mathrm{base})$ draws a bleeder current of $4 \times 64\mu\mathrm{A} = 256\mu\mathrm{A}$ at 800V. Assuming these bleeder currents, the high voltage system has to supply a total current of approximately 190 mA (1488 $\times$ 0.095 mA $\approx$ 142 mA for M16 tubes and 752 $\times$ 0.064 mA $\approx$ 49 mA for M4 tubes). Thus an additional requirement for the high voltage system is that currents per channel should be in the mA range and measurement of individual current is not essential due to the constant load from the resistor chains.

The CAEN SY 527 A733 high voltage supply meets all the mentioned requirements and so the decision was made to use it for supplying high voltage to the photomultiplier tubes of the RICH detector. The CAEN high voltage system consists of a SY527 main frame unit with a full front panel control, equipped with ten model A733 plug in modules. Each module has 16 high voltage channels with a voltage range between 0 V and 2500 V and a maximal current of 3 mA. The module allows full monitoring and control of voltage and current for each channel independently. The CAEN SY 527 main frame equipped with ten A733 boards can thus supply the total current of 480 mA. The main features of the CAEN high voltage boards are listed in Table 4.2. The unit is programmed, operated and controlled through a fast serial CAENET connection or via a VT100 terminal.

Model	Polarity	No. of channels	Supply voltage	Max. current	Voltage resolution	Current resolution
A733AN	neg.	16	0-2500 V	3.0 mA	0.2 V	1 μ A

Table 4.2: Properties of A733A CAEN high voltage boards for the SY527 main frame.

According to CAEN A733 modules highest allowed current level, up to 7 baseboards equipped with M16 photomultiplier tubes or up to 11 baseboards equipped with M4 photomultiplier tubes can be connected to one high voltage channel. The main drawback of grouping is that more than one photomultiplier tube is turned off if one tube in the group fails in such a way that the supply voltage has to be switched off. This, however, happened only on one occasion, imediately after the installation, and the tube turned out to

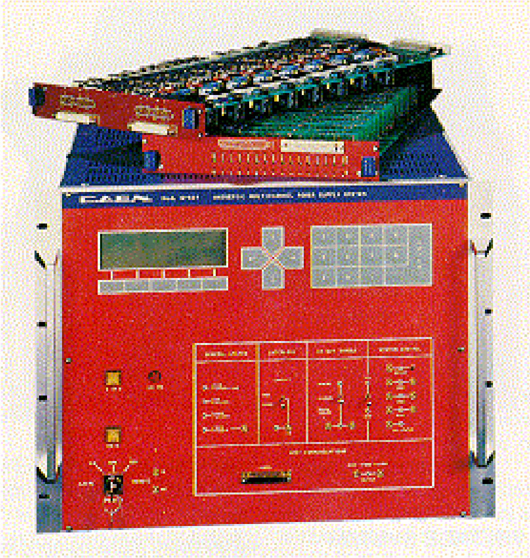

Figure 4.20: The CAEN SY 527 high voltage system mainframe with two multichannel supply boards A733A.

be broken with an internal short.

A single baseboard of M16 (M4) photomultiplier tubes represents 0.24% (0.06%) of the total number of channels. A disconnected high voltage channel which connects four baseboards represents a loss of 0.95 $\%$ (0.24 $\%$), but actually three quarters of this could be recovered by manually disconnecting the faulty baseboard. The grouping is therefore optimised to minimise the loss of acceptance if a failure does occur. If one groups four baseboards together, one needs 120 high voltage channels. A configuration with 10 A733 CAEN supply modules with a total of 160 channels thus also opens a possibility to group only two or three base boards together if more convenient. Thus a group is composed of either two, three, four or five baseboards, due to the arrangement of M4 and M16 photomultiplier tubes in the photon detector plane. The CAEN high voltage supply is positioned on the first floor of the electronic hut. The high voltage cabling distribution is organised in such a way that one long cable for each group of baseboards is used and a daisy chain scheme to connect the baseboards in one group. A schematic of this layout is shown in Fig. 4.21 and in in Fig. 4.22. Photographs of the upper and the lower photon detector after high voltage daisy chaining was done is presented in Fig. 4.23.

Thus 50 m long, high voltage coaxial cable bundles (10 $\times$ 16) are laid between the upper detector and the first floor of electronic hut as well as between the lower detector and the trailer. About 8000 m of halogen free cables with outer diameter of 3.3 mm are used for the RICH high voltage cabling distribution. Long high voltage cable bundles are equipped with mini connector plugs at the detector side and multi pin high voltage connectors at the supply side. Baseboards are daisy chained using short Amphenol Universal Power jumper cables.

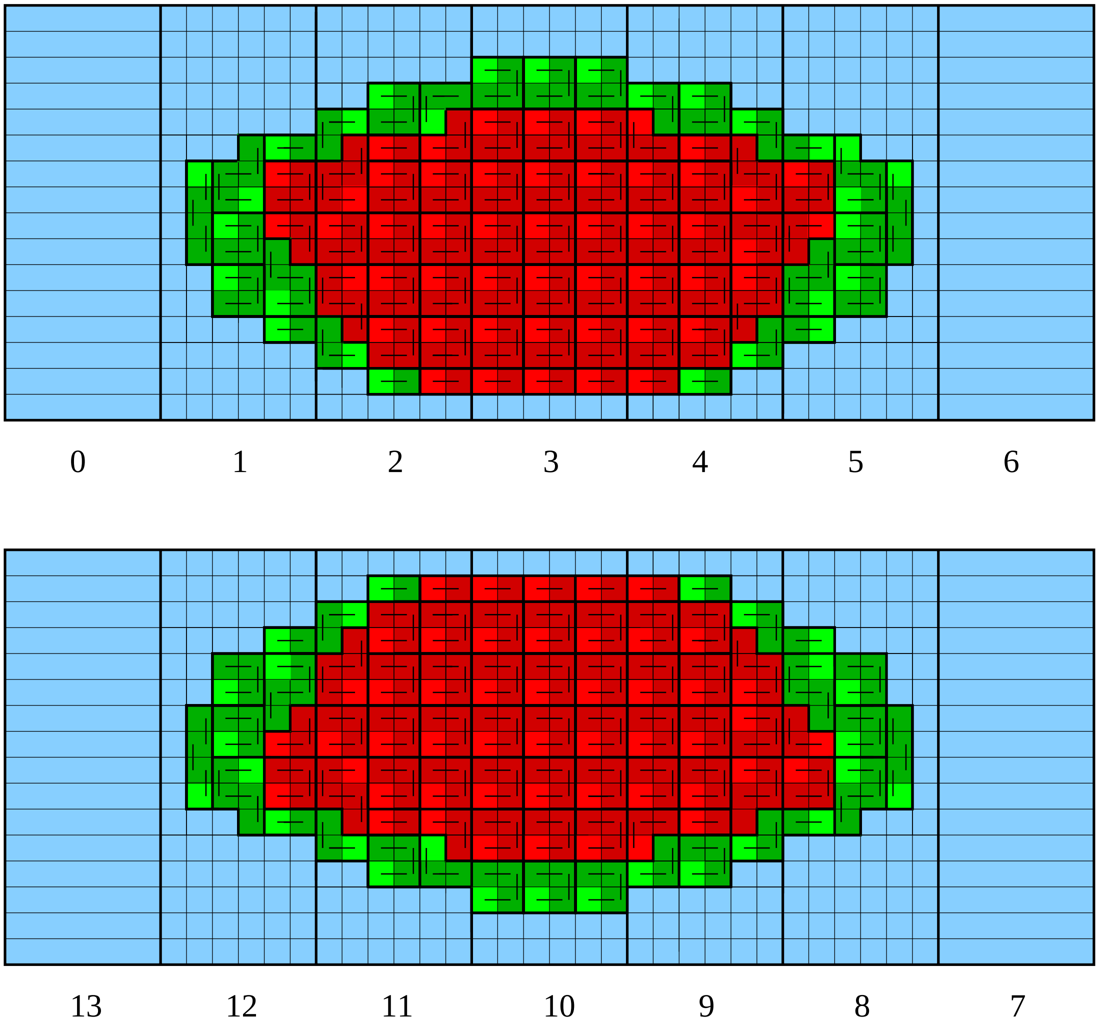

Figure 4.21: High voltage daisy chain cabling scheme in between baseboards of the upper and lower photon detector plane. Groups using photomultiplier tubes of type M16 are coloured red, while groups using photomultiplier tubes of type M4 are coloured green. The baseboards which are connected to the high voltage supply directly via long cables are denoted with brighter colour.

4.8 Front end electronics boards arrangement

The front end electronics (FEE) boards were arranged according to their optimal threshold voltage, by using test data. Two types of tests were performed in Barcelona [44], one looking at the response of all the channels using the test pulse, and the other surveying the response of each channel. Both tests were repeated for different heights of the pulses and different values of threshold voltages.

The threshold voltage supplied to the front end electronics boards cannot be adjusted individually for each board, but it is common for all the boards connected to the photomultiplier tube base modules positioned in two neighbouring columns of the supermodule.

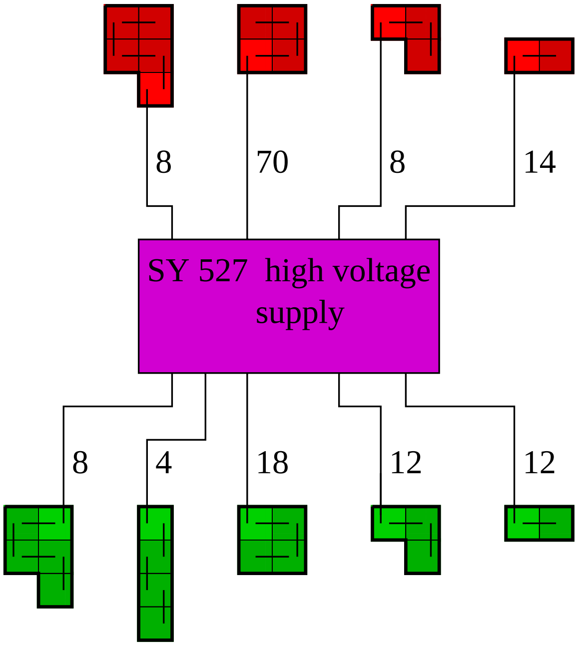

Figure 4.22: High voltage cabling distribution using one cable for several base boards and a daisy chain connection in between. The number near the connecting cable denotes the number of baseboard groups with the same configuration in the photon detector plane.

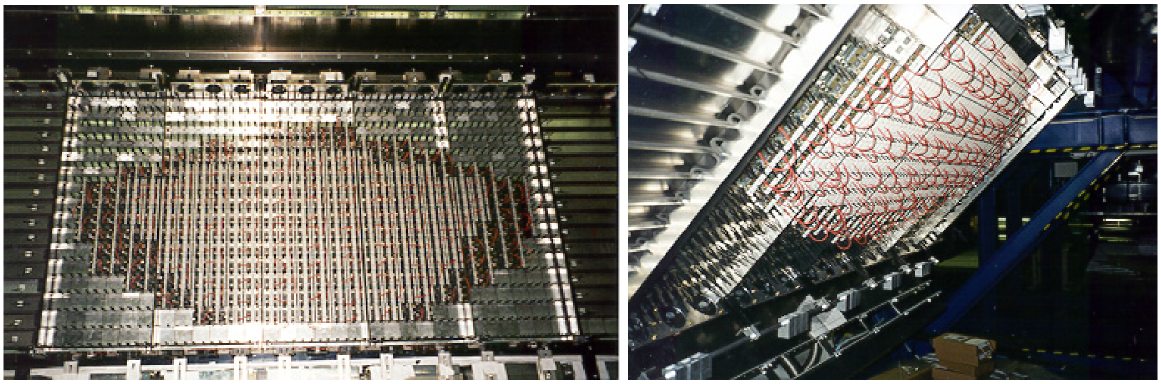

Figure 4.23: Upper (left side) and lower (right side) photon detector back plane with high voltage daisy chain connections between baseboards.

The boards were thus classified into groups (see Appendix E) according to performed assessment and mounted to the photomultiplier tube baseboards according to the mean threshold value over all channels at which they respond to 50% of the test pulses.

In order not to introduce any asymmetry in the detector, the groups were distributed symmetrically in the detector (see Appendix E), as well the boards within a group were not sorted for their other properties, but randomised.

4.9 Low voltage distribution

The low voltage distribution system delivers $\pm 3\mathrm{V}$ to each front end electronics board of the photomultiplier tube base modules. Low voltage power supplies are positioned in the second floor of the electronic hut. From each of the power supplies a direct line goes to either upper or lower distribution box (see Fig. 4.27), from where a connection is made to copper rods of each cable holder mounted on the supermodule structure (see scheme in Fig. 4.24). Each supermodule is equipped with a set of three aluminium cable holders which can be moved along holding rods fixed on the top and bottom of the supermodule structure. A schematic top and bottom view of the cable holder structure is presented in Fig. 4.25. The cable holder houses up to eight distribution daughter boards (see Appendix H), which are fixed on copper rods. Each distribution daughter board distributes low voltage to the electronic boards of four photomultiplier modules, equipped either with M4 or M16 photomultiplier tubes. The connections between distribution daughter boards and power connectors of electronic boards are made using flat ten wire cables, which are equipped with five and two ten pin connectors for M16 and M4 base modules, respectively. See scheme in Fig. 4.26 and photograph in Fig. 4.27.

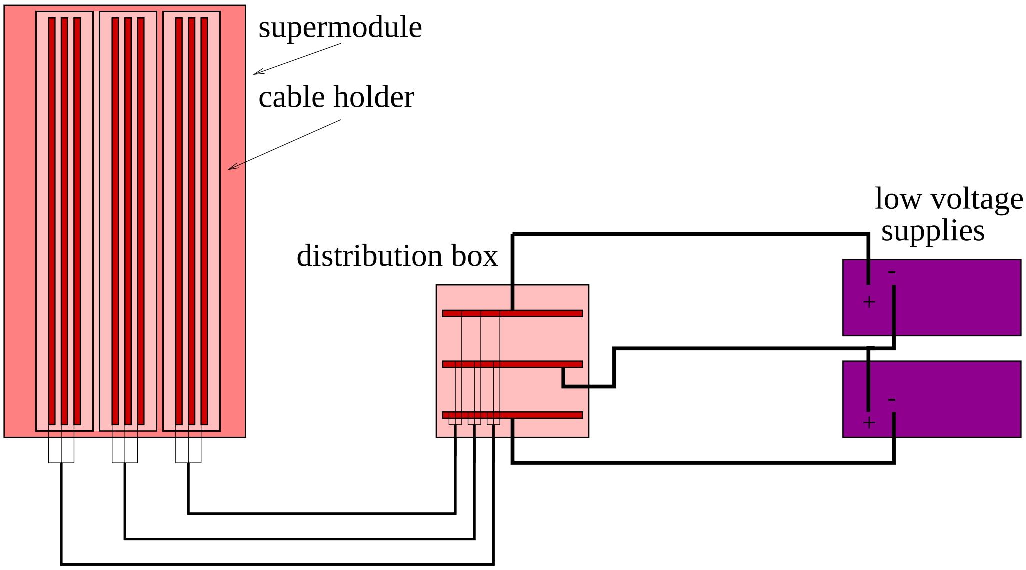

Figure 4.24: Schematic view of the low voltage distribution. Only connections to cable holders of one supermodule structure are presented.

Each front end electronics board draws $85\ \mathrm{mA}$ at the voltage of $+\ 3\ \mathrm{V}$ and $80\ \mathrm{mA}$ at the voltage of $-\ 3\ \mathrm{V}$. The current consumptions of the electronics belonging to each cable holder are listed in Table 4.9. One can see that front end electronics boards of each part of the photon detector draws a total current of approximately 70 A of each polarity, which determines the choice of power supplies. The low voltage supply system is thus powered by four KEPCO ATE 6-100DM supplies (see Fig. 4.28) with output

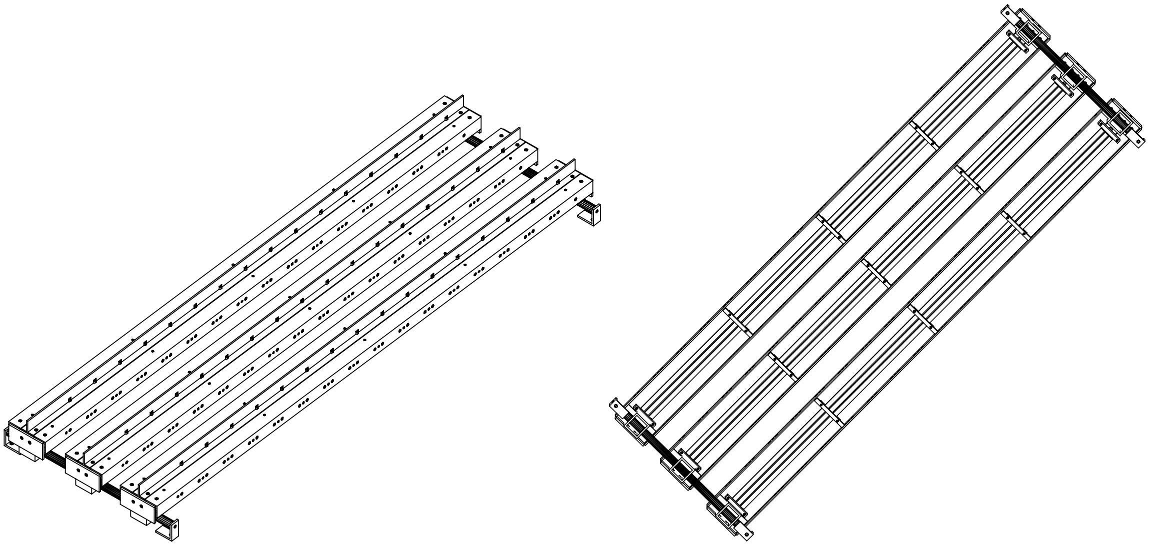

Figure 4.25: Top (left side) and bottom (right side) view of cable holders of one supermodule structure.

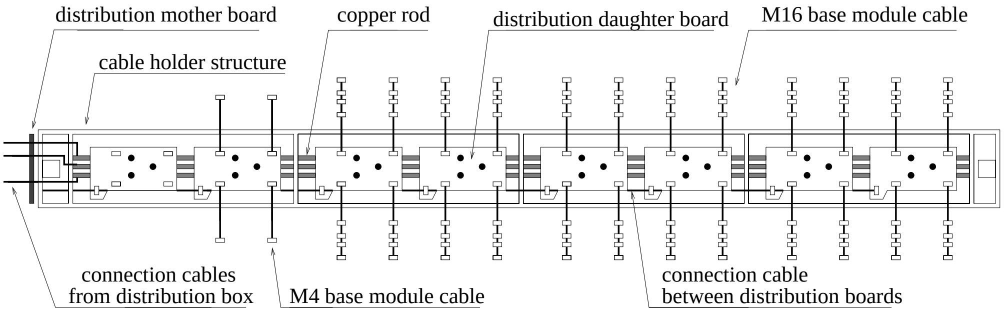

Figure 4.26: Schematic view of the cable holder bottom side. Distribution daughter boards fixed on the copper rods with M4 and M16 base module cables and distribution mother board mounted at the end of the cable holder are presented.

voltage range up to 6 V and current range up to $100\ \mathrm{A}$. Two power supplies, one per each polarity, are needed for each photon detector plane. About 210 m of cable with $95\ \mathrm{mm}^2$ cross section was used to connect power supplies with distribution boxes of upper and lower detector. Connections between copper rods and distribution boxes are made using 10 m long cables with cross section of $16\ \mathrm{mm}^2$. Each cable holder of the middle three supermodules has its own connection, while cable holders of outermost supermodules have only one connection, due to less electronics boards.

The front end electronics boards discriminators also need to be supplied with threshold voltage. This is done by the National Instruments FieldPoint system [45]. The distribution system is composed of three modular FieldPoint subsystems which communicate through network modules. A controlling subsystem is positioned in the electronic hut

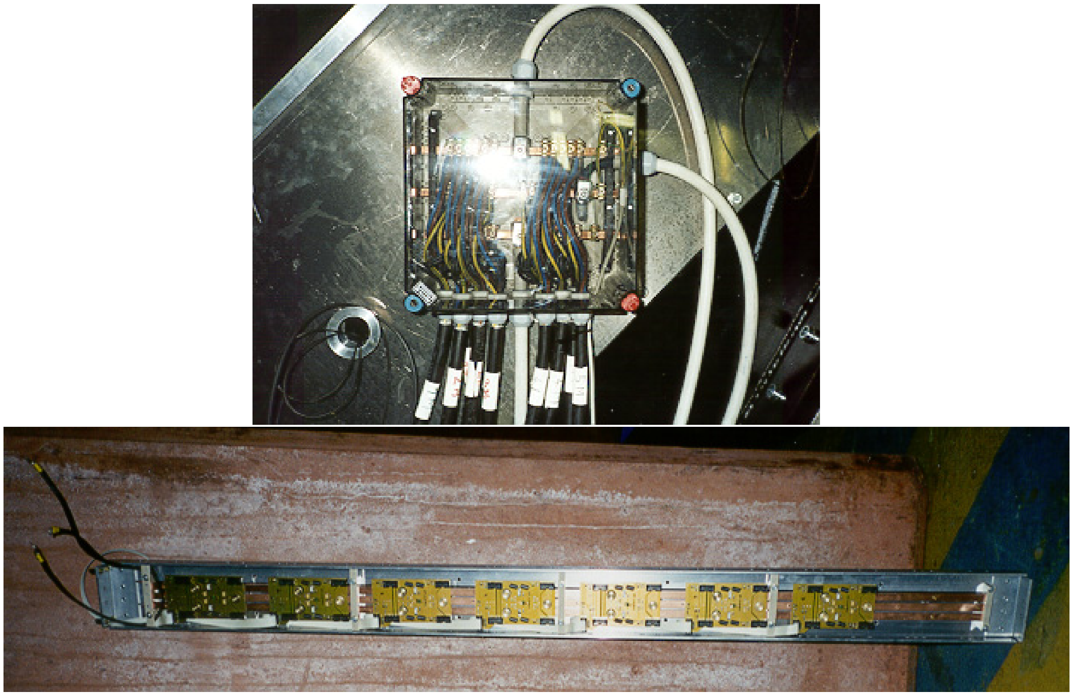

Figure 4.27: Low voltage distribution box mounted on the side wall of the upper photon detector (top) and cable holder with integrated low voltage distribution boards.

Figure 4.28: Low voltage supply.

communicating with a VME CETIA computer. Two other subsystems, composed also of control and monitor units, are positioned near upper and lower photon detector (see Fig. 4.29). Subsystems are supplying threshold voltages to distribution mother boards (see Appendix H) which are mounted at the end of each cable holder (see Fig.4.26. The distribution mother board further divides threshold voltages to the distribution daughter boards integrated in the cable holder through flat ten wire cable (see Fig. 4.30). If a finer granularity is needed the distribution system allows an upgrade which would supply

supermodule/ cable holder	M4/M16 PMT base modules	No. of FEE/ distr. boards	I + (mA)	I - (mA)	V + (mV)	V - (mV)
1 and 12 /left	4/0	4/2	340	320	4	3
1 and 12 /middle	13/0	13/4	1105	1040	12	11
1 and 12 /right	9/7	37/5	3145	2960	33	31
2 and 11 /left	6/14	62/5	5270	4960	56	53
2 and 11 /middle	6/18	78/7	6630	6240	70	66
2 and 11 /right	3/21	87/7	7395	6960	79	74
3 and 10 /left	4/22	92/7	7820	7360	84	78
3 and 10 /middle	4/22	92/7	7820	7360	84	78
3 and 10 /right	4/22	92/7	7820	7360	84	78
4 and 9 /left	3/21	87/7	7395	6960	79	74
4 and 9 /middle	6/18	78/7	6630	6240	70	66
4 and 9 /right	6/14	62/5	5270	4960	56	53
5 and 8 /left	9/7	37/5	3145	2960	33	31
5 and 8 /middle	13/0	13/4	1105	1040	12	11
5 and 8 /right	4/0	42	340	320	4	3
$\sum$	94/186	838/81	71230	67040		

Table 4.3: Some parameters of the photon detector front end electronics composition. Number of front end electronics and distribution daughter boards belonging to each cable holder, current consumption and voltage drops for each cable holder are listed.

threshold voltages to each distribution board. In addition to threshold voltage distribution the FieldPoint system is also used to monitor low voltage, threshold and temperature values on the detector plane.

4.10 Signal cables installation

Outputs of the front end electronics boards and inputs of the front end driver system, positioned in the upper and lower platforms near the photon detectors, are connected with the signal cables. A single cable length of $7.5\ \mathrm{m}$ for the whole photon detector is used, thus simplifying the production of cables and allowing their flexibility. Halogen free 3M 34 wires twisted flat cables are used. The cables are bended in the cable holder level in order to match their upper surface, which is used as a support plane to which they are fastened with plastic ties (see Fig. 4.31 and Fig. 4.32). After leaving the cable holder support structure, the cables are fastened on the grid ceiling or laid under the floor on the upper and lower platform, respectively, from where they join the front end driver system.

The front end driver system is composed of front end driver crates which accept front end driver daughter and mother boards. The front end driver daughter board is designed

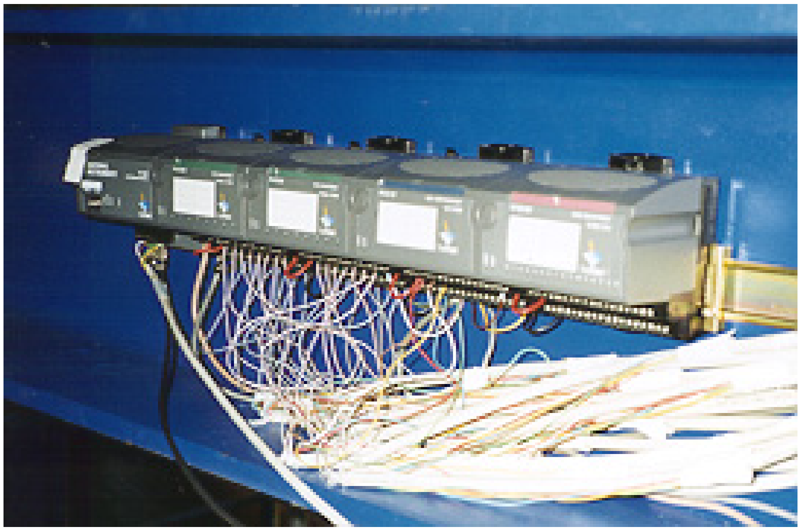

Figure 4.29: The FieldPoint modular system supplies threshold voltages to front end electronics and is also used for monitoring the values of the low voltage, threshold voltage and air temperature.

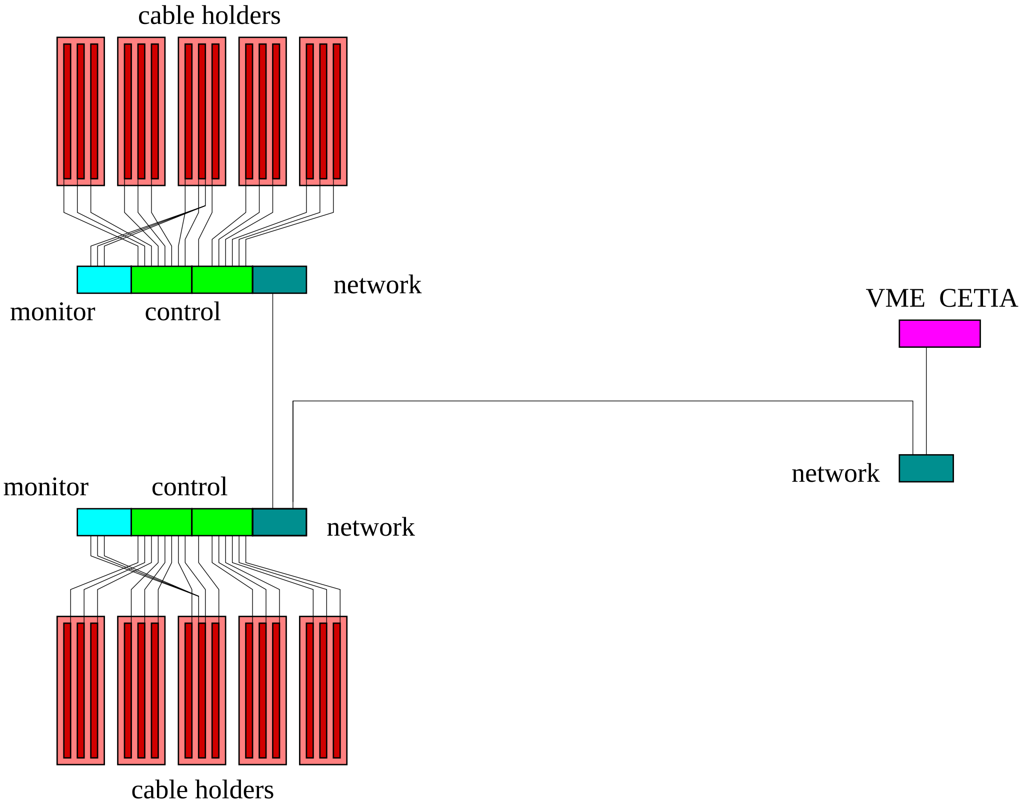

Figure 4.30: Threshold voltage distribution and control.

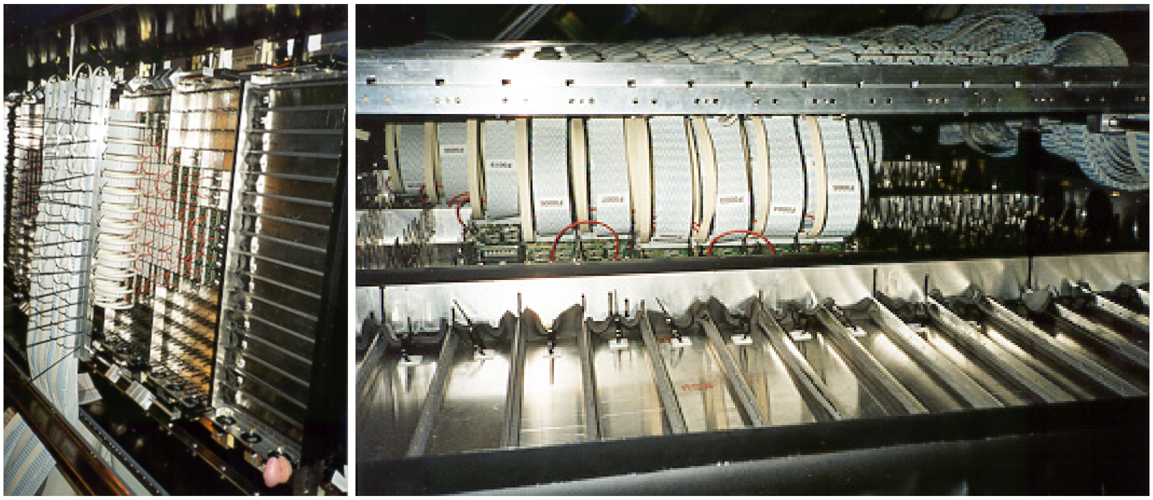

Figure 4.31: Initial phase of the signal cables arrangement in the lower photon detector in the left side photograph and close up view of the outermost supermodule cabling in the right side photo.

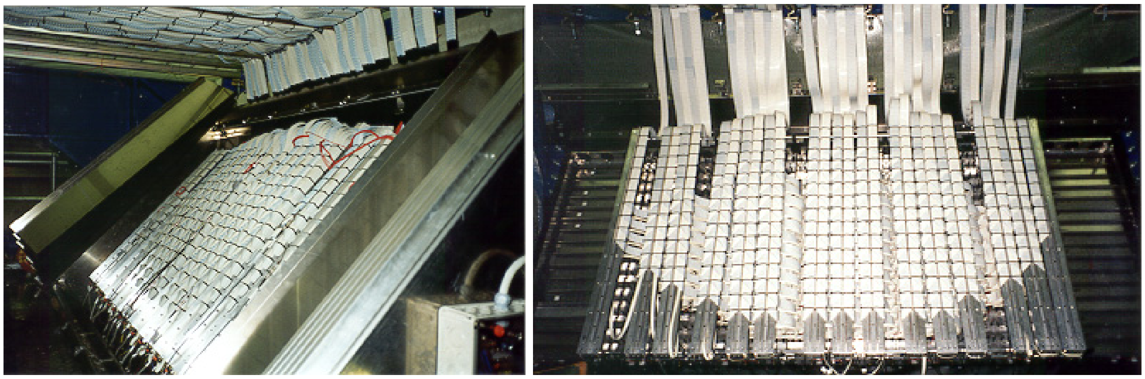

Figure 4.32: Two different views of the upper photon detector plane after signal cables were laid.

to detect hit events. It accepts 16 signal cables and thus supports 256 channels. The input data is stored in an input buffer with 128 locations at the bunch crossing period of 96 ns until the first level trigger indicates an event of interest. The front end driver mother board is designed as a control and transmitter unit for event detection application. It reads the channels of four front end daughter boards. The implemented high speed SHARC link interface then transmits the data from all channels to a host SHARC processor system. The front end driver crate houses up to eight front end daughter boards and up to two front end driver mother boards. In order to connect all 838 twisted flat signal cables of one photon detector plane, up to seven fully equipped front end driver crates are used. The front end driver system arrangement is presented schematically in Fig. 4.33 and in photographs in Fig. 4.34

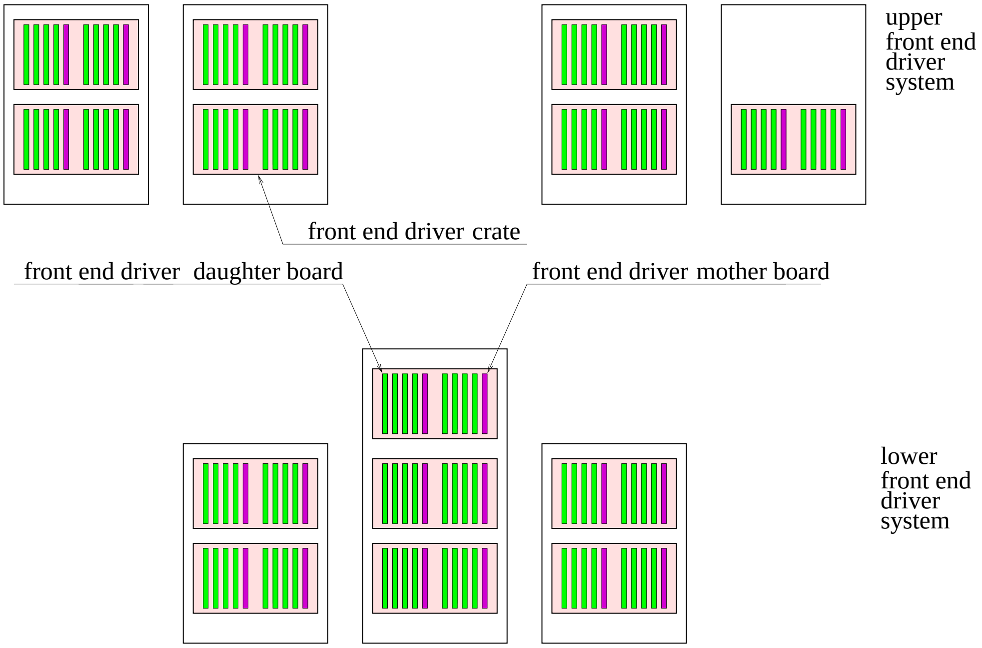

Figure 4.33: Front end driver arrangement of crates for the upper and lower photon detector.

Figure 4.34: Two phases in the arrangement of signal cables on the front end driver system side. In the left side photograph the initial phase of cabling is presented. Also one front end driver daughter board with partially connected signal cables is seen, while on the right side photo, the final cable arrangement is seen.

5

Tests of the photon detector prototype with electron beam

5.1 Apparatus

In order to test the performance of the detector in a realistic experimental environment similar to HERA-B, measurements with a fully equipped photon detector prototype were performed with Čerenkov radiation of 3 GeV/c electrons at the DESY experimental area T24. The test counter was made of a 5 m long aluminium cylinder with a diameter of 80 cm. The cylinder was closed on both ends with lids and aligned along the electron beam direction. A schematic diagram of the test beam set up is shown in Fig. 5.1. The trajectories of the electrons along the cylinder axis were measured with one multiwire proportional chamber mounted on the beam entrance lid and another multiwire proportional chamber on the beam exit lid.

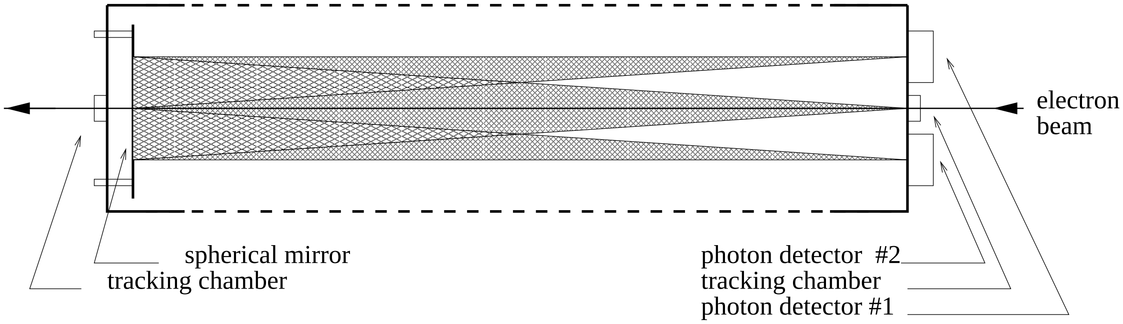

Figure 5.1: Schematic side view of a large prototype of the RICH detector in the test beam area.

The beam entrance lid was equipped with two quartz windows one above and the other below the tracking chamber. With such a configuration, the performance of two photon detector types can be directly compared, which was done in the previous tests with a gaseous TMAE based chamber and a multiwire chamber with solid CsI photocathode [46, 47, 48, 49, 50, 51]. When testing the performance of the detector based on photomultiplier tubes, the prototype supermodule under investigation was mounted on the lower quartz window of a radiator tank, while the upper quartz window was not in use and thus closed. On the inside of the beam exit lid a spherical mirror with 5 m focal length was mounted at three points (see Fig. 5.2).

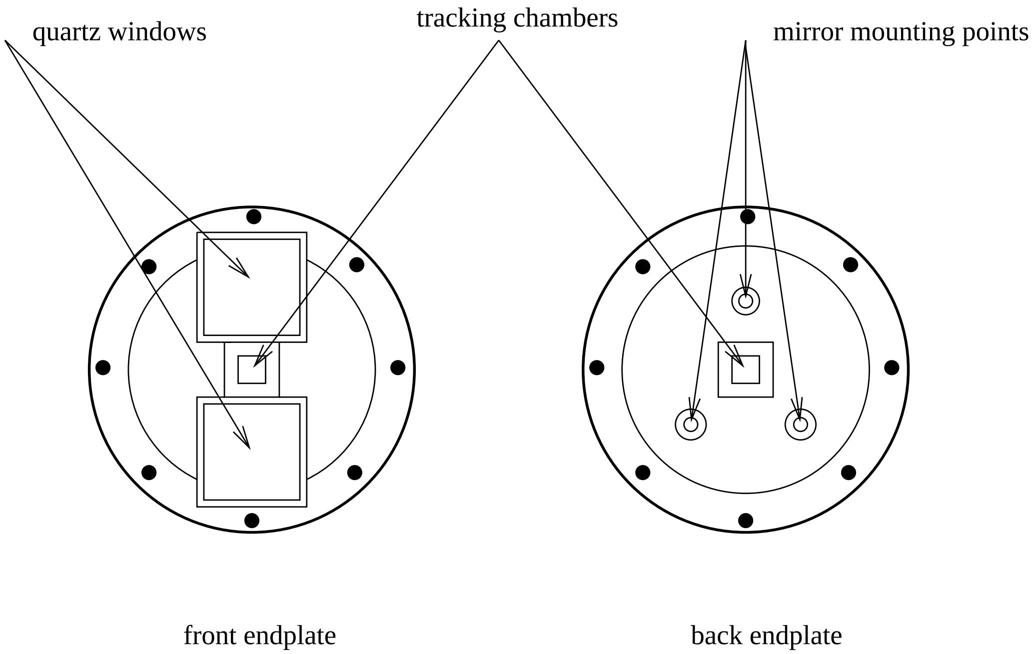

Figure 5.2: Two 12 mm thick end plates with a diameter of 800 mm are shown. The front end plate, shown on the left side is equipped with two photon detectors and a tracking chamber. The back lid shown on the right side, holds the mirror and the second tracking chamber.

The vessel (see Fig. 5.3) was filled with C_4F_{10} gas during a previous test, which took place six months before the measurements with the fully equipped photon detector. The vessel was closed in the meantime and the concentration of C_4F_{10} in the gas mixture after half a year was estimated to 37%, according to the measured Čerenkov ring radius.

In the experimental set up, the supermodule prototype was positioned with its longer side horizontally as shown in Fig. 5.4. The part of the photon detector, relevant to the exit window of the radiator vessel, was equipped with photomultiplier tubes as shown in Fig. 5.5. The subdivision between M4 and M16 tubes remained the same as in the previous supermodule tests in order to use the existing cabling and was thus not optimal for the measurement. Employed photomultiplier tubes were organised according to the optimum high voltage, as determined from the quality assessment tests [34, 35]. The chosen M4 and M16 tubes had their optimal high voltage within an interval of $30\ \mathrm{V}$ and $15\ \mathrm{V}$, respectively. High voltages was supplied to the photomultiplier tubes by a computer controlled multi channel CAEN power supply. As indicated in Fig. 5.5, four high voltage power supply channels were used.

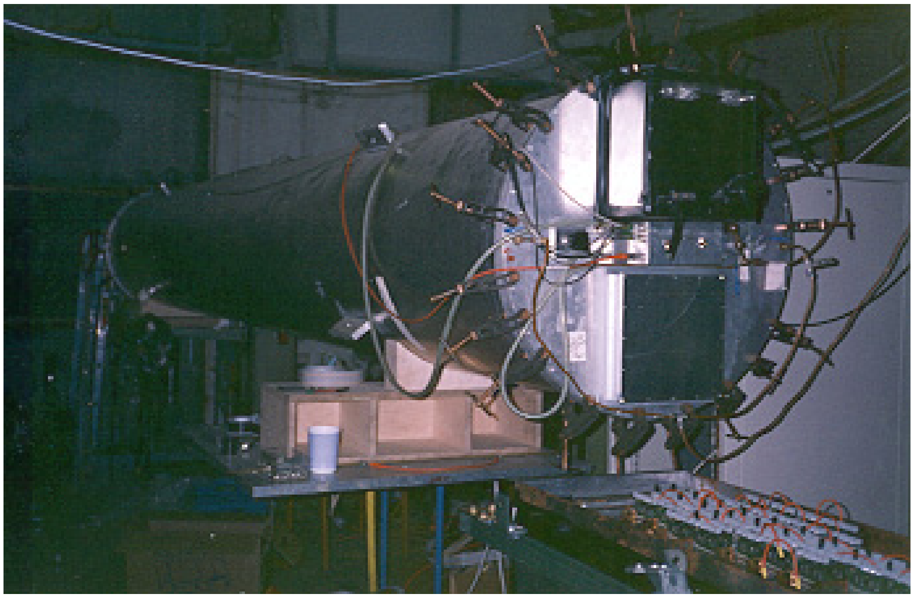

Figure 5.3: A large scale prototype of the RICH counter in the test beam area.

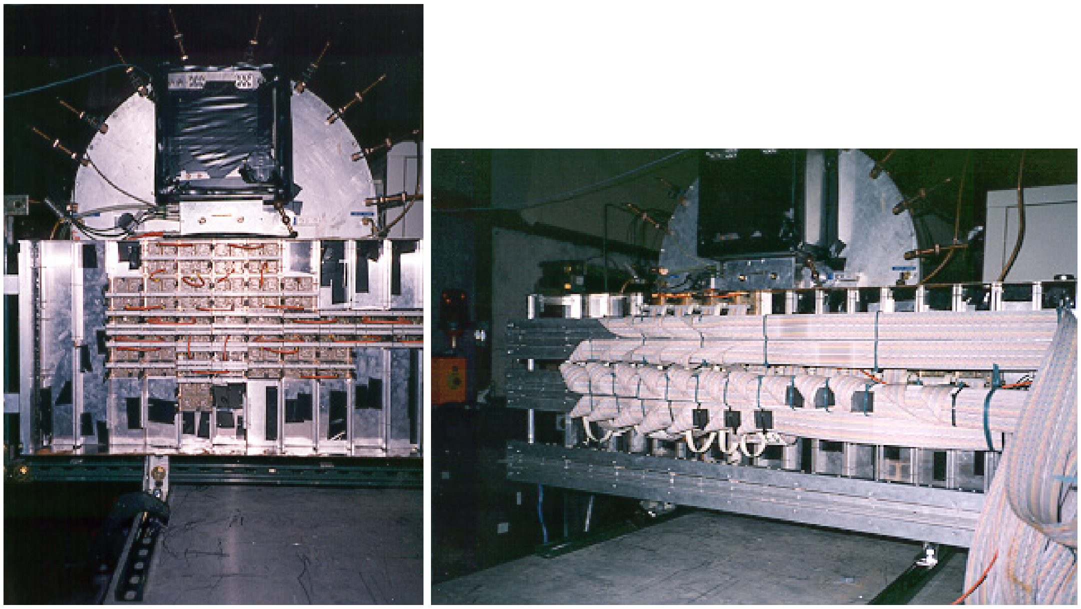

Figure 5.4: The photon detector supermodule prototype without (left) and with (right) cable holder mechanics equipped with signal cables in front of the vessel entrance lid.

The same version of front end electronics was used as in the final design (see previous chapter). So digital signals from ASD8 chips were led to the front end driver boards, which were in turn readout by sharc boards. The system behaved stably with an exception of two front end electronics boards connected to M16 tubes, which oscillated, due to

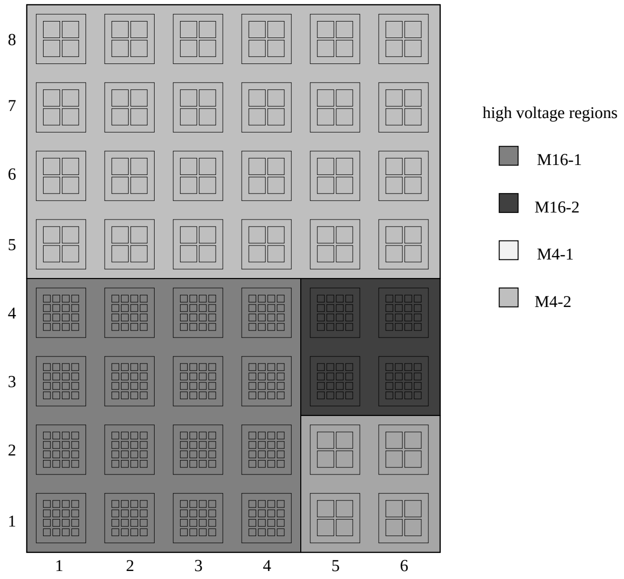

Figure 5.5: The photomultiplier tubes arrangement of the photon detector surface. The groups of photomultiplier tubes with a common high voltage supply channel are indicated in grey scale.

imperfect grounding.

Two multiwire proportional chambers composing the tracking system had an active area of $50 \times 50\,\mathrm{mm}^2$. The anode plane was made of 24 wires with diameter of $15\,\mu\mathrm{m}$ and two outermost wires with diameter of $20\,\mu\mathrm{m}$. The cathode plates were divided into 1.6 mm wide strips with 2 mm pitch. Strips were on one cathode plane perpendicular and on the other parallel to anode wires. The cathode to anode plane distance was 1.5 mm. On the printed circuit board of each cathode plane a delay line was capacitively connected to the cathode strips [52]. Induced signal was divided into two parts, each traveling to either end of the delay line. So from the difference in signal arrival times the information of the hit coordinate was derived. Tracking chambers were filled with P10 $(90\%\mathrm{Ar} + 10\%\mathrm{CH}_4)$ gas. Anode wires were on high voltage, while cathode strips were on the ground potential. All four signals from delay lines of one tracking chamber and the anode signal were amplified by a charged sensitive preamplifiers [53] and with ORTEC FTA 820 amplifiers. The amplified signals from delay lines were led to the constant fraction ORTEC CF8000 discriminator. The time delay of logical signals was measured by a time to digital converter LeCroy 1176. The anode signals were connected to the LeCroy 623B discriminator, the outputs of which were used in trigger decision. In front of the entrance tracking chamber a scintillation counter also used for timing information was fixed.The triggers were created by a 3 fold coincidence of a beam scintillator and two tracking chambers. The data acquisition is possible only when the system is prepared to take data, which is done by the anti coincidence of trigger and veto signal set by the data acquisition program (see Fig. 5.6).

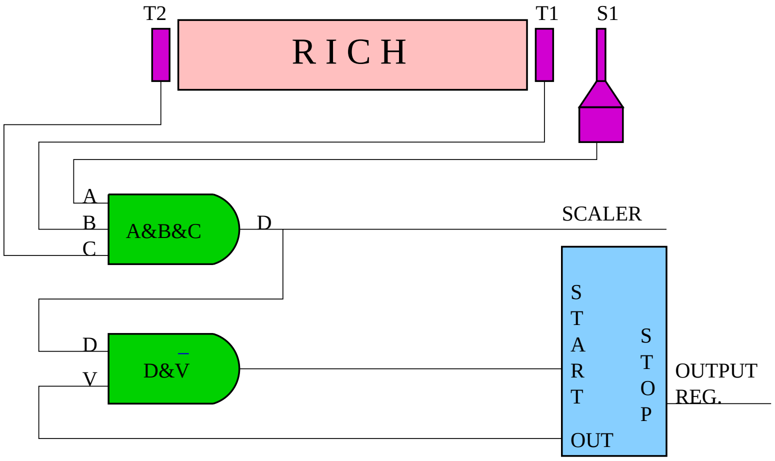

Figure 5.6: Trigger arrangement. The trigger signal is provided by a coincidence of signals from the plastic scintillator S1, and the anodes of both tracking chambers T1 and T2.

To check the high voltage setting, a high voltage scan was carried out, and each group of tubes was separately analysed. From the set of measurements the high voltage value of 800 V for the M16 photomultiplier tubes, and 750 V for M4's were chosen for optimal running.

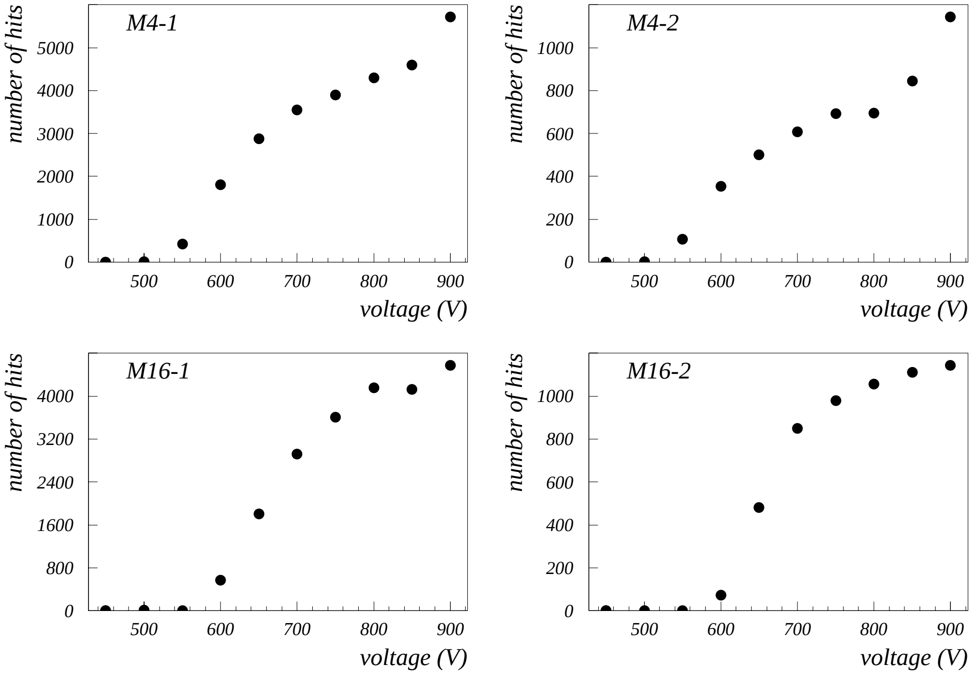

Figure 5.7: High voltage scans of four photomultiplier tube groups.

5.2 Measurements

Several measurements were performed in order to check the photon detector operation and response of the complete light collection system. Tests

- with bare photomultiplier tubes attached to the vessel and
- with the photon detector equipped with complete light collection system (see Fig. 5.8)

were carried out. Both types of tests were performed with and without 3 mm thick plexi glass window sheet mounted on the quartz window flange to simulate the influence of HERA-B RICH vessel window.

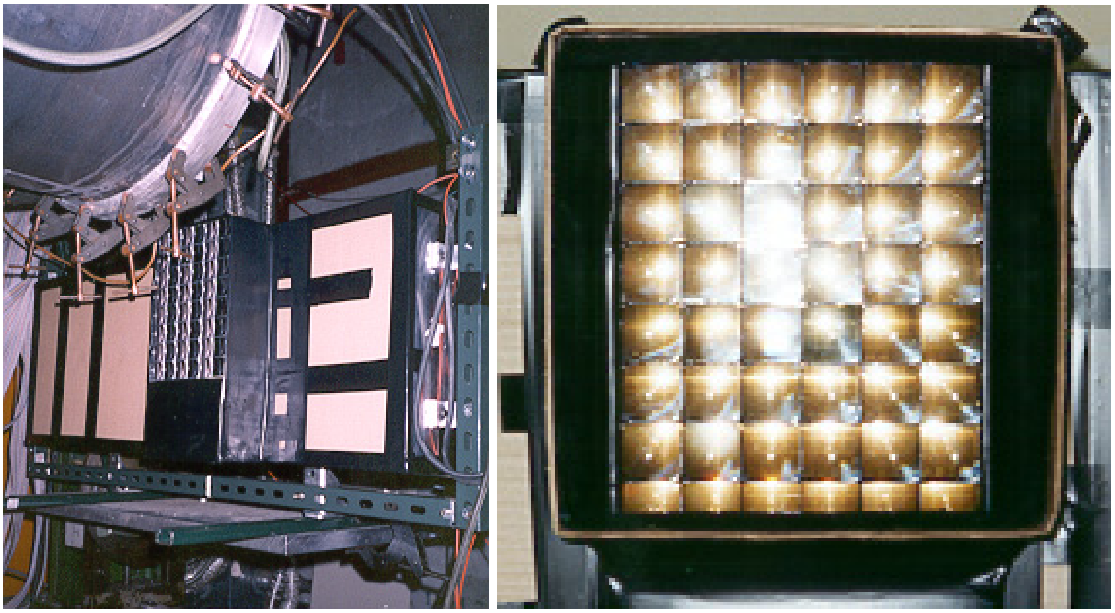

Figure 5.8: Photon detector prototype supermodule equipped with the light collection system (left) and closeup of the part relevant to the vessel exit window.

For each measurement, the raw data were analysed by first correcting the hit coordinates with tracker information on an event by event basis. Some of the resulting accumulated Čerenkov rings are shown in Fig. 5.9 and Fig. 5.10.

By moving two out of three mirror mounting points, the mirror position was tilted so that the ring position on the photon detector moved into the region covered with M16 photomultiplier tubes as can be seen in Fig. 5.11.

Several contributions to the background were studied. For the first test, data were recorded without high voltage on the photomultiplier tubes. Less than 0.01 background hits were observed per event (a $1\ \mu\mathrm{s}$ time interval) per photon detector area.

With high voltage switched on, hits in consecutive pipelines were investigated. While in the proper pipeline step 9.7 hits per event were observed, in consecutive pipes there

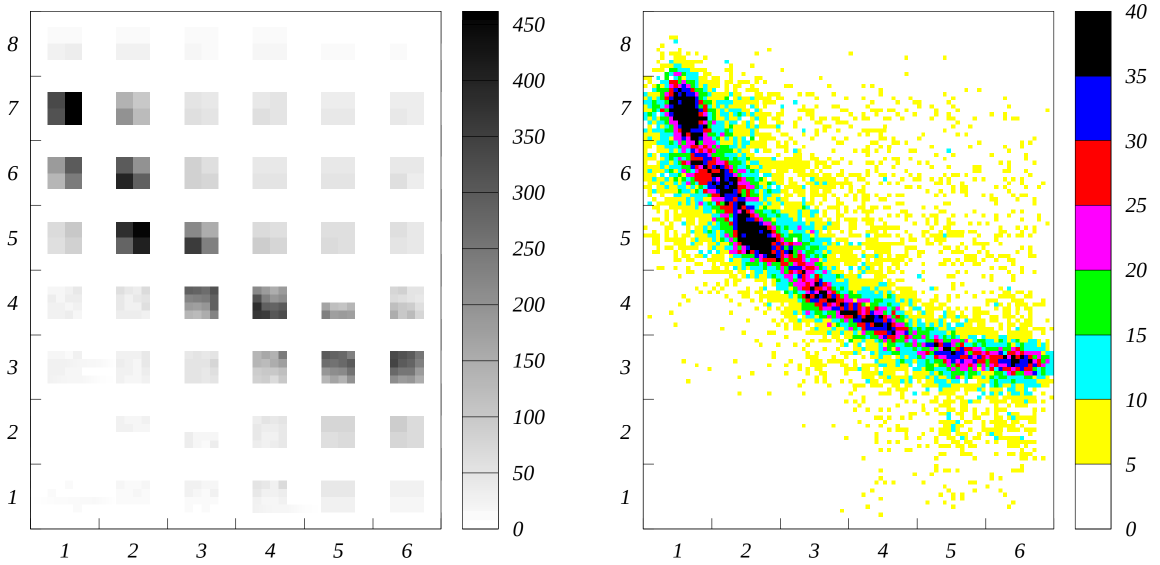

Figure 5.9: The accumulated raw data (left) and the corresponding Čerenkov ring obtained by taking the measured beam particle direction into account (right) for photon detector equipped with bare tubes and plexi glass window.

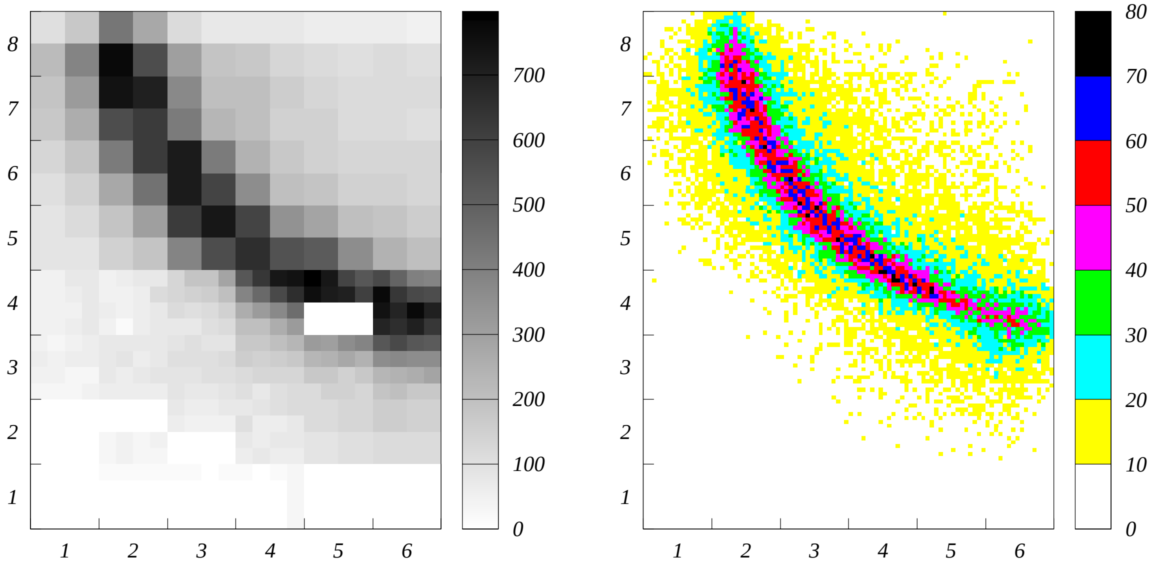

Figure 5.10: The accumulated raw data (left) and the corresponding Čerenkov ring obtained by taking the measured beam particle direction into account (right) for photon detector equipped with lens system and plexi glass window.

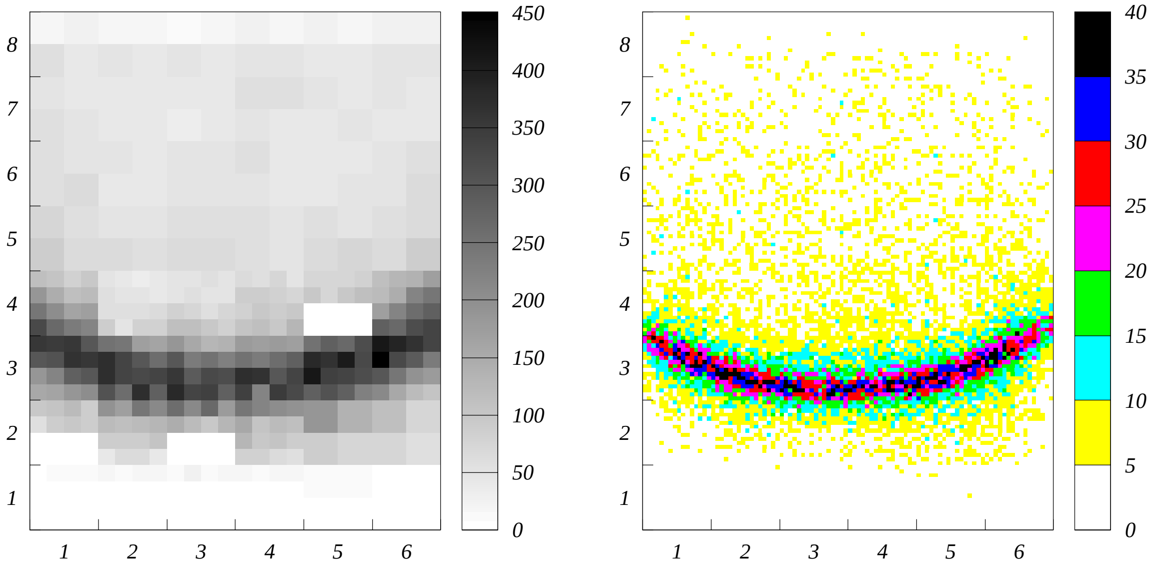

Figure 5.11: The accumulated raw data in the region of photon detector covered with M16 photomultiplier tubes (left) and the corresponding Čerenkov ring obtained by taking the measured beam particle direction into account (right) for photon detector equipped with lens system and plexi glass window.

were only 0.5 hits per event. From this value a background rate of 3.3 kHz per M4 pad and 0.75 kHz per M16 pad were estimated.

The dominant background contribution was, however related to the electron beam which becomes evident comparing hit distributions over ring radius for different ring positions. The level of background is correlated to the amount of material in the beam in the upstream zone and uncorrelated with the Čerenkov ring position on the photon detector. Such a background distribution was also observed with other photon detectors in the same set up and is related to the start of an electron shower. Much lower levels were observed in the previous beam tests when no experiment was mounted upstream [27, 57].

5.3 Resolution in the Čerenkov angle

The Čerenkov ring radius resolution of the counter was determined from the distribution of measured hits over ring radius by correcting the hit coordinates with tracker information on an event by event basis. The Čerenkov ring radius distributions are shown in Fig. 5.12. Distributions are composed of a narrow peak of Gaussian shape lying on the background contributions due to the electron shower radiation and Čerenkov photons radiated by electrons whose tracks were not correctly measured. By fitting the distributions with a sum of a Gaussian function (for photons radiated by electrons with correctly measured tracks) and an additional Gaussian function plus a linear function (describing the background), the standard deviation of Čerenkov ring radius distribution can be determined. (See value of parameter P_3 in Fig. 5.12).

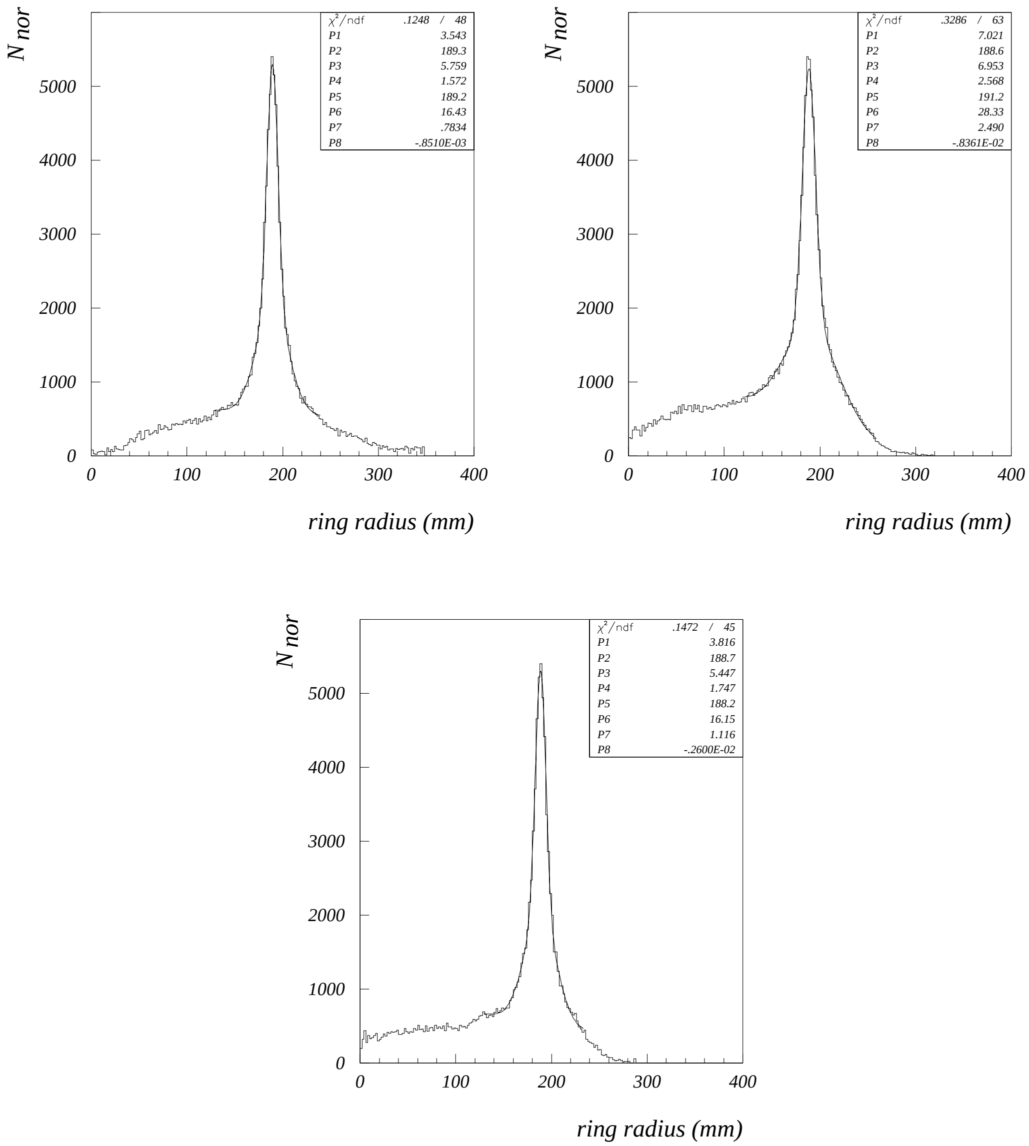

Figure 5.12: The Čerenkov ring radius distribution normalised over the detector effective area for single photons for the photon detector equipped with bare tubes and a plexi glass window (top left), for the photon detector equipped with lens system and plexi glass window with the Čerenkov ring positioned in the area of the photon detector dominated by M4 photomultiplier tubes (top right), and for Čerenkov ring in the region covered by M16 tubes (bottom). The ring distributions are fitted with a sum of two Gaussian and a liner function $N = P_1 \cdot e^{\frac{(r-P_2)^2}{2P_3^2}} + P_4 \cdot e^{\frac{(r-P_5)^2}{2P_6^2}} + P_7 + P_8 \cdot r$.

The resolution in Čerenkov angle measured with the photon detector prototype in the test beam area is expected to be dominated by the following contributions:

- the radiator gas dispersion estimated to

$$\sigma_\vartheta{}^{dis} \approx 0.3 \ \ \mathrm{mrad}, \tag{5.1}$$

- the detector granularity

$$\sigma_\vartheta{}^{det} = \frac{a}{f\sqrt{12}}, \tag{5.2}$$

  where f, the focal length of the spherical mirror is 5 m and a is photon detector pad size. Because two different sizes of pads were used in a photon detector and measurements were done with and without lens system that leads to four possible standard deviations

$$\sigma_\vartheta{}^{det,M4} = 0.52 \ \ \mathrm{mrad}, \quad \sigma_\vartheta{}^{det,M4+lens} = 1.04 \ \ \mathrm{mrad},$$

$$\sigma_\vartheta{}^{det,M16} = 0.23 \ \ \mathrm{mrad} \ \ \mathrm{and} \ \ \sigma_\vartheta{}^{det,M16+lens} = 0.52 \ \ \mathrm{mrad}, \tag{5.3}$$

- multiple Coulomb scattering of electrons with 3 GeV/c momentum in 5 m of radiator gas mixture amounts to

$$\sigma_\vartheta{}^{msc} = \frac{2}{3}\frac{E_o}{\beta cp}\sqrt{\frac{x}{X_0}} = 0.80 \ \ \mathrm{mrad}, \tag{5.4}$$

  where E_o = 13.6 MeV and the radiation length X_0 is 73 m [18],

- optical imperfections of the mirror surface estimated to [1]

$$\sigma_\vartheta{}^{mi} \approx 0.2 \ \ \mathrm{mrad}, \tag{5.5}$$

- tracking system resolution amounts to [27]

$$\sigma_\vartheta{}^{tr} = \frac{s_a\sqrt{2}}{l\sqrt{12}} = 0.2 \ \ \mathrm{mrad}, \tag{5.6}$$

  where l, the distance between tracking chambers, is 5200 mm and s_a, anode wire pitch, is 2 mm and

- the photon detector prototypes displacement from mirror focal plane due to the fact that the whole system was originally prepared for testing different types of photon detectors. The photon detector prototype without lens system was displaced for 220 mm, while the prototype using lenses was displaced for 150 mm and the error amounts to

  $$\sigma_{\vartheta}{}^{pos} = 0.47 \ \mathrm{mrad} \quad \mathrm{and} \quad \sigma_{\vartheta}{}^{pos,lens} = 0.32 \ \mathrm{mrad}, \tag{5.7}$$

  respectively.

Listed errors are uncorrelated and so the combined error is obtained by summing them in quadrature. The resulting expected resolutions for different photon detector arrangements are summarised in the Table 5.1.

	expected σ_{ϑ} (mrad)	expected σ_{r} (mm)	measured σ_{r} (mm)
M4	1.14	5.7	5.8
M4 + lens	1.40	7.0	7.0
M16	1.05	5.3	/
M16 + lens	1.08	5.4	5.4

Table 5.1: The expected and measured resolution inČerenkov angle for photon detector prototype depending on use of lens system and photomultiplier tube types.

These results are in agreement with measured angular resolution presented in Fig. 5.12.

5.4 Detector response parameter $\mathrm{N_0}$ and number of detected photons

In order to understand the performance of the photon detector, the expected number of detected photons has to be compared with the measured number of detected photons. The photon detector response parameter, as already noted in equation 2.7, depends on the following quantities

$$\mathrm{N_0} = \left(\frac{\mathrm{e}_0^2}{4\pi\varepsilon_0\hbar^2\mathrm{c}^2}\right)\int \mathrm{T_r(E)R_m(E)}\epsilon_{\mathrm{d}}\mathrm{(E)\ dE}.$$

If one takes into account the values for the RICH photon detector

- $\mathrm{T_r}$ radiator gas transparency (≈ 1),
- $\mathrm{R_r}$ mirror reflectivity (see Fig. 5.13) and

- ε_{d} the detection efficiency of the photon detector, which depends on
  - photomultiplier tubes quantum efficiency (see Fig. 5.13),
  - lens system transparency (see Fig. 5.13),
  - plexi glass window transparency (see Fig. 5.13),
  - quartz window transparency (≈ 0.9),
  - photon detector geometrical acceptance (≈ 0.9) and
  - transfer and collection efficiencies of photoelectrons (≈ 0.75).

one calculates the merit factor $\mathrm{N}_0 = 43\,\mathrm{cm}^{-1}$ and using the equation 2.6 the expected number of photons for particles approaching the velocity of light

$$N_{det} = N_0 L \sin^2\vartheta = 32.$$

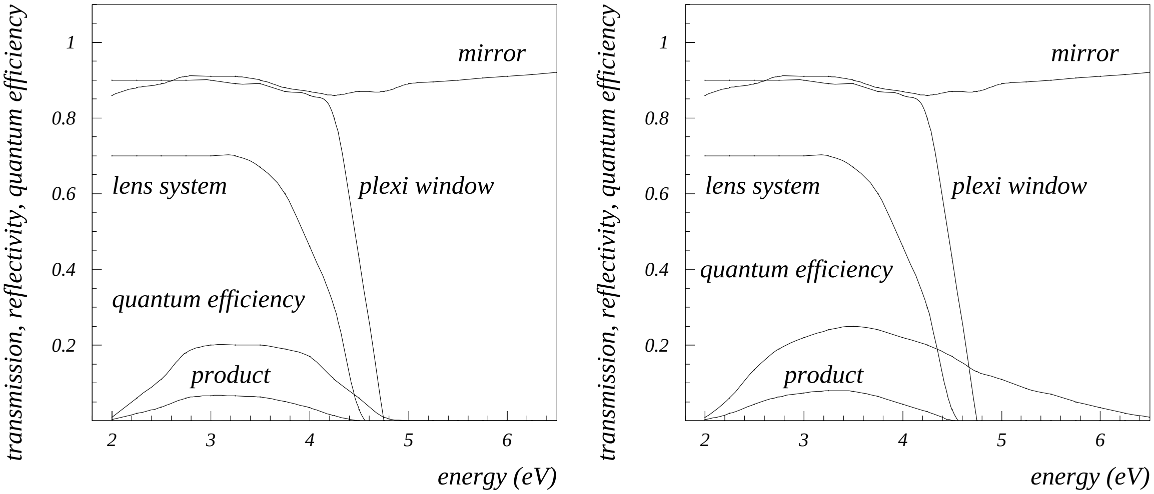

Figure 5.13: Mirror reflectivity, plexi glass window and lens system transparency and quantum efficiency for photomultiplier tubes with borosilicate window (left) and with UV light transparent window (right) as a function of photon energy. Also the product of the mentioned factors with consideration of quartz window transparency, absorption in the radiator gas, geometrical acceptance of the photon detector and photoelectron detection efficiency are presented for both cases.

In order to evaluate the detector performance the number of detected Čerenkov photons per ring were determined from the distribution of measured hits over ring radius. In Fig. 5.14 and in Fig. 5.15 the distributions are plotted as the hit surface density over Čerenkov ring radius which values are not corrected with tracker chambers information in order to simplify the calculations of hits acceptance. The hit distributions over raw radius, normalised to the full Čerenkov ring coverage, for both the arrangements with only bare photomultiplier tubes as well as for the completely equipped photon detector with light collection system are presented. The distributions are fitted with a sum of a Gaussian and linear function. The number of detected photons is thus calculated by integration of the fitted Gaussian function

$$\mathrm{N_{det}} = 2\pi \int_0^\infty \left(\mathrm{P_1 e^{\frac{(r-P_2)^2}{2P_3^2}}} \right) \mathrm{rdr}, \tag{5.8}$$

and a figure of merit $\mathrm{N_0}$ is derived by taking into account that the radiator length L of $5\ \mathrm{m}$ and the Čerenkov angle determined from the average ring radius of $188.8(1 \pm 0.011)\ \mathrm{mm}$ amounts to $37.7(1 \pm 0.011)\ \mathrm{mrad}$

$$\mathrm{N_0} = \frac{\mathrm{N_{det}}}{\mathrm{Lsin^2}\vartheta}. \tag{5.9}$$

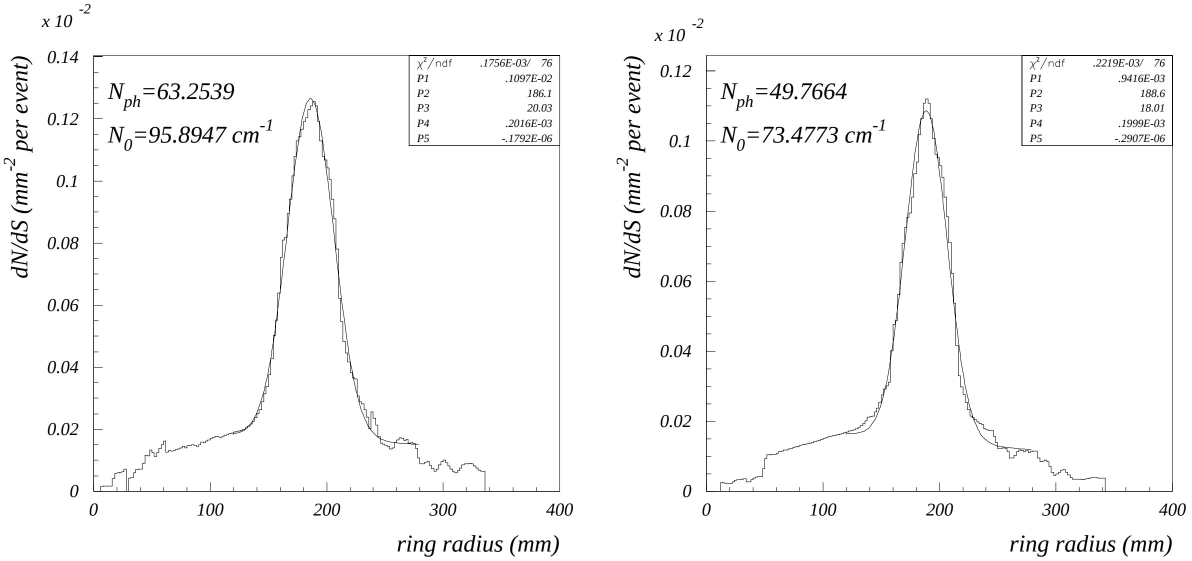

Figure 5.14: The hit surface density distributions overČerenkov ring radius with indicated results of fit with a sum of Gaussian and a liner function $\mathrm{\frac{dN}{dS} = P_1 \cdot e^{\frac{(r-P_2)^2}{2P_3^2}} + P_4 + P_5 \cdot r}$ for the photon detector equipped with bare photomultiplier tubes (left) and added plexi glass window (right). The number of observed hits is normalised to the fullČerenkov ring and full detector coverage, although the photomultiplier tubes cover only 23% of the active surface.

To estimate one of the possible systematic errors, measurements were carried out with the spherical mirror tilted by different angles, and the data with different positions of the ring on the photon detector were analysed in the same way as described before. For the detector equipped with lenses and plexi glass window , four different ring positions were

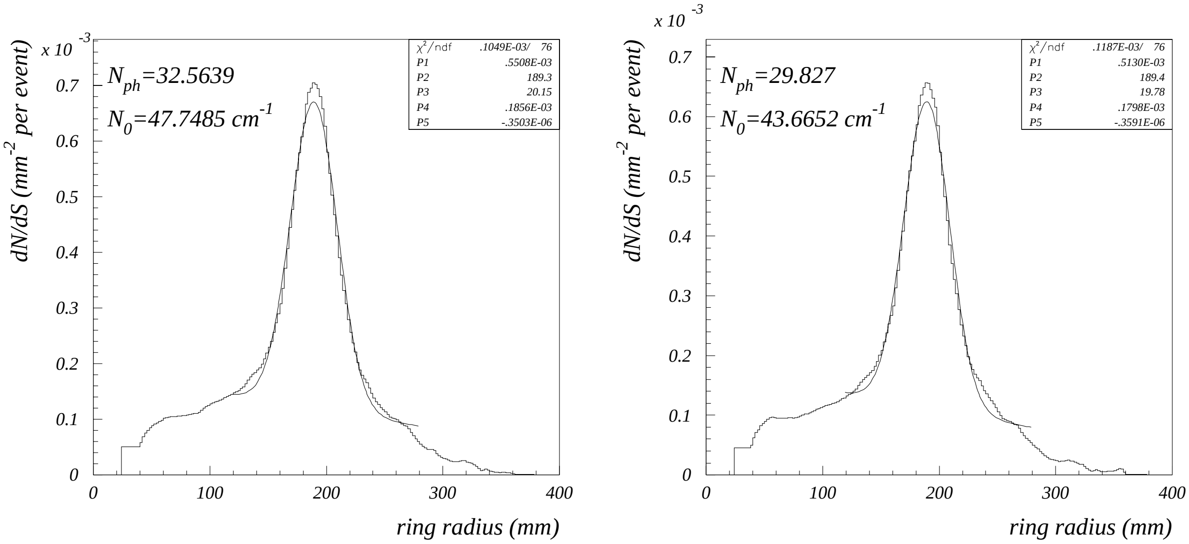

Figure 5.15: The hit surface density distributions overČerenkov ring radius with indicated results of fit with a sum of Gaussian and a liner function $\frac{\mathrm{dN}}{\mathrm{dS}} = \mathrm{P}_1 \cdot \mathrm{e}^{\frac{(\mathrm{r}-\mathrm{P}_2)^2}{2\mathrm{P}_3^2}} + \mathrm{P}_4 + \mathrm{P}_5 \cdot \mathrm{r}$ for photon detector equipped with complete light collection system (left) and added plexi glass window (right). The number of observed hits is normalised to the fullČerenkov ring.

analysed. The corresponding numbers of photons per ring are 29.8, 28.6, 30.5, 29.2. This in turn shows that the measurements agree within sigma of $2.5\ \%$.

Additional cross checks were done by studying the influence of the parametrisation of the background below the Čerenkov peak, on the number of detected photons. With the assumption that the background follows a linear function, the starting point of a line was set at a ring radius value of 120 mm and the end point of the line varied up to a ring radius value of 330 mm. The estimated error due to the linear function slope variation of the background parametrisation amounts to a sigma of 3%.

Thus in the evaluation of the error in the number of detected Čerenkov photons two sources, the parametrisation of background and the dependence of the result on the ring position, are taken into account, while in determination of the error of the figure of merit also the error in ring radius is added. The results of measurements with various set ups are summarised in the Table 5.2 below.

From the deduced number of photons one can calculate the efficiency of the light collection system. The results of measurements with various set ups are summarised in the Table 5.3 and compared with calculated values. Since the M4 photomultiplier tubes are sensitive in the UV region as well, and ring position was such that M4 and M16 tubes coverage was approximately at a proportion of 2 to 1, the present measurements only give average values of the stand alone transmission of the plexi glass, lenses, or lenses combined with plexi glass. All measured transmissions are thus weighted towards the

Set up	N_{det}	$N_0(cm^{-1})$
bare tubes	63.3 ± 2.6	95.9 ± 4.4
tubes with plexi	49.8 ± 2.0	73.5 ± 3.4
tubes with lenses	32.6 ± 1.3	47.7 ± 2.2
tubes with lenses and plexi	29.8 ± 1.2	43.6 ± 2.0

Table 5.2: The number of detected Čerenkov photons and the figure of merit for different photon detector set ups. The values are normalised to the full Čerenkov ring and full detector coverage.

calculated values for M4 photomultiplier tubes.

Component	Calculated transmission		measured transmission
	M16	M4	
lenses for tubes with plexi	0.61	0.59	0.60
plexi glass for tubes with lenses	0.93	0.92	0.92
plexi glass for bare tubes	0.89	0.70	0.76
lenses for bare tubes	0.59	0.45	0.49
lenses and plexi for bare tubes	0.55	0.41	0.46

Table 5.3: Comparison of measured and calculated light collection system transmissions.

Clearly, the most relevant number is the figure of merit for the fully equipped system,

$$N_0 = (43.6 \pm 2)\ cm^{-1},$$

because it can be used to estimate the figure of merit for HERA-B RICH detector. It should be noted that in HERA-B RICH case there is an additional mirror if compared to the test set up, and there is no quartz window, the transmission of which is somewhat better than the reflectivity of the mirrors. On the other hand, the spherical mirror used in the set up is expected to be somewhat inferior compared to the HERA-B spherical mirrors. Without better information available, it is therefore reasonable to assume that both effects roughly cancel, and the figure of merit remains the same for the HERA-B case. The final value of N_0 can thus be used to determine the number of photons in the case of HERA-B RICH, where the radiator is shorter (L=2.7 m), and the average Čerenkov angle is expected to be equal 51.5 mradians for particles approaching the velocity of light. The expected number of detected Čerenkov photons in HERA-B RICH detector is thus

$$N_{det} = N_0 L \sin\theta_c{}^2 = 31 \pm 2,$$

which is consitent with the estimated value using detector transparency, reflectivity and efficiency parameters (see Chapter 3).

6

Measurements

6.1 Introduction

During the HERA shutdown period of winter 97 and spring 98, the RICH detector was installed to a large extent. The upper and the lower photon detector supermodules were equipped with photomultiplier tube base modules. High voltage and low voltage distribution systems were installed and signal cables were laid and connected to the front end daughter boards. Only the gas system was not operational until the beginning of 99, which didn't present any limitation for the evaluation of the initial photon detector performance, which was thus done using air as Čerenkov radiator. With the start of the operation of the data acquisition system in summer 98 a possibility of performing test measurements in order to check the photon detector functioning was enabled. A set of measurements was done in order to determine the optimal working high voltage and threshold voltage of the photon detector. Also proper signal cabling, channel mapping and time synchronisation between front end driver boards were checked. Measurements were also carried out in real experimental conditions, when the HERA proton beam was available and the HERA-B target was in position. In the beginning of 99, measurements with the $\mathrm{C_4F_{10}}$ gas as Čerenkov radiator were made, and the number of detected photons, radiated by particles approaching the velocity of light were evaluated. The detector capability was periodically improved during monthly one day accesses to the detector area, when smaller failures were repaired and some additional monitoring devices were mounted which assured a more controllable operation.

In the following a collection of initial tests the measurements and corresponding results of the RICH detector are presented.

6.2 Tests with signal pulses

Part of the low voltage distribution system can be employed in order to test the performance of the photon detector front end electronics boards. The threshold distribution mother boards, fixed on each cable holder, are equipped with an additional lemo connector to receive test pulses. Test pulses are provided by a pulse generator which sends signals to the threshold distribution mother boards from where they are further distributed to distribution boards incorporated in the cable holder construction. Front end electronics board receives test pulses through one of the pins in the ten pin power socket, connected to the distribution board by short flat cable used also for low and threshold voltage distribution.

The present set up allows only testing groups of front end electronics boards belonging to five cable holders. That means that six measurements are needed to survey the whole photon detector.

In Fig. 6.1 the response after applying the test pulse signal is presented for the left part of the upper detector and middle part for the lower detector. Properly working tested

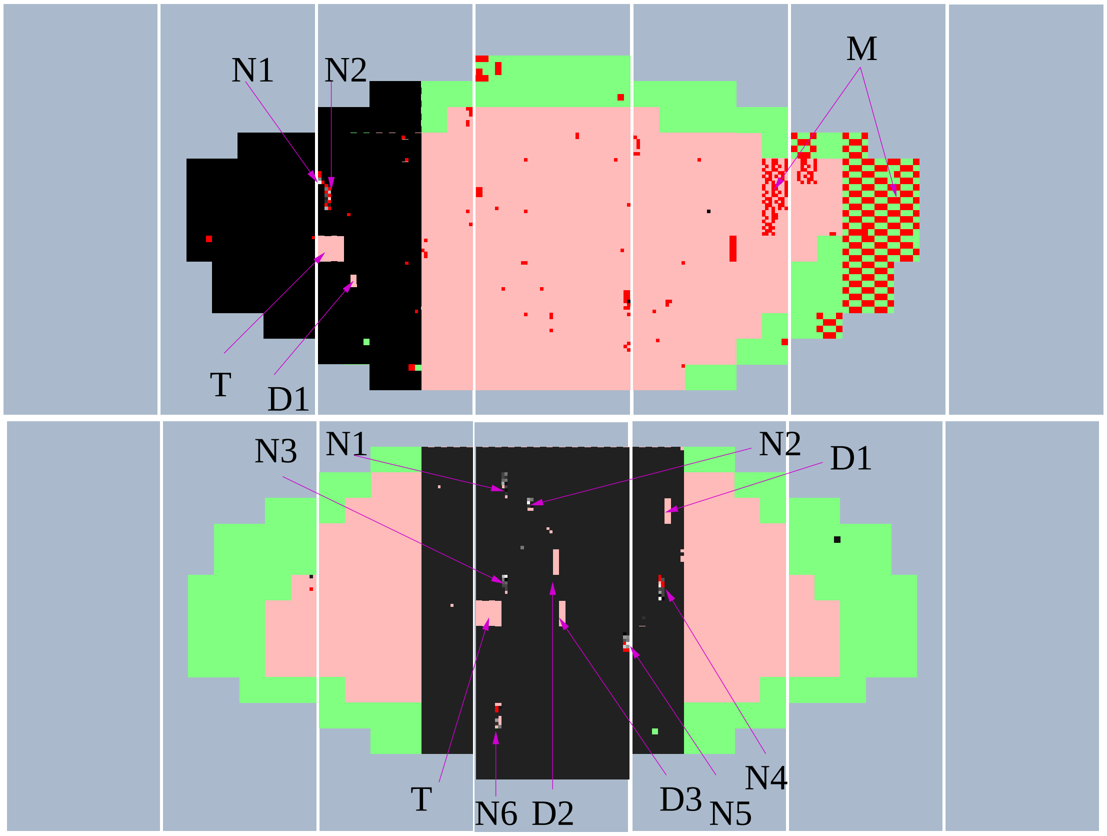

Figure 6.1: Tests of the photon detector front end electronics boards with signal pulses. The areas covered with electronics not receiving test signals are coloured green (M4) and pink (M16). Electronics receiving test signals performing well is presented in black. Not responding groups of front end electronics channels are marked with capital D, while noisy channel groups are noted with N. Areas which do not receive test pulses are marked with T, while M marks areas which have problems with front end driver boards. In the upper detector some groups of noisy channels can be seen which are due to the disconnected cables for setting the threshold voltage.

channels of the front end electronics which are receiving test pulses are presented in black. It can be seen that most of the tested electronics is performing well, except some channels which are not responding. Not responding (dead) channels are presented in green (M4) or in pink (M16) colour depending of the type of photomultiplier tube to which they are connected. In addition to dead channels also some channels painted red can be seen. They present noisy electronics. The channels are giving more counts than expected due to the disconnected cables for setting the threshold voltage or due to misplaced connectors in the sockets. Most of the so called dead or noisy channels are grouped and belong to the same front end electronic board. Isolated dead or noisy channels are due to failure in the front end electronics single channels. In both presentations also two dead areas of square shape are seen. The front end electronics in these parts is not responding due to test pulse distribution failure.

In Fig. 6.2 the test signal response of channels on the front end driver daughter boards of upper and lower photon detector are presented. It should be noted that response on the front end driver daughter boards shown in Fig. 6.2 corresponds to response on the photon detector shown in Fig. 6.1. Each line presents 16 channels belonging to one front end electronics board. A column of 16 lines presents channels connected to one front end driver daughter board. One row of eight front end daughter boards belongs to one front end crate. In both figures areas of interest are marked and the type of failure is indicated

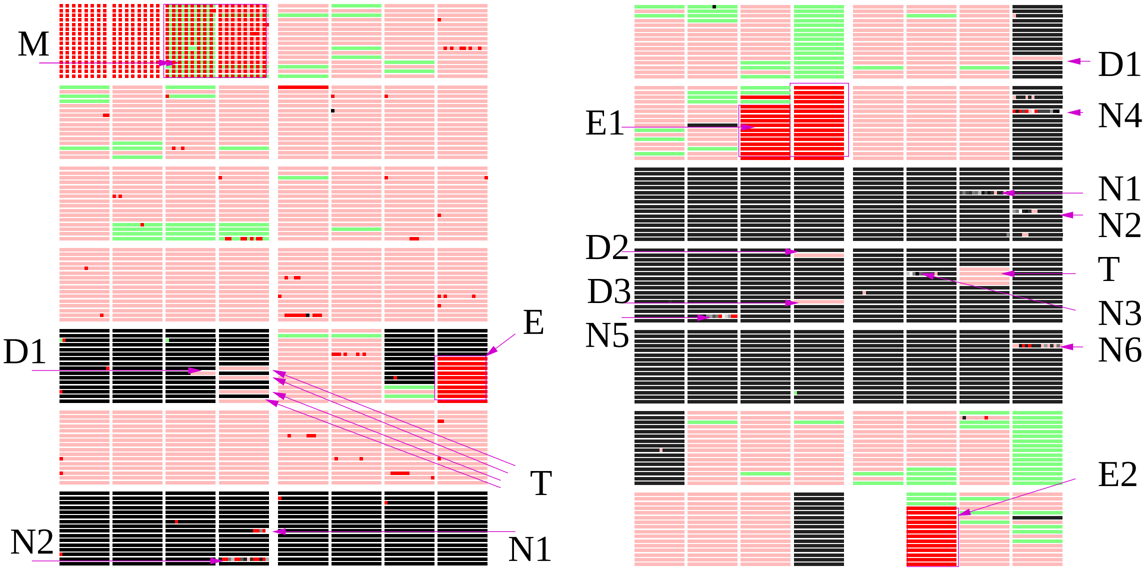

Figure 6.2: Front end driver daughter boards of the upper (left) and lower (right) detector response (see Fig. 6.1) to the test pulses is presented. Noisy channels belonging to one front end electronic board are marked with N, while dead channels belonging to one front end electronic board are noted with D. The areas with test pulse distribution problems are signed with T and noisy front end driver motherboard with M. Areas noted with E present front end daughter boards which are not used.

by the same signs as in Fig. 6.1. Front end driver daughter board presentation also points to the cause of the chess board pattern shown on the right side of the photon detector in Fig. 6.1. The failure is caused by in proper position of the front end driver mother board in the crate.

Sixteen front end electronics boards, eight of the upper and eight of the lower detector, equipped with analog output adapters (Appendix K) present an additional diagnostic instrument for monitoring the performance of the photon detector operation. Although only a small fraction of electronics boards are equipped with adapters they give supplementary information of detector response which can be monitored from the electronics trailer, outside of the spectrometer area.

6.3 Tests with light from light emitting diodes

The light emitting diodes system [58] was mounted on the RICH photon detector windows for testing and monitoring the multianode photomultipliers operation. The system uses several plexy glass semi cylindrical bars, placed on the outer surface of the RICH

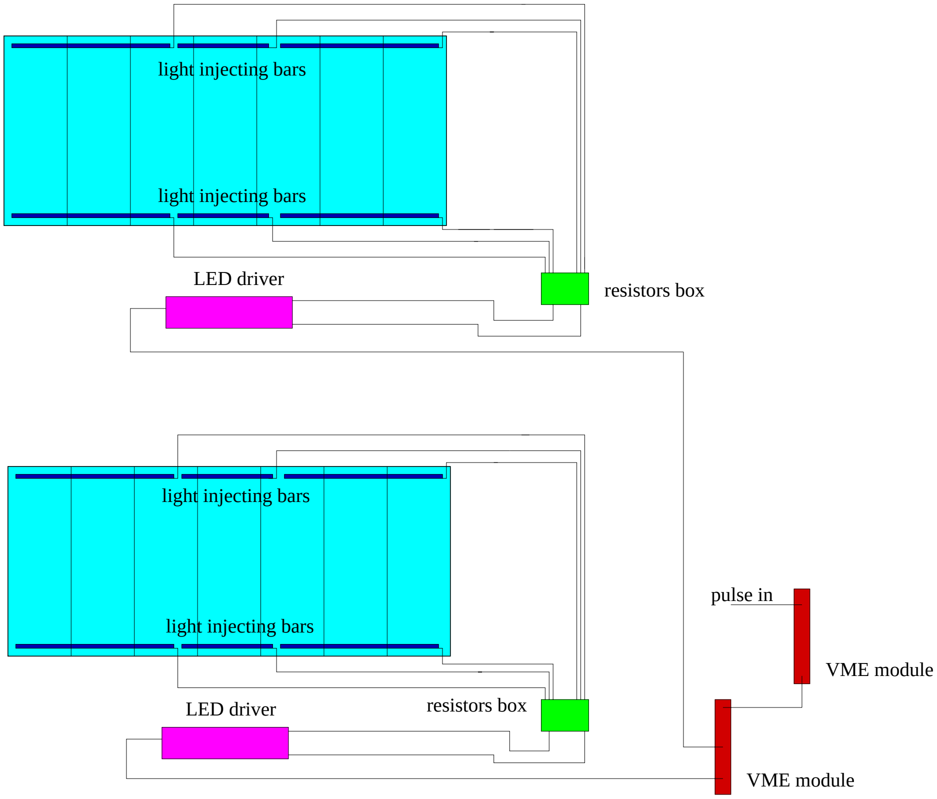

Figure 6.3: The design of the photon detector monitoring system based on light emitting diodes coupled to plexiglass bars. Light from diodes is diffused in the exit window and also reflected from the planar mirrors.

vessel plexy glass window. The cylindrical bars are equipped with light emitting diodes on each end. The bars are placed close to the window edges and are secured in place by mechanical holders (see Fig. 6.3). The optical contact between the bars and the RICH window is achieved with silicon strips, while the curved bars undergoes are covered with aluminized mylar foil. The light from the diodes sent into the bars suffers multiple reflections and eventually enters to the window. In addition to the light which travels inside the window, there is some direct light which is reflected back to the photo detector by the RICH mirrors [58].

The signals from the pulse generator, wider than 100 ns and higher than 4 V, initiate switching the diodes of the light emitting system. Analog front end electronics outputs can be monitored and $\sim$ 30 mV high and $\sim$ 30 ns wide pulses can be seen on the scope. The readout system is initiated by a random trigger, which is good enough for initial tests, while an upgrade with synchronisation with the diodes triggering is foreseen.

6.3.1 Mapping

The proper photon detector cable positions and readout software mapping can be checked, employing tests with light emitting diodes. The testing can be performed in a way that only photomultiplier tubes belonging to selected regions are powered with high voltage and correctness of their positions is checked on the display. The mentioned tests are presented in Fig. 6.4 and Fig. 6.5. As can be seen in Fig. 6.4 some discrepancies between expected and actual region positions were found on the upper photon detector. The cause of discrepancies was found in wrong software mapping, which was corrected and the whole detector was surveyed in the same way again (see Fig. 6.5). With information of actual region positions (Appendix I) the correctness of corrected mapping can be

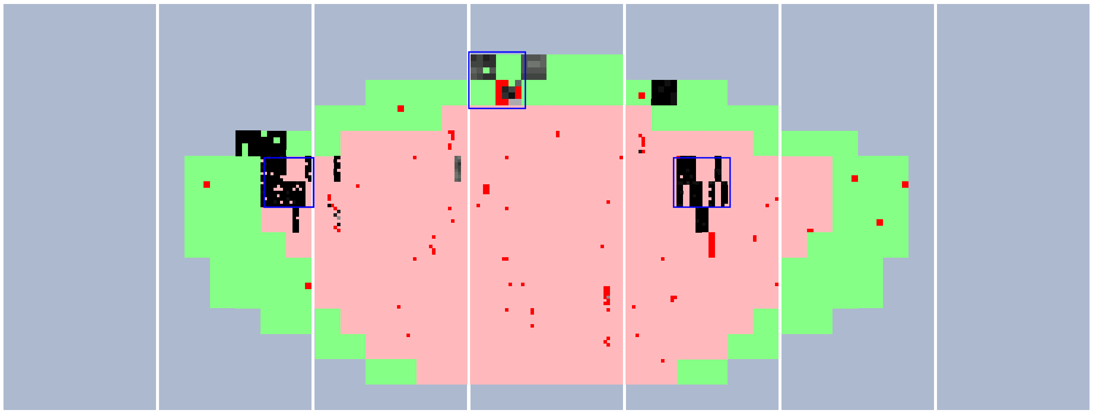

Figure 6.4: Test of the photon detector channels mapping. Only photomultiplier tubes belonging to regions 7, 30 and 61 of the upper detector have high voltage switched on (see Appendix I). The expected positions of these regions are presented by blue squares. Some discrepancies between expected and actual positions can be clearly seen.

confirmed.

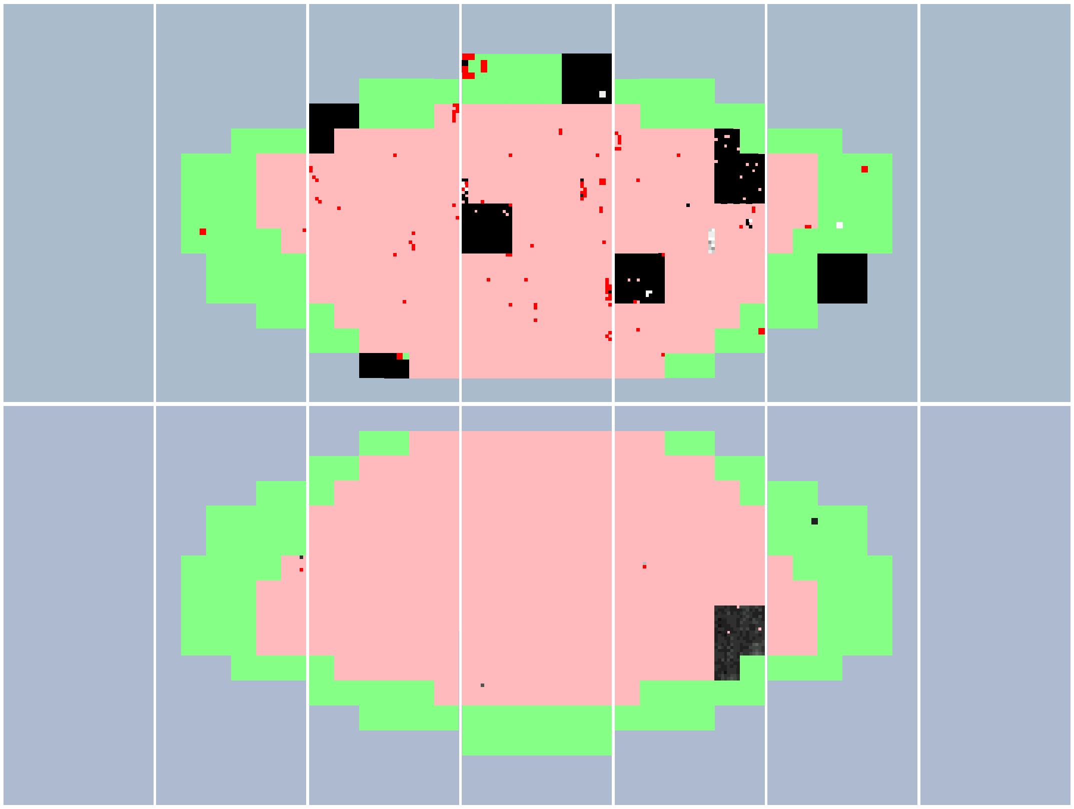

Figure 6.5: Test of the photon detector channels mapping. Only photomultiplier tubes belonging to regions 11, 22, 33, 45, 56, 67 and 78 of the upper detector have high voltage switched on, while only one region 147 is on in the lower detector. The correctness of the mapping can be confirmed by comparison with the actual region positions (see Appendix I). In the upper detector also some groups of noisy channels coloured red can be noticed due to disconnected cables for setting the threshold voltage.

6.3.2 Hit distribution on the photon detector

The next step in the testing procedure is the check the whole photon detector response to light from the diodes. Regions of the detector positioned closer to the cylindrical bars of the light emitting system are expected to receive more hits compared to more distant parts. The pattern of hits, presented in Fig. 6.6 and in Fig. 6.7, confirms the expectations, and the distribution of hits reflects the geometry of the light emitting system.

The hit distribution is presented in gray scale, where brighter colours mark regions which receive more hits. Non responding channels are omitted in this figure, while noisy ones are marked red. It can be noticed that the number of noisy channels of the upper

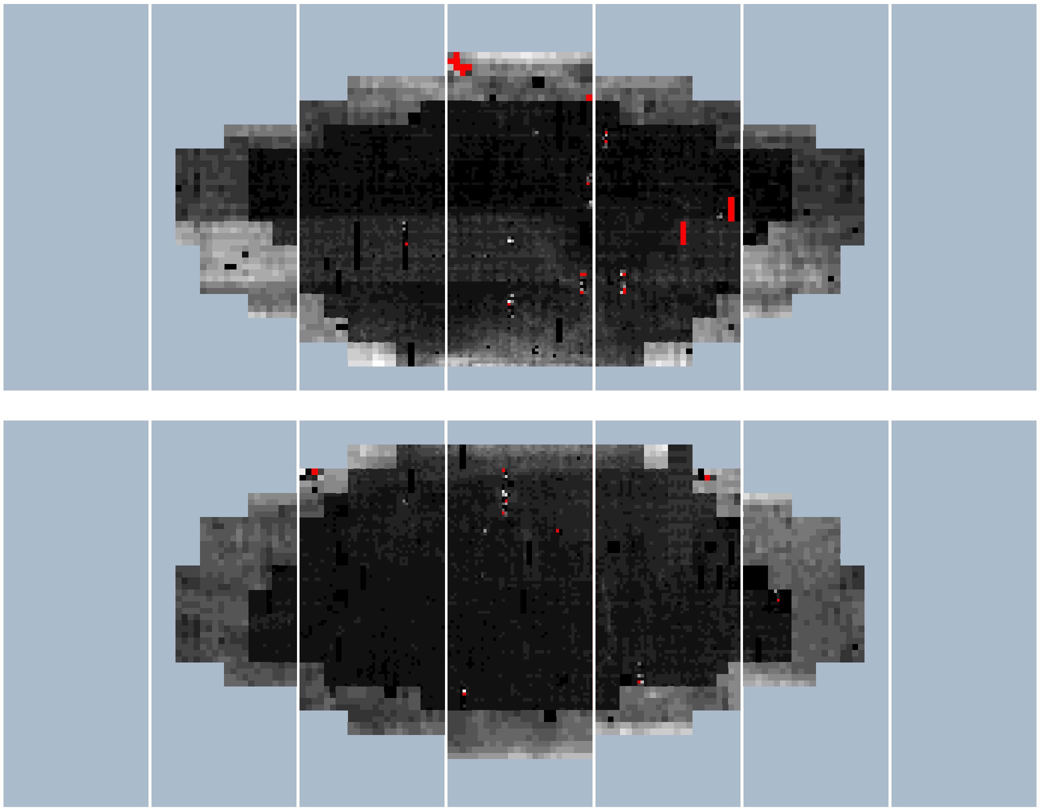

Figure 6.6: Pattern of hits on the photon detector due to light from diodes, with the dead channels removed from the distribution (black) and noisy channels marked red.

photon detector is reduced, if compared with previous photon detector displays showing mapping tests. The improvement is due to repairs performed during access to the detector area.

The hit distribution of the upper photon detector, presented in Fig. 6.6, also reveals a part in the middle of the detector where more hits are detected than expected. This is not due to more sensitive photon detectors or distortion of the detector window in this area, but is due to the arrangement of the light emitting system. This statement is confirmed with additional tests with different light sources, presented in the following where the mentioned part of the detector responds as expected.

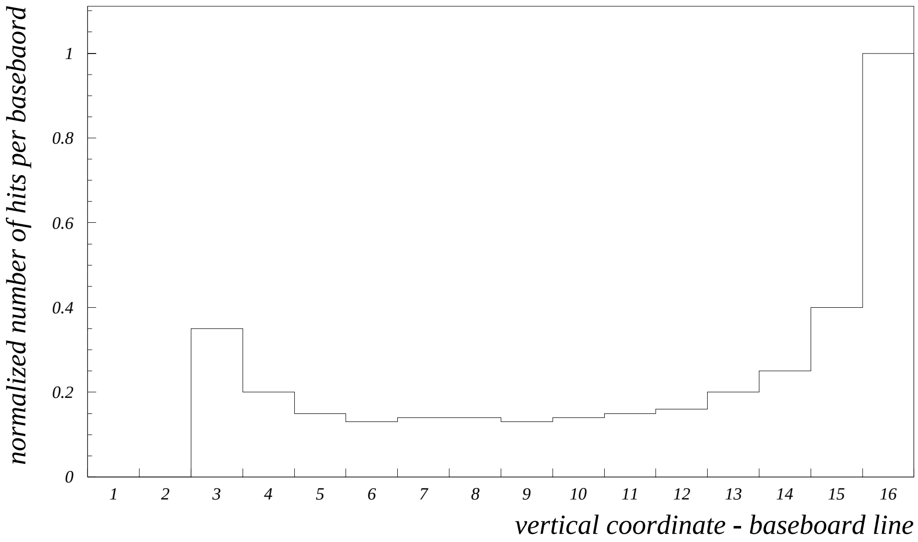

Figure 6.7: The distribution of hits in a vertical slice of the hit pattern on the lower photon detector, reflecting the geometry of diodes. The histogram gives the middle supermodule vertical hit distribution taking hits per photomultiplier tube base module as a basic unit.

6.3.3 High voltage scans

Although the photomultiplier tubes are grouped to their optimal high voltage values, according to the results of quality assessment tests, the dependence of their response on light from diodes by varying the applied high voltage should be periodically checked and compared with previous data. In Appendix I information about optimal high voltage of photon detector regions is summarised. In Fig. 6.8 and in Fig. 6.9 some high voltage scans of M4 and M16 photomultiplier tubes types are presented. In each figure four high voltage scans of photomultiplier tubes belonging to one base module are presented.

Together with the data points representing in situ measurement, a curve measured during quality assessment is also given in each figure. Measurements are made at high voltages from 500 V to 900 V in steps of 50 V at the front end electronics threshold voltage of -1.2 V. It is seen that the present data agree with the quality assessment results for both types of photomultiplier tubes and the optimal high voltage value for both cases is set to 800 V.

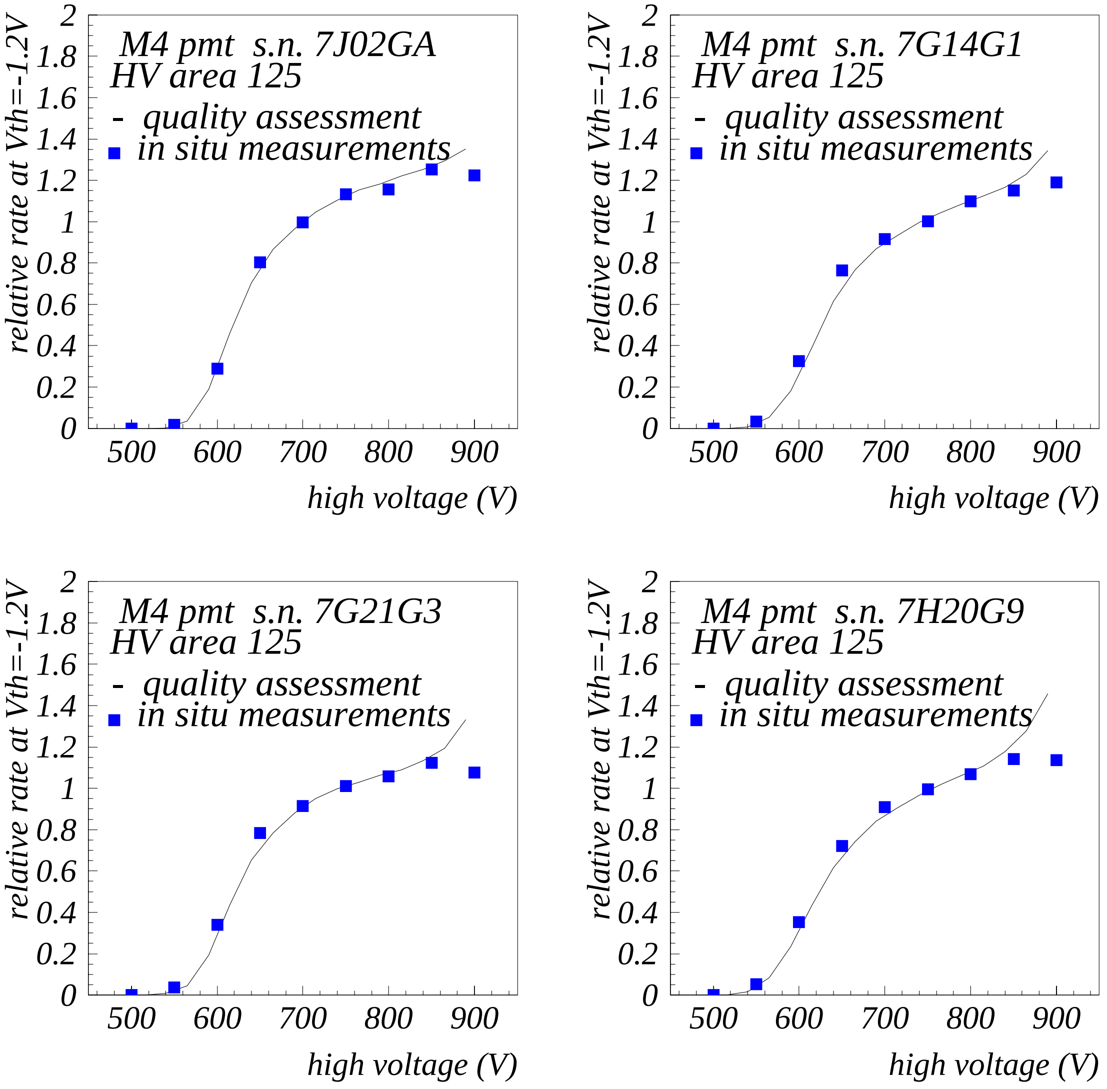

Figure 6.8: The plateau curves for four M4 photomultiplier tubes of one base module in region marked 125. The data labelled in situ represent values measured during the photon detector testing in its final position, while the curve labelled quality assessment correspond to measurements made in the laboratory during on the bench quality tests. The data is normalised to the average of the three points at 750 V, 800 V and 850 V.

It should be noted that, for the M16 photomultiplier tubes the initial part of the plateau curve of the quality assessment measurements is shifted towards higher voltages for 50 V compared to data gained from the in situ measurement. This shift is in good agreement with expectations due to different signal damping resistors on quality assessment baseboards. The baseboard used during the quality assesment was equipped with damping

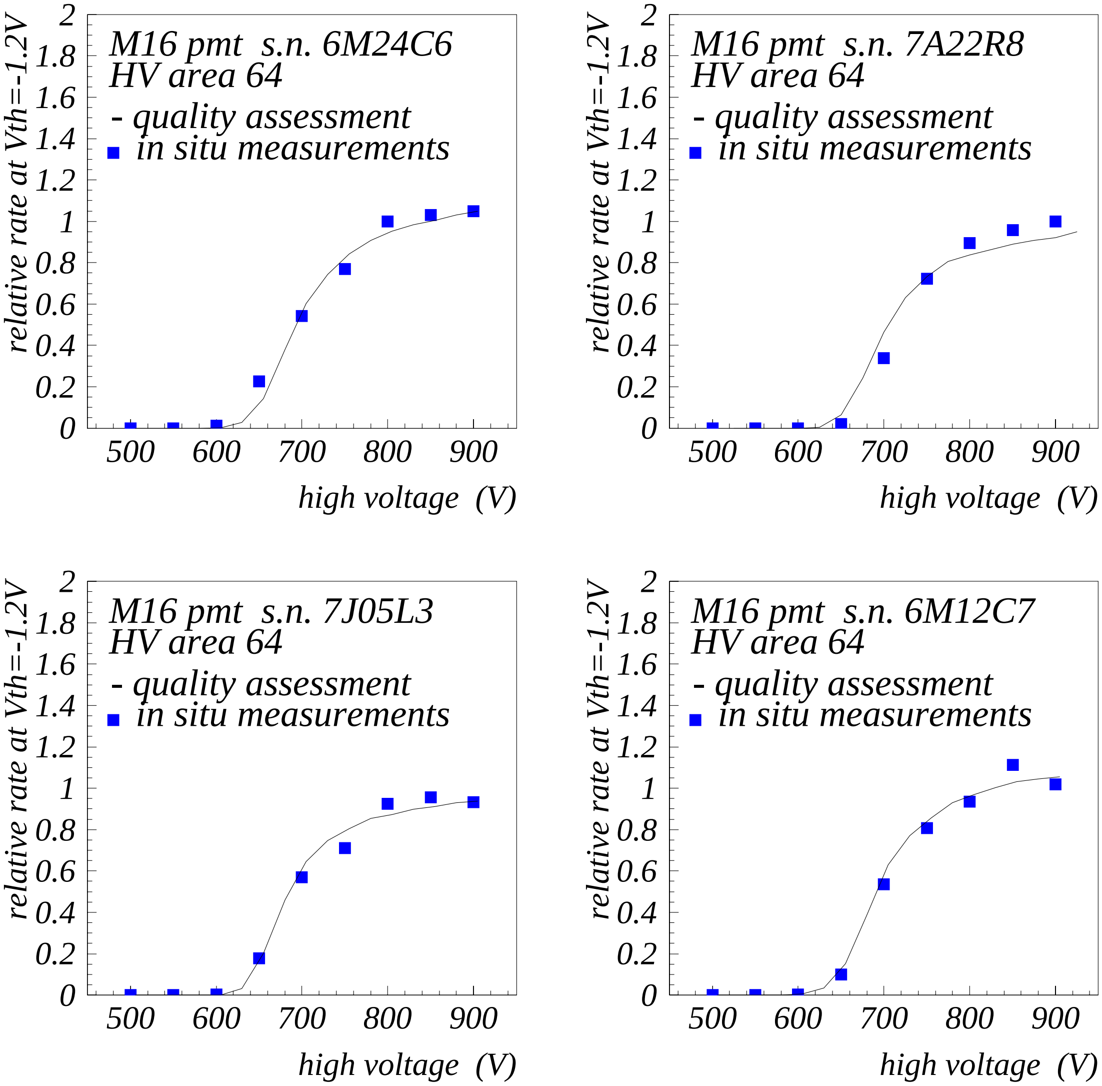

Figure 6.9: The plateau curves for four M16 photomultiplier tubes of one base module in region marked 64. The data labelled in situ represent values measured during the photon detector testing in its final position, while the curve labelled quality assessment correspond to measurements made in the laboratory during on the bench quality tests. The data is again normalised to the average of the three points at 750 V, 800 V and 850 V.

resistor of $500\ \Omega$, while final baseboards are equipped with $1\ \mathrm{k}\Omega$ damping resistors. This approximately presents two times lower signal when using final baseboards, which can be compensated with 50 V higher supply voltage (See Appendix D).

6.3.4 Threshold voltage scans using light from diodes

The influence of applied front end electronics threshold voltage for signal discrimination to the detector performance is presented in Fig. 6.10.

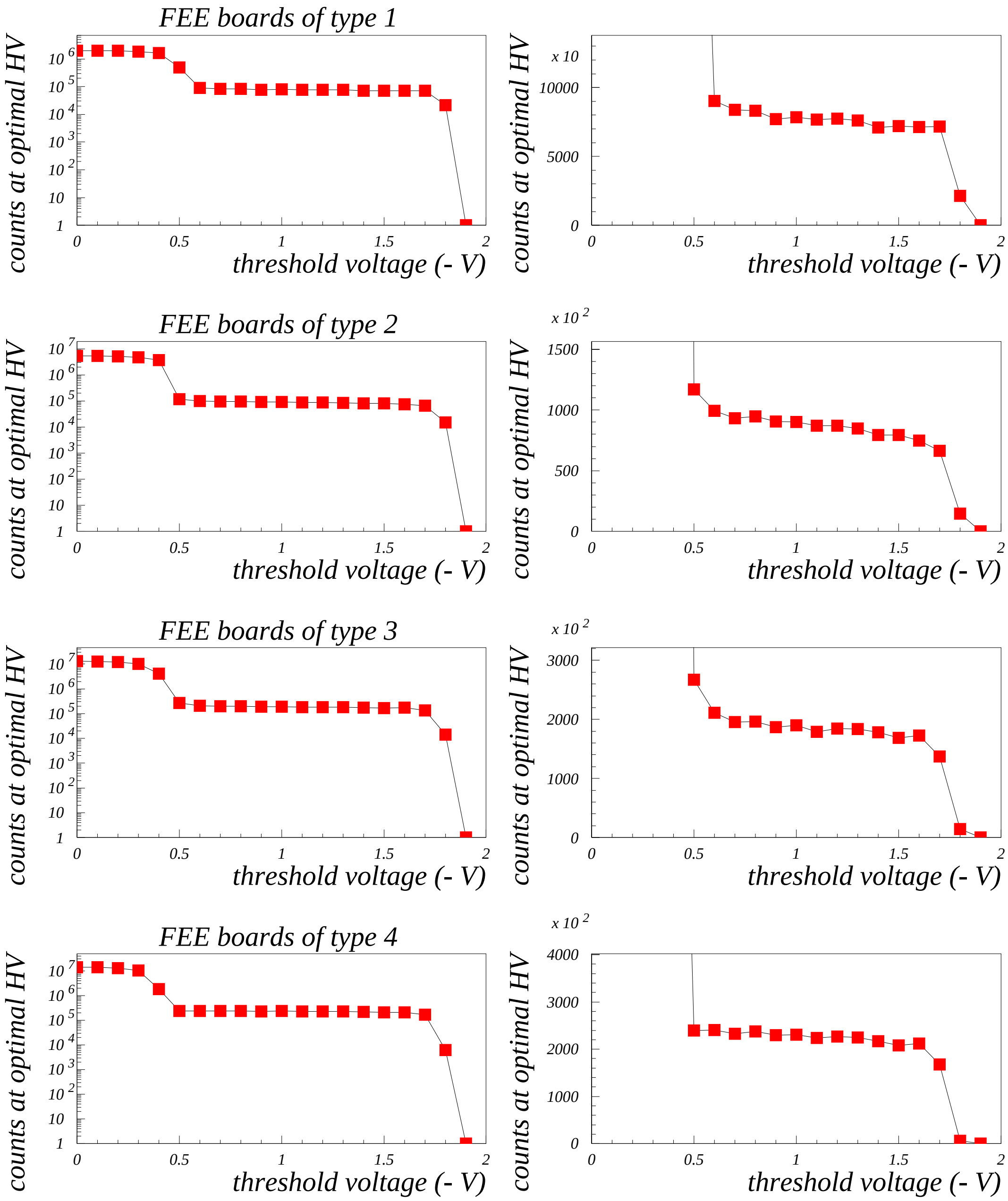

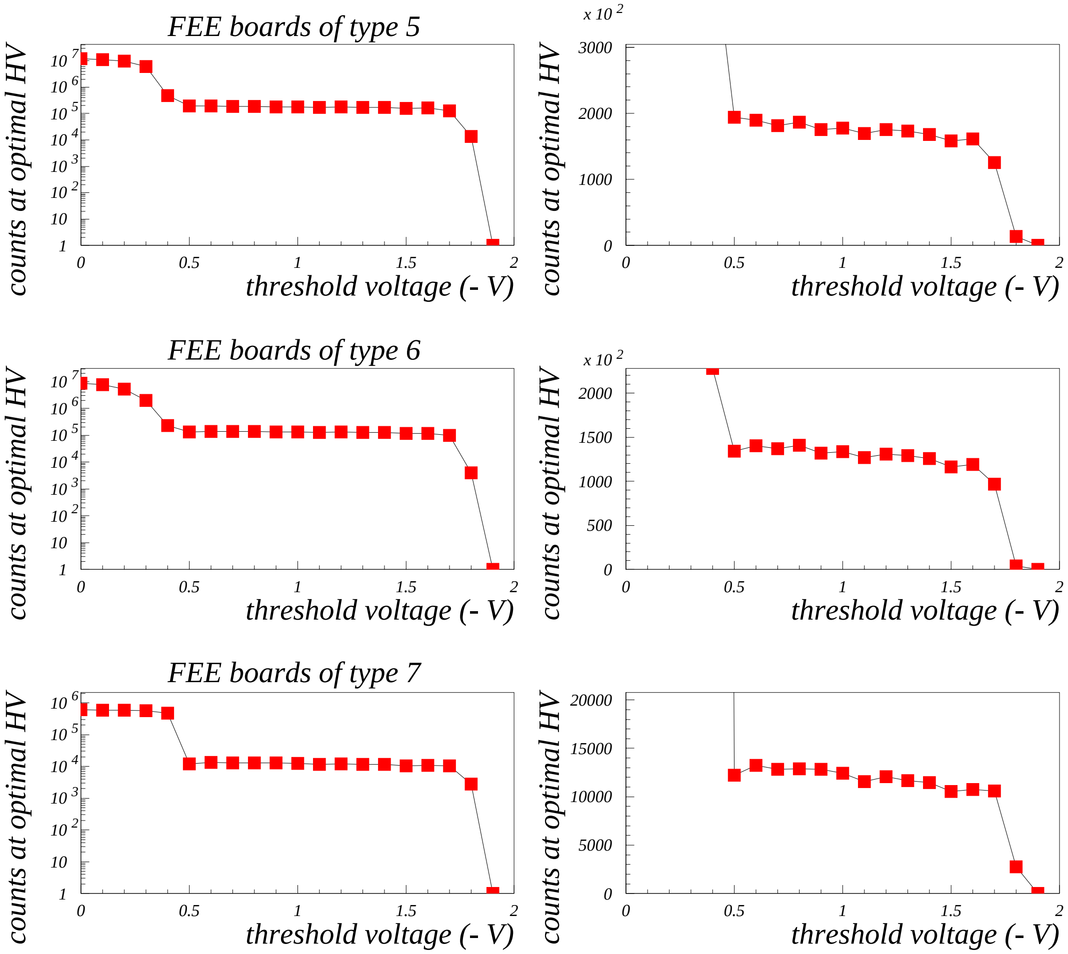

Figure 6.10: The photon detector count rate versus front end electronics discriminator threshold voltage presented in logarithmic and linear scale. Fourteen threshold scans are presented, two for each group of front end electronics board types as determined by quality assessment.

During the threshold voltage scan photomultiplier tubes are powered at optimal high voltages and light from emitting diodes is used as a light source. Scans over all seven types of front end electronics boards are shown. It is seen that for all front end electronics boards the noise is cut off at - 0.6 V discrimination level, while the signal reaches up to - 1.8 V. The wide threshold voltage plato of the curve opens the possibility of setting the same threshold voltage for all the front end electronics. Threshold voltage of - 1.2 V is selected.

6.4 Measurements with proton beam

After the successful first phase of the RICH photon detector calibration, the detector was finally exposed to realistic experimental conditions. When the HERA proton beam was available, the HERA-B target wire positions were varied and measurements were carried out at different target interaction rates. In Fig. 6.11 the accumulated hit distribution on the photon detector due to photons initiated from background events is presented, while in Fig. 6.12 accumulated hit distribution is presented for an arrangement when the HERA-B target was in its place and tuned to interaction rate of 30 MHz. Using the unbiased random trigger for initiation of data acquisition and with no magnetic field, most detected photons are expected to originate from electrons and positrons which originate from electromagnetic showers in various parts of apparatus. Two rings structure dominated by Čerenkov photons radiated by high energetic charged particles produced at small angles can be clearly seen in Fig. 6.12.

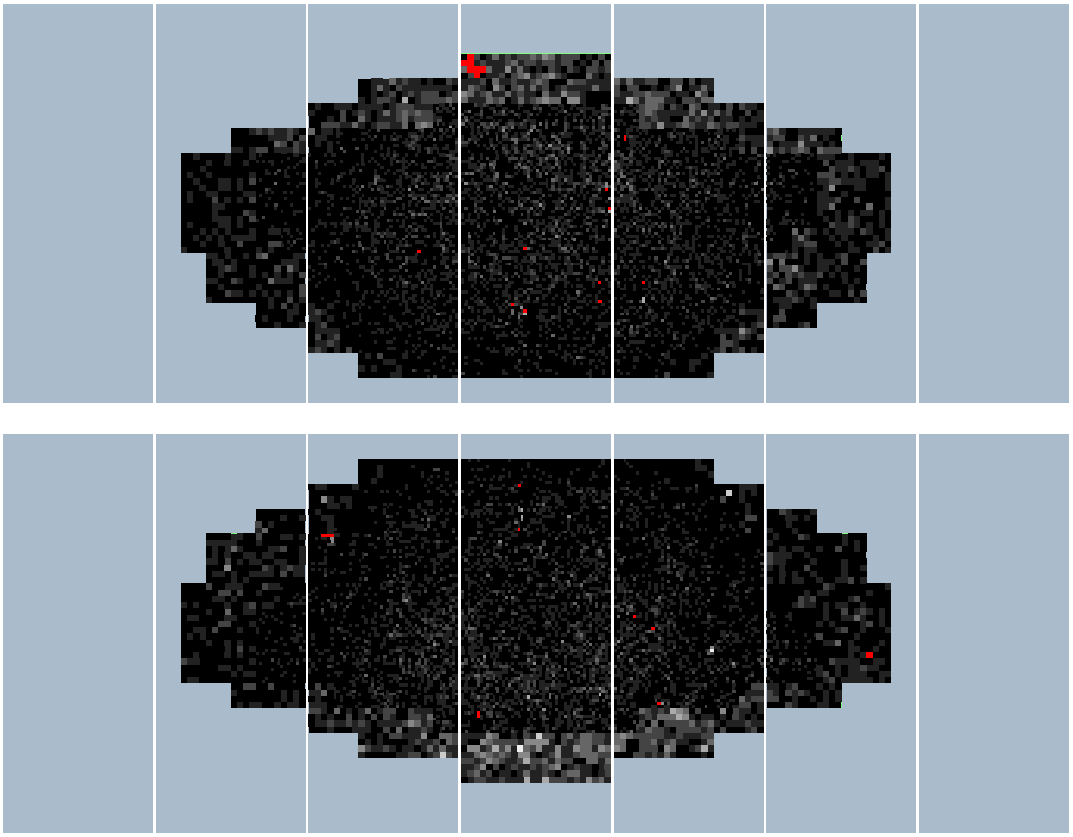

Figure 6.11: Accumulated hit distribution on the photon detector after 5000 triggered events for the case when the HERA-B target was not in use and thus hits due to background were recorded. The average occupancy per 9×9 mm^2 pad is 0.05 %.

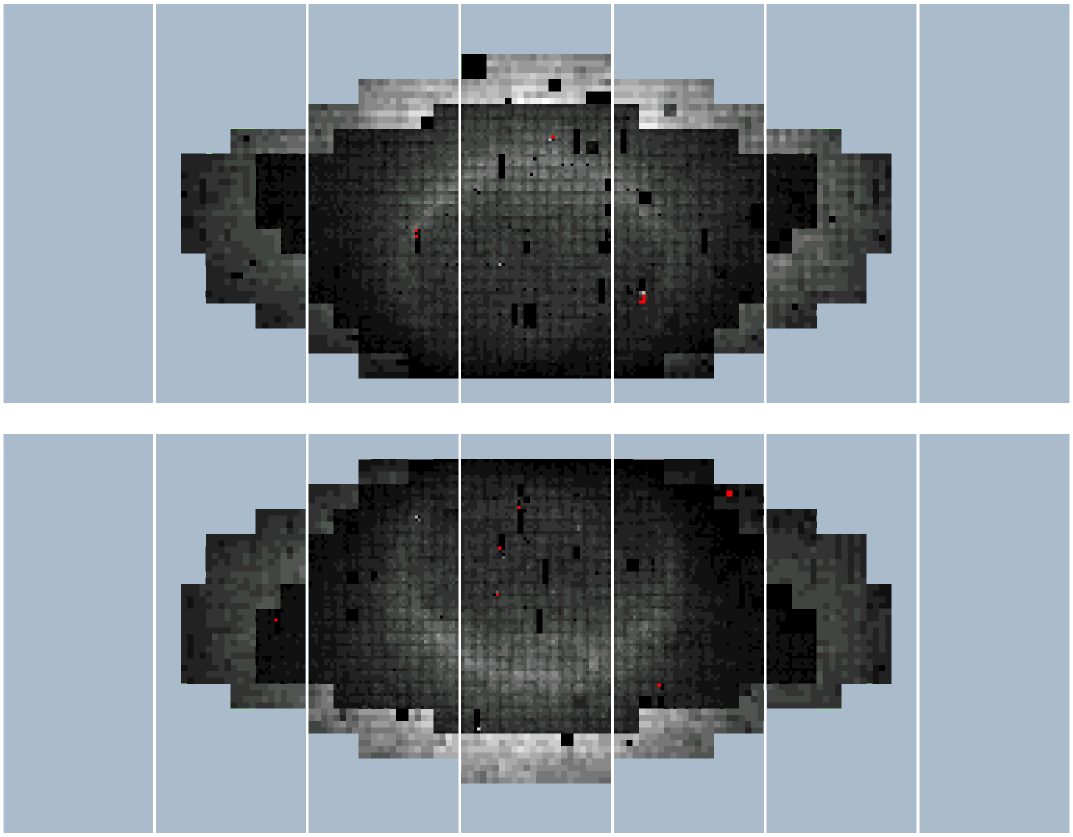

Figure 6.12: Accumulated hit distribution on the photon detector after 10000 triggered events for the case when the HERA-B target was tuned to 30 MHz interaction rate. The maximum occupancy per $9 \times 9\ \mathrm{mm}^2$ pad is 4 % , while per $18 \times 18\ \mathrm{mm}^2$ pad is 6.5 % .

6.4.1 The dependence of the photon count rate on the target interaction rate

The performance of the RICH detector was also checked by varying the interaction rate of the wire target. In a set of measurements the response of the detector was recorded at target rates of 1 MHz, 5 MHz, 10 MHz, 20 MHz, 30 MHz and 40 MHz. In Fig. 6.13, accumulated number of hits on both photon detectors as a function of target interaction rate is presented. A good linearity can be seen in the interaction rate dependence for both the lower and the upper photon detector.

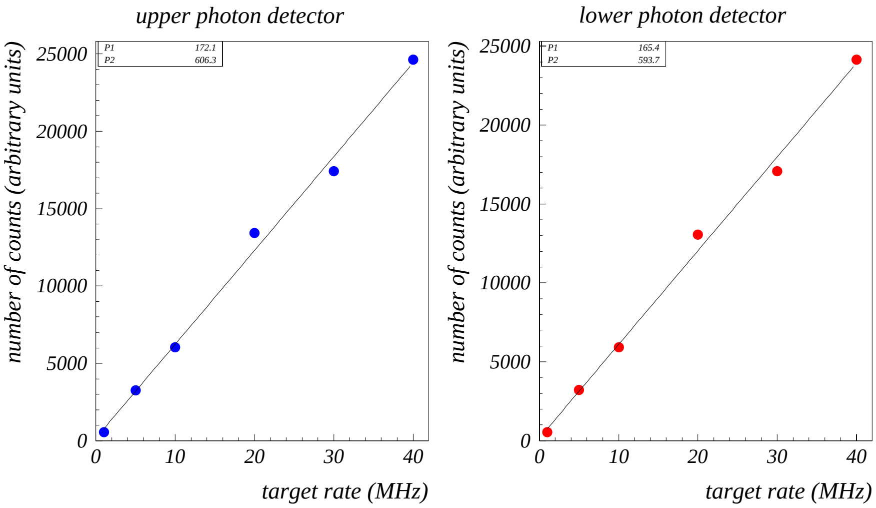

Figure 6.13: Accumulated number of hits on photon detectors versus target interaction rate. Measurements were made at target interaction rates of 1 MHz, 5 MHz, 10 MHz, 20 MHz, 30 MHz and 40 MHz. A good linearity can be found. Noisy channels which were hit in more than 20% of events are suppressed.

6.4.2 Čerenkov rings

First observation of Čerenkov rings on the RICH photon detector was made on August 16, 1998, during the operation with target tuned to the interaction rate of 30 MHz. The upper photon detector was unfortunately not read out during this measurement thus only events on the lower detector were recorded. The RICH vessel was filled with air. The

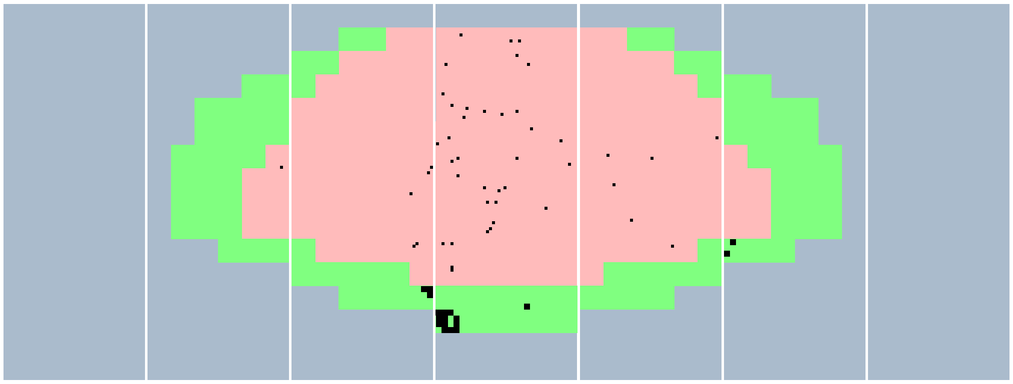

Figure 6.14: Online display of a typical event recorded on the lower photon detector when running at target interaction rate of 30 MHz. Many intersecting rings can be distinguished on a display, with photomltiplier tubes hits represented as black squares. Some noisy channels (belonging to one front end electronics board positioned in the lower left corner of the middle supermodule) indicate hits on essentially every event.

Čerenkov angle for $\beta = 1$ tracks is estimated to 23.5 mrad and the expected number of photon hits per ring is 6.3 ± 1.1. A typical event is depicted in Fig. 6.14, while a few events have clear, isolated Čerenkov rings (see Fig. 6.15). The number of detected photons per Čerenkov ring and Čerenkov ring radius are consistent with expected values.

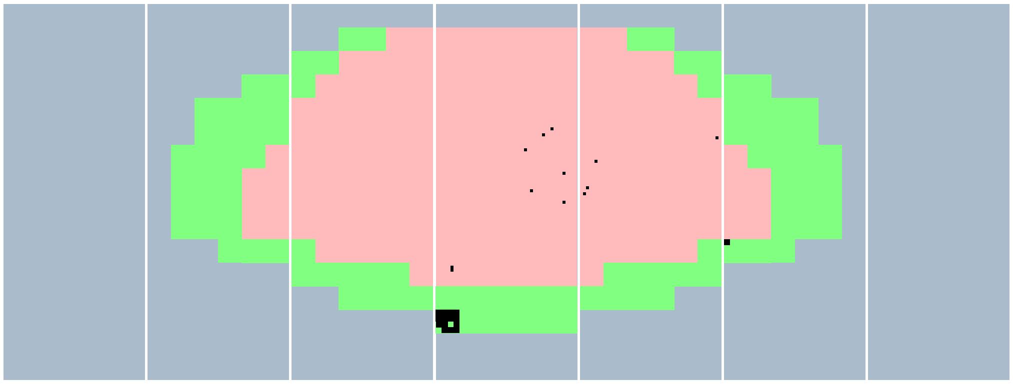

Figure 6.15: Display of an event with one isolated Čerenkov ring with 8 detected photons.

Also one ring with 15 hits, shown in Fig6.16, was found during the event by event scan. This ring is probably due to Čerenkov radiation of an overlapping e^+e^- pair, which originates from symmetric conversion of a high energetic photon In addition to presented types of events many of them are blank or have a diffuse pattern of hundreds of hits. The character of the observed events is thus consistent with expectations that most of detected photons come from electrons and positrons which originate from electromagnetic showers in various parts of apparatus [59].

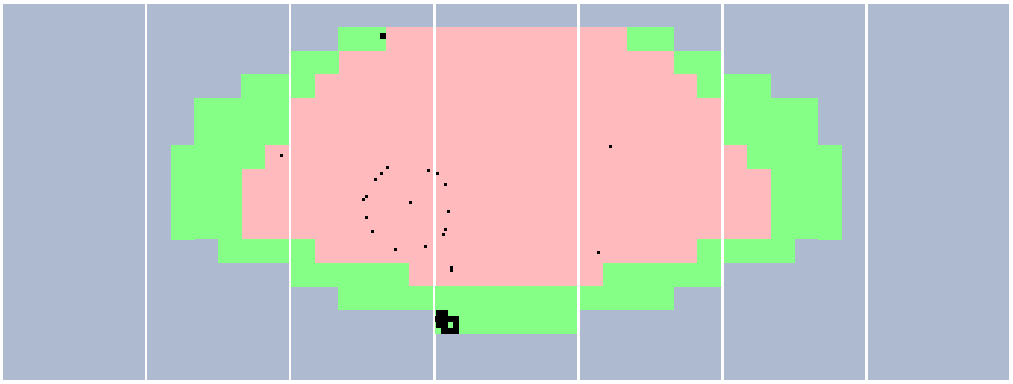

Figure 6.16: Display of an event with one clear Čerenkov ring with 15 detected photons.

Finally over the New Year's 99 shutdown the RICH vessel was filled with C_4F_{10} gas. This change should bring three related consequences:

- Čerenkov rings radii from highly relativistic particles are more than doubled due to increase of Čerenkov angle to $(\vartheta = 51.5\mathrm{mrad})$,
- nearly five times (4.9) as many photons contribute to rings, proportional to the square of Čerenkov angle and
- the threshold momentum for particles to radiate Čerenkov light is reduced by the factor of 2.2.

Data taken with the HERA proton beam and target in its position in the next months confirmed expectations. Limiting Čerenkov angle for particles approaching the speed of light changed from 23.5 mrad in air to 51.5 mrad in C_4F_{10} and the number of detected photons increased by the expected factor. Also Čerenkov rings with smaller diameter than the others can be found indicating that they are radiated by the slower particles. Some typical events with well pronounced single (see Fig. 6.18 and Fig. 6.17) and intersecting (see Fig. 6.19) Čerenkov rings are presented in the following.

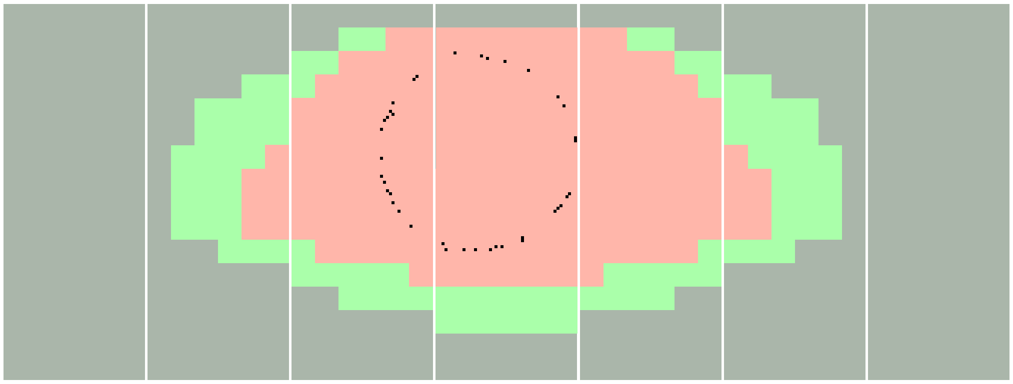

Figure 6.17: Display of an event with single Čerenkov ring with 33 detected photons. From ring radius Čerenkov angle of $51.9\ \pm 0.5\ \mathrm{mrad}$ is deduced and according to calculations 31 ± 2 detected photons would be expected.

It should be noted that Čerenkov rings were detected and read out by many separated front end driver motherboards positioned in different front end driver crates of the data acquisition system and spanned between up to three photon detector supermodules. The fact that the hits fall so accurately on the expected ring shape, as can be also seen in the presented figures, gives an additional confirmation that photomultiplier tubes cabling is correct, the front end driver mother boards time settings are good and the data acquisition system is properly synchronised to single bunch crossing.

Due to non availability of the particle tracking system information, the Čerenkov rings radii were deduced by finding the rings which best fit the detected hits on the photon

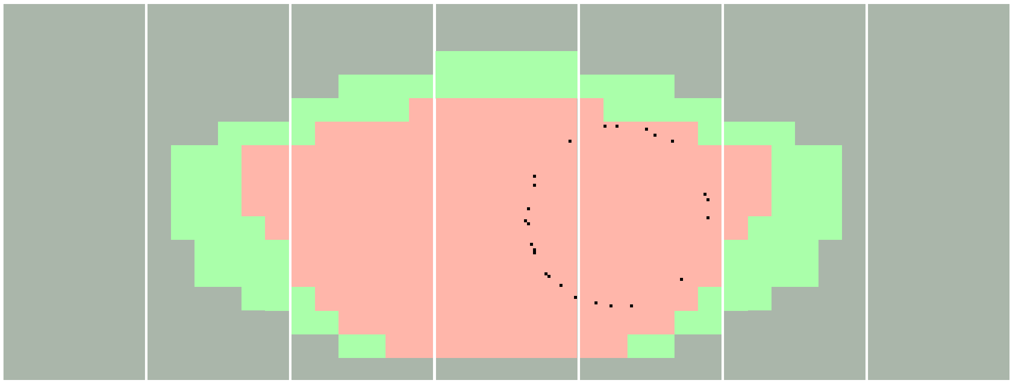

Figure 6.18: Display of an event with Čerenkov ring with smaller radius than presented in previous figure, showing that it oringates from Čerenkov radiation of slower particle. 25 photons are detected and Čerenkov angle of 47.6 ± 0.5 mrad is found which leads to the expected number of hits 26 ± 1.7.

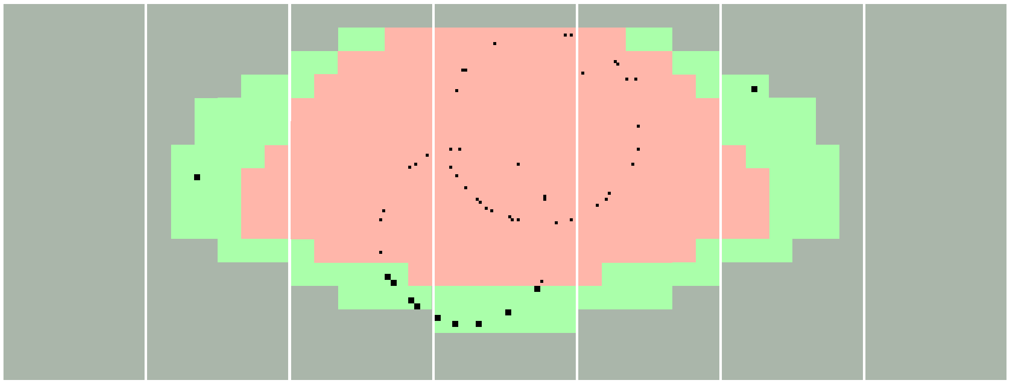

Figure 6.19: Two intersecting Čerenkov rings are presented: a lower one with 22 photons detected by four and sixteen channel photomultiplier tubes, measured Čerenkov angle of 45.5 ± 0.5 mrad and expected number of 23.8 ± 1.5 hits and upper one with 27 photons detected exclusively by sixteen channel photomultiplier tubes, 49.8 ± 0.5 mrad Čerenkov angle and expected 28.5 ± 1.8 hits.

detector. Thus only events which depict well separated Čerenkov rings were employed in a simple analysis. In analysis one counts the detected photons per Čerenkov ring by looking at appropriate events and measures the corresponding ring radius. The number of counted hits per Čerenkov ring is plotted as a function of Čerenkov angle in Fig. 6.20. The lines drawn on the plot correspond to hypothesis that 31 photons in average are radiated from particles approaching the velocity of light and assuming an error of $\pm\sqrt{31}$.

If one takes into account only events with rings radiated by particles approaching velocity of light the average number of detected photons per ring would be 30.2 ± 3.6 (see Fig. 6.21). In Fig. 6.22 the photon detector response parameter distribution for analysed events is presented. It's average value is $43.8 \pm 3.5\ \mathrm{cm}^{-1}$.

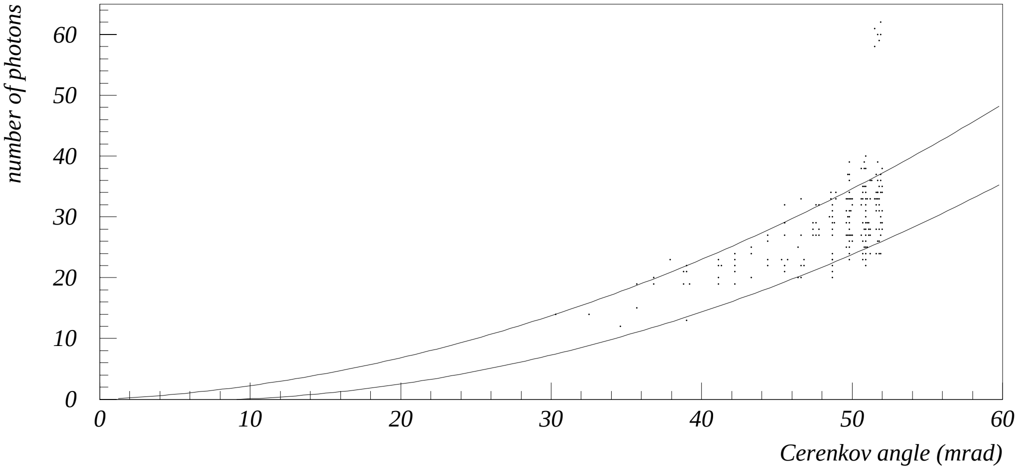

Figure 6.20: Number of detected photons versus Čerenkov angle for nearly 200 rings which could be well separated. Also few events with two times more detected photons per ring, as would be expected are presented. They are due to Čerenkov radiation of an overlapping e^+e^- pair.

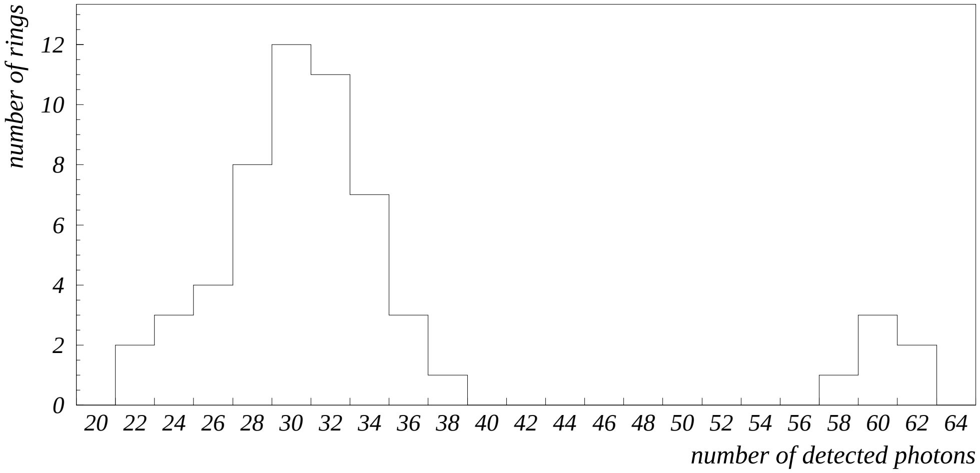

Figure 6.21: The number of detected photons per ring radiated by particles approaching velocity of light (Čerenkov angle $\vartheta > 51\ \mathrm{mrad}$). The average value of detected photons, calculated without taking into account overlapping rings, is 30.2 and RMS is 3.6.

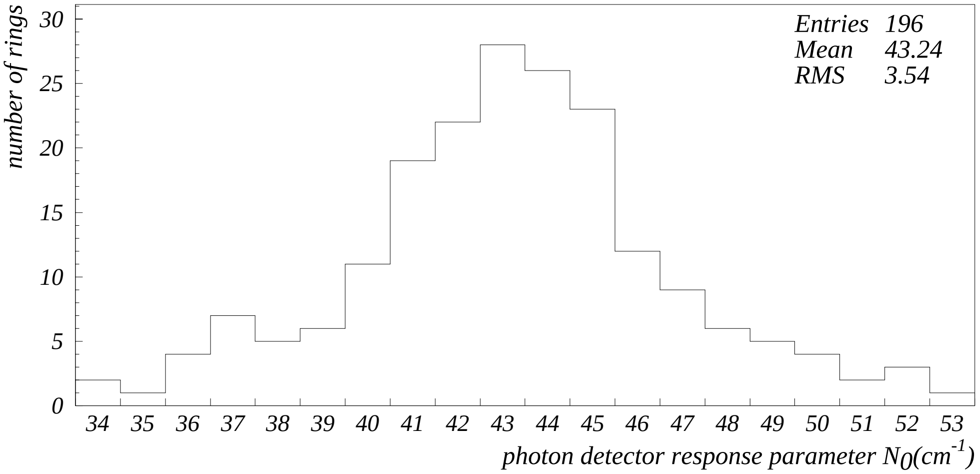

Figure 6.22: The photon detector response parameter N_0 distribution.

The average value of the photon detector response parameter as well as the average number of detected photons per ring are consistent with the expectations.

7

Conclusions

This doctoral thesis is dedicated to the development of the Ring Imaging Čerenkov counter ranging from investigations of the imaging properties of the photon detector to the observation of the first Čerenkov ring images obtained in the experimental area.

The environment of the HERA B experiment, its physics goals and the required particle identification determined the choice of the RICH photon detector technique. Due to the short time available for research and development, it is not surprising that some problems related to the extremly high rate environment occured. Originally it was proposed to use wire chambers for the photon detector; either pixel chambers operated with saturated TMAE gas or CsI pad chambers. After extensive experimental work it was realised that neither of the proposed candidates met the design criteria, due to severe aging under HERA B conditions and difficulties to obtain the required number of detected photons per Čerenkov ring. Simultaneously a new generation of multianode photomultiplier tubes become available, which fulfilled the requirements of HERA B experiment.

In order to test the performance of the new technology used in photon detector in a realistic experimental environment similar to HERA B's, measurements with the fully equipped photon detector prototype were performed with Čerenkov light from 3 GeV/c electrons at the DESY experimental area T24. Several tests were performed in order to check the photon detector operation with bare photomultiplier tubes, and with the photon detector equipped with the complete light collection system.

As a result, the number of detected photons per Čerenkov ring was measured and the prototype detector response figure of merit was estimated to be

$$\mathrm{N_0} = 43.6 \pm 2\ \mathrm{cm}^{-1}.$$

This value was used to determine the expected number of detected photons per Čerenkov ring for particles approaching the velocity of light in the HERA B RICH counter. The estimated number of detected photons is 31 ± 2.

The RICH photon detector was installed in winter 97 and spring 98, while the gas system started to operate in the beginning of 99. The detector was continuously upgraded during long and short shut downs of the accelerator.

In order to ensure that the RICH counter is functioning as expected, a set of calibration procedures was performed prior to the beginning of measurements. The optimal high voltage supplied to the photomultiplier tubes and the threshold voltage for the front end electronics were determined. In addition also proper channel mapping and time synchronisation between different front end driver boards and bunch crossings were checked.

Measurements with the proton beam and the internal target in position confirmed the expectations of the RICH detector performance. In the analysis, the detected photons per Čerenkov rings were counted and their radii were measured. Due to problems with the particle tracking system, only events with well separated Čerenkov rings were employed in the analysis. The obtained average number of detected photons per ring radiated by particles approaching the velocity of light is consistent with the expected value and amounts to 30.2 ± 3.6. This value assures a reliable $3\sigma_\beta$ separation of pions from kaons up to momenta of 50 GeV/c.

According to the presented results it can be concluded that the HERA B RICH counter operates reliably and as expected. It will contribute to a successful operation of the HERA B spectrometer in the near future. Although the beginning of the full HERA B operation is delayed by about one year with respect to the original schedule, preliminary results are expected from the running period next year. The HERA B experiment will thus represent the pioneering B factory, probing technologies and physics for the second generation experiments at the highest energy colliding beams.

8

Appendices

8.1 Appendix A: $\mathrm{C_4F_{10}}$ properties

The refractive index dependence in the energy interval between 4 eV to 7 eV is adopted from DELPHI RICH data and extrapolated to lower energies [60]. Their best fit is

$$\vartheta = a \cdot E^2 - b \cdot E + c,$$

where $\mathrm{a} = 0.26\,\mathrm{eV}^{-2},\ \mathrm{b} = 1.28\,\mathrm{eV}^{-1}$ and $\mathrm{c} = 52.90$

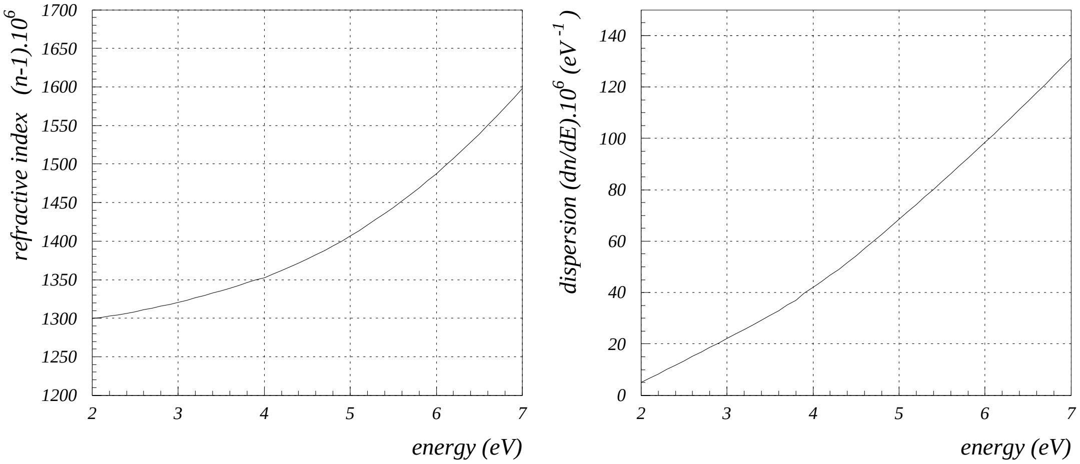

Figure 8.1: Refractive index and dispersion of $\mathrm{C_4F_{10}}$ gas.

Some chemical properties of $\mathrm{C_4F_{10}}$ are gathered in the following table [26].

One mole	0.238 kg
Boiling point	$-\ 1.7^{o}$ C
Gas density	$9.935\ \mathrm{kg/m^3}$
Liquid density	$1517\ \mathrm{kg/m^3}$
Critical temperature	$113^{o}\mathrm{C}$
Critical pressure	$2323\ \mathrm{kPa}$
Critical volume	$1.58\ \mathrm{dm^3/kg}$

Table 8.1: $\mathbf{C_4F_{10}}$ chemical properties.

8.2 Appendix B: Spherical mirrors quality assessment

- The spherical mirror reflectance curve in the wavelength interval between 250 nm and 600 nm shows that the reflectivity exceeds 85% in the whole interval [23].

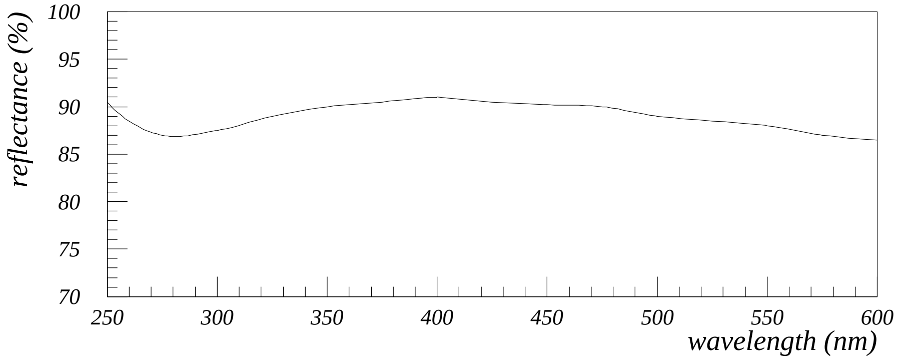

Figure 8.2: Reflectivity of spherical mirrors in the wavelength interval 250 nm to 600 nm.

- The radius of curvature was measured by putting a laser near the centre of curvature of a mirror and observing the smallest focusing spot on a screen next to the laser. Five mirrors do not have an acceptable radius of curvature

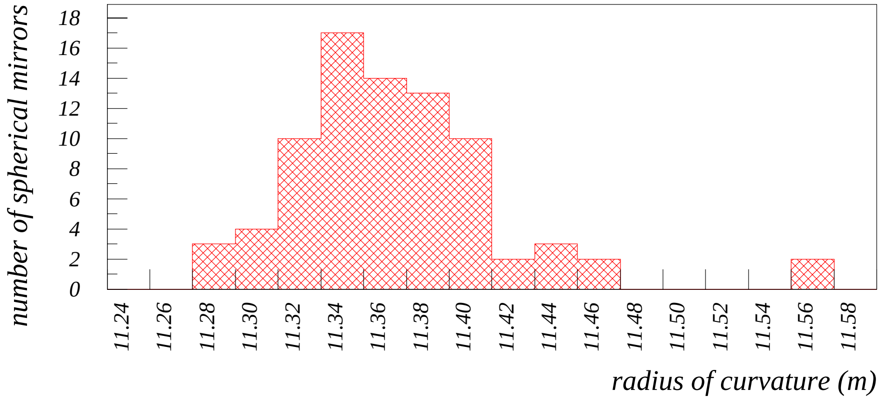

Figure 8.3: Number of mirrors versus mirror radius.

- A photodiode with a variable aperture was placed next to a light source near the centre of curvature of a mirror. The acceptance test requires that 95% of the reflected light be focused into a 7 mm aperture. Only two mirrors focused less than required.

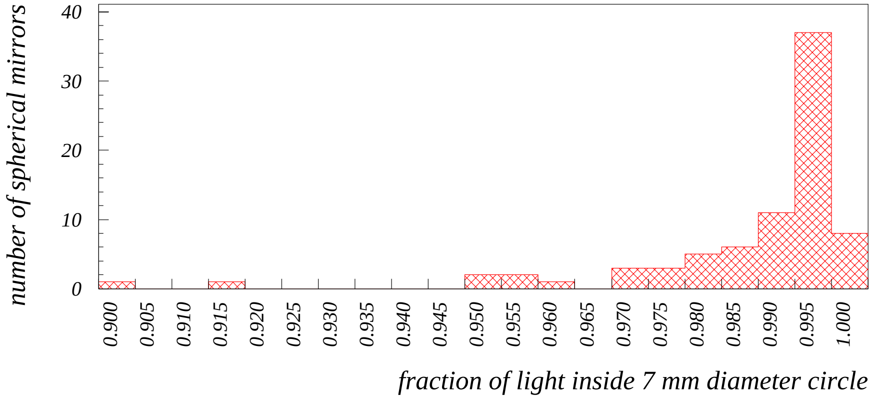

Figure 8.4: Number of mirrors versus percentage of power reflected into 7 mm aperture.

- Ronchi tests were used to map and record departures from the ideal spherical reflecting surface. Test is made by viewing a mirror through a grating placed near the centre of curvature. The source of illumination is placed behind the same grating. A series of light and dark bands is observed against the outline of the mirror. Ideally, the bands are straight and their number is proportional to the distance from the grating to the centre of curvature. When the grating is placed exactly at the centre of curvature, a perfect mirror will appear completely dark or light, depending on details of the setup. Departures of observed bands from straight lines and incomplete darkening at the average centre of curvature indicate errors in the shape of the reflecting surface. The distorted bands appear over regions of the mirror where the surface errors are located [61].

Spherical mirror segments tiling scheme:

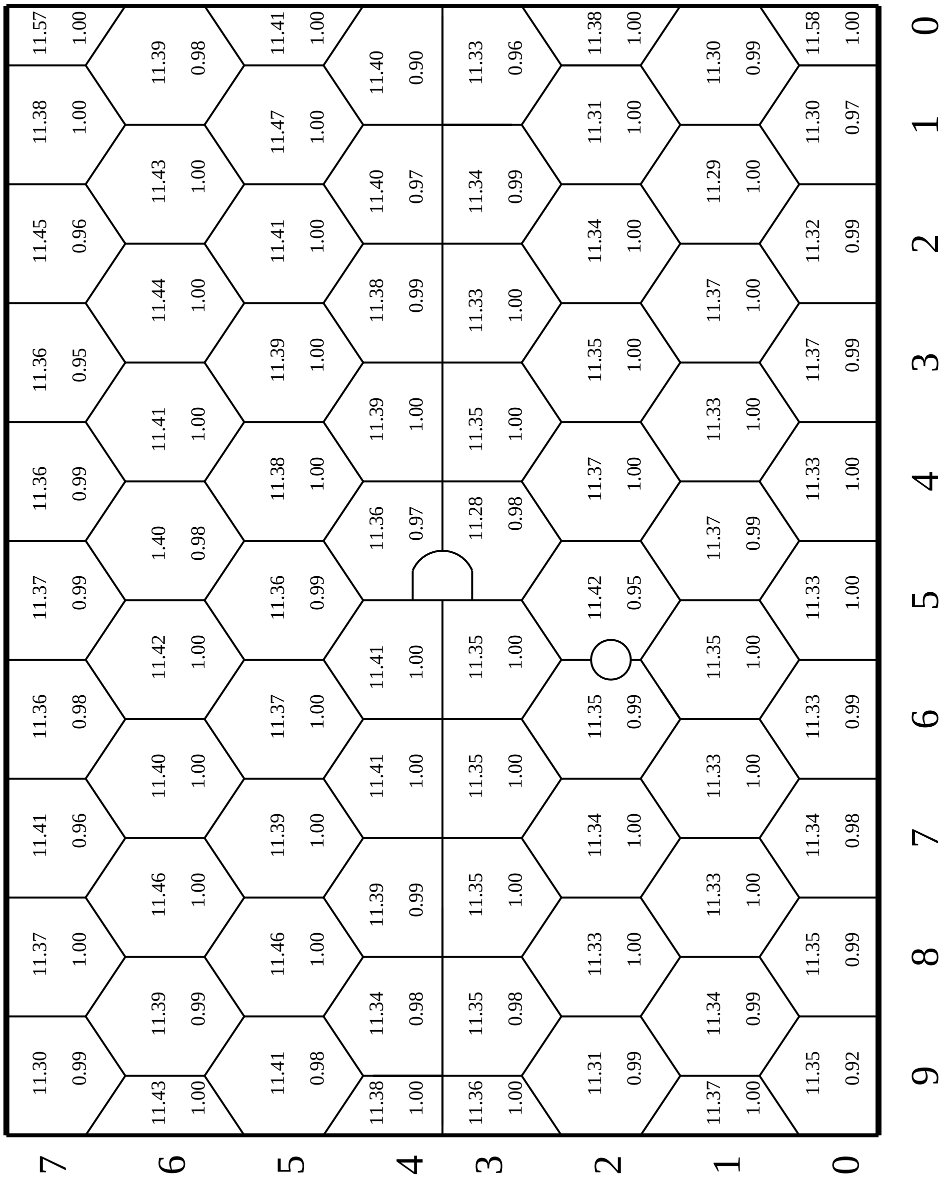

Figure 8.5: Spherical mirrors tilling scheme. In each segment radius of curvature and fraction of power from a point source focused into 7 mm aperture are noted [23].

8.3 Appendix C: Supermodule construction

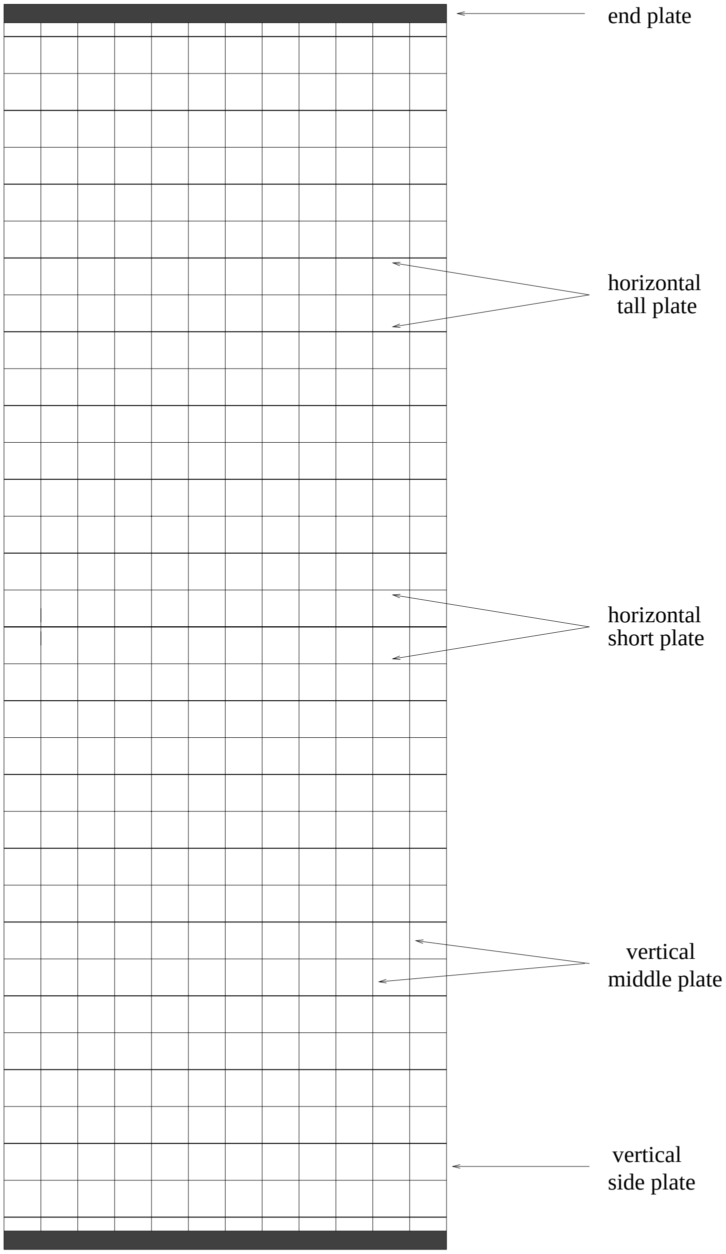

Figure 8.6: Supermodule grid construction design.

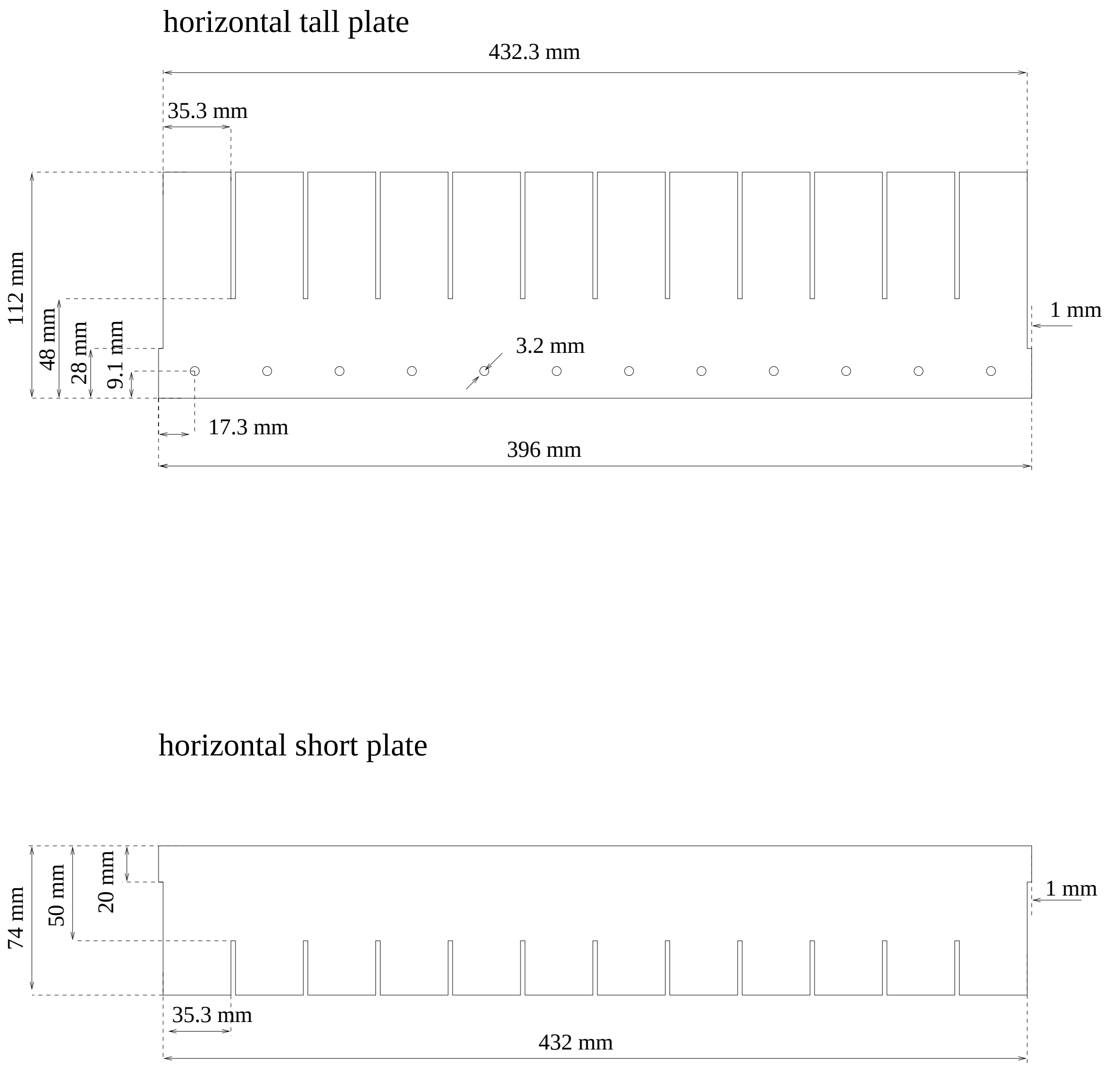
horizontal tall plate

horizontal short plate

Figure 8.7: Supermodule horizontal tall and short plate design .

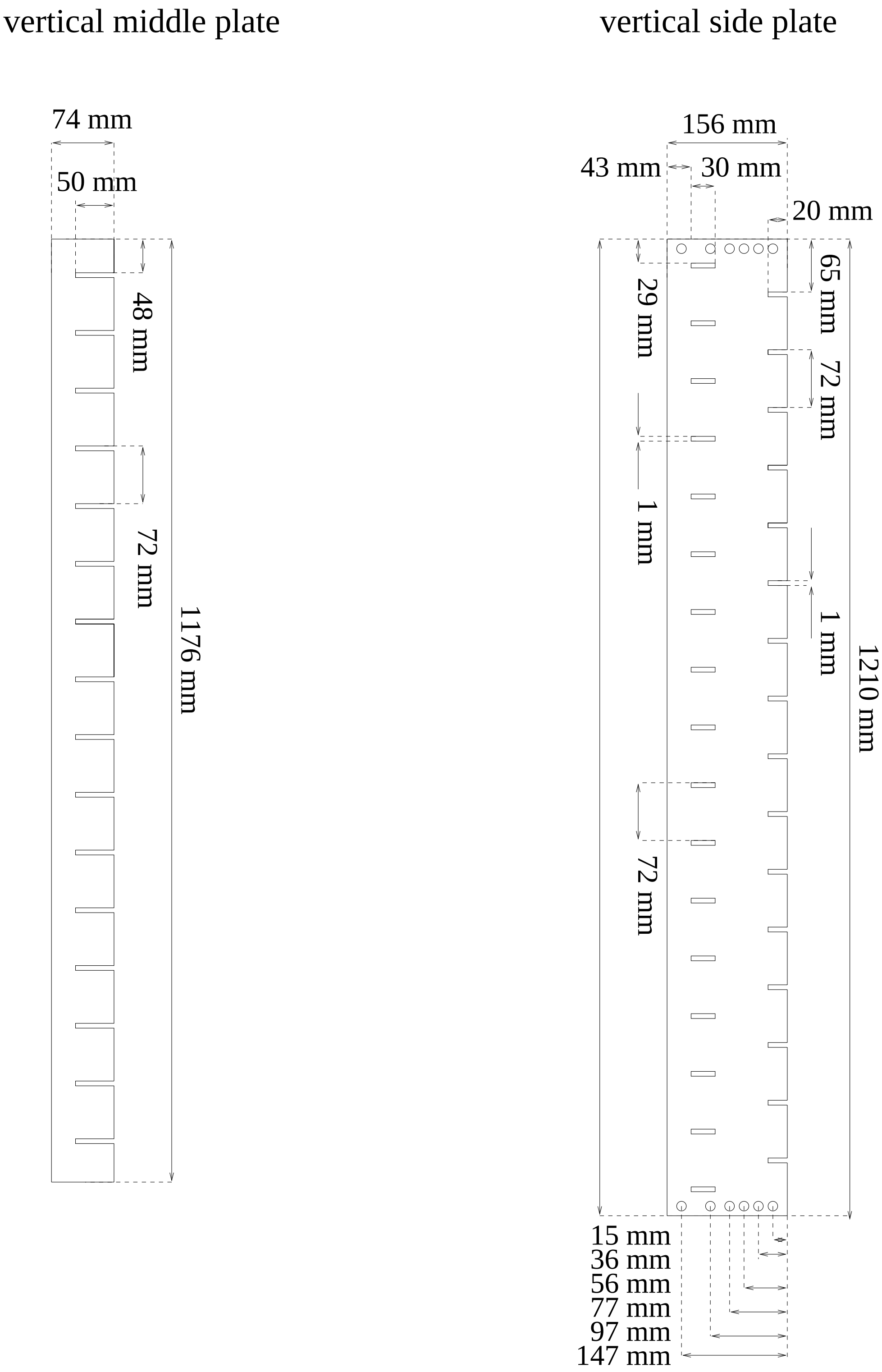

Figure 8.8: Supermodule vertical middle and side plate design.

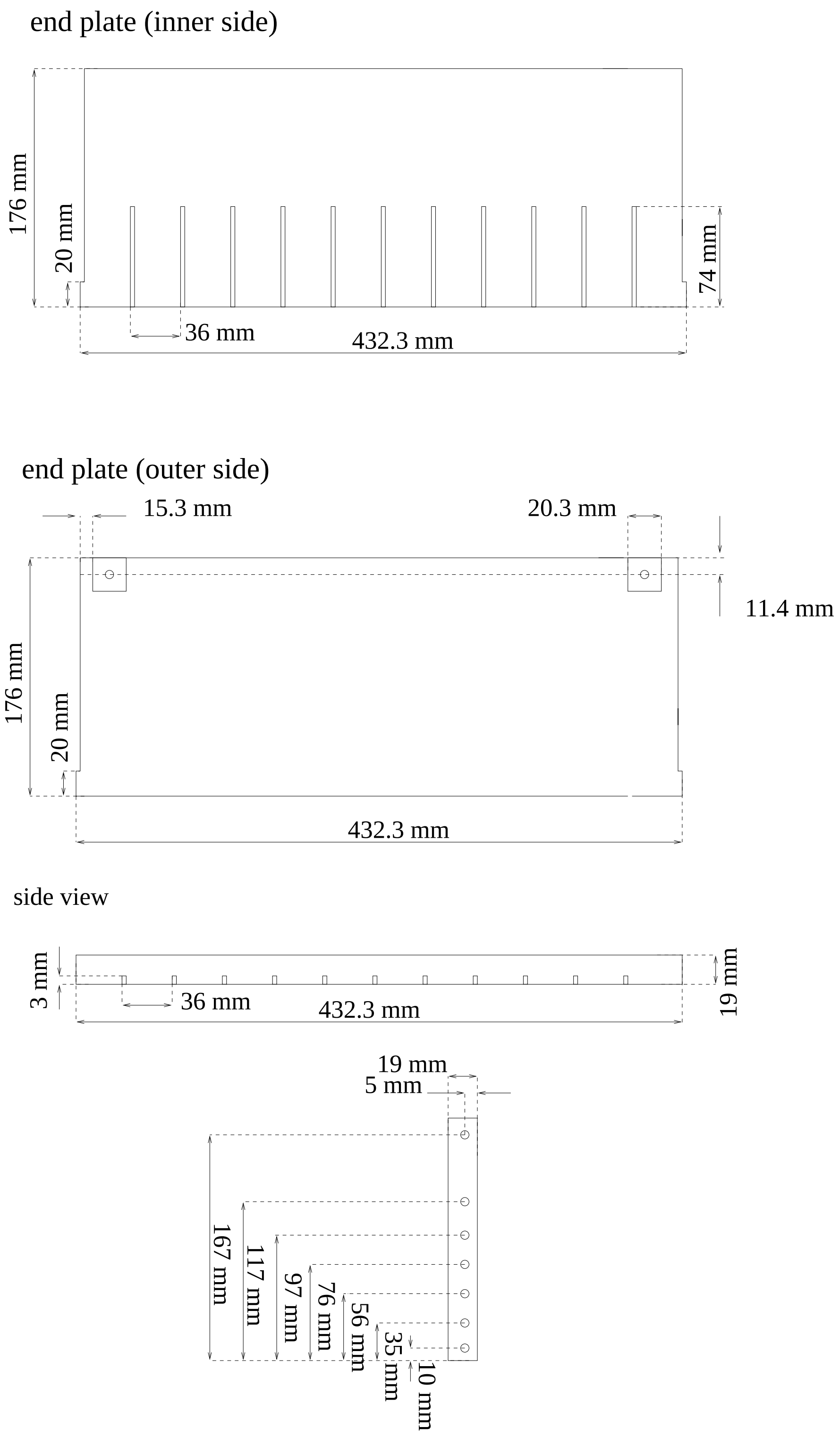

end plate (inner side)

end plate (outer side)

side view

Figure 8.9: Supermodule end plate design.

8.4 Appendix D: Hamamatsu photomultiplier tubes R5900

	photomultiplier tube R5900-00-M16	photomultiplier tube R5900-03-M4	
spectral response	250 nm - 650 nm 1.9 eV - 4.8 eV	185 nm - 650 nm 1.9 eV - 6.7 eV	Fig.8.10
maximum response at wavelength (energy)	420 nm (2.9 eV)	420 nm (2.9 eV)	Fig.8.10
quantum efficiency at peak	$20\,\%$	$23\,\%$	Fig.8.10
photocathode: material	bialkali	bialkali	
(minimum effective area)	$17.5 \times 17.5\ \mathrm{mm}^2$	$18 \times 18\ \mathrm{mm}^2$	Fig.8.11
window material	borosilicate glass	UV light transparent glass	
dynode system: structure (number of stages)	metal channel dynode (12)	metal channel dynode (10)	Fig.8.12
anode size	$4 \times 4\ \mathrm{mm}^2$	$9 \times 9\ \mathrm{mm}^2$	Fig.8.11
weight	28 g	24 g	
maximum supply voltage	1000 V	900 V	
gain	3.3×10^6	1.8×10^6	Fig.8.13
time response: anode pulse rise time	0.83 ns	1.2 ns	Fig.8.14
transit time spread (FWHM)	0.3 ns	0.3 ns	Fig.8.14
magnet field influence			Fig.8.15

Table 8.2: Photomultiplier tube R5900 characteristics [33].

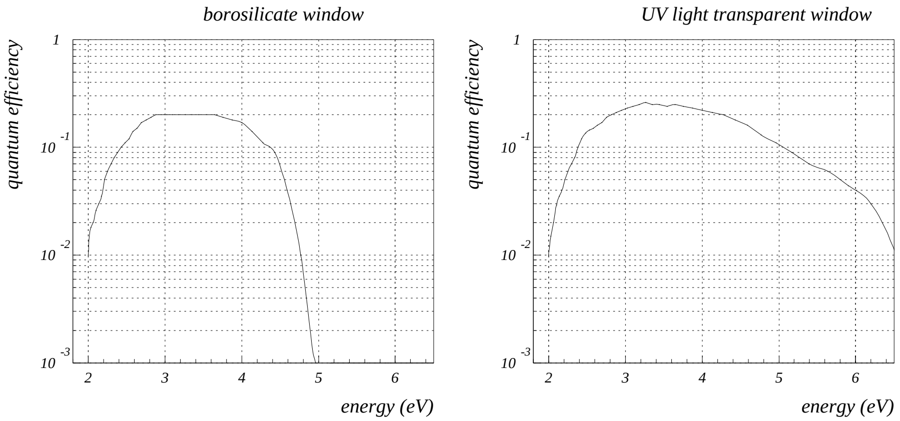
borosilicate window

UV light transparent window

Figure 8.10: Photomultiplier tube R5900-00-M16 and R5900-00-M16 quantum efficiency [33].

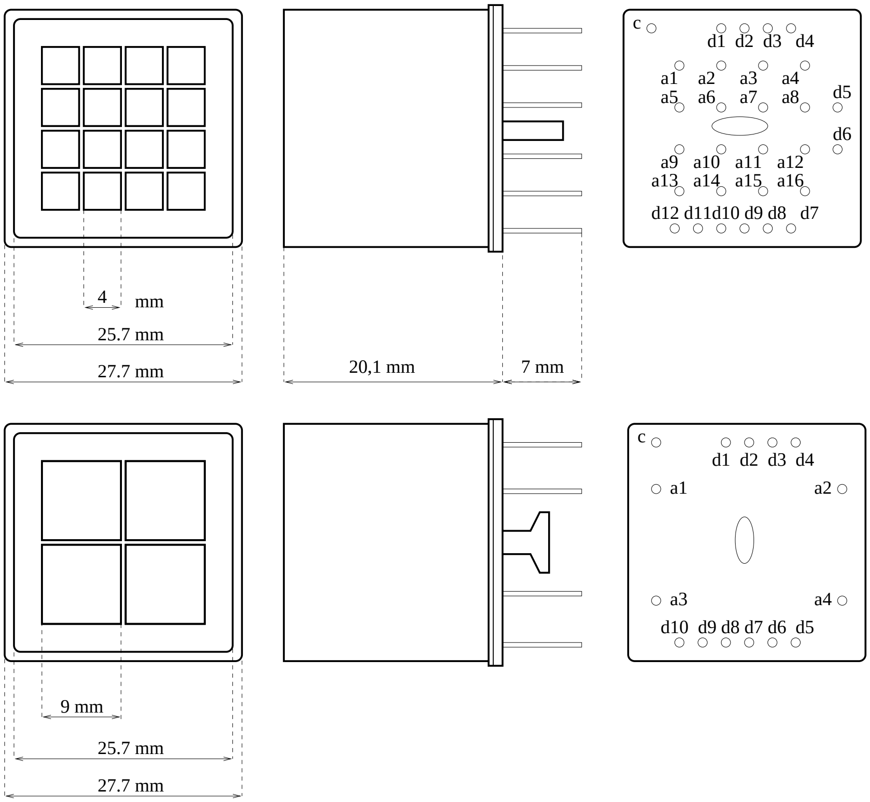

Figure 8.11: Photomultiplier tube R5900-00-M16 and R5900-00-M4 geometrical specifications [33].

Figure 8.12: Metal channel dynode system cross section with electron trajectory [33].

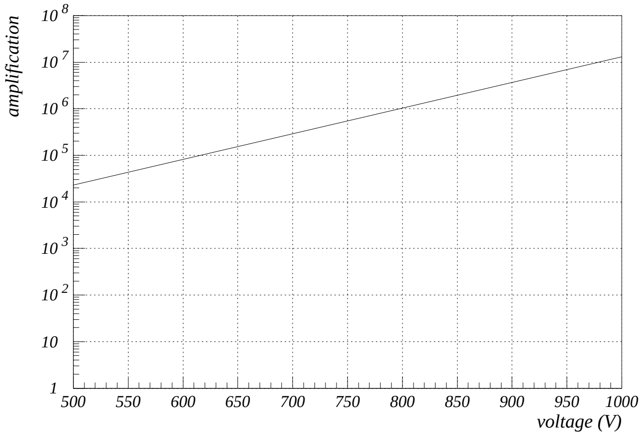

Figure 8.13: Amplification versus supply voltage for photomultiplier tube type R5900-00-M16 [33].

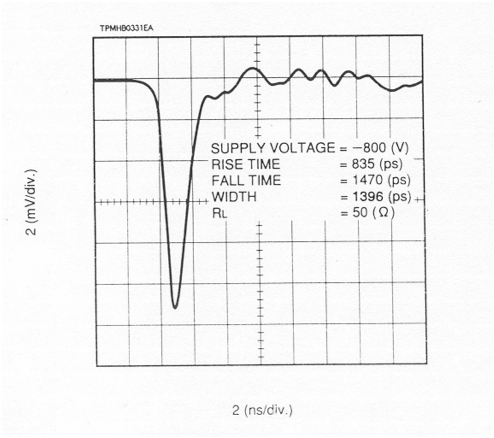

SUPPLY VOLTAGE = −800 (V)
RISE TIME = 835 (ps)
FALL TIME = 1470 (ps)
WIDTH = 1396 (ps)
R_L = 50 (Ω)

Figure 8.14: Typical time response for photomultiplier tube type R5900-00-M16 [33].

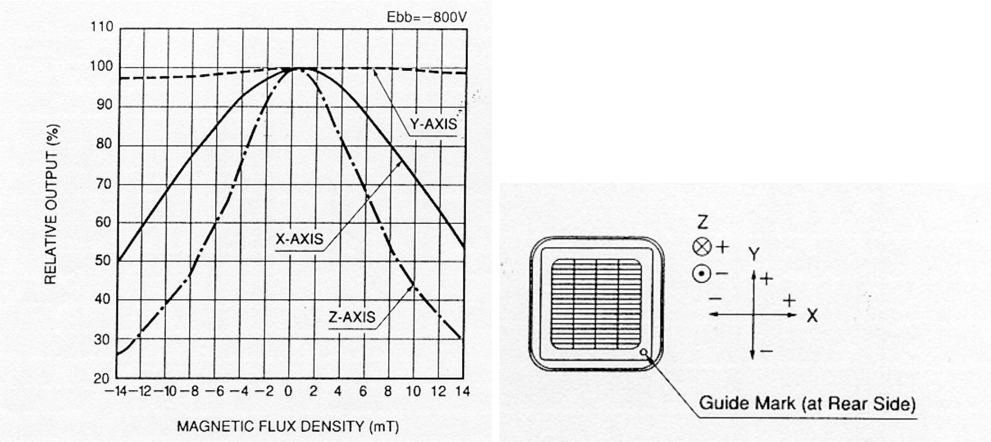

Figure 8.15: Typical effects of magnetic field on photomultiplier gain loss [33].

8.5 Appendix E: Front end electronics boards

The ASD8 chip is a bipolar integrated circuit that provides eight channels of amplifier, shaper and discriminator on a silicon substrate. It was designed for use in the straw based central tracking system of the SDC detector at the SSC. Requirements which ASD8 chip satisfies are short measurement time ($5\mathrm{ns}$), good double pulse resolution ($20\mathrm{ns}$), low power consumption ($18\mathrm{mW}/\mathrm{channel}$) and low operational threshold ($1\mathrm{fC}$). The preamplifier converts charge at the input into a voltage output minimazing the noise added to signal. The shaper eliminates the preamplifier tail utilising pole zero cancellation technique. The shaped signal is then coupled into a two stage timing discriminator. The ASD8 is designed to work with $3\mathrm{V} \pm 0.6\mathrm{V}$ positive and negative supplies [43]. Multi layer front end electronics board carries two ASD8 chips with 2×8 $\mathrm{channels}$. The analog and digital ground planes and five supply voltages are separated. A test pulse can be applied at the ten pin power connector. The positive input of an ASD8 amplifier is connected to a test pulse bus and the negative input is connected to the photomultiplier tubes outputs. Front end board schematic view is shown in Fig.8.16, while its electronics circuit design is presented in Fig.8.17

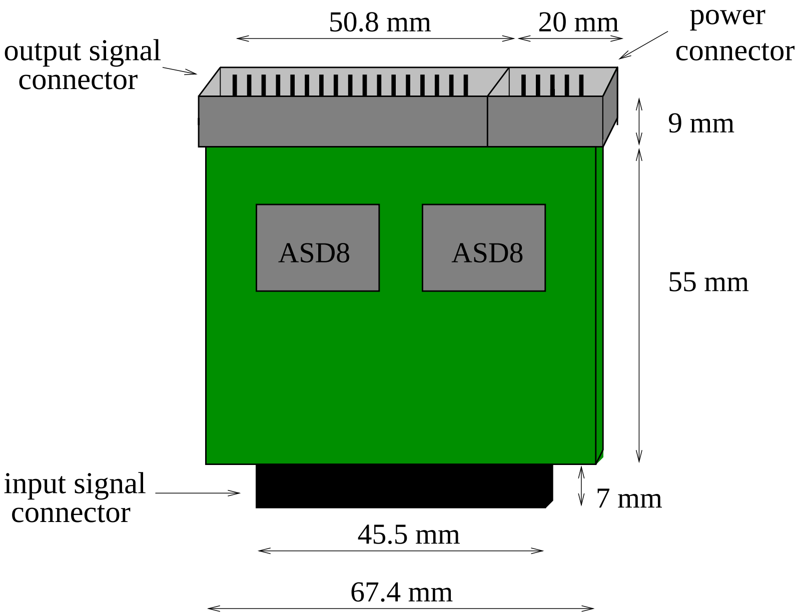

Figure 8.16: Front end electronics board schematic view.

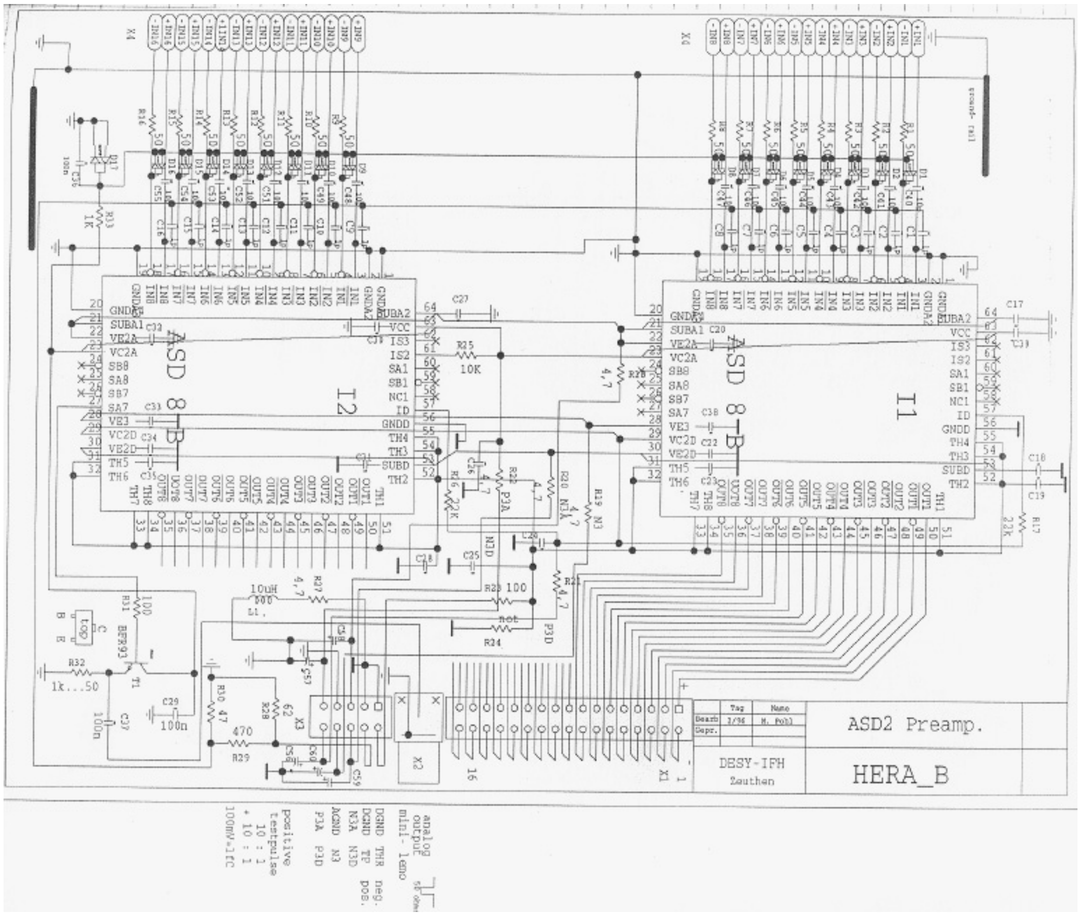

Figure 8.17: Electronics circuit design of front end electronics board.

The front end electronics boards were classified into 7 groups [44] according to the mean threshold value over all channels at which they respond to 50% of the 8 fC pulses (see Table 8.5).

supermodule/ cable holder	front end board sign	threshold value (mV)
1 and 12 /left	7	-1.15 to -1.21
1 and 12 /middle	1	-1.36 to -1.40
1 and 12 /right	2	-1.35 to -1.36
2 and 11 /left	6	-1.21 to -1.29
2 and 11 /middle	5	-1.29 to -1.31
2 and 11 /right	3	-1.33 to -1.35
3 and 10 /left	4	-1.31 to -1.33
3 and 10 /middle	4	-1.31 to -1.33
3 and 10 /right	4	-1.31 to -1.33
4 and 9 /left	3	-1.33 to -1.35
4 and 9 /middle	5	-1.29 to -1.31
4 and 9 /right	6	-1.21 to -1.29
5 and 8 /left	2	-1.35 to -1.36
5 and 8 /middle	1	-1.36 to -1.40
5 and 8 /right	7	-1.15 to -1.21

Table 8.3: Front end electronics boards are sorted according the threshold voltage value at which they respond to 50% of 8 fC pulses.

8.6 Appendix F: Baseboard electronics circuit designs

8.6.1 Baseboard for photomultiplier tube M16 base module

Photomultiplier tube baseboard contains four layers: photomultiplier tube layer, ground layer, high voltage layer and readout layer

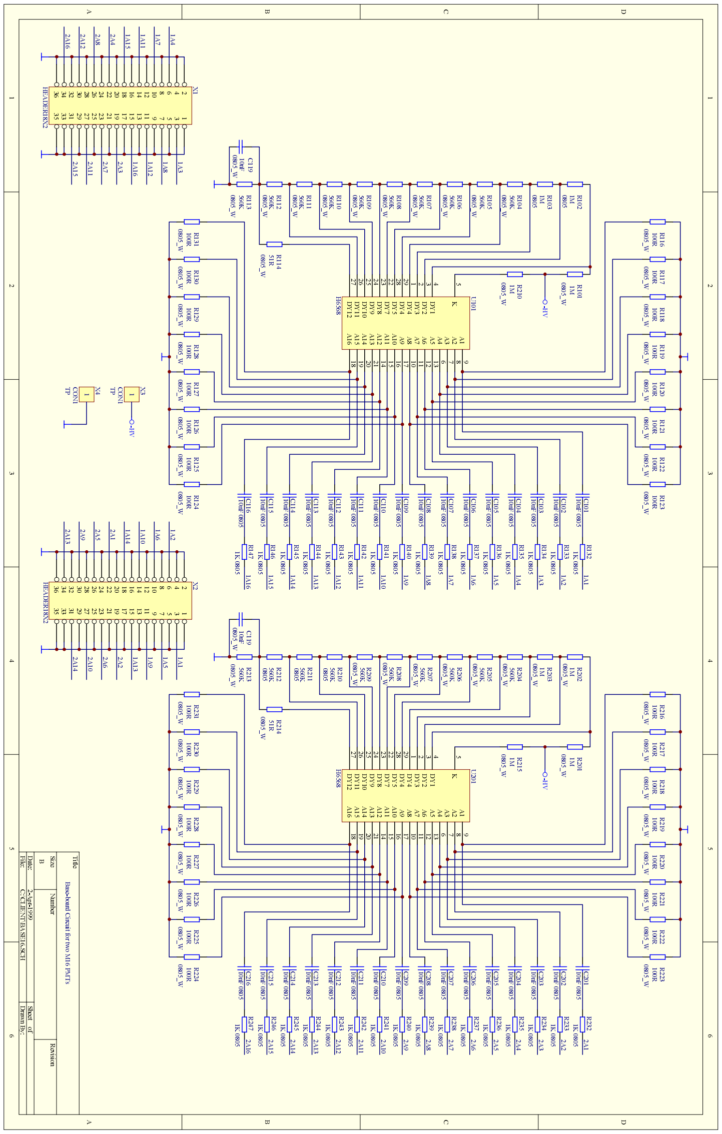

Figure 8.18: Baseboard electronics circuit. High voltage divider chain: 1MΩ for first two dynodes, 560kΩ for the rest and 10 nF over last stage. Anode outputs: 100Ω load to ground, 10 n F in series with 1kΩ for signal attenuation.

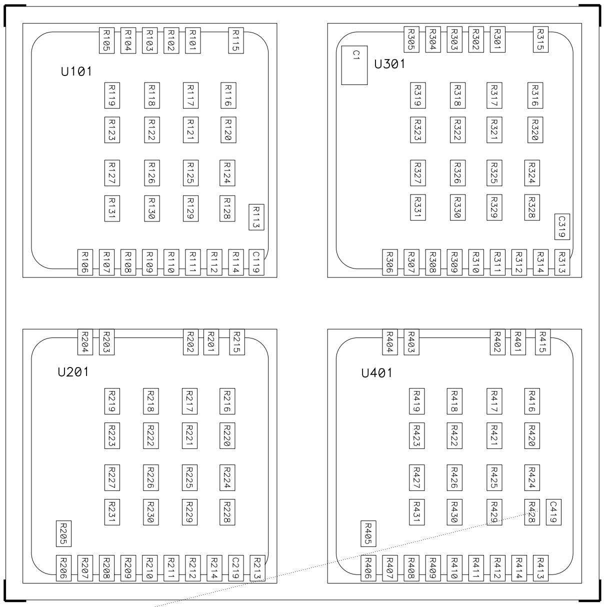

Figure 8.19: Baseboards photomultiplier tube side is equipped with high voltage divider chain and load resistors.

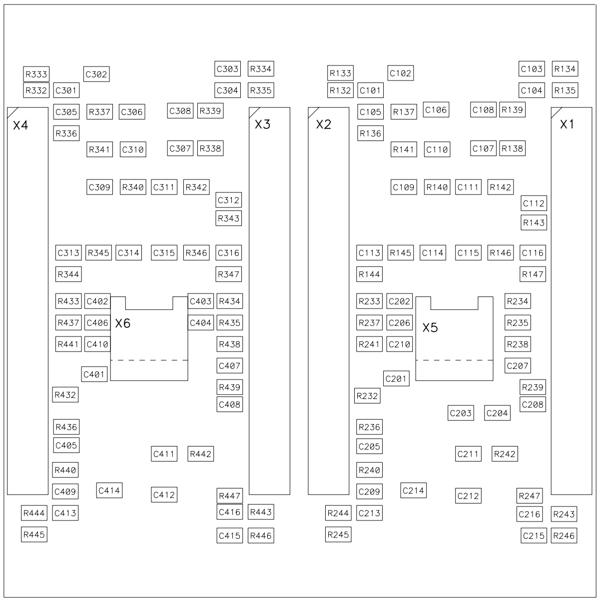

Figure 8.20: Baseboard signal side is equipped with four connectors for readout boards, signal splitters and two high voltage connectors.

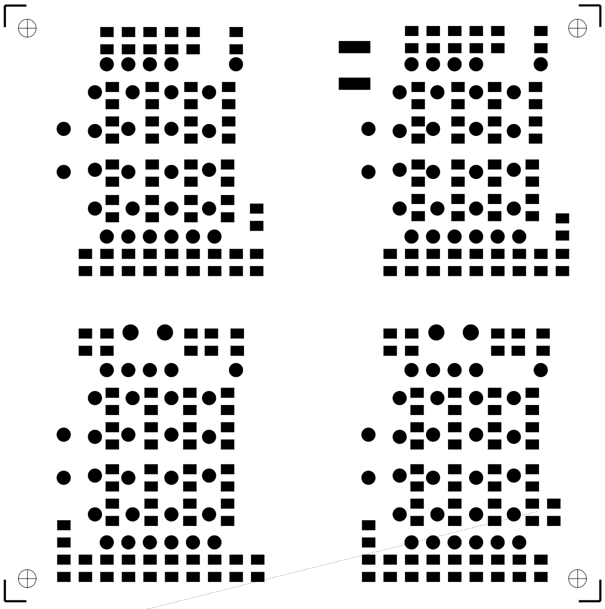

Figure 8.21: Baseboard photomultiplier tube side outer layer.

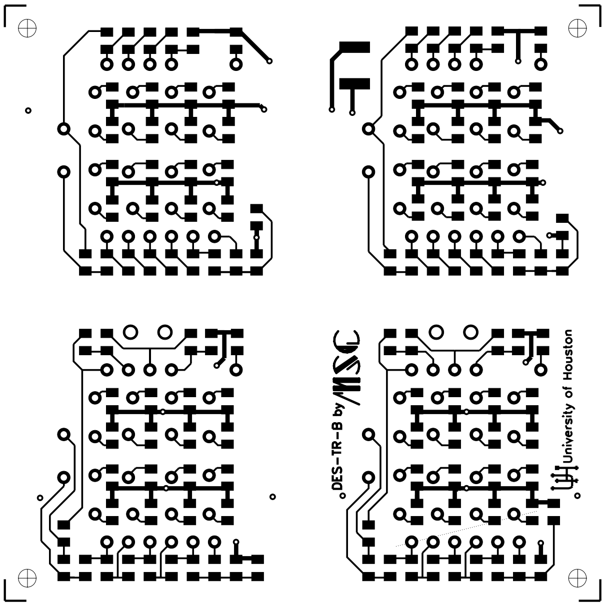

Figure 8.22: Baseboard photomultiplier tube side inner layer.

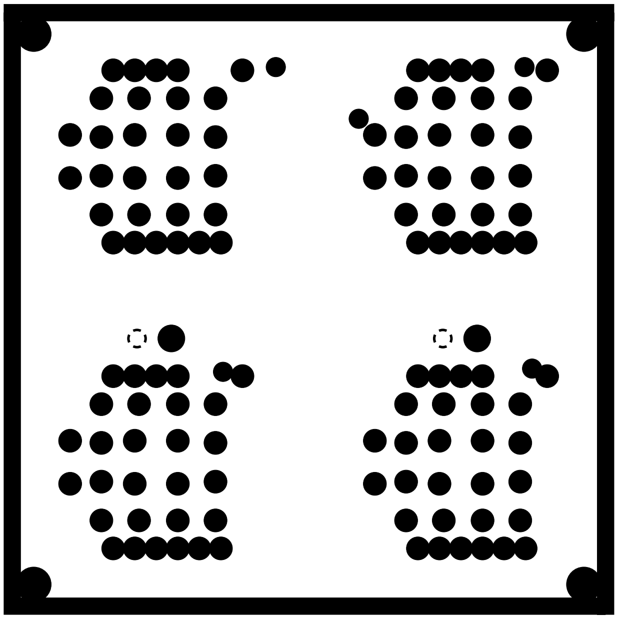

Figure 8.23: Baseboard ground layer.

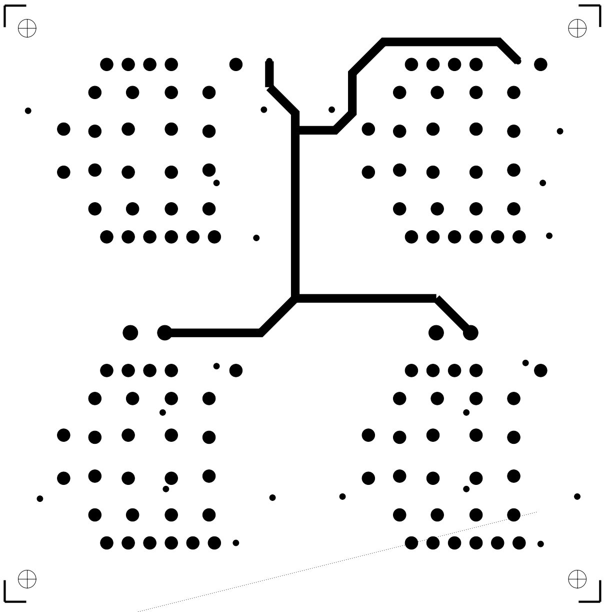

Figure 8.24: Baseboard high voltage distribution layer.

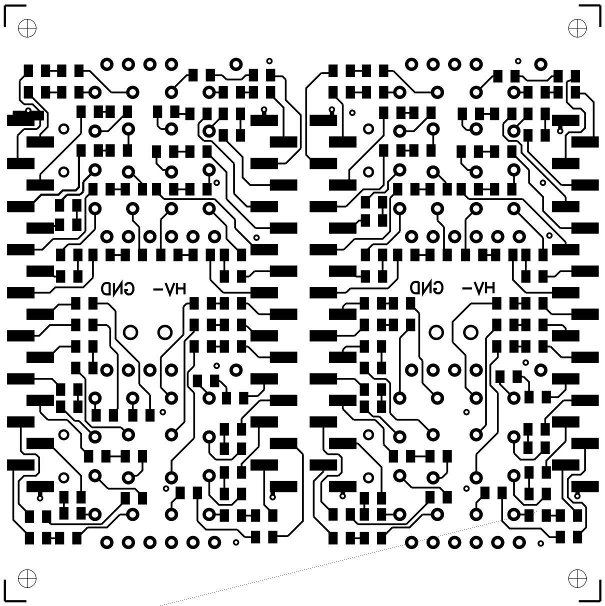

Figure 8.25: Baseboard readout inner layer

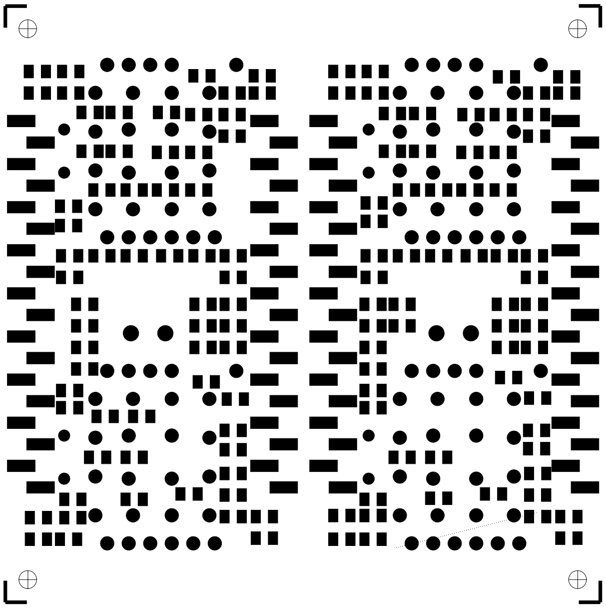

Figure 8.26: Baseboard readout side outer layer.

8.6.2 Baseboard for photomultiplier tube M4 base module

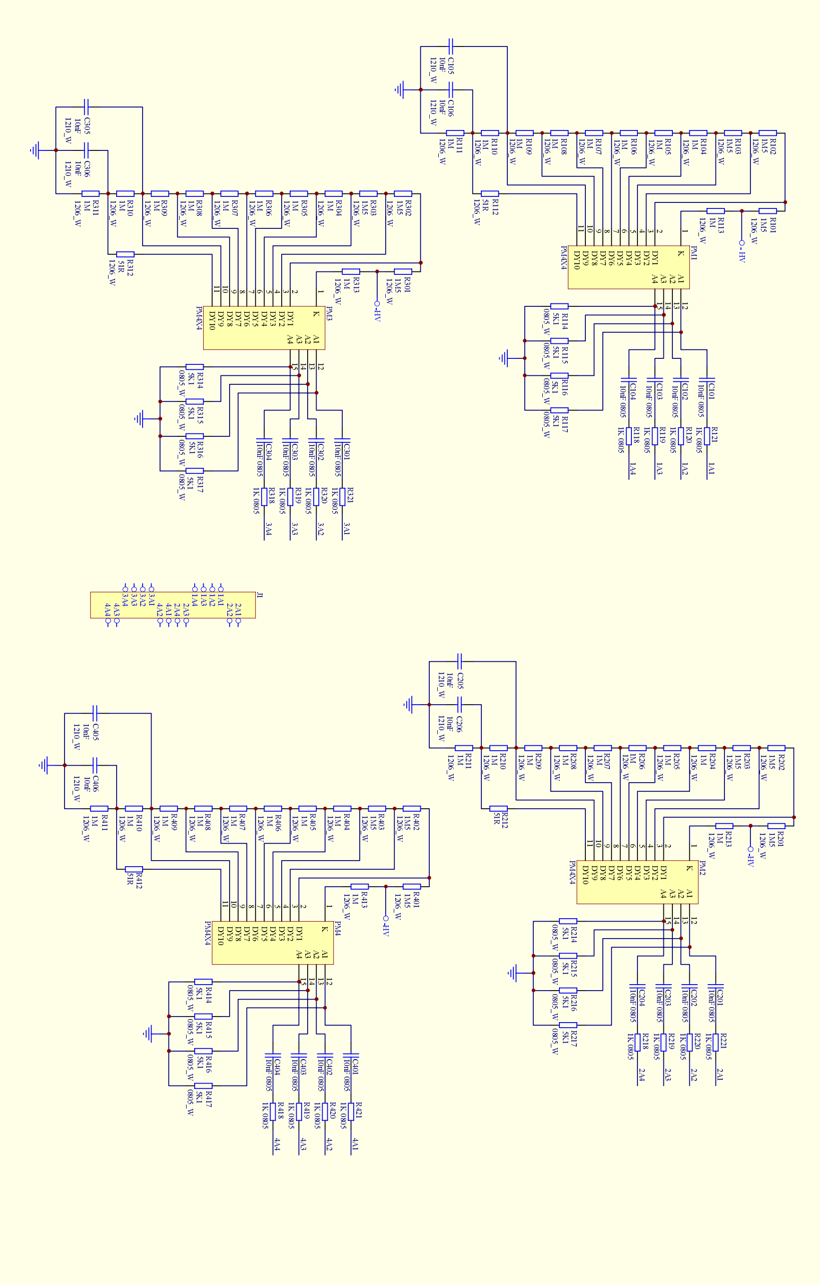

Figure 8.27: Baseboard electronics circuit. High voltage divider chain: 1.5MΩ for first two dynodes, 1MΩ for the rest and 10 nF over last two stages. Anode outputs: 510Ω load to ground, 10 n F in series with 1kΩ for signal attenuation.

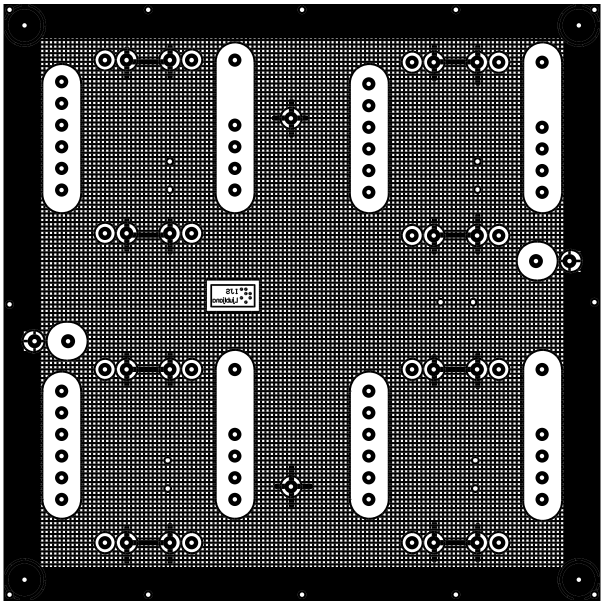

Figure 8.28: Baseboards photomultiplier tube side.

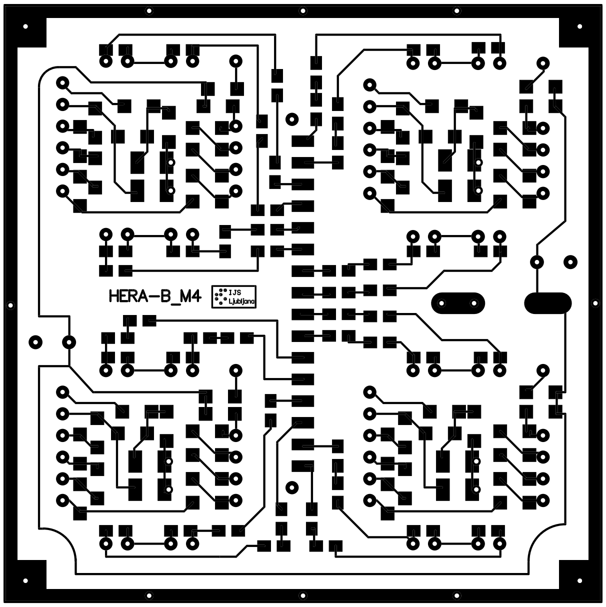

Figure 8.29: Baseboard signal side.

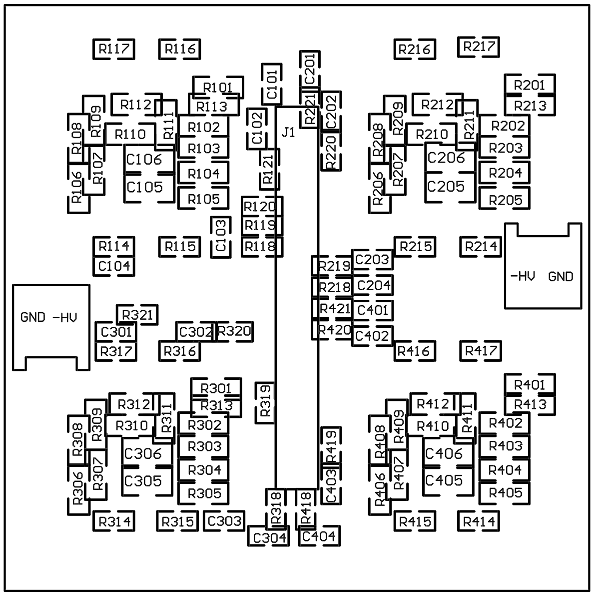

Figure 8.30: Baseboard signal side is equipped with one connector for readout board, two high voltage connectors, high voltage divider chain, signal splitters and load resistors.

8.7 Appendix G: Clamp and L shaped bracket design

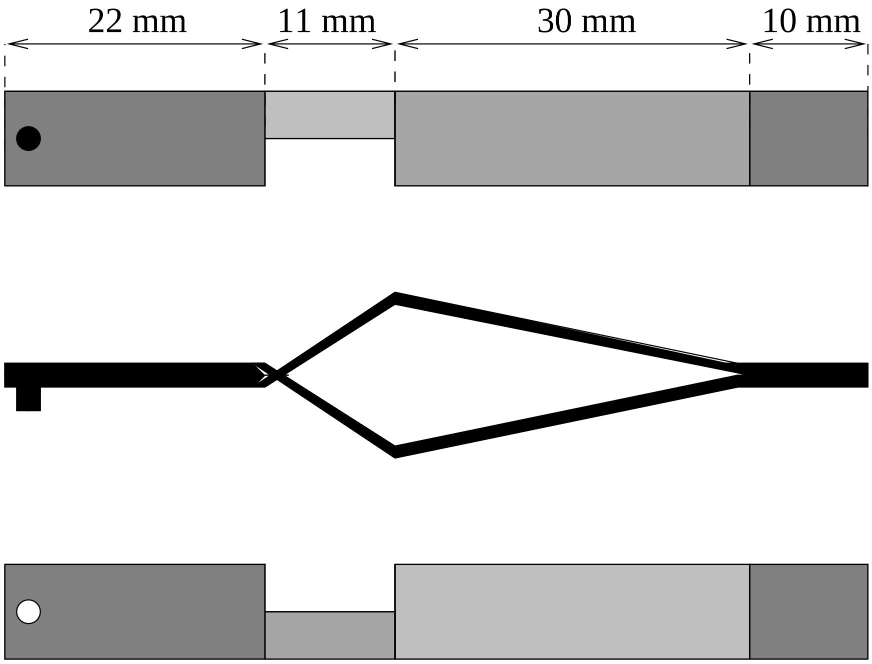

Figure 8.31: Clamp design. Clamps are used to fasten and align photomultiplier tube modules to the supermodule grid construction.

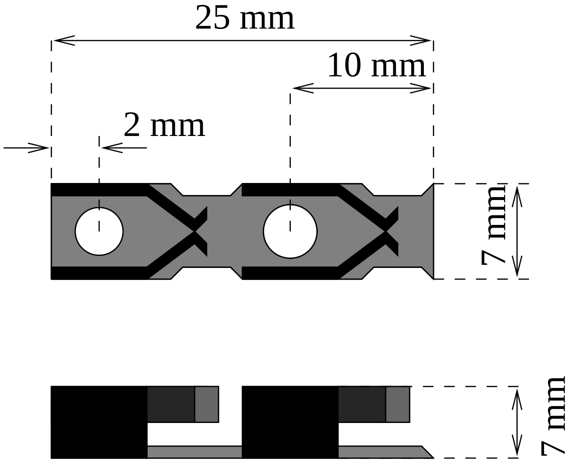

Figure 8.32: Nickel covered guide rail design. Spring rails are attached to bracket to provide electrically ground connection between baseboards and readout cards

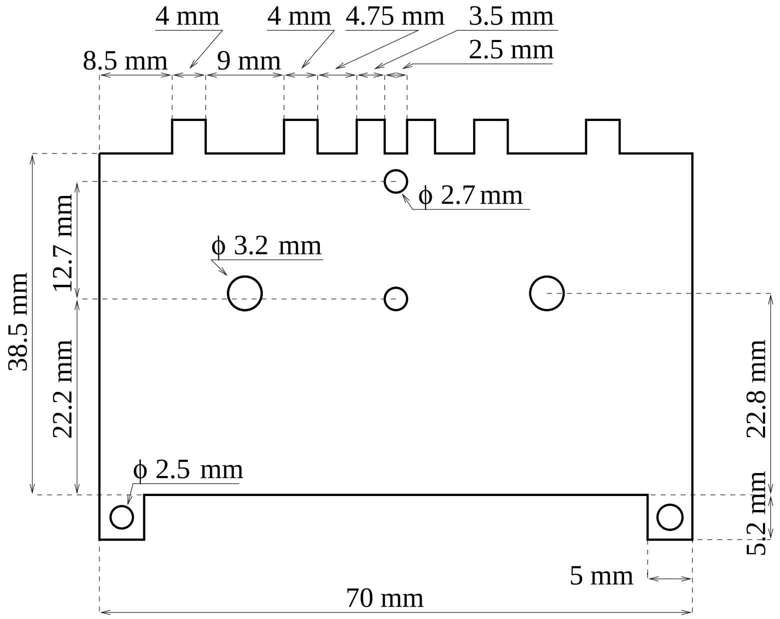

Figure 8.33: L shaped bracket design used in modules housing M4 type photomultiplier tubes. Brackets are made of 0.4 mm thick bronze plate covered by nickel.

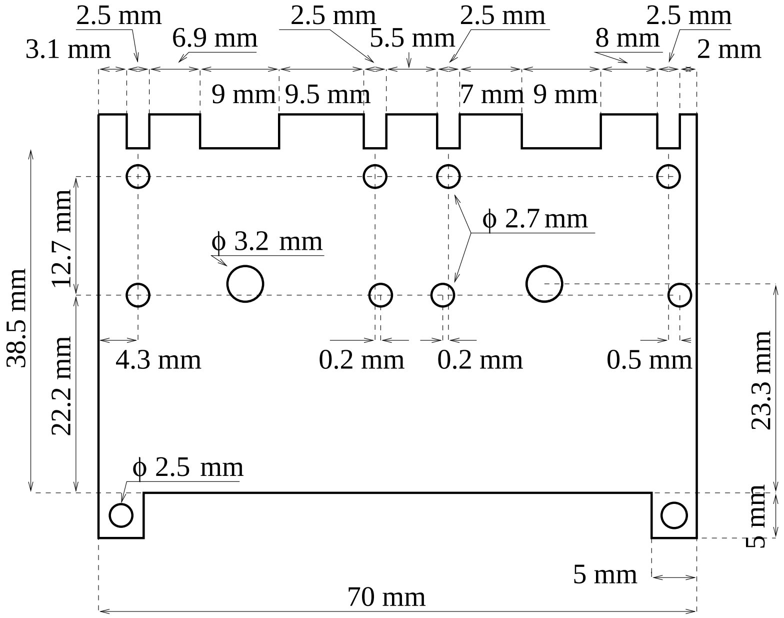

Figure 8.34: L shaped bracket design used in modules housing M16 type photomultiplier tubes. Brackets are made of 0.4 mm thick bronze plate covered by nickel.

8.8 Appendix H: Distribution boards

8.8.1 Distribution daughter board

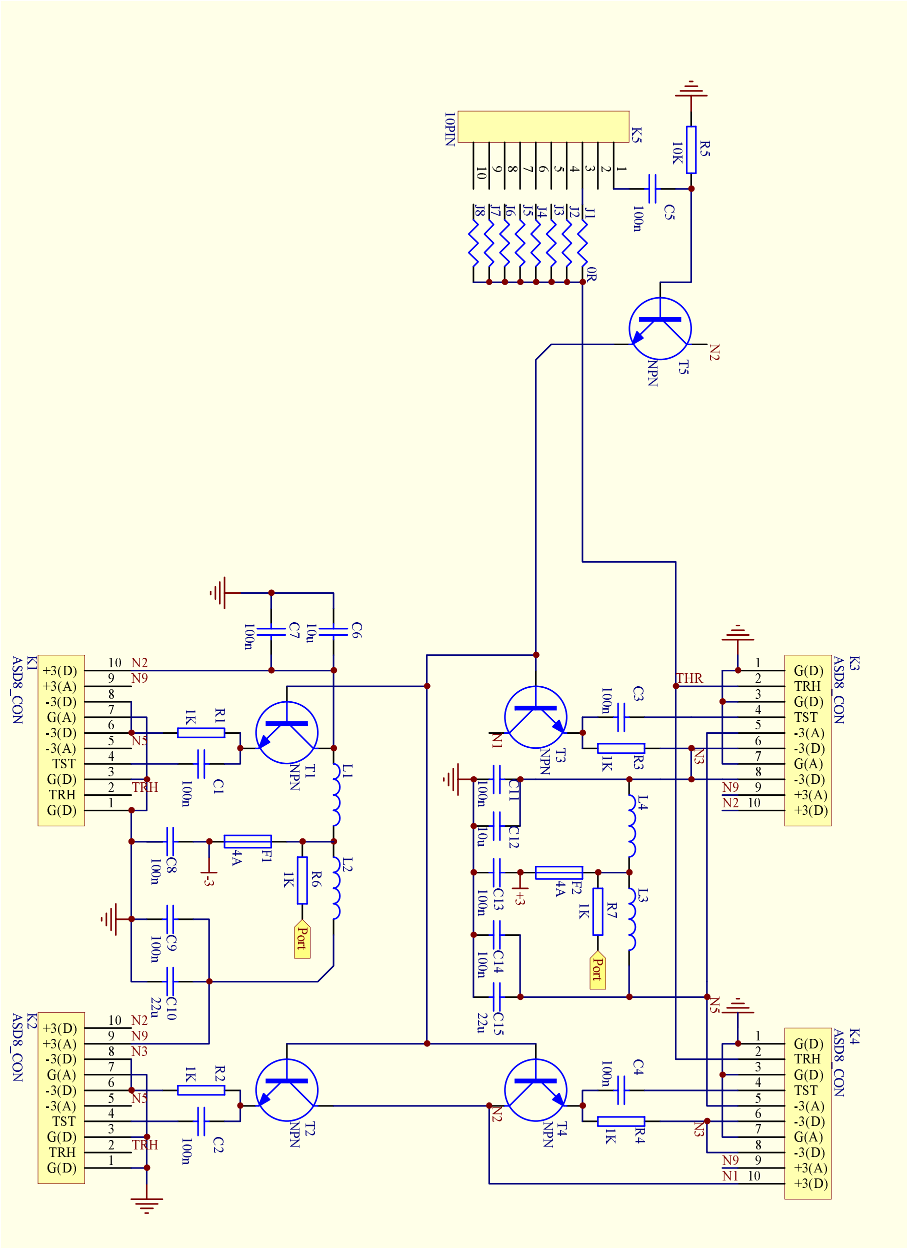

Figure 8.35: Distribution daughter board.

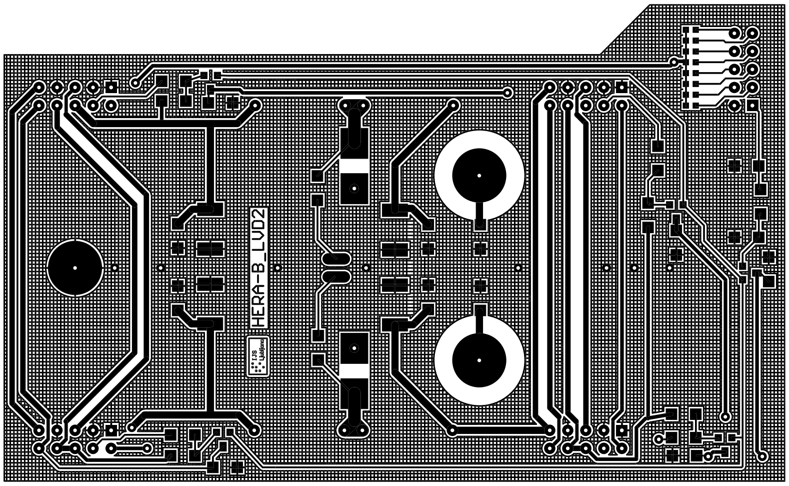

Figure 8.36: Printed circuit board, top layer.

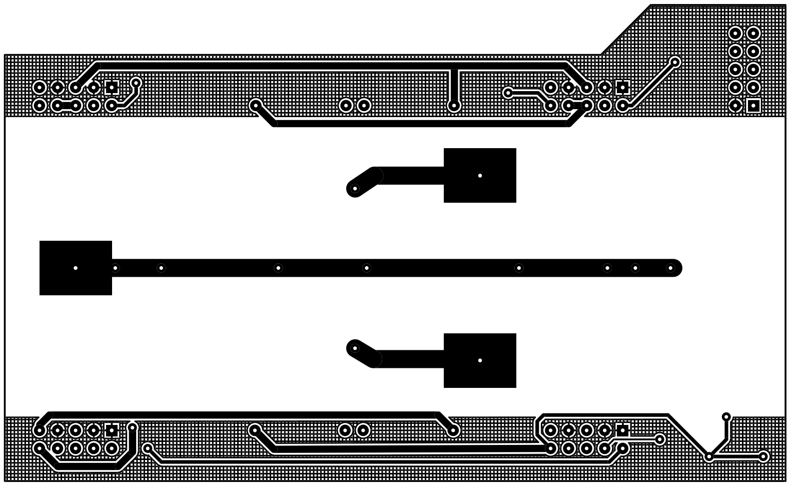

Figure 8.37: Printed circuit board, bottom layer.

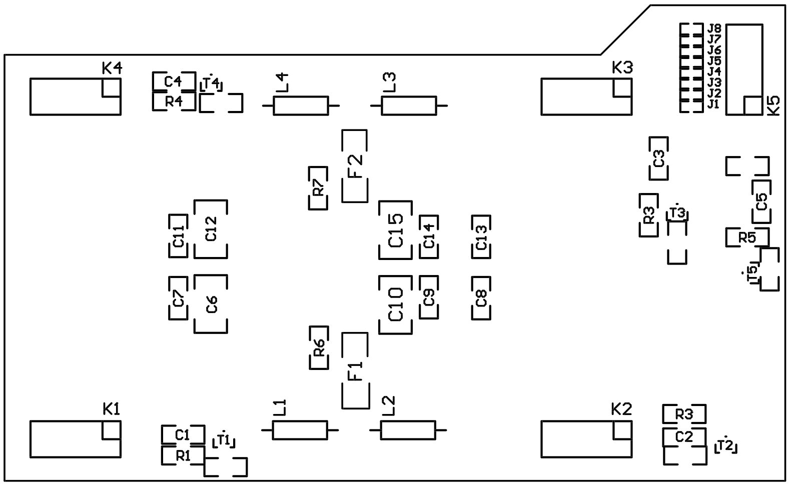

Figure 8.38: Electronics elements of the distribution daughter board.

8.8.2 Distribution mother board

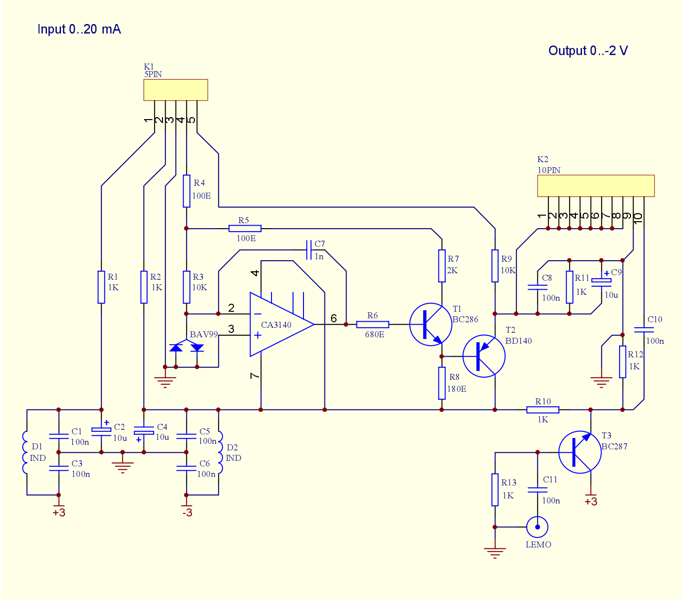

Figure 8.39: Distribution mother board.

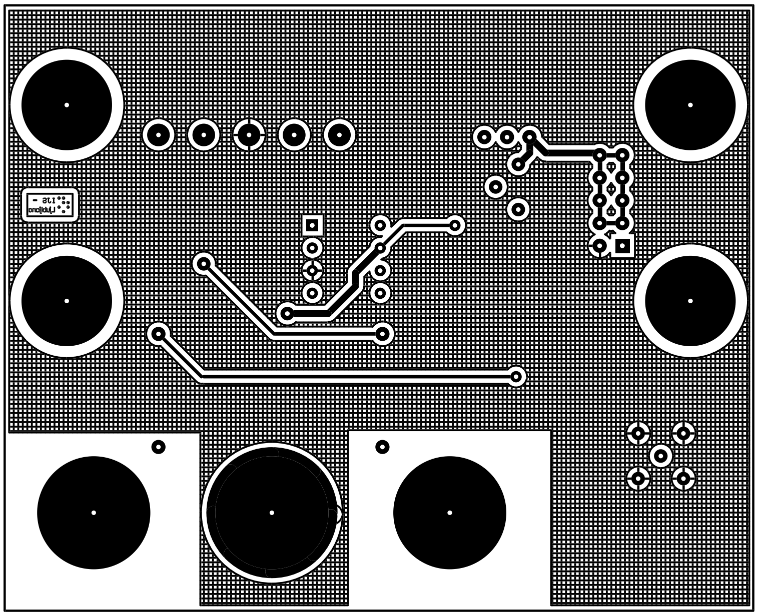

Figure 8.40: Printed circuit board, bottom layer.

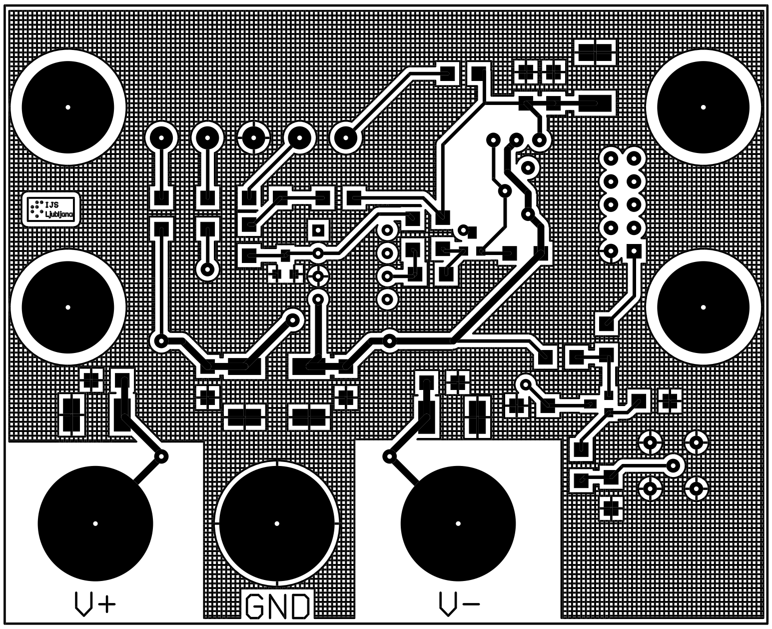

Figure 8.41: Printed circuit board, top layer.

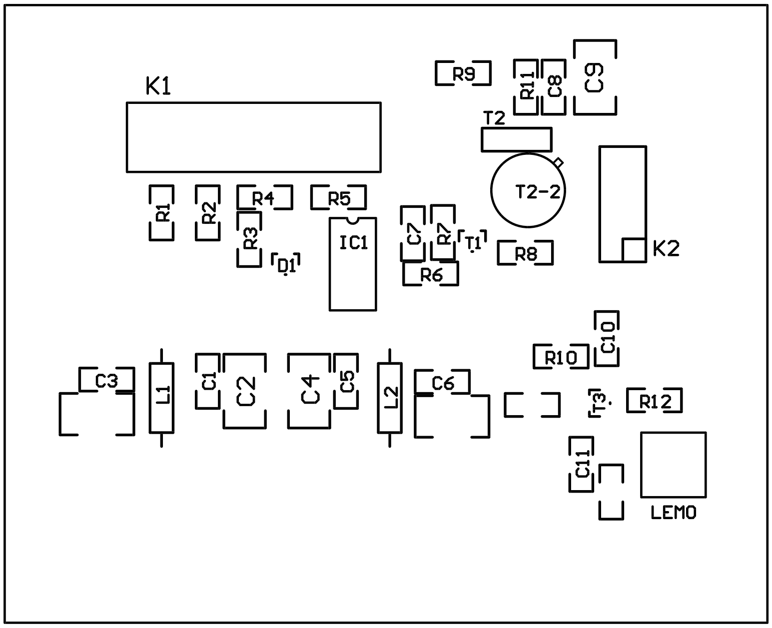

Figure 8.42: Electronics elements of the distribution mother board.

8.9 Appendix I: High voltage regions

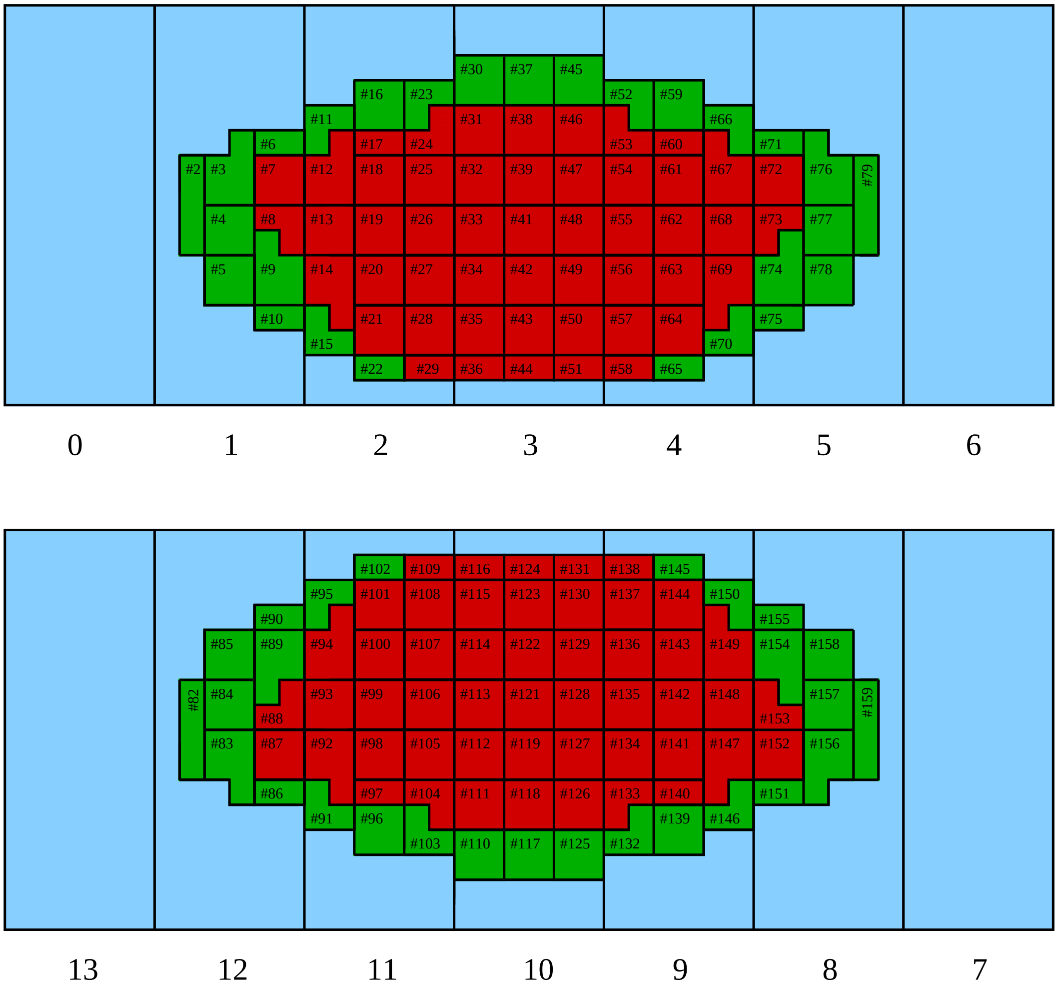

Figure 8.43: Photon detector planes division into 154 regions. Photomultiplier tubes belonging to one group are powered by the same high voltage.

area	voltage (V)	area	voltage (V)	area	voltage (V)	area	voltage (V)
# 1	spare	# 21	820	# 41	800	# 61	820
# 2	830	# 22	820	# 42	800	# 62	820
# 3	810	# 23	800	# 43	810	# 63	820
# 4	780	# 24	820	# 44	810	# 64	820
# 5	780	# 25	800	# 45	790	# 65	820
# 6	800	# 26	820	# 46	800	# 66	800
# 7	840	# 27	820	# 47	800	# 67	820
# 8	840	# 28	820	# 48	800	# 68	820
# 9	800	# 29	820	# 49	800	# 69	820
# 10	810	# 30	800	# 50	810	# 70	790
# 11	810	# 31	800	# 51	800	# 71	800
# 12	850	# 32	800	# 52	800	# 72	840
# 13	840	# 33	800	# 53	800	# 73	840
# 14	840	# 34	800	# 54	800	# 74	800
# 15	810	# 35	800	# 55	800	# 75	810
# 16	800	# 36	820	# 56	800	# 76	810
# 17	820	# 37	800	# 57	800	# 77	800
# 18	820	# 38	800	# 58	800	# 78	800
# 19	820	# 39	800	# 59	800	# 79	840
# 20	820	# 40	spare	# 60	820	# 80	spare
# 81	spare	# 101	850	# 121	780	# 141	850
# 82	840	# 102	800	# 122	800	# 142	850
# 83	780	# 103	800	# 123	800	# 143	850
# 84	760	# 104	800	# 124	800	# 144	850
# 85	800	# 105	840	# 125	800	# 145	820
# 86	770	# 106	830	# 126	800	# 146	760
# 87	850	# 107	840	# 127	800	# 147	870
# 88	825	# 108	820	# 128	820	# 148	870
# 89	800	# 109	840	# 129	800	# 149	870
# 90	820	# 110	775	# 130	800	# 150	820
# 91	800	# 111	800	# 131	800	# 151	775
# 92	875	# 112	800	# 132	800	# 152	840
# 93	850	# 113	800	# 133	850	# 153	890
# 94	850	# 114	800	# 134	850	# 154	780
# 95	820	# 115	800	# 135	850	# 155	800
# 96	750	# 116	780	# 136	820	# 156	800
# 97	860	# 117	800	# 137	820	# 157	800
# 98	850	# 118	800	# 138	850	# 158	800
# 99	850	# 119	800	# 139	840	# 159	775
# 100	840	# 120	spare	# 140	850	# 160	spare

Table 8.4: Optimal high voltage values of the photon detector regions.

Appendix J

8.10 Appendix J: Front end electronics analog output adapter

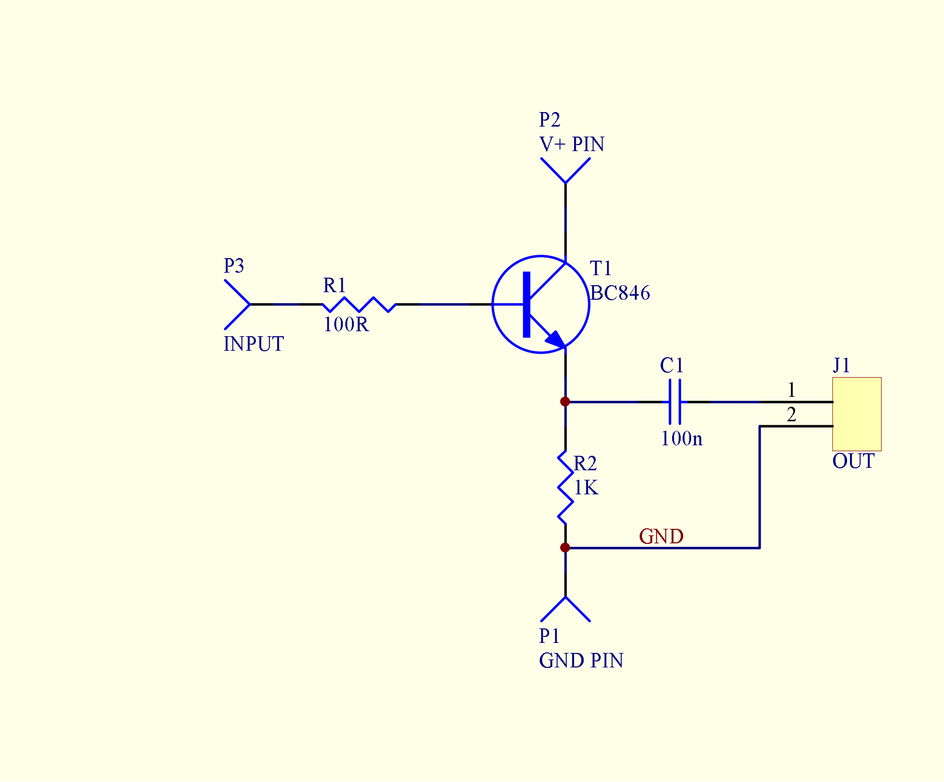

Figure 8.44: Front end electronics analog output adapter.

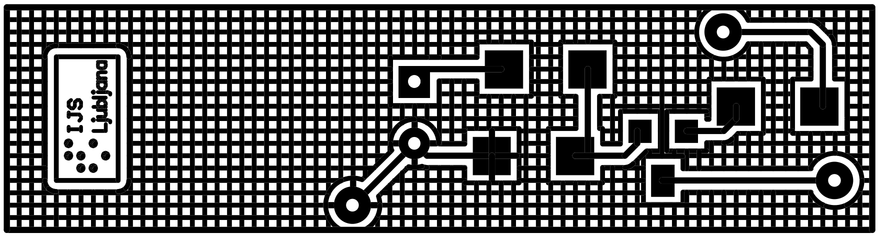

Figure 8.45: Top layer of the front end electronics analog output adapter printed circuit board.

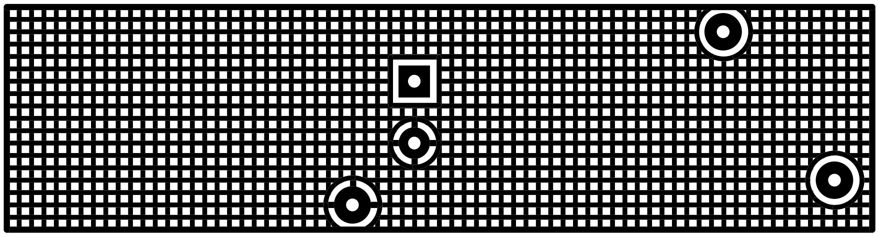

Figure 8.46: Bottom layer of the front end electronics analog output adapter printed circuit board.

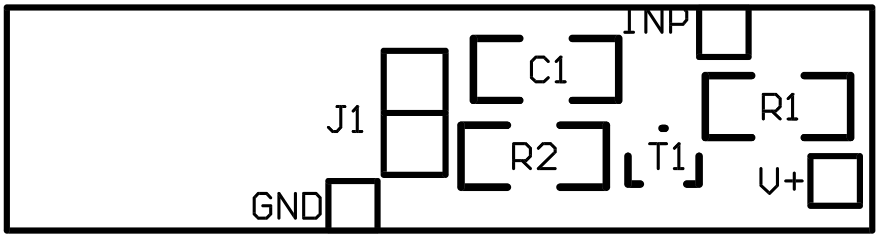

Figure 8.47: Elements of the front end electronics analog output adapter.

9

Povzetek doktorskega dela

9.1 Uvod

Tema doktorskega dela je povezana z gradnjo spektrometra HERA-B, ki ga mednarodna kolaboracija pripravlja v zahodni hali trkalnika HERA v raziskovalnem centru DESY v Hamburgu. Trkalnik HERA je namenjen trkom protonov z energijo 920 GeV z elektroni energije 30 GeV. Spektrometer HERA-B je postavljen v protonski obroč in uporablja žično tarčo na obrobju žarka protonov. Tako ne moti ostalih postavljenih eksperimentov, ki opazujejo trke med elektroni in protoni. Eksperiment je namenjen meritvi kršitve simetrije CP v sistemu nevtralnih mezonov B. Meril bo razpada B^0 in $\overline{\mathrm{B}}^0$ v J/Ψ in $\mathrm{K_s}^0$. Ta razpad pusti v spektrometru značilno sled, ki jo sestavljata par visoko energijskih leptonov z invariantno maso $\mathrm{m_{J/\Psi}}$ ter par nabitih pionov z invariantno maso $\mathrm{m_{K^0}}$ in premaknjenim mestom nastanka za tipično 1 m,

$$\mathrm{B^o}\ \text{ali}\ \overline{\mathrm{B}}^0 \to \mathrm{J}/\Psi\ \mathrm{K_s}^0 \to \ell^+\ell^-\pi^+\pi^-.$$

Pri tej vrsti razpadov mezona B v stanje z določeno parnostjo simetrije CP, teorija napoveduje zaznavno razliko med verjetnostima razpadov B^0 ali $\overline{\mathrm{B}}^0$, kar bi bil znak za kršitev simetrije CP. Omenjeni razpad je tako eksperimentalno in teoretično najprimernejši za opazovanje kršitve simetrije CP in zato je spektrometer HERA-B nanj optimiziran.

Za meritev so torej potrebni nevtralni mezoni B z znanim začetnim stanjem B^0 in $\overline{\mathrm{B}}^0$. Identifikacija nevtralnega mezona B sloni na meritvi para leptonov in pionov. Ker nastaneta kvarka b in $\overline{\mathrm{b}}$ v paru, lahko določimo začetno stanje nevtralnega mezona B, tako da določimo okus kvarka b v mezonu, ki je nastal skupaj z njim. To dosežemo z merjenjem naboja kaona kot razpadnega produkta spremljajočega mezona B. Zato te kaone imenujemo označevalne, ker določajo začetno stanje nevtralnega mezona B.

Iz ocenjenega preseka in razvejitvenega razmerja za te reakcije sledi, da želeni razpad mezonov B^0 nastopi na vsakih 10^{11} interakcij protona z jedri v tarči. Da bi lahko zaznali nekaj tisoč razpadov B^0 na leto, je potrebna interakcijska pogostost 40 MHz. Ker je časovni interval med zaporednimi prehodi gruč protonov 96 ns, potrebujemo pri prehodu gruče štiri interakcije.

Zaradi velike energije protonov leti večina produktov interakcije s tarčo v smeri protonov in pod majhnim kotom glede na smer žarka. Zato je spektrometer načrtovan tako, da pokriva $220\ \mathrm{mrad} \times 160\ \mathrm{mrad}$ prostorskega kota, kar zadošča za 90 % geometrijski izkoristek pri detekciji razpadnih produktov. Spektrometer je sestavljen iz večih detektorjev, ki jih lahko glede na njihovo naloge razdelimo v dva sistema. En sistem detektorjev skrbi za informacijo o sledeh delcev, drugi za njihovo identifikacijo. Sledilni sistem sestavljajo magnet, silicijevi pozicijsko občutljivi detektorji ter glavni sledilni sistem. Detektor prehodnega sevanja, detektor obročev Čerenkova, elektromagnetni kalorimeter in detektor mionov pa gradijo sistem za identifikacijo delcev. Shematski prikaz detektorja je predstavljen na sliki 9.1.

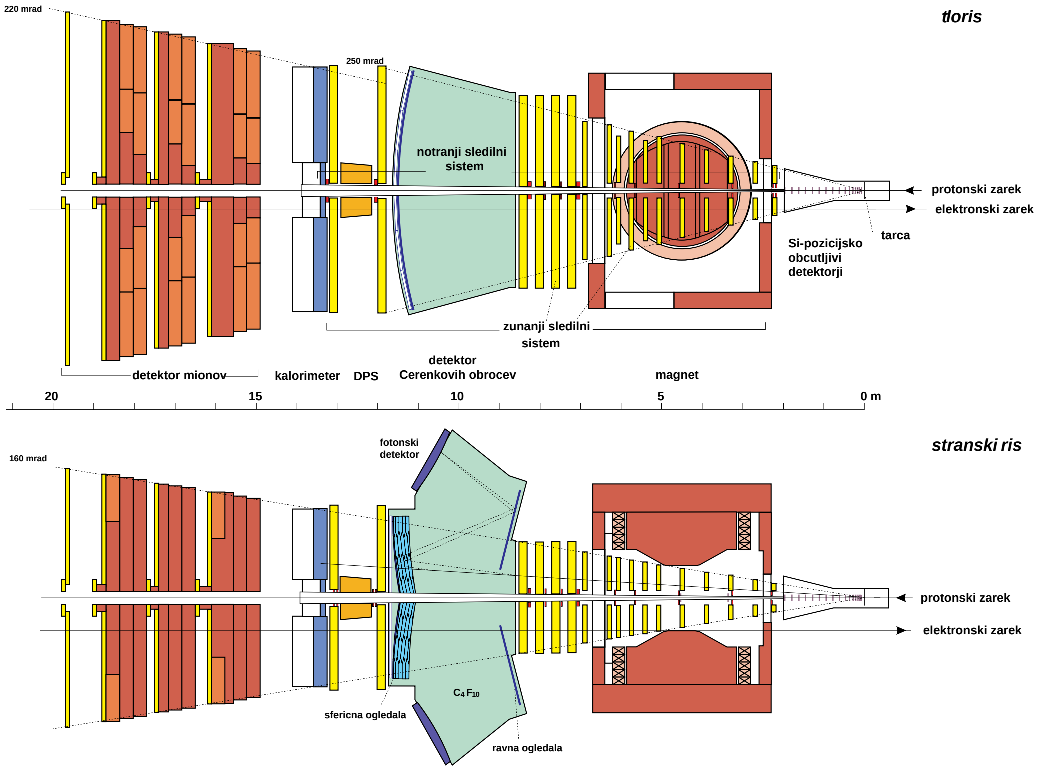

Slika 9.1: Prikaz vodoravnega in navpičnega vzdolžnega prereza detektorja HERA-B.

Detektor obročev Čerenkova (RICH Ring Imaging CHerenkov detector) je namenjen identifikaciji nabitega kaona, ki je nastal pri kaskadnem razpadu pridruženega mezona B. Pričujoče doktorskego delo obsega izdelavo in preizkus delovanja posameznih komponent detektorja obročev Čerenkova v elektronskem testnem žarku in na mestu, kjer je eksperiment HERA-B postavljen, ter umeritev celotnega detektorja v eksperimentalni dvorani.

9.2 Števec obročev Čerenkova

Nabiti delec, ki se giblje s hitrostjo βc v snovi z lomnim količnikom n, seva fotone Čerenkova, če je njegova hitrost večja od hitrosti svetlobe v snovi c/n. Polarni kot Čerenkova ϑ je

$$\cos\vartheta = \frac{1}{n(E)\beta}, \tag{9.1}$$

porazdelitev po azimutnem kotu φ pa je enakomerna med 0 and 2π.

Število fotonov, ki jih izseva delec na enoto energijskega intervala, podaja Frank Tammova enačba [15]:

$$\frac{dN}{dE} = \left(\frac{e_0^2}{4\pi\varepsilon_0\hbar^2c^2}\right)Z^2L\left[1-\left(\frac{1}{n(E)\beta}\right)^2\right]. \tag{9.2}$$

kjer je dN število fotonov z energijo med E in $E + dE$, L dolžina poti delca v snovi in Ze naboj delca.

Leta 1977 sta T. Ypsilantis in J. Seguinot predlagala izvedbo detektorja, ki za svoje delovanje izkorišča pojav Čerenkova. Delovanje detektorja ni omejeno le na identifikacijo delcev, ki letijo v določeni smeri, ampak pokriva velike prostorske kote in je tako uporaben tudi v spektrometrih. Glavni sestavni deli detektorja obročev Čerenkova so sevalec, optični sistem in fotonski detektor. Na poti skozi sevalec nabiti delci sevajo Čerenkove fotone. Optični sistem, sestavljen iz krogelnega in ravnega zrcala, usmeri svetlobo Čerenkova proti fotonskemu detektorju, ki je postavljen v goriščni ravnini zrcala. Naloga fotonskega detektorja je meritev mesta zadetka posameznega fotona Čerenkova in s tem določitev kota ϑ pod katerim je bil izsevan, z enačbo $\tan\vartheta = 2r/R$, kjer je r izmerjeni radij obroča Čerenkova, R pa radija sferičnega ogledala.

Ob določitvi gibalne količine delca iz ukrivljenosti tira v magnetnem polju, postane ločevanje v masi ekvivalentno ločevanju v hitrosti, kot je razvidno iz naslednje enačbe

$$p = \frac{m_0c\beta}{\sqrt{1-\beta^2}}. \tag{9.3}$$

Porazdelitev označevalnih kaonov, ki nam določajo tip razpadlega mezona B v opazovanem kanalu po gibalni količini pri poskusu HERA-B je prikazana na sliki 9.2. Porazdelitev je rezultat simulacijskega poskusa [1] in pove, da potrebujemo identifikacijo kaonov do gibalne količine 50 GeV/c, kar v tem primeru pomeni predvsem njihovo ločevanje od pionov. Pri visokih gibalnih količinah $pc \gg mc^2$ je razlika v hitrostih dveh delcev obratno sorazmerna s kvadratom gibalne količine

$$\Delta\beta \approx \frac{m_K^2c^2 - m_\pi^2c^2}{2p^2}. \tag{9.4}$$

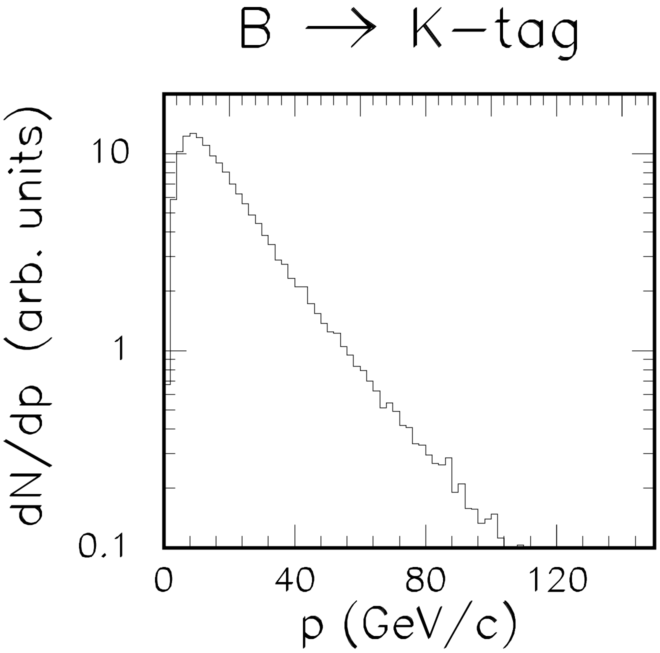

Slika 9.2: Porazdelitev označevalnih kaonov po njihovi gibalni količini pri eksperimentu HERA – B.

Razlika v hitrosti med pioni in kaoni pri gibalni količini 10 GeV/c je $\Delta\beta = 1.1 \times 10^{-3}$, pri 50 GeV/c pa $\Delta\beta = 4.5 \times 10^{-5}$.

Za mejno gibalno količino, pri kateri še ločimo pione od kaonov, izberemo vrednost, pri kateri se β pionov in kaonov razlikujeta za $3\sigma_\beta$. σ_β je natančnost pri meritvi hitrosti in je omejena z napako pri določitvi radija obroča Čerenkova in zaradi disperzije sevalca.

$$\frac{\sigma_\beta}{\beta} = \sqrt{\sum_{\mathrm{i}} \left(\sigma_\vartheta^{\mathrm{i}}\right)^2} \tan\vartheta, \tag{9.5}$$

K napaki meritve kota Čerenkova prispevajo nenatančnost optičnega sistema, napaka pri meritvi poti delca, večkratno sipanje delca v sevalcu ter predvsem napaka meritve kraja zadetka fotona na fotonskem detektorju

- krajevna ločljivost fotonskega detektorja, v primeru enakomerne porazdeljenosti zadetkov po osnovni detekcijski celici z osnovnim robom a je

$$\sigma_\vartheta{}^{\mathrm{det}} = \frac{\mathrm{a}}{\mathrm{f}\sqrt{12}}, \tag{9.6}$$

kjer je f goriščna razdalja krogelnega zrcala.

Ker energije fotonov ne merimo, ne moremo upoštevati znane disperzije v sevalcu in je zato

- napaka pri meritvi zaradi spreminjanja lomnega količnika

$$\sigma_{\vartheta}{}^{dis} = \frac{1}{n\sqrt{n^2\beta^2 - 1}}\frac{dn}{dE}\sigma_E \approx \frac{1}{\sqrt{2n-1}}\frac{dn}{dE}\sigma_E \tag{9.7}$$

  kjer je $\sigma_{\mathrm{E}} = \sqrt{< \mathrm{E}^2 > - < \mathrm{E} >^2}$ na področju občutljivosti fotonskega detektorja in sta v drugem delu uporabljena približka $(\mathrm{mc/p}) \ll 1$ in $(\mathrm{n} - 1) \ll 1$.

Napake, ki prispevajo k nenatančnosti meritve so za posamezne fotone istega delca neodvisne in je tako kvadrat napake obratno sorazmeren s številom zaznanih fotonov.

9.3 Lastnosti detektorja obročev Čerenkova pri poskusu HERA-B

Načrtovanje detektorja obročev Čerenkova so vodili naslednji kriteriji:

- Dolžina sevalca mora biti vsaj nekaj metrov, da lahko nabiti delci izsevajo dovolj fotonov (enačba 9.2).

- Fotonski detektor mora stati na mestu izven glavnega curka nabitih delcev. S tem se zmanjša pogostost sunkov in omogoči znižanje detekcijskega praga za zaznavanje posameznih fotonov Čerenkova.

- Površina fotonskega detektorja mora biti razdeljena na manjše osnovne detekcijske enote, kar omogoča meritev mesta zadetka fotonov.

- Goriščna razdalja krogelnih zrcal mora biti vsaj nekaj metrov, da dosežemo zahtevano ločljivost pri meritvi kota Čerenkova ob predpostavki, da je dolžina osnovne detekcijske celice $\leq$ $1\mathrm{cm}$ (enačba 9.6).

9.3.1 Izbira sevalca

Izbira sevalca pri poskusu HERA-B je zaradi zahteve po ločevanju pionov od kaonov z gibalnimi količinami med 5 GeV/c in 50 GeV/c omejena na pline z lomnim količnikom $\mathrm{n} - 1 \approx 10^{-3}$ [27]. Uporabljeni plinski sevalec, perfloro butan $\mathrm{C_4F_{10}}$ z lomnim količnikom n(3.3 eV) = 1.00133, ima nizko disperzijo, $\mathrm{dn/dE} = 3 \times 10^{-5}\mathrm{eV}^{-1}$. Prag za Čerenkovo sevanje je za pione pri gibalni količini 2.7 GeV/c in za kaone 9.6 GeV/c. Kot Čerenkova za delce z $\beta = 1$ je 51,5 mrad. Razlika v kotu Čerenkova med π in K je 34 mrad pri gibalni količini 10 GeV/c in se zmanjša na 0.9 mrad pri gibalni količini 50 GeV/c.

9.3.2 Pričakovano število zaznanih fotonov Čerenkova

Število zaznanih fotonov v obroču Čerenkova, za delec katerega pot skozi sevalec je dolga L je enako

$$\mathrm{N_{det}} = \int \mathrm{T_r(E)} \cdot \mathrm{R_m(E)} \cdot \epsilon_\mathrm{d}(\mathrm{E}) \cdot \frac{\mathrm{dN(E)}}{\mathrm{dE}}\,\mathrm{dE}, \tag{9.8}$$

kjer je $\mathrm{T_r(E)}$ prepustnost sevalca, $\mathrm{R_m(E)}$ odbojnost zrcal, $\epsilon_\mathrm{d}(\mathrm{E})$ izkoristek fotonskega detektorja za detekcijo fotonov in dN(E)/dE Frank Tammova enačba za število izsevanih fotonov na enoto energije (enačba 9.2).

Če pri izračunu števila zaznanih fotonov ne upoštevamo disperzije, enačbo 9.8 lahko zapišemo

$$\mathrm{N_{det}} = \mathrm{N_0 Z^2 L sin^2}\vartheta, \tag{9.9}$$

kjer je N_0 parameter odziva fotonskega detektorja

$$\mathrm{N_0} = \left(\frac{\mathrm{e_0^2}}{4\pi\varepsilon_0\hbar^2\mathrm{c}^2}\right)\int \mathrm{T_r(E)R_m(E)}\epsilon_\mathrm{d}(\mathrm{E})\,\mathrm{dE}, \tag{9.10}$$

konstanta pred integralom pa ima vrednost

$$\left(\frac{\mathrm{e_0^2}}{4\pi\varepsilon_0\hbar^2\mathrm{c}^2}\right) = 370\mathrm{cm^{-1}eV^{-1}}. \tag{9.11}$$

Z upoštevanjem podatkov za fotonski detektor števca obročev Čerenkova pri poskusu HERA-B

- $\mathrm{T_r}$ prepustnost sevalca (≈ 1) [26],
- $\mathrm{R_r}$ odbojnost zrcal(slika 9.3)
- ε_d učinkovitosti detekcije fotonskega detektorja
  - kvantni izkoristek fotopomnoževalk (slika 9.3),
  - prepustnost optičnega zbiralnega sistema (slika 9.3),
  - prepustnost okna iz pleksija (slika 9.3),
  - delež aktivne površine detektorja fotonov (≈ 0.9) in
  - zbiralni izkoristek za fotoelektrone in izkoristek elektronike (≈ 0.75) [33].

ocenimo parameter odziva $\mathrm{N_0} = 43\,\mathrm{cm^{-1}}$ ter pričakovano število zaznanih fotonov za delce z $\beta \approx 1$

$$N_{det} = N_0 L \mathrm{sin}^2\vartheta = 31.$$

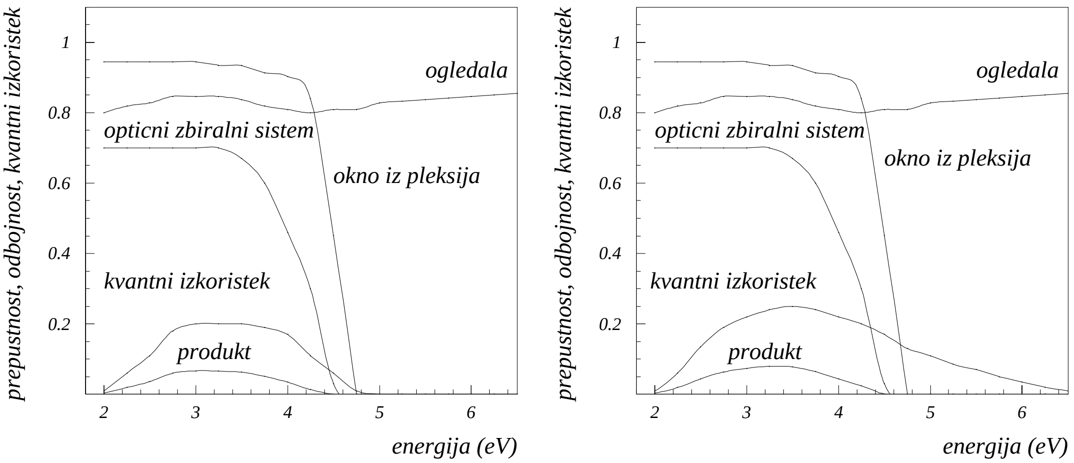

Slika 9.3: Odbojnost zrcal, prepustnost okna iz pleksija in optičnega zbiralnga sistema, in kvantni izkoristek fotopomnoževalk z borosilikatnim oknom (levo) in z oknom prepustnim za ultravijolične fotone (desno) v odvisnosti od energije fotonov. Za oba primera je predstavljen tudi produkt omenjenih prispevkov.

9.3.3 Pričakovana krajevna ločljivost detektorja obročev Čerenkova

K nenatančnosti meritve kota Čerenkova prispevajo:

- napaka pri meritvi kota Čerenkova zaradi disperzije v sevalcu, ki je enaka

$$\sigma_\vartheta{}^{\mathrm{dis}} \approx \frac{1}{\sqrt{2\mathrm{n}-1}}\frac{\mathrm{dn}}{\mathrm{dE}}\sigma_{\mathrm{E}} = 0.36\ \ \mathrm{mrad} \tag{9.12}$$

  kjer je $\sigma_{\mathrm{E}} = 0.57\ \mathrm{eV}$,(slika 9.3)

- napaka pri meritvi koordinate zadetka fotona na detektorju.

$$\sigma_\vartheta{}^{det,n} = 0.46\ \ \mathrm{mrad}\ \ \ \mathrm{in}\ \ \ \sigma_\vartheta{}^{det,z} = 0.92\ \ \mathrm{mrad} \tag{9.13}$$

  pri čemer je goriščna razdalja krogelnega ogledala 5.70 m in osnovna površinska enota detektorja fotonov $9\ \mathrm{mm} \times 9\ \mathrm{mm}$ na notranjem delu in $18\ \mathrm{mm}\times\ 18\ \mathrm{mm}$ na zunanjem delu fotonskega detektorja (slika 9.7),

- napaka zaradi večkratnega Coulombovega sipanja nabitega delca [17], ki znaša

$$\sigma_\vartheta{}^{\mathrm{msc}} = \frac{2}{3}\frac{\mathrm{E_o}}{\beta\mathrm{cp}}\sqrt{\frac{\mathrm{x}}{\mathrm{X_0}}}\left(1+\mathrm{k}\ln\left(\frac{\mathrm{x}}{\mathrm{X_0}}\right)\right) = 0.1\ \ \mathrm{mrad}, \tag{9.14}$$

  kjer je debelina plinskega sevalca $\mathrm{C_4F_{10}}$ x = 2.7 m, radiacijska dolžina $\mathrm{X_0} = 35\mathrm{m}$ [18], in $\mathrm{E_o}$ = 13.6 MeV, k = 0.038, ter je ocena narejena za gibalno količino p = 50 GeV/c,

- sferična aberacija zaradi nagnjenosti krogelnega zrcala za 9° glede na vpadni kot delcev prispeva [20]

$$\sigma_\vartheta{}^{\mathrm{sa}} = 0.16 \ \mathrm{mrad}, \tag{9.15}$$

- odstopanje zrcal od idealne oblike krogle oziroma ravine in nepravilne nastavitve položaja zrcal [1]

$$\sigma_\vartheta{}^{\mathrm{mi}} = 0.15 \ \mathrm{mrad \ in} \ \sigma_\vartheta{}^{\mathrm{al}} = 0.18 \ \mathrm{mrad}, \tag{9.16}$$

- napaka pri določitvi smeri sevajočega delca, kot jo določi sledilni sistem [1]

$$\sigma_\vartheta{}^{\mathrm{tr}} = 0.06 \ \mathrm{mrad}. \tag{9.17}$$

Našteti prispevki so med seboj neodvisni, zato je celotna napaka enaka korenu vsote kvadratov posameznih prispevkov. Ocena napake pri meritvi kota Čerenkova, določenega na osnovi posameznega zadetka za delce z visoko gibalno količino je torej

$$\sigma_\vartheta^{1,\mathrm{n}} = 0.65 \ \mathrm{mrad \ in} \ \sigma_\vartheta^{1,\mathrm{z}} = 1.02 \ \mathrm{mrad} \tag{9.18}$$

za obe zrnatosti fotonskega detktorja. Odgovarjujoči ločljivosti v β sta $\sigma_\beta{}^{1,\mathrm{n}} = 3 \times 10^{-5}$ in $\sigma_\beta{}^{1,\mathrm{z}} = 5 \times 10^{-5}$.

Ob predpostavki, da bo detektor zaznal 31 fotonov Čerenkova, pri delcih z $\beta \approx 1$ bo napaka pri meritvi hitrosti

$$\sigma_\beta{}^{N,n} = 6.1 \times 10^{-6} \ \mathrm{and} \ \sigma_\beta{}^{N,z} = 9.5 \times 10^{-6}. \tag{9.19}$$

Števec obročev Čerenkova bo tako na notranjem delu detektorja fotonov omogočal $3\sigma_\beta$ $\pi - \mathrm{K}$ ločevanje do gibalne količine 80 GeV/c, v primerih ko se obroči Čerenkova ne prekrivajo in lahko z gotovostjo pripišemo izmerjeno mesto zadetka fotona pravemu delcu. Računalniška simulacija dogajanja v detektorju pa pokaže [19], da predvidena ločljivost zadošča za ločevanje do gibalne količine 50 GeV/c.

9.4 Zgradba detektorja obročev Čerenkova pri poskusu HERA-B

Ogrodje detektorja obročev Čerenkova pri poskusu HERA-B tvori posoda za plinski sevalec, ki jo vodoravna ravnina v višini cevi protonskega žarka deli na zgornjo in spodnjo polovico. Shematski prikaz prereza detektorja je predstavljen na sliki 9.4. Zgornjo in spodnjo polovico detektorja pa sestavljajo

- krogelno zrcalo, ki usmeri fotone Čerenkova proti ravnemu ogledalu v smeri pod in nad osjo protonskega žarka,
- ravno zrcalo, ki usmeri svetlobo Čerenkova proti fotonskemu detektorju in
- krajevno občutljiv fotonski detektor sestavljen iz 2240 fotopomnoževalk z visoko učinkovitostjo detekcije in dobro ločljivostjo v dveh dimenzijah.

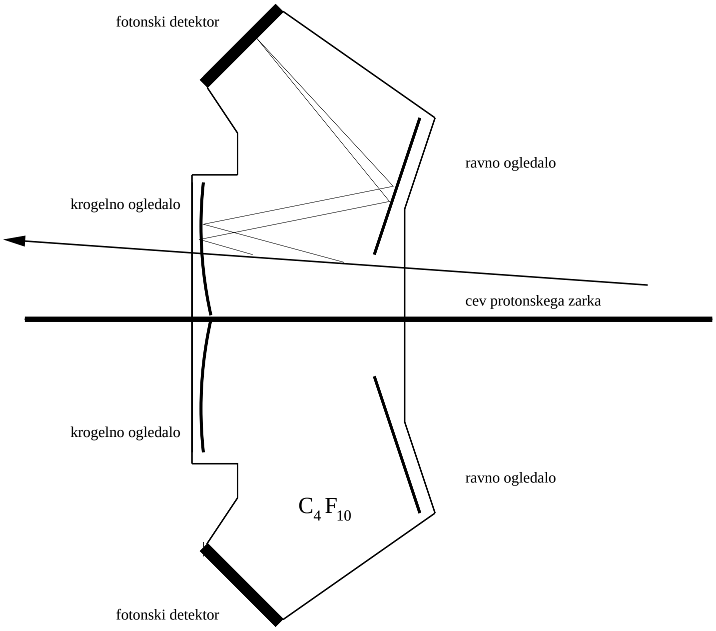

Slika 9.4: Prerez detektorja obročev Čerenkova.

9.4.1 Fotonski detektor

Aktivna površina fotonskega detektorja števca obročev Čerenkova pri poskusu HERA-B je približno $3\ \mathrm{m}^2$ in je razdeljena na manjše enote, ki so samostojni elektronski kanali in tako omogočajo enolično krajevno detekcijo istočasnih fotonov.

Na robu zgornjega in spodnjega vstopnega okna fotonskega detektorja je pritrjenih po sedem nosilcev z mrežno strukturo, imenovanih tudi supermoduli. Njihova konstrukcija nudi podporo osnovnim detekcijskim modulom in omogoča natančno razporeditev fotopomnoževalk ter poskrbi, da je cel sistem, skupaj z elektroniko učinkovito oklopljen proti zunanjim motnjam. Struktura posameznega supermodula lahko sprejme 384 fotopomnoževalk, razporejenih v 32 vrst in 12 stolpcev.

Pri opremi fotonskega detektorja s fotopomnoževalkami smo si pomagali z računalniško Monte Carlo simulacijo zastopanosti zadetkov po njegovi površini. Tako so na predelih, kjer simulacija napoveduje prekrivanje zadetkov, ki pripadajo različnim obročem Čerenkova, nameščene fotomomnoževalke z manjšo zrnatostjo in sicer šestnajstkanalne fotopomnoževalke Hamamatsu R9500-M16 s površino zrna $4.5 \times 4.5\ \mathrm{mm}^2$, na ostali površini pa štirikanalne fotopomnoževalke Hamamatsu R5900-M4 s površino zrna $9 \times 9\ \mathrm{mm}^2$. Aktivno površino fotonskega detektorja tako pokriva 1488 šestnajstkanalnih fotopomnoževalk in 752 štirikanalnih fotopomnoževalk.

Omejen proračun, namenjen opremi fotonskega detektorja, ni dopuščal nakupa fotopomnoževalk za celotno površino. Tako skrajna supermodula, kot tudi predeli supermodulov, ki pokrivajo področja za katere simulacija pove, da je tam zastopanost dogod-

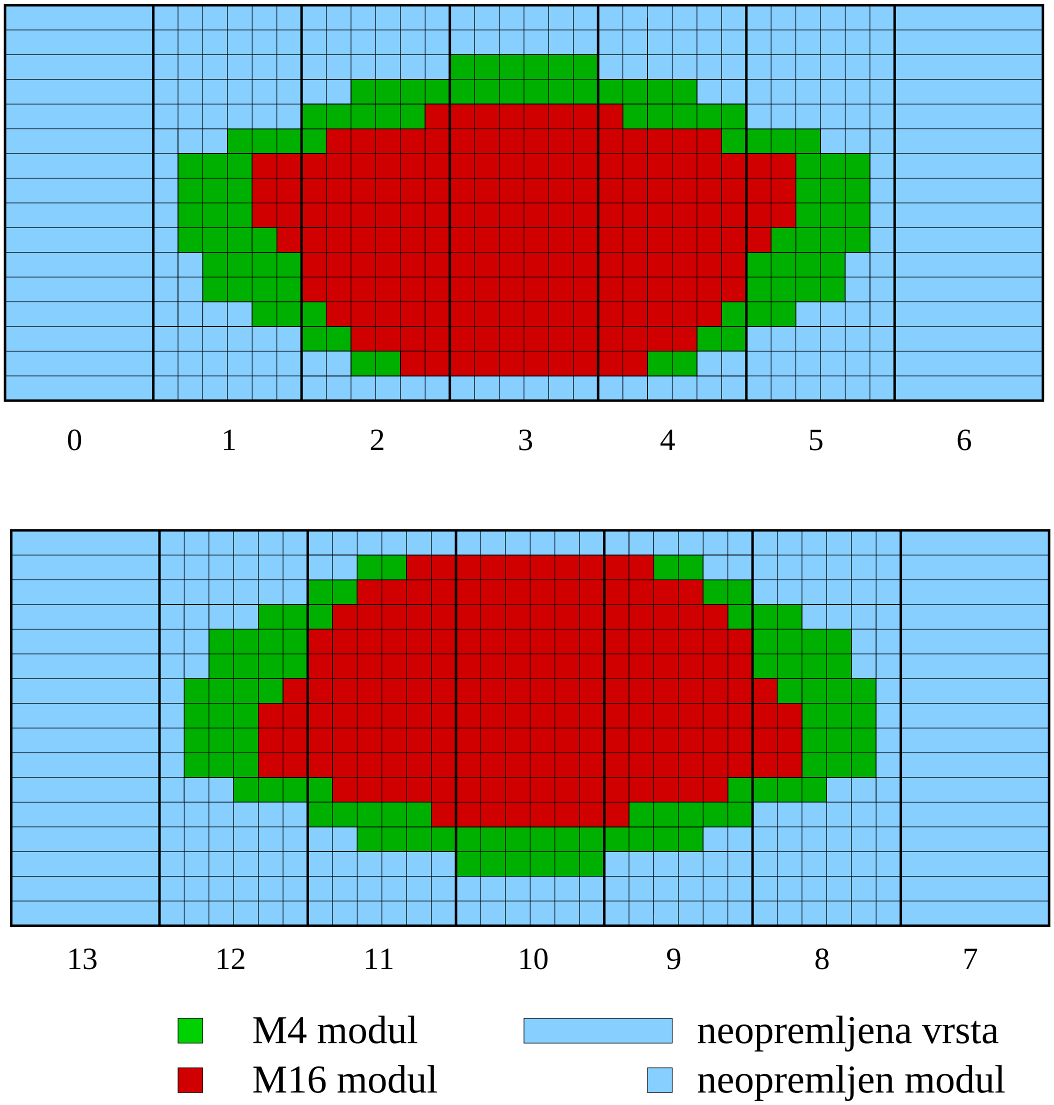

Slika 9.5: Površina fotonskega detektorja. Aktivni del pokrivajo štiri in šestnajstkanalne fotopomnoževalke.

kov manjša, niso opremljeni s fotonskimi detektorji. Ker pa je na delih detektorja, kjer je zastopanost dogodkov manjša, identifikacija obročev možna že na osnovi delno zaznanega obroča, je aktivna površina izbrana tako, da je spre jem nost detektorja čim manj okrnjena. Razporeditev aktivne in neaktivne površine fotonskega detektorja je prikazana na sliki 9.5.

Osnovni modul fotonskega detektorja sestavlja bazna tiskanina s štirimi fotopomnoževalkami in tiskaninami za elektronsko obdelavo signala. Bazna tiskanina nosi uporovno verigo fotopomnoževalkinih baz ter omogoča razpeljavo visokonapetostnega napajanja. Hkrati s signalnimi linijami povezuje izhodne enote fotopomnoževalk z elektronskimi kanali. Zaradi uporabe dveh različnih tipov fotopomnoževalk sta uporabljena dva osnovna modula fotonskega detektorja, ki sta predstavljena na sliki 9.6.

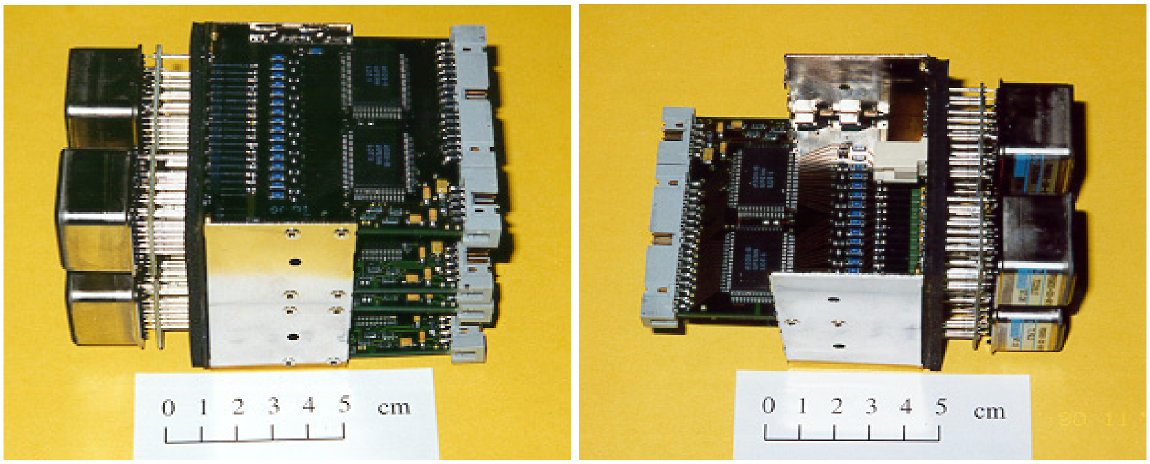

Slika 9.6: Osnovna modula fotonskega detektorja sestavljena iz štirih 16 kanalnih (levo) in štirih 4 kanalnih fotopomnoževalk

Ker aktivna površina fotopomnoževalk pokriva le $23\ \%$ površine fotonskega detektoja, je na ogrodje supermodula pritrjen optični zbiralni sistem sestavljen iz dveh konveksnih leč. Optika prilagodi zrnatost v goriščni ravnini zrnatosti fotopomnoževalk in obenem štirikrat poveča aktivno površino fotonskega detektorja. Ker optični sistem prepusti v povprečju 65% fotonov Čerenkova, se z njegovo uporabo poveča število zaznanih fotonov Čerenkova 2.8 krat . Shematski prikaz optičnega zbiralnega sistem je predstavljen na sliki 9.7.

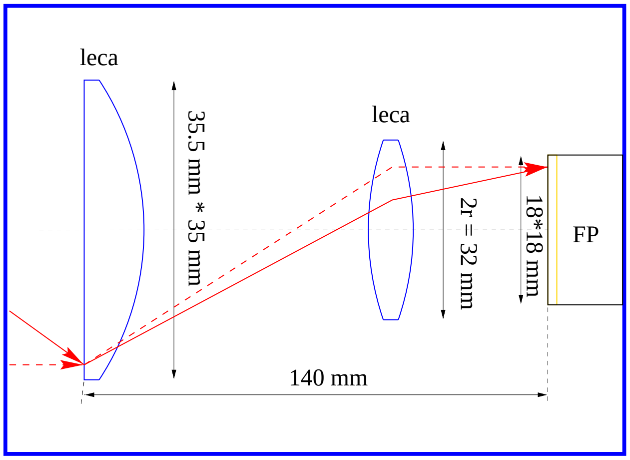

Slika 9.7: Optični zbiralni sistem sestavljen iz dveh konveksnih leč.

9.5 Testi v elektronskem žarku

V preskusnem žarku elektronov z energijo 3 GeV sem preizkusil delovanje prototipa, končne verzije supermodula detektorja fotonov. Glavni namen testiranj je bilo preverjanje delovanja posameznih komponent detektorja fotonov, ter meritev parametra odziva detektorja in ločljivosti pri meritvi radija Čerenkovega obroča.

Testni detektor obročev Čerenkova sestavlja 5 m dolga cev iz aluminija s premerom 80 cm, ki ga spredaj iz zadaj zapirata pokrova. Posoda je bila napolnjena z mešanico perfloro butana (37%) in zraka (63 %). Oba pokrova sta opremljena z večžičnima proporcionalnima komorama, ki merita poti elektronov. Na notranji strani zadnjega pokrova je pritrjeno krogelno ogledalo, ki usmeri fotone Čerenkova proti sprednjemu pokrovu, kjer sta dve kvarčni okni, mesti na katera lahko pritrdimo detektorje fotonov. Pri opisanem testiranju sem prototip detektorja fotonov namestil k spodnjemu eksperimetalnemu mestu, zgornje pa ni bilo v uporabi in je bilo zato pokrito. Površina okna omogoča preizkus delovanja 48 fotopomnoževalk z optičnim zbiralnim sistemom razporejenih v 8 vrst in 6 stolpcev. Zgornja polovica je bila opremljena s štirikanalnimi fotopomnoževalkami, spodnja pa s šestnajstkanalnimi fotopomnoěvalkami.

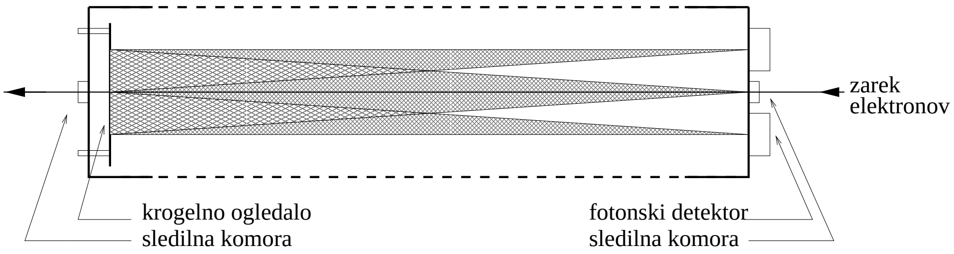

Slika 9.8: Shema testnega detektorja obročev Čerenkova. Elektroni na poti skozi sevalec sevajo fotone Čerenkova, ki jih krogelno zrcalo zbere na prototipu detektorja fotonov.

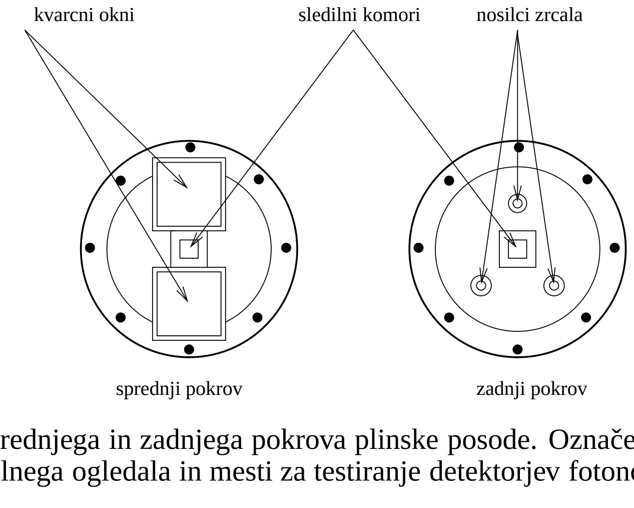

Slika 9.9: Shema sprednjega in zadnjega pokrova plinske posode. Označeni so položaji sledilnih komor, nosilci krogelnega ogledala in mesti za testiranje detektorjev fotonov.

Sistem za zajemanje podatkov je med meritvami shranjeval informacijo o smeri preleta elektronov ter mesta zadetkov fotonov na fotopomoževalkah. Na sliki 9.10 sta predstavljeni porazdelitvi zadetkov na detektorju fotonov, ko je Čerenkov obroč na mestu, ki ga pokrivajo štirikanalne fotopomnoževalke, brez in s premikom središča obroča v skupno točko z upoštevanjem popravkov iz sledilnega sistema. Na sliki 9.11 pa sta predstavljeni porazdelitvi zadetkov na detektorju fotonov, ki ga pokrivajo šestnajstkanalne fotopomnoževalke.

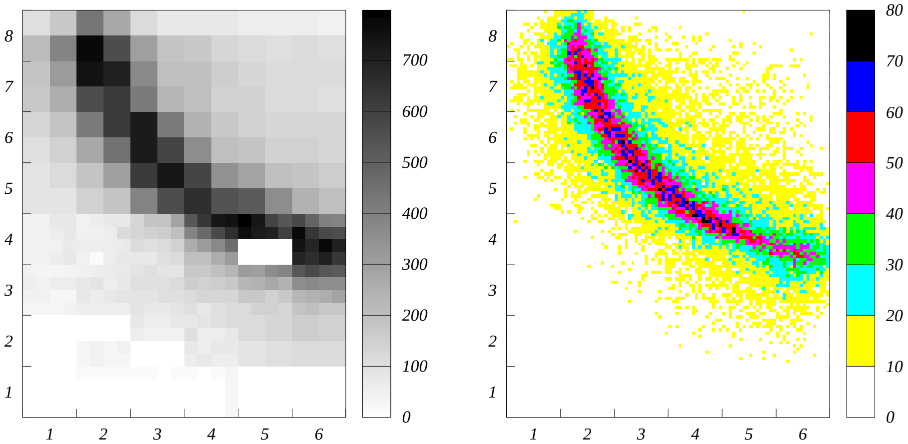

Slika 9.10: Porazdelitev zadetkov fotonov na detektorju fotonov, ki ga pokrivajo štirikanalne fotopomnoževalke (levo) in porazdelitev popravljena s podatki iz sledilnega sistema (desno).

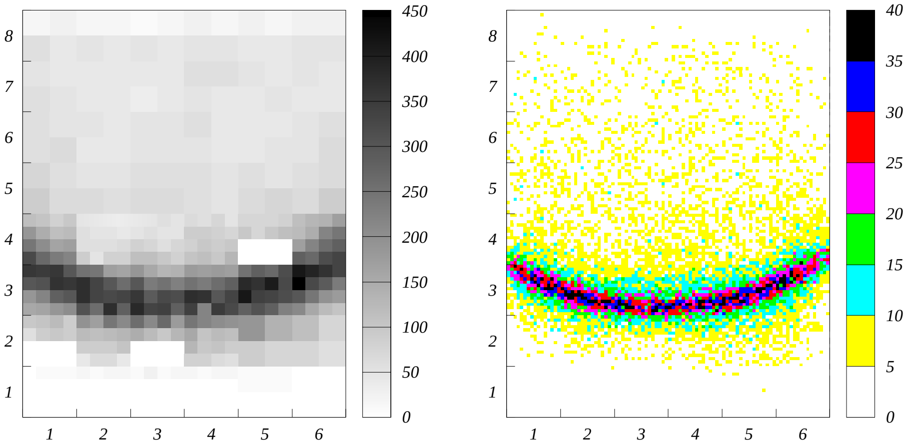

Slika 9.11: Porazdelitev zadetkov fotonov na detektorju fotonov, ki ga pokrivajo šestnajstkanalne fotopomnoževalke (levo) in porazdelitev popravljena s podatki iz sledilnega sistema (desno).

9.5.1 Meritev radija Čerenkovega obroča

Ker je naloga detektorja Čerenkovih obročev določitev kota pod katerim so Čerenkovi fotoni izsevani in s tem hitrosti nabitega delca, me je zanimalo s kolikšno natančnostjo lahko ta kot izmerim. Napako sem določil iz porazdelitve vseh zadetkov po radiju obroča Čerenkova. Porazdelitvi fotonov po Čerenkovem radiju za zadetke na detektorjih fotonov na področju z obema zrnatostima sta prikazni na sliki 9.12.

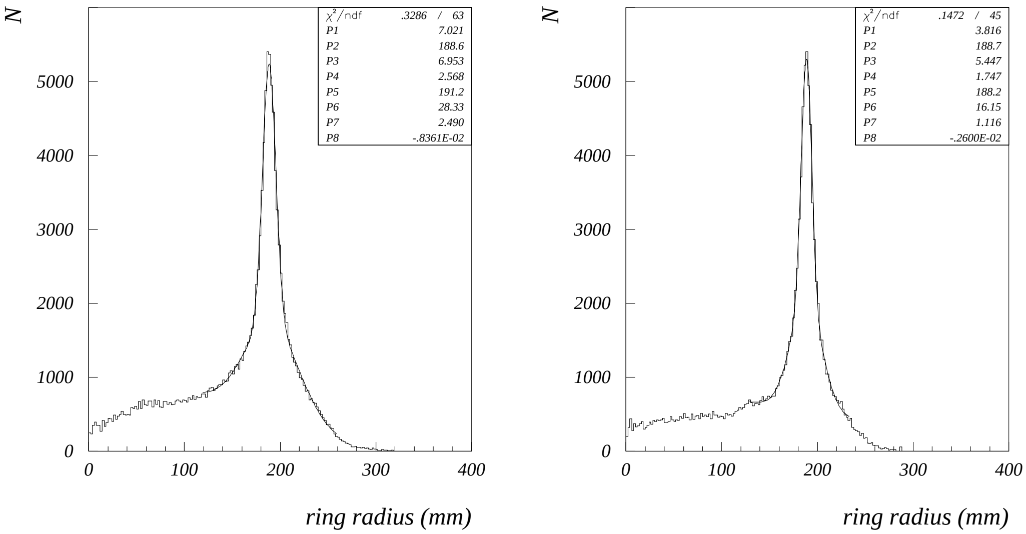

Slika 9.12: Porazdelitvi po Čerenkovem radiju za zadetke na detektorju fotonov pri uporabi štirikanalnih (levo) in šestnajstkanalnih (desno) fotopomnoževalk. Prikazana sta tudi rezultata prilagajanja s funkijo, ki je vsota dveh gaussovih in linearne funkcije $\mathrm{N} = \mathrm{P}_1 \cdot \mathrm{e}^{\frac{(\mathrm{r}-\mathrm{P}_2)^2}{2\mathrm{P}_3^2}} + \mathrm{P}_4 \cdot \mathrm{e}^{\frac{(\mathrm{r}-\mathrm{P}_5)^2}{2\mathrm{P}_6^2}} + \mathrm{P}_7 + \mathrm{P}_8 \cdot \mathrm{r}$.

Na grafu vidimo ozek vrh, ki ima obliko Gaussove krivulje in leži na ozadju.

To ozadje je posledica, v sevalcu detektorja, izsevanih fotonov Čerenkova, nabitih delcev elektromagnetnega plazu, ki so ga v postavitvi pred detektorjem obročev sprožili elektroni. Hkrati k ozadju prispevajo tudi fotoni Čerenkova elektronov, katerih pot ni bila pravilno izmerjena. S prilagajanjem Gaussove krivulje (za fotone delcev s pravilno izmerjeno potjo) in vsote Gaussove in linearne funkcije (za ozadje) sem dobljeni porazdelitvi določil širino ozkega vrha in s tem širino obroča Čerenkova na detektorju fotonov.

Rezultata napovedi in meritev sta zbrana v tabeli 9.1 in kažeta na dobro ujemanje. Pri tem je treba omeniti, da je ločljivost prototipa slabša od ločljivosti detektorja obročev pri poskusa HERA-B (enačba 9.19), zaradi večje napake, ki jo prispeva večkratno Coulombovo sipanje nabitih delcev in zamika optičnega zbiralnega sistema iz gorišče ravnine krogelnega zrcala.

	napoved σ_ϑ (mrad)	napoved σ_{r} (mm)	meritev σ_{r} (mm)
M4	1.40	7.0	7.0
M16	1.08	5.4	5.4

Tabela 9.1: Pričakovana in izmerjena ločljivost pri meritvi kota Čerenkova iz zadetka posameznega fotona za detektor fotonov opremljen s fotopomnoževalkami M4 in M16 ter optičnim zbiralnim sistemom.

9.5.2 Parameter odziva detektorja fotonov

Za ovrednotenje kakovosti delovanja detektorja obročev Čerenkova sem izmeril še povprečno število zaznanih fotonov v obroču Čerenkova in izračunal parameter odziva detektorja fotonov. Pri določitvi merjenega števila fotonov na dogodek sem upošteval, da detektor fotonov pokriva le del obroča Čerenkova. Iz izmerjenih podatkov sem najprej izračunal povprečno gostoto zadetkov detektorja fotonov za en delec v odvisnosti od razdalje do centra obroča Čerenkova (slika 9.13). Pri izračunu sem zaradi enostavnosti pri določanju sprejemnosti, uporabil porazdelitev brez upoštevanja podatkov sledilnega sistema. Dobljeni porazdelitvi sem prilagajal vsoto Gaussove krivulje za opis fotonov Čerenkova in linearne funkcije za opis ozadja.

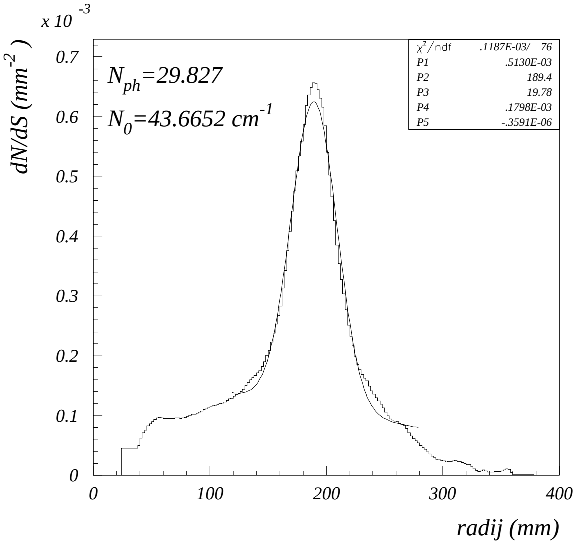

Slika 9.13: Povprečna gostota zadetkov za en elektron v odvisnosti od oddaljenosti od središča obroča in prilagajana funkcija, vsota Gaussove in linearne funkcije, $\frac{\mathrm{dN}}{\mathrm{dS}} = \mathrm{P}_1 \cdot \mathrm{e}^{\frac{(\mathrm{r}-\mathrm{P}_2)^2}{2\mathrm{P}_3^2}} + \mathrm{P}_4 + \mathrm{P}_5 \cdot \mathrm{r}$

Iz porazdelitve na sliki 9.13 dobim tako število zaznanih fotonov z integracijo

$$\mathrm{N_{det}} = 2\pi \int_0^\infty \left(\mathrm{P_1 e^{\frac{(r-P_2)^2}{2P_3^2}}} \right) \mathrm{rdr}. \tag{9.20}$$

Parameter odziva detektorja fotonov $\mathrm{N_0}$ pa sem določil z enačbo

$$\mathrm{N_0} = \frac{\mathrm{N_{det}}}{\mathrm{Lsin^2}\vartheta} = 43.6 \pm 2\ \mathrm{cm}^{-1}, \tag{9.21}$$

kjer sem upoštevl dolžino sevalca L = 5 m in kota Čerenkova $37.7(1 \pm 0.011)\ \mathrm{mrad}$. Pri oceni napake sem upošteval prispevka zaradi izbire opisa ozadja in napake pri meritvi radija Čerenkovega obroča. Pri tem je treba povedati, da je izračunani parameter odziva prototipa detektorja enak parametru odziva detektorja pri poskusu HERA-B ($\mathrm{N_0} = 43\mathrm{cm}^{-1}$).

9.6 Umeritev detektorja obročev Čerenkova

Detektor obročev Čerenkova pri poskusu HERA-B je bil pozimi 97 in spomladi 98 sestavljen. Detektor fotonov je bil opremljen s fotopomnoževalkami, optičnim zbiralnim sistemom in vso pripadajočo elektroniko, signalni izhodi pa so bili povezani z elementi čitalnega sistema. Ko je v začetku poletja 98 začel delovati sistem za zajemanje podatkov, je bila s tem omogočena izvedba testiranj, ki so bila potrebna za umeritev detektorja obročev Čerenkova. Manjše napake v delovanju detektorja, ki smo jih odkrili med testiranji, so bile odpravljene v enodnevnih vsakomesečnih dostopih do detektorja. Med takimi dostopi smo namestili tudi dodatne senzorje za nadzor in spremljanje delovanja detektorja iz kontrolne sobe.

Prva testiranja sem izvedel tako, da sem s kontrolnim izvorom svetlobe šibko, približno enakomerno osvetlil detektor fotonov, in opazoval njegov odziv in delovanje čitalnega sistema. Pri tem je bil glavni namen poiskati področja, ki ne delujejo pravilno, bodisi da se ne odzivajo (mrtvi kanali) ali imajo stalni odziv (šumeči kanali). Hkrati s tem sem preveril povezave med izhodnimi kanali fotopomnoževalk in vhodnimi kanali čitalnega sistema, tako da sem primerjal položaj področij na samem detektorju s krajem, ki jih ta mesta zasedajo na prikazovalniku površine detektorja fotonov.

Vse uporabljene fotopomnoževalke so bile, predno smo jih razvrstili po površini fotonskega detektorja, podvržene kontrolnim meritvam v laboratoriju, s katerimi smo ugotovili njihove lastnosti in pogoje, pri katerih je njihovo delovanje optimalno. Z meritvami v eksperimentalni dvorani sem v primeru šibke osvetljenosti detektorja fotonov s kontrolnim izvorom, ponovno izvedel sklop meritev za določitev optimalne napajalne napetosti fotopomnoževalk. Meritve so bile izvedene pri napajalnih napetostih med 500 in 900 V v korakih po 50 V. Na sliki 9.14 sta predstavljeni primerjavi laboratorijske in in situ meritve za oba tipa fotopomnoževalk. Predstavljeni podatki kažejo dobro ujemanje med laboratorijskimi meritvami in tistimi izvedenimi s končno postavitvijo detektorja.

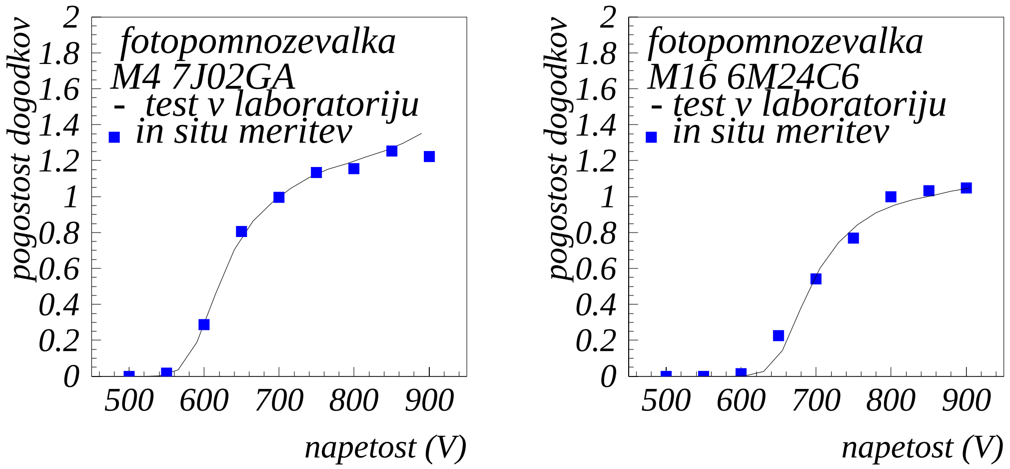

Slika 9.14: Pogostost zaznanih dogodkov na fotopomnoževalkah v odvisnosti od napajalne napetosti. S črto so predstavljeni podatki dobljeni med testiranji v laboratoriju, s kvadratki pa meritve pri devetih različnih napajalnih napetostih v eksperimetalni dvorani. Na levi sliki je predstavljena primerjava za štirikanalno fotopomnoževalko, na desni pa za šestnajstkanalno. Podatki so normirani s povprečno vrednostjo pogostosti dogodkov pri napetostih 750 V, 800 V in 850 V.

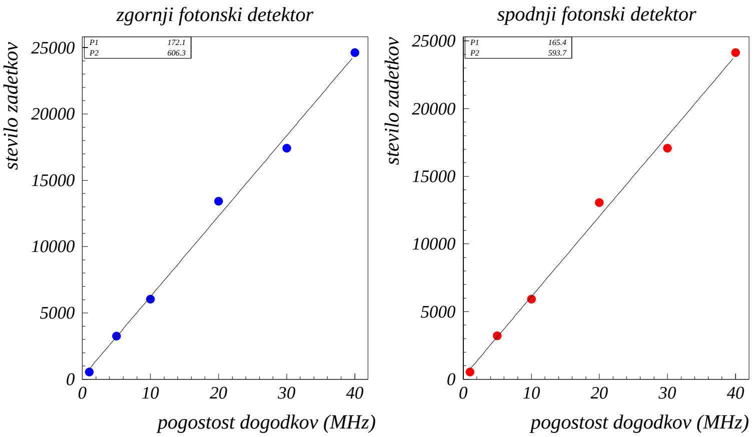

Slika 9.15: Število dogodkov na detektorju fotonov kot funkcija interakcijske pogostosti na območju med 1 MHz in 40 MHz.

Drugi sklop testiranj detektorja fotonov sem izvedel v eksperimentalnih pogojih kot jih pričkujemo med samimi meritvami. Tarča eksperimeta HERA-B je bila postavljena na obrobje protonskega žarka. Ta je v tarči sprožal reakcije, katerih nabiti reakcijski produkti so sevali svetlobo Čerenkova, ki jo je zaznal detektor fotonov. Preveril sem odziv detektorja v odvisnosti od interakcijske pogostosti. Na sliki 9.15 so predstavljene odvisnosti števila zaznanih zadetkov na obeh polovicah detektorja fotonov pri interakcijskih pogostostih 1 MHz, 5 MHz, 10 MHz, 20 MHz, 30 MHz in 40 MHz. Odziva obeh polovic detektorja fotonov odlikuje pričakovana sorazmernost z interakcijsko pogostostjo.

Končni test delovanja detektorja obročev Čerenkova je bil povezan z iskanjem obročev Čerenkova ter primerjavo zaznanega števila zadetkov v obroču s predvidevanji. Ker sledilni sistem spektrometra še ni deloval in tako nisem mogel uporabiti podatkov o poteh nabitih delcev za določitev središča obročev Čerenkova, sem se pri svojih analizah omejil le na dogodke, kjer sem lahko položaj obročev Čerenkova nedvoumno določil že samo na osnovi zaznanih zadetkov na detektorju fotonov. Dva primera takih dogodkov, s primerjavo števila zaznanih in pričakovanih zadetkov v obroču, sta predstavljena na slikah 9.16 in 9.17.

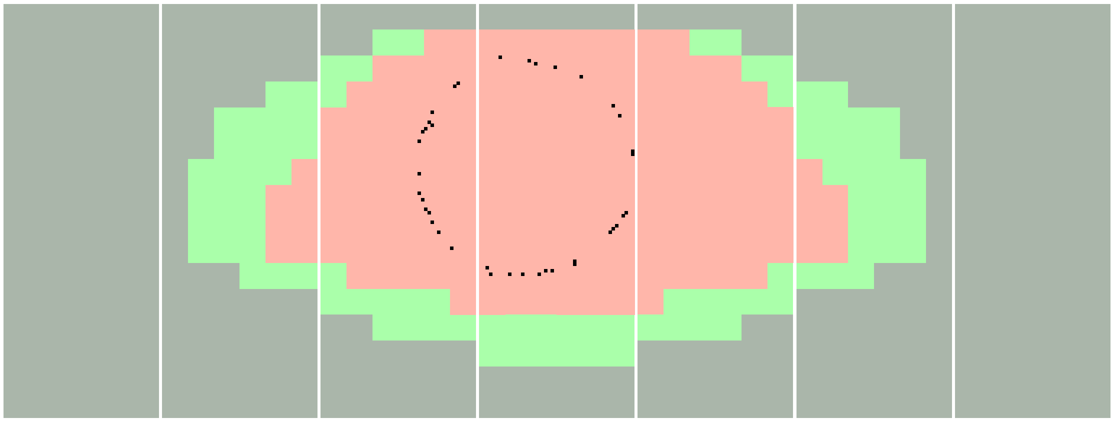

Slika 9.16: Površina detektorja fotonov z obročem Čerenkova in 33 zaznanimi fotoni. Iz radija obroča Čerenkova izračunani kot Čerenkova je 51.9 ± 0.5 mrad, pri katerem izračun predvideva 31 ± 2 zaznanih fotonov.

Na sliki 9.18 je predstavljena odvisnost števila detektiranih fotonov v obroču Čerenkova od kota Čerenkova za skoraj 200 analiziranih dogodkov skupaj z linijama, ki označujeta širino porazdelitve zaradi Poissonove porazdelitve po številu fotonov.

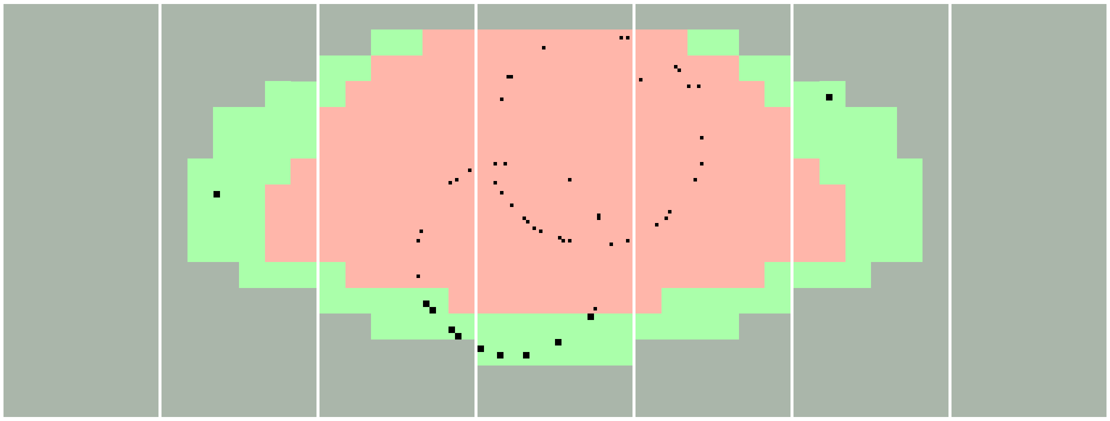

Slika 9.17: Dogodek z dvema zaznanima obročema Čerenkova na detektorju fotonov: spodnji obroč z 22 zaznanimi fotoni na področju, ki ga pokrivajo tako 4 kot 16 kanalne fotopomnoževalke in izmerjenim kotom Čerenkova $45.5\ \pm 0.5\ \mathrm{mrad}$, pri katerem izračun predvideva 23.8 ± 1.5 zadetkov ter zgornji obroč s 27 zadetki in kotom Čerenkova $49.8\ \pm 0.5\ \mathrm{mrad}$ ter pričakovanimi 28.5 ± 1.8 zadetki.

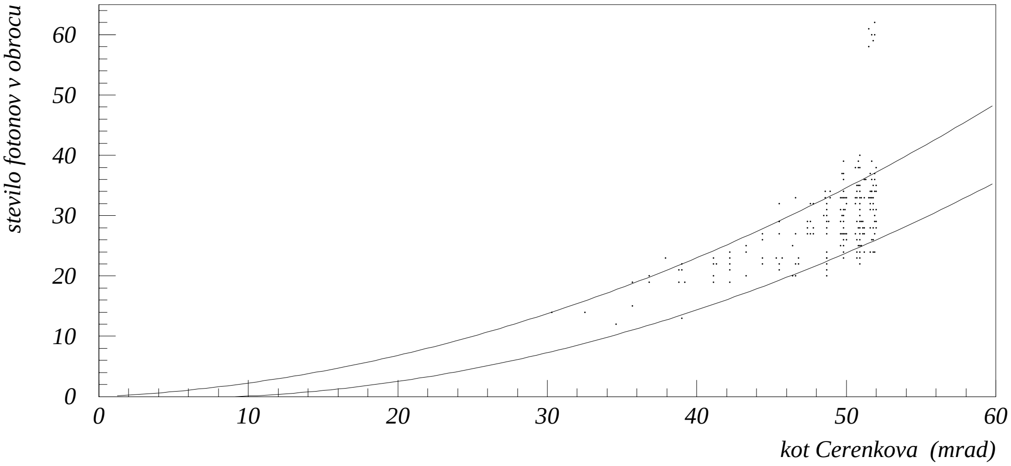

Slika 9.18: Število detektiranih fotonov v obroču Čerenkova v odvisnosti od kota Čerenkova.

9.7 Zaključek

Na osnovi opravljenih meritev lahko zaključim, da je delovanje števca obročev Čerenkova pri poskusu HERA-B zanesljivo in bo omogočalo ločevanje med pioni in kaoni do gibalnih količin 50 GeV/c. Tako bo prispeval k uspešnemu delovanju celega spektrometra HERA-B in hkrati preizkušal nove tehnologije za naslednjo generacijo eksperimentov v fiziki visokih energij. Prve preliminarne rezultate eksperimeta HERA-B lahko pričakujemo v naslednjem letu.

References

[1] T. Lohse *et al.*, An Experiment to Study CP Violation in the B System Using an Internal Target at the HERA Proton Ring, Proposal, DESY-PRC 94/02 (1994)

[2] T. Lohse et al., *An Experiment to Study CP Violation in the B System Using an Internal Target at the HERA Proton Ring, Design Report*, DESY-PRC 95/01 (1995)

[3] I.Y. Bigi et al., in C. Jarlskog (ed.): CP violation: *Advanced Series on Directions in High Energy Physics,* **Vol 3** p. 175, World Scientific, Singapore(1989).

[4] T. Alexopoulos et al. (E771 Collaboration), FERMILAB PUB-97-246-E, 1997

[5] T. Lohse *et al.,* Nucl. Instr. and Meth. **A408** (1998) 154

[6] W.R. Leo, *Techniques for Nuclear and Particle Physics Experiments,* Springer-Verlag, Berlin (1987).

[7] J. H. Christenson, J. W. Cronin, V. L. Fitch, R. Turlay, Phys. Rev. Lett. **138** (1964) 13

[8] A. Ali *B Decays - Introduction and Overview,* B Decays, World Scientific Publishing, 1994. (editor Sheldon Stone)

[9] Y. Nir and H. R. Quinn *Theory of CP Violation in B Decays,* B Decays, World Scientific Publishing, 1994. (editor Sheldon Stone)

[10] K. Ehret, Performance of the HERA B target and interference with HERA operation, Near Beam Symposium Proceedings, FNAL Sept. 1997

[11] F. Sauli et al., IEEE Trans.Nucl.Sci.44,646, (1997)

[12] K. Riechmann, Overview of the HERA B Vertex Detector System and First Results from Prototype Runs, HERA B Report (97-251)

[13] K. T. Knöpfle, Nucl. Instr. and Meth. **A368** (1995) 192.

[14] D. Ressing, DAQ architecture for HERA B, HERA B Internal Note

[15] J. V. Jelley, *Cherenkov Radiation*, Pergamom Press, New York (1958)

[16] C. Grupen, *Particle Detectors*, Cambridge University Press, Cambridge (1996).

[17] Y. Ypsilantis and J. Seguinot, Nucl. Instr. and Meth. **A343** (1994) 30

[18] Particle Data Group, Rewiew of Particle Properties, Phys. Rev. **D 50** (1994) 1253

[19] G. Močnik, Efficiency of b Flavour Tagging with Kaonic Charge in the HERA B Spectrometer, B. Sc. Thesis Ljubljana (1996)

[20] P. Križan and M. Starič Nucl. Instr. and Meth. **A379** (1996) 124

[21] D. Dujmić and R. Schwitters, Location of best focus for RICH photon detectors, RICH Internal Report (February, 1998)

[22] P. Križan et. al., Nucl. Instr. and Meth. **A371** (1996) 295

[23] D. Dujmić, K.Reeves, Mirror Tiling for RICH Detector, RICH Internal Report (October, 1997)

[24] G. Lenzen *et al.* (DELPHI Coll.), Nucl. Instr. and Meth. **A343** (1994) 268

[25] P. Križan et. al., HERA-B RICH Notes 96-013, Cleaning System for the C_4F_{10} Gas - a Survey of Systems under Design

[26] D. Broemmelsiek HERA-B RICH Radiator Gas System Report, RICH Internal Report (April, 1997)

[27] S. Korpar, Development, assembly and test of a ring imaging Čerenkov detector, Ph. D. Thesis, Ljubljana (1997)

[28] D. Škrk, The performance of a wire chamber with the light sensitive mixture methane - TMAE at high counting rates, M. Sc. Thesis, Ljubljana (1996)

[29] S. Korpar, P. Križan, A. Stanovnik, M. Starič and D. Škrk, Aging and rejuvenation of a TMAE+ methane multiwire photon detector, to be published in IEEE Trans. Nucl. Sci.

[30] R. Pestotnik, A multianode photomultiplier as a position sensitive detector of Čerenkov photons, B. Sc. Thesis, Ljubljana (1996)

[31] HERA-B RICH Decision Memorandum (1996)

[32] J. McGill, RICH Photon Detector Mechanical Design, Austin meeting summary (March, 1997)

[33] Hamamatsu, Preliminary specifications for R5900 M16 and M4 photomultiplier tubes, 1995

[34] S. Korpar, R. Pestotnik, P. Križan, quality assessment tests of Hamamatsu M16 photomultipliers IJS Report IJS-DP 7681(April, 1997)

[35] S. Korpar, R. Pestotnik, P. Križan, Quality assessment tests of Hamamatsu M16 and M4 photomultipliers IJS Report IJS-DP 7769 (July, 1997)

[36] T. Oest, A study of a RICH photon detector design, HERA B Internal Report (September, 1996)

[37] P. Križan, M. Starič, PMT tiling Schemes, IJS Report (November, 1997)

[38] J. McGill and R. Schwitters, Simulating imaging properties of the two lens prototype light collector, RICH Internal Report (September 1997)

[39] D. Broemmelsiek, Aspherical lens design for HERA-B RICH light collection, RICH Internal Report (April 1997)

[40] D. Broemmelsiek, The photon detector of the HERA-B RICH (Poster Session), RICH 98 International workshop, Ein-Gedi, Israel (November 1998)

[41] R. Eckmann, M. Ispirian, S. Karabekyan, J. McGill, R. Schwitters, D. Broemmelsiek, Measurements of HERA-B RICH two lens telescope properties, RICH Internal Report (September 1997)

[42] J. L. Rosen, Nucl. Instr. and Meth. **A408** (1998) 191

[43] F. M. Newcomer, S. Tedja, R. Van Berg, J. Van der Spiegal and H.H. Williams, IEEE Transactions on Nuclear Science, **40**, 4, (August 1993) 630

[44] I. Ariño, M. Chmeissani, A. Garcia, Ll. Garrido, R. Miquel, D. Peralta and J. Sieiro, Test of the ASD8 boards, RICH Internal Report (March, 1998)

[45] FieldPoint User Manual, National Instruments Corporation

[46] P. Križan et. al., Nucl. Instr. and Meth. **A371** (1996) 151

[47] P. Križan et. al., IEEE Trans. on Nucl. Sci. **VOL. 42** (1995) NO. 4

[48] T. Hamacher et. al., Nucl. Instr. and Meth. **A371** (1996) 289

[49] J. Pyrlik et. al., Nucl. Instr. and Meth. **A414** (1998) 170

[50] T. Hamacher, Nucl. Instr. and Meth. **A368** (1995) 234

[51] P. Križan et. al., Nucl. Instr. and Meth. **A387** (1997) 146

[52] M. Starič, Development, construction and tests of an apparatus for positron emission tomography, Ph. D. Thesis Ljubljana (1992)

[53] M. Zavrtanik, IJS-DP-6470, Ljubljana (1993)

[54] P. Križan et. al., Nucllear Physics B (Proc. Suppl.) **44** (1995) 252

[55] P. Križan et. al., Nucl. Instr. and Meth. **A367** (1995) 257

[56] P. Križan, Nucl. Instr. and Meth. **A394** (1997) 27

[57] S.Korpar, R. Pestotnik, P. Križan, Beam test of a RICH with C_4F_{10} gas as radiator and an array of MA PMTs for photon detection, IJS Report IJS-DP 7673 (March, 1997)

[58] J. Bastos et al., Monitoring of the HERA B RICH photodetector, IEEE Nuclear Science Symposium, Poster Session on Nuclear Science, **N20-2**, (November 1998)

[59] R. Schwitters, First Light, HERA B Report **98-142** (August, 1998)

[60] O. Ullaland, private communication

[61] R. Schwitters, Testing Mirror Quality, RICH Internal Report (January, 1997)

[62] J. Pyrlik, K. Lau Proposal for a High Voltage System for the RICH, RICH Internal Report (July, 1997)

Izjavljam, da je disertacija rezultat samostojnega raziskovalnega dela.

Damijan Škrk

Ljubljana, junij 1999